2014

Electrochemical, Interfacial, and Surface Studies of the Conversion of Carbon Dioxide to Liquid Fuels on Tin Electrodes

Jingjie Wu
University of South Carolina - Columbia

Recommended Citation

Wu, J.(2014). *Electrochemical, Interfacial, and Surface Studies of the Conversion of Carbon Dioxide to Liquid Fuels on Tin Electrodes.* (Doctoral dissertation). Retrieved from http://scholarcommons.sc.edu/etd/2681

ELECTROCHEMICAL, INTERFACIAL, AND SURFACE STUDIES OF THE CONVERSION OF CARBON DIOXIDE TO LIQUID FUELS ON TIN ELECTRODES

by

Jingjie Wu

Bachelor of Science
Wuhan University of Technology, 2006

Master of Science
Wuhan University of Technology, 2009

Submitted in Partial Fulfillment of the Requirements

For the Degree of Doctor of Philosophy in

Chemical Engineering

College of Engineering and Computing

University of South Carolina

2014

Accepted by:

Xiao-Dong Zhou, Major Professor

John W. Weidner, Committee Member

John R. Regalbuto, Committee Member

Qian Wang, Committee Member

Lacy Ford, Vice Provost and Dean of Graduate Studies

DEDICATION

To my parents and my wife, Ying

ACKNOWLEDGEMENTS

I am grateful to so many people that have provided me invaluable help and support in completing this dissertation. Firstly, I'd like to send my special thanks to my advisor Dr. Xiao-Dong Zhou for his insightful suggestion of my doctoral research project and critical mentorship during my years in his group. He taught me to have the sense of thinking deep and beyond, which is so beneficial to not only my research but also my future career. I also own gratitude to the committee members, Dr. John W. Weidner, Dr. John R. Regalbuto and Dr. Qian Wang, for their constructive suggestions to my research.

I would also like to thank my colleague, Dr. Fusheng Ke for his useful help in the experimental setup and inspired discussions of the results. I am also thankful to Pranav Sharma, Frank Risalvato, and Bradley Harris for their help in data collecting and analyzing. I am also grateful to Dr. Perry J. Pellechia for his help to quantify my samples with nuclear magnetic resonance spectroscopy. I also thank all the faculties that delivered me the fabulous lectures on the fundamentals of chemical engineering. These courses provided me useful tools to carry out my research deeper.

I also thank my many classmates and friends that I met here at University of South Carolina. In particular, Jingyi, Tingting, Hong and Song brought a lot of fun in my life and provided strong support in my study. This precious friendship is an extra invaluable gift for me in addition to doctorate degree over the years in Columbia.

Finally, I am grateful to my family, especially my wife Ying, for their love, support and encouragement.

ABSTRACT

The electrochemical reduction of carbon dioxide (CO_2) into liquid fuels especially coupling with the intermittent renewable electricity offers a promising means of storing electricity in chemical form, which reduces the dependence on fossil fuels and mitigates the negative impact of anthropogenic CO_2 emissions on the planet. Although converting CO_2 to fuels is not in itself a new concept, the field has not substantially advanced in the last 30 years primarily because of the challenge of discovery of structural electrocatalysts and the development of membrane architectures for efficient collection of reactants and separation of products. An efficient catalyst for the electrochemical conversion of CO_2 to fuels must be capable of mediating a proton-coupled electron transfer reaction at low overpotentials, reducing CO_2 in the presence of water, selectively converting CO_2 to desirable chemicals, and sustaining long-term operations (**Chapter 1**). My Ph.D. research was an investigation of the electroreduction of CO_2 on tin-based electrodes and development of an electrochemical cell to convert CO_2 to liquid fuels.

The initial study focused on understanding the CO_2 reduction reaction chemistry in the electrical double layer with an emphasis on the effects of electrostatic adsorption of cations, specific adsorption of anion and electrolyte concentration on the potential and proton concentration at outer Helmholtz plane at which reduction reaction occurs. The variation of potential and proton concentration at outer Helmholtz plane accounts for the difference in activity and selectivity towards CO_2 reduction when using different electrolytes (**Chapter 2**).

Central to the highly efficient CO_2 reduction is an optimum microstructure of catalyst layer in the Sn gas diffusion electrode (GDE) consisting of 100 nm Sn nanoparticles to facilitate gas diffusion and charge transfer. This microstructure in terms of the proton conductor fraction and catalyst layer thickness was optimized to maximize the triple phase boundary length for simultaneous high current density and selectivity towards formate formation (**Chapter 3**). The Sn GDEs was incorporated into a home-designed scalable full electrochemical cell which features a buffer layer of circulating liquid electrolyte mediating the proton concentration at cathode electrode surface. The Sn GDEs exhibited excellent short-term performance for CO_2 reduction with high selectivity towards formate formation at low overpotentials in the full electrochemical cell. Additionally, coupling water oxidation and CO_2 reduction was demonstrated in this full electrochemical cell to mimic biosynthesis (**Chapter 4**).

The rapid degradation of selectivity towards formate formation on Sn GDEs in the full electrochemical cell, however, was observed during long-term operation. The degradation mechanism was unraveled due to the decrease of electrode potential resulted from substantial increase of internal ohmic resistance of the full electrochemical cell. The unexpected rise of internal ohmic resistance was attributed to the pulverization of 100 nm Sn nanoparticles due to the hydrogen diffusion induced stress. Based on the understanding of the origin of Sn nanoparticles pulverization, SnO_2 nanoparticles of 3~3.5 nm close to the critical size were utilized and reduced in situ to form Sn catalyst for electrochemical reduction of CO_2. The pulverization was suppressed and subsequently a stable performance of electrodes was obtained (**Chapter 5**).

Due to the affinity to oxygen, Sn nanoparticle surface is covered by a native thin oxide layer. The performance of Sn GDEs towards CO_2 reduction strongly depends on the initial thickness of the surface oxide layer. The selectivity towards formate production dropped while the hydrogen yield increased as the initial thickness of the oxide layer increased (**Chapter 6**). These results suggest the underlying importance of surface structure on the selectivity of Sn electrode for CO_2 reduction and provide insight into the development of more efficient catalysts.

TABLE OF CONTENTS

LIST OF TABLES

LIST OF FIGURES

LIST OF SYMBOLS

T_c	Critical temperature.
P_c	Critical pressure.
ρ_c	Critical density.
ΔG_f^o	Gibbs free energy of formation.
ΔG	Gibbs free energy of reaction.
ΔS	Entropy change of reaction.
ΔH	Enthalpy change of reaction.
E^o	Standard potential.
$E^{o'}$	Apparent standard potential.
E_2	Potential at Outer Helmholtz Plane.
η	Faradaic efficiency.
ζ	Zeta potential.
F	Faraday’s constant.
C	Total coulomb of electrons passed during the duration of electrolysis.
κ	Debye length.
α	Curvature radius of the electrode.
C_i	Bulk concentration of ion i in the electrolyte.
z_i	Ionic valence.
ε	Dielectric constant of aqueous solution.
R	Gas constant.

T	Absolute temperature.
p^o	Standard pressure, 1.013 bar.
$[H^+]$	Proton concentration.
α	Conversion factor based on calibration of the GC with a standard sample.
θ	Photoelectron take-off angle.
λ_{ox}	Inelastic mean free path of the oxide.
λ_m	Inelastic mean free path of the metal.
I_{ox}	Area percentages of the oxide peak in the high resolution X-ray photoelectron spectroscopy.
I_m	Area percentages of the metal peak in the high resolution X-ray photoelectron spectroscopy.
N_m	Volume densities of the metal atoms in the metal.
N_{ox}	Volume densities of the metal atoms in the oxide.

LIST OF ABBREVIATIONS

AES	Auger Electron Spectroscopy
ASR	Area Specific Resistance
CCM	Catalyst Coated Membrane
CCS	Carbon Dioxide Capture and Sequestration
DR	Dry Reforming
EDL	Electrical Double Layer
EDS	Energy Dispersive X-ray Spectroscopy
EIS	Electrochemical Impedance Spectroscopy
FE	Faradaic Efficiency
FT	Fischer-Tropsch
GC	Gas Chromatography
GCS	Gouy Chapman Stern
GDE	Gas Diffusion Electrode
GDL	Gas Diffusion Layer
HER	Hydrogen Evolution Reaction
HRTEM	High-resolution Transmission Electron Microscopy
IHP	Inner Helmholtz Plane
IMFP	Inelastic Mean Free Path
NMR	Nuclear Magnetic Resonance
OHP	Outer Helmholtz Plane

ORR	Oxygen Reduction Reaction
PEMFC	Proton Exchange Membrane Fuel Cell
PZC	Point of Zero Charge
RWGS	Reverse Water Gas Shift
SCE	Saturated Calomel Electrode
SEM	Scanning Electron Microscopy
SOEC	Solid Oxide Electrolysis Cell
SOFC	Solid Oxide Fuel Cell
TEM	Transmission Electron Microscopy
TSP	Sodium 3-(trimethylsilyl) propionate 2, 2, 3, 3-d (4)
XPS	X-ray Photoelectron Spectroscopy

Chapter 1

Introduction and Literatures Review

1.1 Challenges in Energy and Climate Change

The world experienced an energy revolution brought upon by black coal two hundred years ago, which launched the Industrial Age. A century later, petroleum and natural gas as versatile and high quality energy products joined coal as principal fuels for the industrialized world's tremendous thirst for energy. At present, about 80% of all primary energy in the world is derived from fossil fuels with oil accounting for 32.8%, coal for 27.2% and natural gas for 20.9% (Energy Information Administration, EIA, 2011). In the coming years, petroleum and coal are projected to remain as the dominant energy sources while natural gas consumption is believed to increase rapidly enough to eventually surpass coal by 2020. Although fossil fuels are still the engine behind the industrialized world, there are significant concerns associated with their sustainability, depletion and cost. The **Figure 1.1** shows the world conventional oil production scenarios. These scenarios were calculated based on the estimation of oil demand growth and world's conventional technically recoverable crude oil resource base. In the case of United States Geological Survey’s (USGS's) mean resource estimate, if 2% production growth continues until peak production, world conventional crude oil production would be expected to peak in 2037 at a volume of 53.2 billion barrels per year and then following a decline at an reserves to production (R/P) ratio of 10. The similar depletion situation also applies to the coal and natural gas. New sustainable energy sources are essential to prevent the energy crisis that will face in the future.

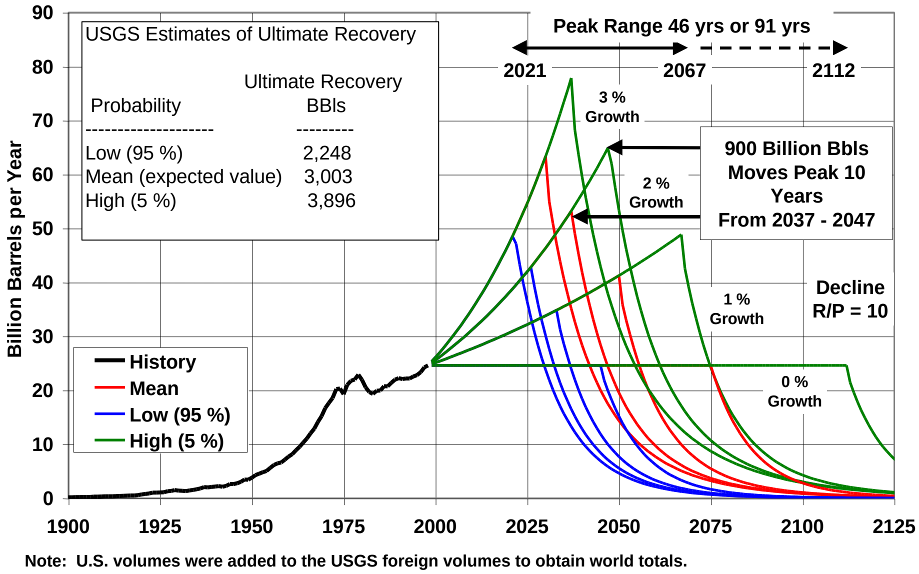

Figure 1.1. EIA world conventional oil production scenarios.

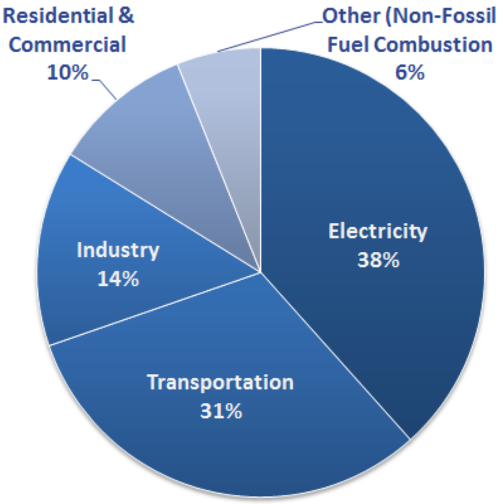

Figure 1.2. U.S. carbon dioxide emissions by source.

Furthermore, the combustion of fossil fuels, e.g. during energy conversion, releases carbon dioxide (CO_2) and other greenhouse gases that contribute to global warming. Energy conversion for electricity and transport is responsible for 70% of CO_2 emissions (**Figure 1.2**). The continuous emission of CO_2 results in the rise of CO_2

concentration in atmosphere. Atmospheric CO_2 concentration increased to 315 ppmv in 1958 and further to 395.15 ppmv in August 2013 based on actual analysis at Mauna Loa Observatory, Hawaii[1], compared to only slightly increase over the period of a thousand years till 20th century, from 280 ppmv in 1000 to 295 ppmv in 1900 based on Antarctica ice core data (**Figure 1.3**). In order to mitigate the global mean temperature increase by 2.0-2.4 °C, the global CO_2 emission would have to be reduced by 50-80% by 2050 (based on the emission level in 2000). [2]

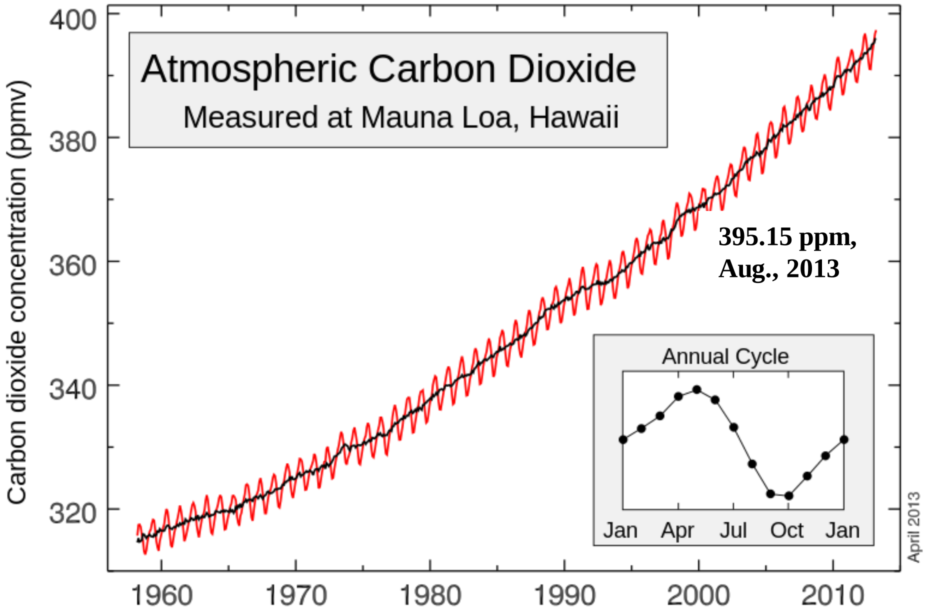

Figure 1.3. Keeling curve of atmospheric carbon dioxide record at Mauna Loa Observa-tory, Hawaii.

1.2 Strategies to Control and Utilize CO_2 for Sustainable Development

In order to control the CO_2 emission, the technology of CO_2 storage as well as utilization needs to be developed to satisfy both energy efficiency and cost.[3-5] The emphasis of CO_2 storage is put on CO_2 capture and geologic storage. CO_2 utilization efforts focus on pathways of developing beneficial uses of the CO_2 where geologic storage may not be an optimum solution. Currently, there are essentially three pathways for CO_2 conversion and utilization as follows (**Figure 1.4**):[4]

- Use CO_2 as feedstock to produce industrially useful chemicals and materials that adds value to the products.
- Recycle CO_2 for fuel synthesis via renewable energy sources for sustainable development.
- Apply CO_2 as a medium for energy recovery, heat transfer and solvent.

The reduction of CO_2 to fuels using non-carbon based energy sources (such as solar, wind, nuclear, or geothermal), although highly challenging, is expected to be a truly sustainable alternative to reduce CO_2 emission.[6] Among the leading synthetic approaches for CO_2 reduction include electrochemical reduction, solar driven photochemical reduction, biological reduction, and thermal catalysis such as hydrogenation.[5, 7] Nevertheless, both the storage and utilization rely on the understanding of the physical and chemical properties of CO_2.

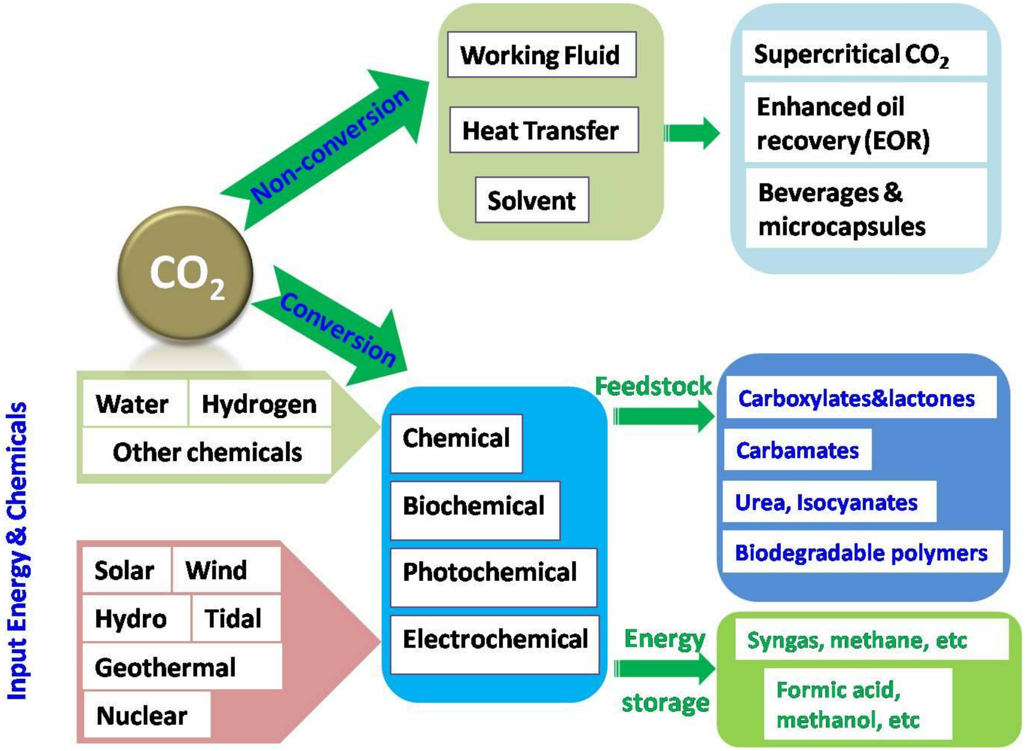

Figure 1.4. Different pathways of utilizing CO_2.

1.2.1 Physical and Chemical Properties of CO_2

CO_2 is a colorless and odorless gas. The molecule is linear with a double bond between the carbon and oxygen atoms (O=C=O). The two C-O bonds are equivalent and are short (116.3 pm). The CO_2 molecular orbitals (MO) diagram is based on a C atom and an O--O ligand fragment. Carbon 1s and oxygen 2s are assumed to be nonbonding. Carbon 2s and $2p_z$ orbitals are hybrized to form sp orbitals. σ-bonding interacts between oxygen $2p_z$ and carbon sp orbital, while π-bonding is formed between oxygen $2p_x$ or $2p_y$ orbitals with "empty" orbitals of the same kinds on the central carbon. The carbon atom in the CO_2 molecule is electrophilic and therefore, can interact via chemisorption with electron rich catalyst (e.g. typically metal) surface resulting in bending of CO_2. The oxygen atom in the bent CO_2 molecule can be easily attacked by protons while the C atom is prone to be attacked by the adsorbed H atom, however, requiring high activation energy. Since CO_2 is centrosymmetric, the molecule has no permanent electrical dipole. Consistent with this fact, only two vibrational bands are observed in the IR spectrum, an antisymmetic stretching mode at 2349 cm^{-1} and a bending mode near 666 cm^{-1}. A symmetric stretching mode at 1388 cm^{-1} is only observed in the Raman spectrum.

Table 1.1 provides a summary of the physical and chemical properties of CO_2.[4] At atmospheric pressure and 0 ^{o}C, the gas CO_2 density is 1.976 g l^{-1}, 1.5 times heavier than air. **Figure 1.5a** shows the phase diagram of CO_2.[3] CO_2 can be transferred to liquid by compressing to 2 MPa and cooling to -18.8 ^{o}C, or by compressing to higher pressure of 5.78 MPa at 21.8 ^{o}C. At the triple point of 56.6 8 ^{o}C and 0.518 MPa, three phases of gas, liquid and solid co-exist. The solid CO_2 can sublimate directly into gas without going

Table 1.1. Physical and chemical properties of carbon dioxide (adapted from ref. 4).

Property	**Value and unit**
Molecular weight	44.01 g/mol
Sublimation point at 1 atm (101.3 kPa)	-78.5 ^{o}C
Triple point at 5.1 atm (518 kPa)	-56.5 ^{o}C
Triple point pressure	5.1 atm
Critical temperature (T_c)	31.04 ^{o}C
Critical pressure (P_c)	7383 kPa
Critical density (ρ_c)	0.468 g/l
Gas density at 0 ^{o}C and 1 atm	1.976 g/l
Liquid density at 0 ^{o}C and 1 atm	928 g/l
Solid density	1560 g/l
Specific volume at 1 atm and 21 ^{o}C	0.546 m^3/kg
Latent heat of vaporization	
at the triple point (-78.5 ^{o}C)	353.4 J/g
at 0 ^{o}C	231.3 J/g
Viscosity at 25 ^{o}C and 1 atm CO_2	0.015 cP
Solubility in water at	
0 ^{o}C and 1 atm	0.3346 g/100g-H_2O
25 ^{o}C and 1 atm	0.1449 g/100g-H_2O
Heat of formation at 25 ^{o}C,	-393.5 kJ/mol
Entropy of formation at 25 ^{o}C,	213.6 kJ/mol
Gibbs free energy of formation at 25 ^{o}C	-394.3 kJ/mol
Heat capacity under constant pressure at 25 ^{o}C	37.1 J/(mol K)
Heat capacity under constant volume at 25 ^{o}C	28.1 J/(mol K)
Thermal conductivity	14.65 mW/(m K)

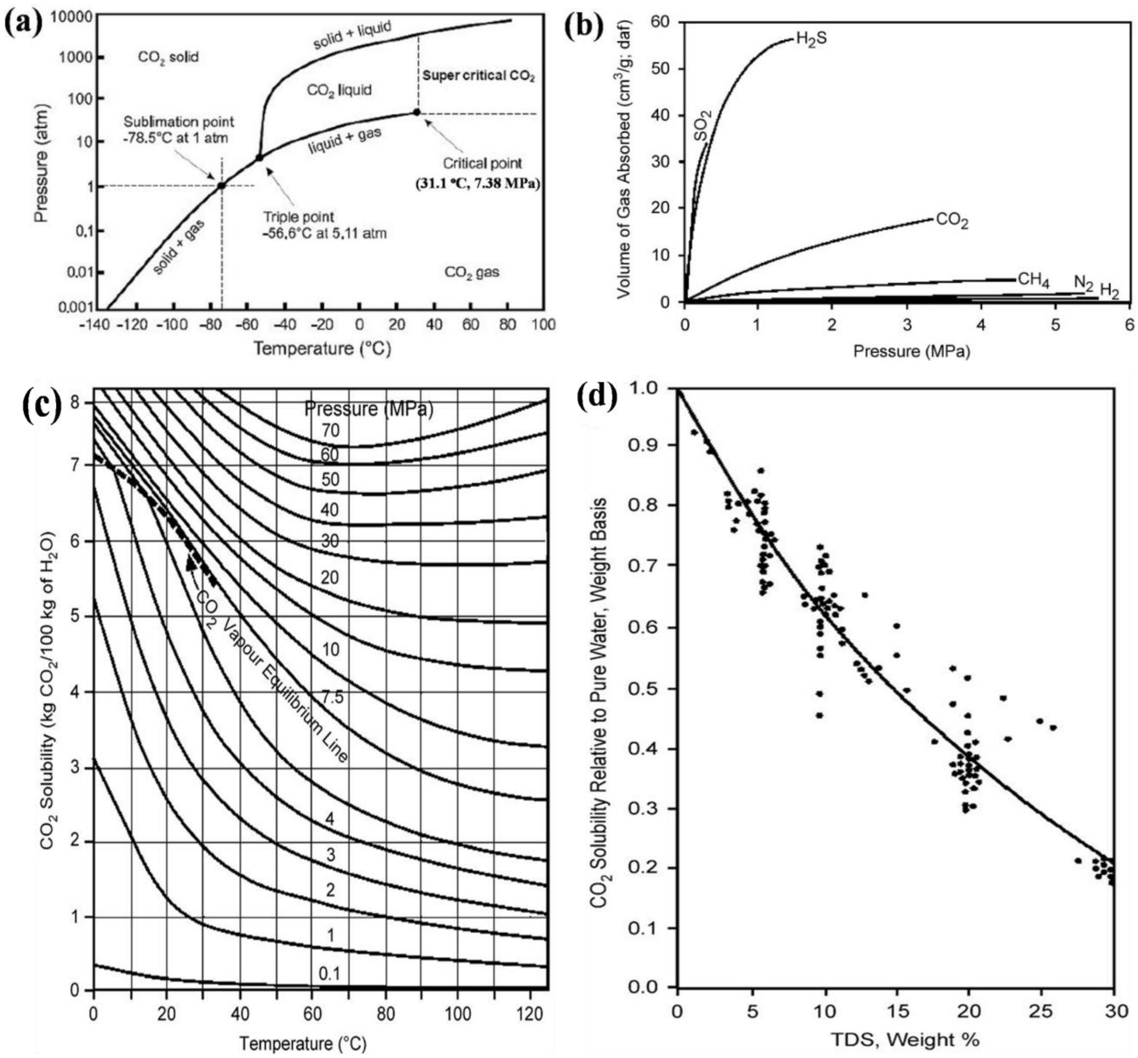

Figure 1.5. Relevant characteristics of CO_2: (a) phase diagram; (b) adsorption on coal (c) solubility in fresh water; and (d) decrease in solubility with increasing water salinity (adapted from ref. 3).

through the liquid phase upon absorbing heat, and thus it is called dry ice. If the pressure on dry ice is reduced to atmospheric pressure, the temperature of dry ice drops to -78.5 ^{o}C. When the temperature and pressure are above the critical point of 31.8 ^{o}C (T_c) and 7.38 MPa (P_c), CO_2 becomes a supercritical fluid which is widely used as a solvent in chemical extraction industry. The characteristic of greater CO_2-coal affinity of adsorption enables sequestering CO_2 in coal seams or enhancing the methane recovery (**Figure 1.5b**). The solubility of CO_2 in water is 0.033 mol l^{-1} at 25 ^{o}C and 1 atm.[8] The solubility in water increases with the increasing of pressure and decreasing of temperature (**Figure 1.5c**) and water salinity (**Figure 1.5d**).

1.2.2 Thermodynamics of CO_2

In order to chemically convert CO_2 to chemicals or fuels, a substantial input of energy and often active catalysts, is required due to its stable molecule involving rather low energy content (ΔG_f^o = -394 kJ mol^{-1} in gas phase). The Gibbs-Helmholtz relationship describes the change of Gibbs energy of a system as a function of temperature (Eq. 1.1). The entropy contribution through the term (-TΔS) makes little contribution to the thermodynamic driving force for any reaction involving CO_2 so that the value of the enthalpy change ΔH is a good guide to thermodynamic feasibility.

$$\Delta G = \Delta H - T\Delta S \tag{1.1}$$

The reaction involving CO_2 as a single reactant is more energy-demaning. For example, in Eq. (1.2), the cleavage of C-O bond in CO_2 to form CO and O_2 associates a large positive under standard conditions (1 atm pressure for each product or reactant and 298 K temperature), ΔH^o (293 kJ mol^{-1}). However a more favorable enthalpy of reaction can be achieved if less stable reactants and more stable products are involved.[9] For example, hydrocarbons can be used as reductants, such as CO_2 reforming as shown in Eq. (1.3) requiring less energy with ΔH^o (247.3 kJ mol^{-1}). The reverse water gas-shift reaction (Eq. 1.4) that is hydrogenation of CO_2 is more thermodynamically favorable.

$$2CO_2 = 2CO + O_2 \qquad \Delta H^o = 293\ \text{kJ/mol}\ CO_2 \tag{1.2}$$

$$CO_2 + CH_4 = 2CO + 2H_2 \qquad \Delta H^o = 247.3\ \text{kJ/mol}\ CO_2 \tag{1.3}$$

$$CO_2 + H_2 = CO + H_2O(g) \qquad \Delta H^o = 41.2\ \text{kJ/mol}\ CO_2 \tag{1.4}$$

If more energy is provided to the reverse water gas-shift reaction by increasing the reaction temperature, for example at 1500 K, the reaction becomes slightly exergonic ($\Delta G^o = -1.07$ kJ mol^{-1}).

Table 1.2. Free Gibbs energy and standard potential for electrochemical reduction of CO_2.

Reaction	**$\Delta G^{o\,a}$ (kJ/mol)**	**E^o / V vs. SHE**	**$E^{o'}$/ V vs. SHE^b**
$CO_2 + e^- = CO_2^{\bullet -}$	183.32	-1.90	-
$CO_2 + 2H^+ + 2e^- = CO + H_2O$	19.88	-0.10	-0.52
$CO_2 + 2H^+ + 2e^- = HCOOH$	38.40	-0.20	-0.61
$CO_2 + 6H^+ + 6e^- = CH_3OH + H_2O$	-17.95	0.03	-0.38
$CO_2 + 8H^+ + 8e^- = CH_4 + 2H_2O$	-130.40	0.17	-0.24
$2CO_2 + 12H^+ + 12e^- = C_2H_4 + 4H_2O$	-40.52	0.07	-0.34
$2CO_2 + 12H^+ + 12e^- = C_2H_5OH + 3H_2O$	-49.21	0.085	-0.3287
$3CO_2 + 18H^+ + 18e^- = C_3H_7OH + 5H_2O$	-52.1	0.09	-0.3237

a. Free Gibbs energy of reaction per mole of CO_2, at 298 K.
b. The apparent standard potential is calculated at pH = 7 and 298 K.

Besides the chemical reactions, the conversion of CO_2 is achieved strategically by utilizing the renewable energy sources, e.g. solar energy. The solar powered conversion can be implemented directly by photochemical or photo-electrochemical reduction or indirectly by electrochemical reduction. In the case of latter process, CO_2 is electrochemically reduced by the incoming electrons and protons to a variety of products depending on the catalysts. The possible products and thermodynamics of electrochemical reduction of CO_2 for receiving two to twelve electrons are listed in **Table 1.2**. Typically, the direct reduction of linear CO_2 to form bent $CO_2^{\bullet -}$ is difficult ($E° = -1.90$ V vs. SHE) and results in a large overpotential in the overall reduction reaction.[10-12] Multiple proton-coupled electron transfer steps favor the electrochemical reduction while they also introduce added complexity with the requirement of the catalyst system to orchestrate the multiple proton/electron inventory which is particularly pertinent to reaction selectivity.

1.2.3 CO_2 Capture and Sequestration

The management of large-scale CO_2 emissions from large point sources such as coal- and gas-fired power plants and refineries can be achieved in many different ways. At present, CO_2 capture and sequestration (CCS) is perhaps the closest to practical application. CO_2 is captured at source prior to potential release and subsequently stored in deep oceans or geological media, or through surface mineral carbonation. Among the three means of CCS, the geological storage of CO_2 currently represents the best and likely the only short-to-medium term option for significantly enhancing CO_2 sinks, thus reducing net carbon emissions into the atmosphere.[3, 13, 14] From a technical point of view, the geological storage of CO_2 shares many similar features with oil and gas accumulations in hydrocarbon reservoirs and with methane in coal beds. Sedimentary basin is the optimum geological media for CO_2 storage, which possesses capacity to accept the intended volume of CO_2, injectivity to take in CO_2 at the rate that it is supplied from the CO_2 emitters and confinement to prevent CO_2 leakage. The geological CO_2 storage is generally achieved through a variety of physical and chemical trapping mechanisms with regarding the properties at the pressure and temperature conditions found in Earth's subsurface as shown in **Figure 1.5**. Physical trapping of CO_2 occurs via either stratigraphic, structural and hydrodynamic trapping or residual-gas trapping. Chemical trapping occurs when CO_2 adsorbs onto organic materials contained on coals and shales (adsorption trapping), or dissolves in subsurface fluids (solubility and ionic trapping) and may then be involved in chemical reactions with the rock matrix (mineral trapping). Despite CCS being the most straightforward solution for reducing CO_2 emission, the extremely large scale coupled with the energy requirements and the potential for environmental consequences as well as CO_2 leakage pose significant obstacles and concern for the implementation of CCS.

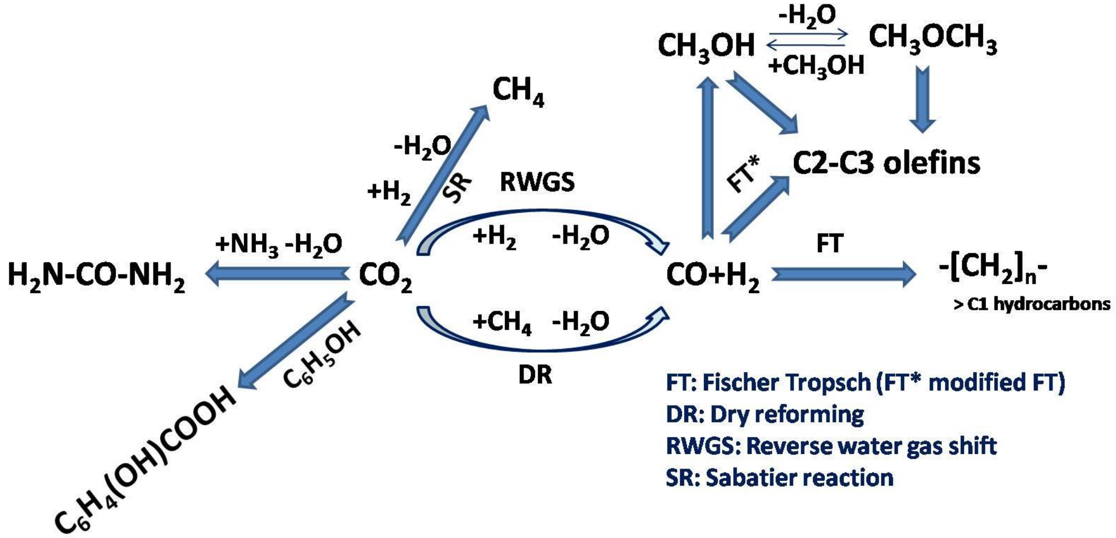

Figure 1.6. Chemical processes of converting CO_2 to useful chemicals and fuels.

1.2.4 Chemical Conversion of CO_2

Among the leading synthetic approaches for CO_2 reduction, the thermal conversion of CO_2 is the only means that is technologically mature and applied in industry. **Figure 1.6** demonstrates the primary chemical processes of CO_2 conversion in chemical industry.[4, 6] The syngas (CO+H_2), which is an important feedstock for many industry chemicals synthesis, is produced via either dry reforming (DR, Eq. 1.3)[15, 16] or the reverse water gas shift reaction (RWGS, Eq. 1.4)[17, 18]. The first challenge in the DR route is high operation temperature (900-1000 ^{o}C) due to the unfavorably thermodynamic ($\Delta G > 0$ kJ mol^{-1}) at temperature below 600 °C and the related mediocre overall efficiency of the process. A second challenge lies in the formation of coke from methane cracking and CO disproportionation, which causes catalyst (normally Ni supported on oxides) deactivation, reactor pressure building up and decrease of heat transfer. Tri-reforming process has been developed to save energy consumption necessary to power the DR reaction through combination with the wet reforming of methane (with H_2O) and its oxidation. [19]

The RWGS is a well-known commercial process occurring on the typical catalyst system of $Cu/ZnO/Al_2O_3$, possibly with additives such as ZrO_2, Ga_2O_3 and SiO_2. The CO from RWGS is further reduced to produce methanol over the similar catalyst used in RWGS (Eq. 1.5). The same catalysts may be also applied to synthesize methanol starting from CO_2. However, the mechanism of reaction and the in situ dynamic behavior of the catalyst as well as the nature of active sites are still obscure.

$$\mathrm{CO} + 2\mathrm{H_2} = \mathrm{CH_3OH} \qquad \Delta H^{o} = -90.6\ \mathrm{kJ/mol\ CO} \qquad (1.5)$$

In the presence of acid sites, DME could be easy formed from methanol by water elimination over mild acid catalyst (Eq. 1.6). It is also possible to develop core-shell catalysts, with a methanol catalyst core and a zeolite shell with controlled acidity to synthetize directly DME from syngas.

$$2\mathrm{CH_3OH} \leftrightarrow \mathrm{CH_3OCH_3} + \mathrm{H_2O} \qquad (1.6)$$

Carbon dioxide can be also hydrogenated to hydrocarbons either by direct or indirect routes. The indirect route widely uses Fischer-Tropsch (FT) synthesis to produce > C1 hydrocarbons from syngas at temperature between 150-300 ^{o}C (Eq. 1.7). The FT catalysts are transition metals like cobalt, iron, and ruthenium containing a number of promoters, including potassium and copper. The direct reaction is similar to FT synthesis, but using a CO_2/H_2 feed. The direct reaction is implemented via a single-stage approach, using a bifunctional catalyst that combines RWGS and FT chain growth activity. Short-chain olefins (ethylene, propylene) could be directly produced from syngas using modified FT atalysts, e.g. Fe/Mn/K or Fe/Cu/Al/K, or indirectly via the formation of methanol following a consecutive conversion to short-chain olefins based on small-pore zeolites.

$$\mathrm{CO + H_2 \rightarrow C_nH_{2n} + C_nH_{2n+2} + CO_2 + H_2O} \qquad (1.7)$$

CO_2 hydrogenation to methane, known as Sabatier reaction (Eq. 1.8), can be achieved over common Ni-based catalysts (e.g. 10 wt.% Ni/CeO_2). But this process is not suitable for the conversion of CO_2 to gas fuels using H_2 with regarding larger consumption of H_2, lower energy per volume and more difficult storage with respect to liquid hydrocarbons.

$$\mathrm{CO_2 + 4H_2 \rightarrow CH_4 + 2H_2O} \quad \Delta H^o = -165\ \mathrm{kJ/mol\ CO_2} \qquad (1.8)$$

Besides the conversion of CO_2 to fuels, CO_2 is also a raw material for useful chemical synthesis in chemical industry. The representative chemical processes are synthesis of urea from ammonia and CO_2 (Eq. 1.9) and production of salicylic acid from phenol and CO_2 (Eq. 1.10). Urea is extensively employed for manufacturing various polymer materials and also for producing fertilizers, while acetyl salicylic acid is used for making Aspirin, a widely used common medicine.

$$\mathrm{CO_2 + 2NH_3 \rightarrow H_2NCONH_2 + H_2O} \qquad (1.9)$$

$$\mathrm{CO_2 + C_6H_5OH \rightarrow C_6H_4(OH)COOH} \qquad (1.10)$$

1.2.5 Photochemical and Photo-electrochemical Reduction of CO_2

Mimicking nature's photosynthesis process, photoreduction of CO_2 is one of the most promising routes for CO_2 conversion due to the abundance and free access of sunlight. Photoassisted reduction of CO_2 methods can be divided into four major categories[20]: 1) homogeneous photochemical reduction by a molecular catalyst, 2) direct heterogeneous CO_2 reduction by a biased semiconductor photocathode, 3) heterogeneous CO_2 reduction by metal particles anchored on a biased semiconductor photocathode, and

4) homogeneous photo-electrochemical CO_2 reduction by a molecular catalyst through a semiconductor/molecular catalyst junction.

A homogeneous CO_2 photochemical reduction system consists of a molecular catalyst, photosensitizer (light absorber), sacrificial electron donor, and/or electron relay. The generic mechanism of the photocatalytic reduction of CO_2 consists of a photosensitizer (P) capable of absorbing radiation in the ultraviolet or visible region and of the generation of an excited state (P*).[21, 22] The excited state is reductively quenched by a sacrificial donor (D) generating a singly reduced photosensitizer (P^-) and oxidized donor ($D^{\cdot+}$). The choice of photosensitizer must be such that P^- is able to transfer an electron efficiently to the catalyst species (cat) to generate the reduced catalyst species (cat^-). In some cases the photosensitizer and the catalyst are the same species. The cat^- is then able to bind CO_2 and proceed with the catalytic mechanism to release the intended products and regenerate catalyst. Common photosensitizers used in these systems include aromatics, e.g. p-terphenyl, phenazine and polypyridine-coordinated transition metal complexes. Ruthenium(II) trisbipyridine ($[Ru(bipy)_3]^{2+}$) is the most often employed transition metal complex due to its strong visible-light absorption and high photo-stability.[23] The macrocycle complexes of Ni, Co and Fe, and $Re(CO)_3bpyX$ ($X=Cl^-$ or Br^-) based complexes are the most efficient catalysts.[24-28] The homogeneous system with macrocycle, however, suffers from low quantum efficiency, low selectivity and low turnover frequency due to significant production of H_2. Although $Re(CO)_3bpyX$ catalysts improve the quantum efficiency and turnover frequency, they lack extended absorption in the visible region.

There are several semiconductors that can serve as photocathode materials with suitable band gap and conduction band potential capable of CO_2 reduction, for example p-GaP (2.3 eV), p-CdSe (1.7 eV), p-Si (1.1 eV), p-GaAs (1.4 eV), and p-InP (1.3 eV).[20] Heterogeneous photo-electrochemical reduction of CO_2 on semiconductor surfaces has been achieved with satisfactory incident selectivity to formate or formic acid and CO.[29-33] P-type GaAs has been used for direct photo-electrochemical reduction of CO_2 to produce methanol.[34] But the mechanism for methanol production is still under arguing. The electrolyte in terms of aqueous and non-aqueous solution has significant impact on the efficiency of the photo-electrochemical reduction, which mainly results from the huge difference of CO_2 solubility. Nonaqueous solvents like acetonitrile, dimethylformamide (DMF), dimethyl sulfoxide (DMSO), and methanol have higher solubility of CO_2 than water. In a truly photoelectrocatalytic system, when a photoelectrode coupled to a catalyst (metal particles, like Cu, Au, Ag, Pd and Ru) is run under illumination, apart from a positive shift in the onset voltage called the photovoltage shift, the dependency of productivity on applied potential has similar behavior to the catalyst alone.[35, 36] Besides the p-type semiconductor, some other oxides with suitable negative and positive redox potential in conductance-band and valence-band edge, respectively, have been under study for CO_2 reduction, for example, ZnO (3.2 eV), V_2O_5 (2.7 eV), WO_3 (2.8 eV), TiO_2 rutile (3.0 eV) and TiO_2 anatase (3.2 eV).[37] However, these oxides have large band gap which requires high energy input to allow electron excitation. For example, TiO_2 anatase, a stable photocatalyst with a large band-gap energy (3.2 eV), only utilize a small UV fraction of around 2-3% solar light. The approaches using photosensitizing dyes and doping transition metal by ion-implantation technique have been developed to enable visible light response.[38, 39] The nanostructure TiO_2 has an improvement of photoreduction activity compared to bulk materials.[40] The highly dispersed TiO_2 on zeolite cavity and framework has a unique local structure and improves the reaction rate and selectivity for the formation of CH_3OH and CH_4.

Photo-electrochemical reduction of CO_2 through p-type semiconductor/molecular catalysts junction involves three critical steps[20]: (a) charge carrier generation and separation in the semiconductor, (b) heterogeneous charge transfer to the molecular electrocatalyst, and (c) homogeneous catalysis. In a given p-type semiconductor/ molecular electrocatalyst junction, the molecular catalyst must be chosen to match the catalytic current density with the photocurrent density corresponding to the illumination intensity and the catalyst's turnover frequency. CO_2 reduction has been studied on p-GaAs and p-GaP photocathodes with $Ni(cyclam)^{2+}$ (cyclam=1,4,8,11-tetraazacyclotetradecane) as the molecular catalyst. A Faradaic efficiency of CO at 80-100% has been achieved on p-GaP, which is 5 times higher than on p-GaAs due to the inherent surface chemistry characteristics.[41, 42] Methanol production from CO_2 with Faradaic efficiency of 63–100% was obtained on the electrode system consisting of p-GaP (111) photocathode and a soluble pyridinium molecular catalyst.[43]

On account of competing advantages of homogeneous catalysts (selectivity, tunability) and heterogeneous catalysts (robustness, easy separation of products from catalysts), there is considerable interest in "heterogenizing" homogeneous catalysts, by covalently linking them to surfaces. But the reported selectivity of this system is slow currently.[44, 45] In addition, more effort in covalently bound of molecular catalyst to the surface is needed to prevent from loosening on the large biased semiconductor.

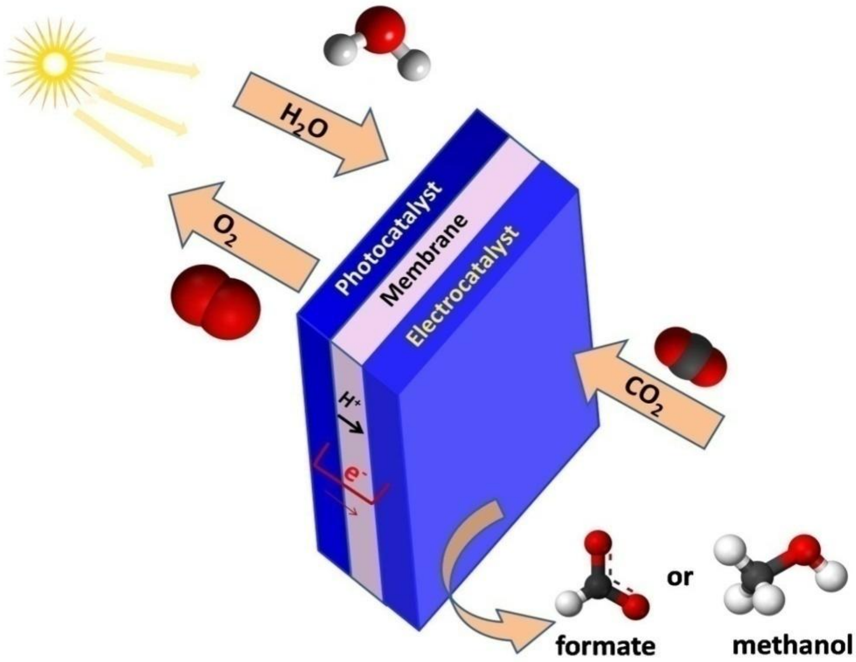

Figure 1.7. Schematic of a CO_2 photo-reduction reactor.

Solar photocatalytic reactors for CO_2 reduction have been designed including two-phase reaction packed bed, three-phase reaction fixed-bed and suspended reactors. A more promising reactor is a photoelectrochemical cell which integrates photochemical oxidation of water, electrochemical reduction of CO_2, and membrane processes (**Figure 1.7**).[46] One half-cell of this reactor is a photoanode consisting of photo-catalysts to split water into protons plus oxygen. Electrons transfer directly to another half-cell, whereas protons are transported through a Nafion membrane. The photons, electrons, and CO_2 molecules meet at the cathode and react at the electrocatalysts to form new products. The implement of the cathode reaction requires understanding of the electro-chemistry of CO_2 reduction on electrocatalysts.

1.2.6 Electrochemical Reduction of CO_2

Electrochemical reduction of CO_2 using renewable sources of electricity is an alternative approach to produce fuels, akin to photosynthesis, thus potentially reducing the dependence on foreign fuels as well as mitigating the concentration of CO_2 in the atmosphere. The electrochemical reduction process, a.k.a. electrolysis, can take place over a wide range of temperatures, from room temperature to over 1000 ^oC. High temperature electrolysis, on the one hand, supplies enough energy to overcome activation energy barrier for C-O bond cleavage in CO_2. On the other hand, the high temperature reaction favors the formation of C1 molecules such as carbon monoxide due to higher kinetic energy while preventing the formation of longer chain molecules.[47] Solid oxide electrolysis cells (SOECs) are applied for the electrochemical conversion of CO_2 into CO or co-electrolysis of H_2O and CO_2 to form syngas (CO and H_2) at temperature between 750 and 1000 ^oC over Ni/YSZ (Yttria Stabilized Zirconia) electrode. SOEC is a reverse process of well-known solid oxide fuel cell (SOFC). The basic principle for a SOEC and SOFC operating on H_2O/H_2 and CO_2/CO is shown in **Figure 1.8**. In general, SOECs exhibit a low overpotential and superior selectivity to CO formation as well as high current density.[48-50] The overarching challenges facing prolonged SOEC operation include the electrode degradation due largely to the formation of coke, sulfur contamination and volatile nickel-carbonyls.[51-53]

In order to produce long-chain products, the development of electrolysis of CO_2 at low temperature (usually room temperature) is imperative in terms of electrocatalysts and reactor design. The development of electrocatalysts requires understanding of the characteristics of CO_2 adsorption, the interactions with catalyst surface and reductants, as well as the molecular energetic. The catalyst surface morphology including defects/kinks/steps and composition potentially influence the catalytic CO_2 reduction. The electrolyte property of dielectric constant and polarity as well as type (aqueous or non-aqueous solution) are also the important parameters that can affect catalysis of CO_2 reduction. In terms of reactor design, the effort in developing bench-scale full electrochemical cell allowing direct gas-phase CO_2 reduction is the priority. The status and prospect of electrochemical reduction of CO_2 at low temperature are reviewed in details in the next section.

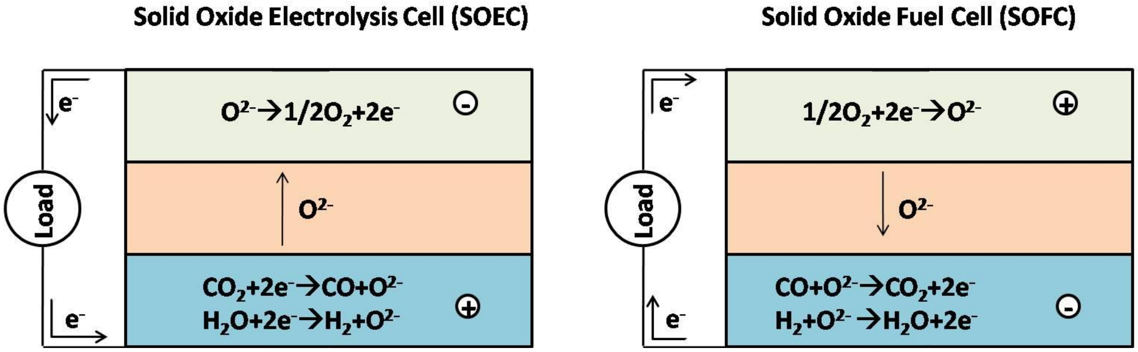

Figure 1.8. Schematic presentation of the operational principle for a solid oxide electrolysis cell (SOEC) and a solid oxide fuel cell (SOFC).

1.3 Review of the Electrochemical CO_2 Conversion at Low Temperature

1.3.1 Molecular Catalysts for Electrochemical Reduction of CO_2

Molecular complexes could be used directly in solution or immobilized at an electrode surface. The insight gained from molecular electrocatalysts can be extended to development of heterogeneous electrocatalysts.[54] Promising examples of molecular electrocatalysts include late transition metal macrocyclic complexes, rhenium bipyridine complexes, palladium triphosphine complexes and bimetallic copper complexes.[55-59]

The popular metal macrocycles include Ni^{II} and Ni^{I} macrocycles[55], Co^{I} tetraazamacrocycles[60], Pd complexes[61, 62], Ru^{II} complexes[63] and Cu^{II} complexes[64]. $[Ni^{II}cyclam]^{2+}$ complex (structure 1, **Figure 1.9**) is a very efficient and selective catalyst in the reduction of CO_2 to form CO in aqueous solution only.[65] In the proposed mechanism, the $[Ni^{I}cyclam]^{+}$ complex is assumed to play a crucial role, and in particular, a $[Ni^{I}cyclam(CO)]^{+}$ intermediate species has been detected in the course of the electrolysis experiment. Systems favoring the formation of the Ni^{I} state are expected to behave as efficient electrocatalysts for the reduction of CO_2. In this connection, the Ni^{II} complexes of some fluorinated cyclams, which exhibit a Ni^{II}/Ni^{I} potential less negative than $[Ni^{II}(cyclam)]^{2+}$, work well for CO_2 reduction.[66] Ni^{II} azacyclam shows a comparable reduction current to that of $[Ni^{II}(cyclam)]^{2+}$ under the same complexes concentration.[55] Fourteen-membered cyclam framework is a crucial pre-requisite for the encircled nickel center to act as catalyst in the CO_2 electro-reduction.

$[Pd(triphosphine)(CH_3CN)]^{2+}$ complexes (structure 2, **Figure 1.9**) are also active catalysts for the electrochemical reduction of CO_2 to CO.[56] In this structure, the dissociation of a weakly coordinating solvent molecule, acetonitrile in structure 2, favors M-O bond formation during the catalytic cycle. In addition, electron-donating substituents on the triphosphine ligand result in increased catalytic rates. The rate constant is between 5 and 300 M^{-1} s^{-1}. Inspired by the CO dehydrogenase enzymes, binuclear palladium complexes (structure 3) in which the two Pd(P3) compartments are separated by a methylene spacer were used for CO_2 reduction.[67] This complex binds CO_2 through two Pd sites, with one metal interacting with C, the other with O. The binuclear palladium complexes show very high catalytic rates for CO_2 reduction (> 10^4 M^{-1} s^{-1}), but with a turnover numbers of ca. 10.

$Re(bipy\text{-}tBu)(CO)_3Cl$ (bipy-tBu = 4,4’-di-tert-butyl-2,2’-bipyridine) complexes (structure 4) also have been reported to rapidly convert CO_2 to CO with Faradaic efficiency of nearly 100% in electrolyte of acetonitrile.[57] Complex of $Re(bipy\text{-}tBu)(CO)_3Cl$ forms a stable Re(0) radical, and significantly less dimer during electrolysis than does its Re(bipy)$(CO)_3Cl$ counterpart, which is attributed to the enhanced catalytic activity.

The electrocatalytic reduction of CO_2 to oxalate was observed recently using a binuclear copper complex (structure 5) of a pre-organised, binucleating tetrapodal disulfide ligand.[58] Reduction of the binuclear Cu(II) complex leads to Cu(I) complex followed purging CO_2 to further form a new tetranuclear Cu(II) bis(oxalate) complex (structure 6) in which the oxalate ligands were found to bridge two adjacent Cu centers. The binuclear oxalate complex was found to react with $LiClO_4$ to regenerate the starting material and produce insoluble $Li_2C_2O_4$. When tetranuclear Cu(II) complex was used as an electrocatalyst in acetonitrile solution containing $LiClO_4$, the catalytic turnover started at -0.03 V versus NHE, a potential that is nearly 2 V less negative than that required for the outer-sphere reduction of CO_2 to $CO_2^{\cdot -}$. The consumption of current continued linearly for more than 3.3 hours, consuming three equivalents of charge (12 electrons) per four copper ions, with concurrent crystallization of lithium oxalate.

Additionally, non-metal-nitrogen based molecular systems have also been reported, including pyridinium (structure 7) and its substituted derivatives.[43, 68, 69] This pyridinium cation acts as one-electron shuttle to perform multiple-electron, multiple-proton reduction of CO_2 effectively in aqueous solution to form products such as formic acid, formaldehyde, and methanol. Using pyridinium cation as catalysts on metal electrode, Faradaic efficiencies of methanol were observed ~30% at overpotentials of only -0.2 V. When this pyridinium ion catalyst was anchored to a p-GaP electrode, this photochemical system yielded nearly 100% Faradaic efficiency of methanol at potential

0.3 V below the thermodynamic potential for the reaction.[43] But the reaction mechanism is unclear and needs more effort of understanding.

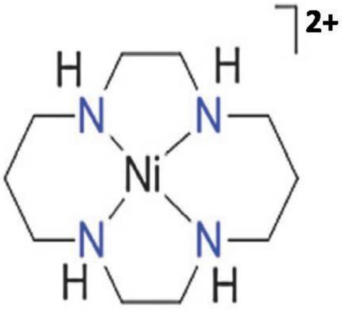

[1]

$[Ni^{II}(cyclam)]^{2+}$

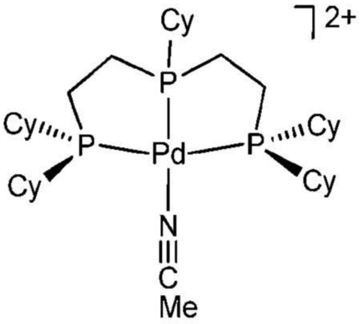

[2]

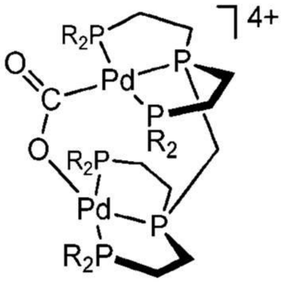

[3]

$[Pd(triphosphine)(CH_3CN)]^{2+}$

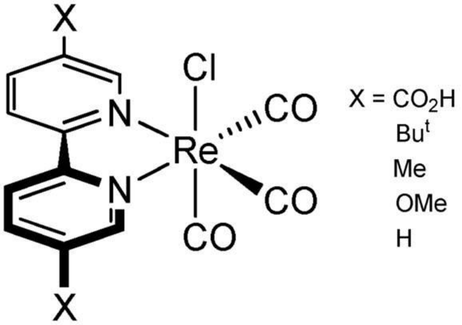

[4]

$Re(bipy(CO)_3Cl$

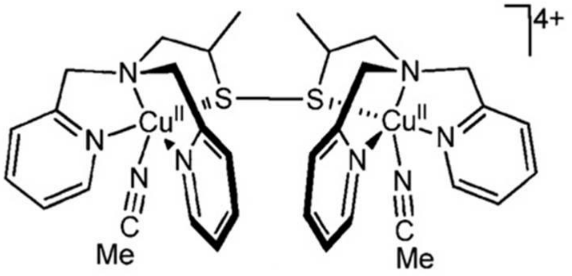

[5]

Binuclear copper complex

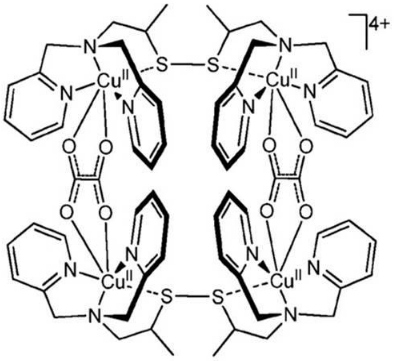

[6]

Tetranuclear copper complex

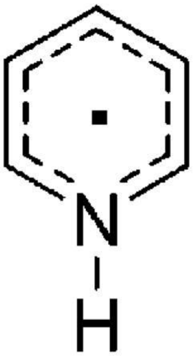

[7]

Pyridinium

Figure 1.9. Molecular catalysts of transition metal complexes.

1.3.2 Heterogeneous Catalysts for Electrochemical Reduction of CO_2

1.3.2.1 Classification of Metal Catalysts

Several good review papers have discussed the heterogeneous metal catalysts for CO_2 reduction, particularly including the work of Hori.[70-72] So far, several classification methods have been used to systematize the impressive amount of data accumulated in CO_2 reduction related work.[71, 73, 74] Most of these classifications are solely based on the nature of the main product obtained in the electrochemical reduction. Four classes of metallic electrodes in aqueous supporting electrolytes and three classes for nonaqueous media can be distinguished. Thus, in aqueous solution (i) metallic Cd, In, Sn, Hg, Tl and Pb are selective for the production of formic acid or formate depending on the electrolyte pH, (ii) metallic Zn, Au and Ag produce carbon monoxide, (iii) Cu is the only metal that exhibits electrocatalytic activity for the formation of hydrocarbons, aldehydes and alcohols, while (iv) metallic Al, Ga and Group VIII elements (except Pd) show low electrocatalytic activity towards CO_2 reduction with the primary product of CO at low Faradaic efficiency. The Faradaic efficiency ratio of CO to formic acid/formate for metal catalysts is in the order of Au>Ag>Cu>Zn>>Cd>Sn>In>Pb>Tl.[75] In nonaqueous supporting electrolytes[70, 71] (i) Pb, Tl and Hg mainly produce oxalic acid; (ii) Cu, Ag, Au, In, Zn and Sn form CO and carbonate ions, while Ni, Pd and Pt are selective for CO formation; and (iii) Al, Ga and Group VIII elements (except Ni, Pd and Pt) form both CO and oxalic acid.

The metals can also be classified into two groups, sp and d metal electrodes, according to the electronic configurations in the d orbital.[71] The group of sp metals is referred to metals with the outermost d orbital completely filled with a d^{10} electronic configuration: Hg, Pd, In, Sn, Cu, Zn, Ag Au and Cd. This classification enables better understanding of the electrocatalytic activity associated with the respective electronic characteristics. When used in aqueous supporting electrolytes, sp metals, such as Hg, In, Sn and Pb favor the reduction of CO_2 to formic acid or formate. While on d metals (e.g., Pt and Pd) CO is the main product. However, the same group of metals behaves differently in nonaqueous supporting electrolytes. On sp group metals (Tl, Pb and Hg) oxalic acid is selectively produced. On several d group metals (Fe, Cr, Mo, Ti and Nb) oxalic acid and CO are the main products. Lastly CO is mainly formed on several sp group metal electrodes (In, Sn, Cd, Zn, Cu, Ag and Au) and d group metal electrodes (Pd, Pt and Ni).[76, 77] The various products of CO_2 reduction on sp and d metals are summarized in **Table 1.3.**

Table 1.3. Productivity of CO_2 electro-reduction on sp and d metals.

Metal		**Product**	
		Aqueous electrolyte	**Nonaqueous electrolyte**
sp metals (d^{10} electronic configuration)	sp metals (Hg, In, Sn, Pb, Cd)	Formic acid	Oxalate (Tl, Pb, Hg)
	sp metals (Zn, Ag, Au)	CO	CO
	sp metals (Cu)	C_2H_4, CH_4, HCOOH, CO, and alcohols.	CO
d metals (partly filled d orbitals)	d metals (e.g., Pt and Pd)	Adsorbed CO	CO (including Ni)
	d metals (e.g., Ru)	Low yield of Hydrocarbons, alcohols, and formaldehyde.	
	d metals (Fe, Cr, Mo, Ti, Nb)	weak performance	Oxalate and CO

1.3.2.2 Electrochemical CO_2 Reduction on sp Group Metals

Cu is the only metal that produces hydrocarbons, e.g. CH_4, C_2H_4, methanol, ethanol and n-C_3H_7OH, from CO_2 reduction.[78, 79, 80] Product distribution is strongly dependent on the surface morphology and chemistry.[81] The main hydrocarbons are CH_4 and C_2H_4 with low Faradaic efficiencies on commercial Cu electrodes,[80-83] and the enhanced yield of CH_4 and C_2H_4 was observed on in-situ deposited Cu electrodes[84]. No formation of CH_4 and C_2H_4 was observed on the electrode with heavily oxidized surface, however, the formation of hydrocarbons recovered after the electrode was cleaned by applying negative potentials for a while.[85] In addition, the pre-electrolyzed electrode from heavy oxide surface increased the long-term activity compared to conventional Cu electrode on which the formation of hydrocarbons decayed fast. Similarly, anodized or thermal treatment electrodes with rough surface showed better durability of performance than smooth electrodes regarding the production of hydrocarbons.[86, 87] Recently, oxide-derived Cu and Au electrodes prepared by reducing a micrometer thick Cu_2O and Au oxide films, respectively, were developed and displayed a great improvement over both selectivity towards targeted products and stability compared to polycrystalline metals.[88-90] Moreover, oxide-derived electrodes reduced CO_2 at lower overpotentials than conventional metal electrodes. It is worth noting that Cu electrodes containing a Cu_2O surface layer demonstrated higher activity towards CH_3OH production.[91, 92] Cu (I) species was considered to play a critical role in the activity of CH_3OH formation. CH_3OH yielded qualitatively follow Cu (I) concentrations. The Cu-based alloys for CO_2 reduction were also investigated**.** Only Cu-Ni alloy (Cu/Ni = 90/10) was observed to help form CH_3OH

while the other alloys e.g. Cu-Sn, Cu-Pb, Cu-Zn, Cu-Cd only tended to form main products of CO and formic acid.[93-97]

CO_2 reduction is sensitive to the surface orientation of Cu electrode. C_2H_4 is favorably produced on Cu(100), and CH_4 on Cu(111), while Cu(110) showed an intermediate product selectivity.[98, 99] The C_2H_4 formation is further promoted by the introduction of (111) or (110) steps to the (100) basal plane (e.g. Cu(S)-[n(100)×(111)] and Cu(S)-[n(100)×(110)]), and could be more further activated by introduction of a certain amount of the step atoms. The highest C_2H_4 selectivity was achieved on the (7 1 1) [4(100) × (111)] surface.[83] CH_4 was enhanced by introducing (100) to (111), e.g. the Cu(S)-[n(111)×(100)] surfaces.[100] The Cu(S)-[n(111)×(111)] surfaces favor the formations of acetic acid, acetaldehyde and ethyl alcohol with the increase of the (111) step atom density. CH_4 formation at the Cu(S)-[n(111)×(111)] electrodes decreases with the increase of the (111) step atom density.[83]

Although Cu tends to form hydrocarbons, the reduction of CO_2 is inefficient, occurring at high overpotentials. The other even bigger problem is the rapid degradation of activity.[87, 90, 101-103] Several mechanisms, like adsorption of organic intermediate[90, 101], black carbon deposition[84, 90], poison of copper oxide patina[102], accumulation of an unknown low vapor pressure and soluble CO_2 reduction product[104], contaminants Fe^{2+} and Zn^{2+} deposition[103], have been proposed to cause the deactivation. However, the real reason behind is still unclear. The pulse electro-reduction[101, 105, 106], anodic polarization[107] and periodic anodic stripping[108] have developed to regenerate the electrode, but with limit positive effect. The third great challenge is to understand the formation mechanism of hydrocarbons[82], though a good start of simulating elements of the reaction mechanism on Cu using DFT[109-111].

Ag and Au electrodes could achieve the formation of CO as high as 90% while Zn shows a little lower Faradaic efficiency of CO in aqueous solution.[75, 112, 113] In non-aqueous electrolyte of 0.1 M TEAP/H_2O, Zn was found to produce formic acid at higher Faradaic efficiency than CO and H_2.[114] Hydrocarbons formation can be obtained on Ag electrode by pulse reduction.[115] The product distribution strongly depends on the anodic (V_a) and the cathodic (V_c) bias. CO and $HCOO^-$ were preferentially produced at less negative potentials of $V_a > -0.4$ V vs. Ag/AgCl, while CH_4, C_2H_4, and C_2H_5OH were major products at $V_a < -0.4$ V vs. Ag/AgCl. The origin of the selectivity was hypothesized to relate to the special affinity of hydrogen and/or proton to electrodes. At more negative V_a such as $V_a < -0.4$ V vs. Ag/AgCl, protons are so abundant on the electrode surface that adsorbed hydrogen-containing carbon molecules are preferentially formed on a Ag electrode. As a result, hydrocarbonization reactions between H_{ad} and $CO_2^{\cdot -}$ are possible, yielding CH_4, C_2H_4, and C_2H_5OH. On the contrary, at less negative V_a (> -0.4 V vs. Ag/AgCl), desorption of H_{ad} occurs, and adsorbed protons are not abundant enough to promote hydrocarbonization reactions. In this case, CO and $HCOO^-$ are preferentially produced. Recently, N-based organometallic silver catalysts including silver pyrazole (AgPz), silver phthalocyanine (AgPc), and silver 3,5-diamino-1,2,4-triazole (AgDAT) were found to show comparable performance of CO_2 reduction with Ag.[116] The advantage of the organometallic catalysts lies in their low mass fraction of silver.

In, Sn, Hg and Pb electrodes all have high overpotential for H_2 evolution, and negligible CO adsorption. In aqueous electrolyte, formic acid/formate is selectively produced with Faradaic efficiency between 70-100% on In, Sn, Hg and Pb electrodes.[117-122] Sn is extremely interesting because of its abundance and low cost as well as higher selectivity towards the production of formic acid/formate in aqueous electrolytes compared to the other three metals.[70, 112, 119] The production of formic acid/formate is promising because it is an economically viable way to store energy. Formic acid, with a free energy of combustion of -233 kJ/mol, is a promising fuel for the generation of electricity in fuel cells.[123-128] In addition, producing formic acid is economical as it has a higher retail value compared to its required formation energy than conventional fuels, such as methanol or methane. The market price of formic acid is about $1200 per metric ton, yet the invested energy in the creation of formic acid is only around 3000 kWh/ton, which leaves a favorable energy-price gap. The usual CO_2 reduction pathway for formic acid/formate formation, as shown in **Figure 1.10**, involves an initial adsorption step followed by a one-electron reduction to form the intermediate $CO_2^{\cdot-}$ species. The weakly adsorbed $CO_2^{\cdot-}$ goes through a protonation reaction, then there is a second electron-transfer to yield formate. The production of formate is accompanied by a parallel disproportionation of the stable $CO_2^{\cdot-}$ radical anion which is adsorbed to produce CO.[71, 121, 129]

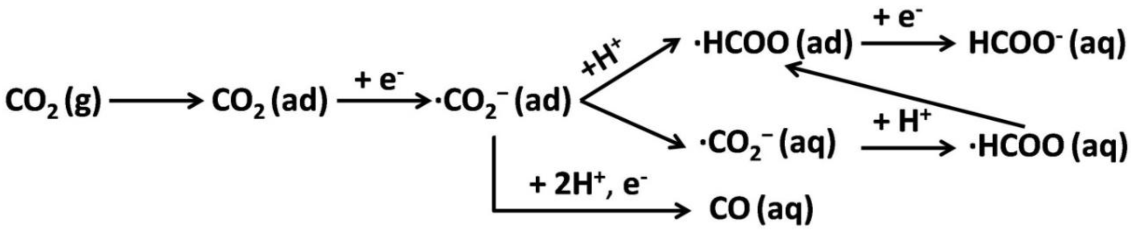

Figure 1.10. A possible route of electrochemical reduction of CO_2 into formate with the by-product CO on Sn electrode.

So far, a variety of Faradaic efficiencies of formate on Sn electrodes due to different experimental conditions have been reported in literatures, which is summarized in **Table 1.4**. The difference in Faradaic efficiency results from variations in electrode property, electrolysis condition, nature of electrolyte and design of reactor. In terms of electrode property, for example, Sn electrodes are natively covered by an oxide film which was found recently to join the CO_2 reduction and determine the activity.[130]

1.3.2.3 Electrochemical Reduction of CO_2 on d Group Metals

This group has low activity to CO_2 reduction while H_2 evolution dominates. For example, on Ni electrodes, only CO, HCOOH, CH_4, and C_2H_4 with Faradaic efficiency less than 1% were detected in aqueous electrolyte.[118] On Pd electrodes, CO and HCOOH are the main products from CO_2 reduction, with maximum Faradaic efficiency < 30% for both products.[118, 131] Under high pressure, e.g. 30 atm, the Faradaic efficiency of CO and HCOOH became comparable to that of H_2.[113] Interestingly, small yield of methanol was reported on Ru electrode.[132, 133] Reduction of CO_2 on alloy Ru-Pd (1:1) manly produced HCOOH with a maximum Faradaic efficiency of 90%.[134] CO_2 is reduced to adsorbed CO (CO_{ad}) on Pt catalysts. The CO_2 reduction on a series of Pt single crystal electrodes was systematically studied. The activity for CO_2 reduction depends remarkably on the symmetry of the surface. Following activity series are obtained for stepped surfaces: Pt(111) < Pt(100) < Pt(S)-[n(111)×(100)] < Pt(S)-[n(100)×(111)] < Pt(S)-[n(111)×(111)] < Pt(110). The initial rate of the CO_2 reduction gets higher with the increase of the step atom density.[135] Moreover, kinked step surfaces, which contain protruding atoms along the step lines, have higher activity for CO_2 reduction than the stepped surfaces.[136]

Table 1.4. Summary of CO_2 reduction on Sn electrodes with various electrolysis conditions in literatures.

Materials	Reduction condition	Electro-lyte	Faradaic efficiency (%)			Ref
			$HCOO^-$	CO	H_2	
Sn	H-type cell, -1.40 V vs. SCE, room temperature (RT)	0.5 M $KHCO_3$	65.5-79.5	2.4-4.1	13.4-40.8	112
Sn GDE	-1.8 V vs. SCE, 20 ^oC	0.35 M Na_2SO_4 (pH=2)	57	7	12	122
Sn	H-type cell, -2.0 V vs. Ag/AgCl, RT	0.1 M TEAP/H_2O	67.5	9.1	29.9	114
Sn (99.999%)	-1.86V vs. Ag/AgCl, 25 ^oC	0.1M $KHCO_3$	63	7.3	26	137
Sn	H-type cell, -2.2 V vs. SCE, 0 ^oC	0.05 M $KHCO_3$	28.5	1.4	67.50	118
Sn	H-type cell, -1.63 V vs. Ag/AgCl, RT	0.1M $KHCO_3$	88.4	7.1	4.6	75
Sn	High pressure cell, -1.8 V vs. Ag/AgCl, RT	0.5 M $KHCO_3$	99.2	–	–	120
Sn (99.9%)	163 mA cm^{-2}, 25 ^oC, 30 atm	0.1M $KHCO_3$	92.3	8	1.3	113
Sn (>99.5%)	E= -1.5 V vs. SCE, ambient pressure and temperature	0.01 mol/l benzalkonium chloride in methanol	0	28	4.40	138
Sn granules	a fixed-bed reactor,-2.0 V vs. SCE, RT	0.1 M K_2CO_3	14.25	–	–	119
	a fixed-bed reactor,-2.0 V vs. SCE, RT	0.5 M $KHCO_3$	47	–	–	
Sn GDE	Microfluid, reactor, -3.0 V	0.5 M KCl (pH=4)	~90			139
Sn foil	H-type cell, -1. 32 V vs. Ag/AgCl, RT	0.5 M $NaHCO_3$	~30			130

1.3.3 Effects of Pressure, Temperature and Supporting Electrolyte

Low CO_2 solubility in aqueous electrolyte resulting in poor mass transport is the limitation to obtain high selectivity at high current density, which is often overcome by operating at elevated pressure, decreased temperature or in alternate organic media. For example, the solubility of CO_2 in water increases with the decreasing of temperature, e.g. 0.058 mol l^{-1} at 269 K compared with 0.033 mol l^{-1} at 298 K under ambient pressure. At 60 atm and 25°C, the solubility of CO_2 in water is over 1 mol l^{-1}. Solubility is also increased through alteration of the solvent system. In methanol the solubility of CO_2 is over 1 mol l^{-1} at 25°C and 8 atm, a considerably lower pressure than that required to maintain an equivalent concentration in an aqueous system.

The dominance of H_2 evolution could be shifted to CO_2 reduction on d group electrodes by increasing the pressure.[113, 118] The formation of hydrocarbons on Cu electrode decreased upon increasing pressure[113, 140], while lowering the temperature improved the hydrocarbons formation[90, 118, 141-143] .

The nature of the supporting electrolyte, like types of anions and cations and their respective concentrations, affects the selectivity and current density towards CO_2 reduction. A greater Faradaic efficiency towards formate production was observed in 0.5 M $KHCO_3$ than in 0.1 M K_2CO_3 with a Sn electrode.[119] The Faradaic efficiency of formate increased with the decreasing of electrolyte concentration, maximum ~ 88.4% in 0.1 M $KHCO_3$[131] versus ~70% in 0.5 M $KHCO_3$[112]. Electrolytes with lower pH could promote the formation of formic acid on Sn electrodes.[139] Different cationic types in the aqueous electrolyte influence the product distribution. On Cu electrodes, overall Li^+ and Na^+ favors formation of CH_4 while K^+, Rb^+ and Cs^+ prefer production of C_2H_4. The

Faradaic efficiency for the formation of C_2H_4 increased with cation in the order $Cs^+ > K^+ > Na^+ > Li^+$, apparently in a manner related to the size of the cation radius.[144-146] Similar trend was observed on Ag electrode for CO_2 reduction to CO.[147]

Nonaqueous solvent system has been utilized in order to obtain a higher concentration of CO_2. Among the various nonaqueous solvents, methanol is an extensively investigated alternate.[148, 149 150, 151] Methanol, a protic solvent, is expected to serve as a hydrogen atom source for the formations of H_2 and/or hydrocarbons. Methanol and CO_2 are completely miscible with each other. The concentration of CO_2 reaches 0.17 mol l^{-1} at 1 atm, and amounts to about 8 mol l^{-1} at 40 atm and about 17 mol l^{-1} at 60 atm, respectively, in a CO_2-methanol mixture at 25 ^{o}C.[148] Moreover, methanol is a stable electrolyte which doesn't participate in the reduction reaction.[118, 152] With the CO_2-methanol system, the Faradaic efficiency of target products increased compared to the aqueous solution.[153, 154] In a cold and high pressure CO_2-methanol system, the CO_2 reduction was favored further.[155]

1.3.4 State-of-art of the Reactor Design for Electrochemical Reduction of CO_2

The reactors for direct gas-phase CO_2 reduction were developed in order to overcome the low solubility of CO_2 in aqueous solution. The earlier work focused on the application of metal-solid polymer electrolyte (SPE) composite electrode with metal catalysts coating on one side of SPE. A typical SPE cell configuration is CO_2/metal/SPE/aqueous electrolyte/Pt as shown in **Figure 1.11a**.[156, 157] With the SPE, the product of CO_2 reduction was seperated from that of anode reaction. In addition, the proton can easily transfer through SPE from the anode to cathode. When the metal was Cu and SPE a proton conducting membrane (Nafion), hydrocarbons like CH_4 and C_2H_4

were formed, but with a Faradaic efficiency < 10%.[156, 157, 158] When the Nafion was replaced with an anion solid polymer electrolyte membrane, the main product of hydrocarbons changed to HCOOH which still had low Faradaic efficiency of about 10%.[158] The SPE composite electrodes including Au and Ag also showed some activity towards gas-phase CO_2 reduction, and the Faradiac efficiency of CO was lower compared to the liquid phase CO_2 reduction.[118, 159, 160] The low selectivity towards CO_2 reduction in SPE cell may result from the acidity of Nafion membrane. Because the formation of C_2H_4 and CH_4 on the Cu SPE cell decreased as the pH of the electrolyte decreased.[161] However, in the condition of short supply of proton, the product may shift to HCOOH as in the case of anion solid polymer electrolyte membrane.

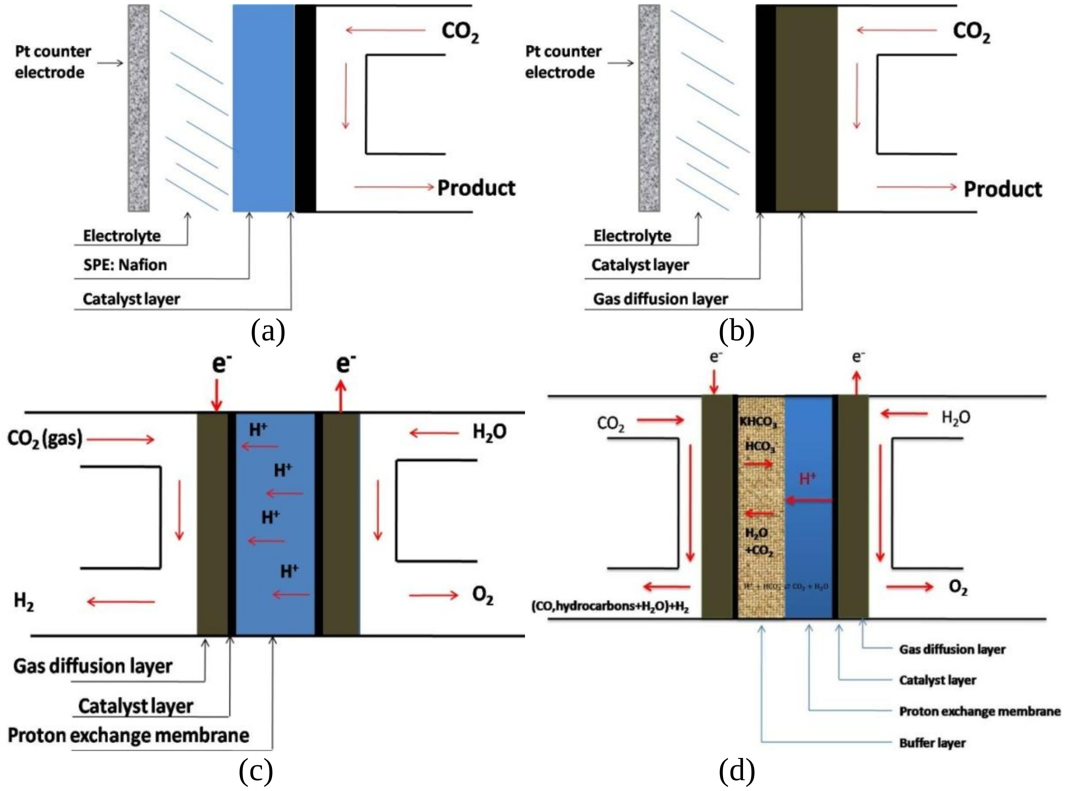

Figure 1.11. Schematic of reactor designs for CO_2 reduction. (a) a SPE cell, (b) a GDE cell, (c) a full electrolysis cell with the same configuration of PEMFC, and (d) a full electrolysis cell including an electrolyte buffer layer.

The gas diffusion electrode (GDE) was incorporated into the cell for gas-phase CO_2 reduction with a typical configuration of **Figure 1.11b**. The reaction at the triple-phase (gas-liquid-solid, GLS) interface not only increased the current density but also promoted the conversion of CO_2 to products.[162-164] The Faradaic efficiency of C_2H_4 increased drastically on GLS interface of a Cu GDE compared to on liquid-solid (LS) interface.[165, 166] The similar phenomenon of enhanced CO_2 conversion to CO was observed on silver GDE.[167] The formation of CH_4 from CO_2 was reported on Pt GDE at high pressure.[168, 169] Formic acid was formed at Ru-Pd (1:1) alloy GDE with Faradaic efficiency as high as 90%.[134] Ethanol was formed at a Faradaic efficiency of 31% at a current density of 180 mA cm^{-2} on a GDE containing $La_{1.8}Sr_{0.2}CuO_4$.[170]

The development of full electrochemical cells was attempted by taking the advantage of SPE electrode and GDE. The first attempt was using the configuration of proton exchange membrane fuel cells (PEMFCs), as shown in **Figure 1.11c**, to directly convert gas phase CO_2 to other species in gas phases.[171] Various hydrocarbons, including CH_4, C_2H_4 and C_2H_6, were observed on a Cu electrode deposited on Nafion® 117 membrane; the overall Faradaic efficiency, however was ~1% due to the acidity of the Nafion® membrane which promoted the competitive hydrogen evolution reaction over CO_2 reduction reaction.[161, 172] Similar results was observed on Ag electrode that H_2 evolution dominated in PEMFC.[172] However, when an anion exchange membrane was used, CO was detected though with a low Faradaic efficiency. Modifications in the physical structure of PEMFCs were adopted to improve the selectivity of the electrodes towards CO_2 reduction.[139, 172-180] One design was to modify the cathode, for instance, a 3D cathode consisting of a Sn-Cu mesh screen, which allowed a co-current flow of CO_2

and catholyte through the cathode, thus providing an aqueous environment for CO_2 reduction.[173] As a consequence, the Faradaic efficiency toward formate formation was substantially improved to ~86% at a cell potential of 3 V. The high operation voltage resulted from great ohmic loss and cathodic overpotential.[9] In addition, the lower solubility of CO_2 in aqueous electrolytes[8] significantly affected cell performance at higher current densities because of mass transfer constraints. An alternative design concept was to insert a layer of aqueous electrolyte between the cathode GDE and SPE (**Figure 1.11d**). Thus, the acidity of Nafion® was mediated by the aqueous electrolyte while Nafion® could still function as a proton transfer medium and gas separator. Based on this concept, a glass fiber saturated with 0.5 M $KHCO_3$ was inserted between the Nafion® membrane and the Ag GDE to prevent excessive buildup of protons near the cathode, which resulted in a significant increase of selectivity towards CO_2 reduction to CO.[172] The glass fibers, however could become dry during electrolysis due to the evaporation of water, resulting in degradation of cell performance. One approach to circumvent this drying issue was to operate the cell with a flowing electrolyte stream in place of saturated glass fiber.[139, 176] With a continuous flowing electrolyte, formate production on Sn GDE was achieved at a Faradaic efficiency of ~70% by using 0.5 M KCl as the electrolyte at pH = 7, while the efficiency increased to ~90% at pH = 4. The cell, however, was operated at high voltages to obtain formate.[139] A high pressure cell of flowing electrolyte was design to enhance the selectivity towards CO formation on Ag GDE. CO generated at 15 atm was 5 times that observed at ambient pressure with Faradaic efficiency as high as 92% observed at 350 mA cm^{-2} at which the cell potential was higher than 3 V.[181] Recently, an ionic liquid was used as the catholyte with Ag GDE to convert CO_2 to CO, which showed substantial improvement over both Faradaic efficiency (~100%) and the overpotential (less negative than -0.2 V) towards CO formation.[12] The ionic liquid, $EMIMBF_4$, was considered to react with CO_2 to form a complex such as CO_2-EMIM at potentials more negative than -0.1 V with respect to a standard hydrogen electrode (SHE). This complex substantially lowered the barrier for formation of the intermediate $CO_2^{\bullet-}$ and suppressed H_2 evolution.[182]

1.4 Remaining Technical Challenges and Opportunities Regarding Electrochemical Reduction of CO_2

Efficient conversion of CO_2 to fuels and useful chemicals using renewable energy sources is a major challenge to the catalysis science community. The electrochemical reduction of CO_2 coupled with photochemical oxidation of water is the promising direction to utilize CO_2 in a carbon neutral way. Although remarkable achievements have been made in electrochemical reduction of CO_2 in the past two decades, there is limited scientific knowledge about CO_2 catalytic reduction. Due to the complexity of the reaction environment and multiple bond-forming and -breaking processes, the detailed knowledge about the elementary pathways is obscured, which results in the difficulty in understanding the reaction kinetics and controlling the reaction chemistry. The determination of the transient catalytic intermediates is still not possible because of their very short lifetimes and low concentrations as well as difficulty in resolving intermediates spectroscopically. The characterization of surface intermediates under working conditions will require the development and application of sensitive ultrafast spectroscopic and pump-probe scattering methods. Coupling with the experimental probing, theoretical modeling, like ab-initio methods and DFT, is needed to calculate the overall reaction energies and activation barriers for important reactions that occur for gas-phase model catalytic systems, which subsequently leads to construct overall potential energy surfaces. However, so far simulating reaction conditions that explicitly treat the effects of surface coverage, electrolyte, electrochemical potential, and appropriate materials property, including the effects of particle size, surface orientation and morphology, presents significant challenges.

For a desired CO_2 catalysis reduction, for example formation of methanol and methane, the process involves simultaneous multi-proton and multi-electron transfer. A real reaction system, particularly including electrolyte, adds more difficulty in controlling the stepwise proton coupled multi-electron transfer conversion. The achievement of multi-proton and multi-electron conversion relies on the development of multi-sites or hybrid catalysts to concert electron and proton transfer. The target product is formed via managing the electron and proton transfer through catalysts, thus enhancing the selectivity towards single product. Additionally, these catalysts are required to lower the energy barrier for the formation of transient intermediates, which means operating at very low overpotential. The stability of catalysts is also a critical issue due to the trade-off that active materials are always inherently degradable.

The simultaneous high current density (>100 mA cm^{-2}) is also important in addition to high energy efficiency and selectivity in the reduction system. To address this issue, it is required to overcome the sluggish kinetics of CO_2 reduction and low solubility of CO_2 in electrolyte. GDEs have already applied in direct gas-phase CO_2 reduction to avoid low CO_2 solubility in electrolyte. The further improvement relies on the optimization of catalyst structure in GDEs via tuning the component volume percentage and using advanced processing methods in order to increase the triple-phase boundary length.

Finally, there is still lack of bench-scale full electrochemical cell for CO_2 reduction coupling solar energy. The full electrochemical cell based on PEMFC configuration which can embed GDEs takes the advantage of the already developed technology in fuel cells over the past decades, for example the flow field optimization, the membrane electrode assembly preparation and even the assembly of fuel cell stacks. A feasible cell not only favors CO_2 reduction over H_2 evolution, but also operates energy-efficiently. Though some flowing electrolyte cells have demonstrated high selectivity towards target products, but the operation requires high overpotential. A new design of full electrochemical cell enabling future “solar driven” is needed to achieve a low energy consuming operation.

1.5 Objectives of This Dissertation

This dissertation ultimately aims to develop an electrochemical system that can efficiently convert CO_2 to liquid fuels for alternative energy sources. This dissertation firstly studied the fundamental topic of CO_2 reduction chemistry in the electrical double layer with a focus on the effects of electrolyte on the activity and selectivity towards CO_2 reduction. And then, a full electrochemical cell featuring a circulating electrolyte buffer layer based on the current PEMFC configuration was designed to meet the requirements of both high current density and energy efficiency for the CO_2 reduction process. The microstructure of the Sn GDE consisting of 100 nm Sn nanoparticles was optimized and incorporated into the full electrochemical cell. Following the study of activity and selectivity towards CO_2 reduction on the Sn GDEs in the full electrochemical cell, the long-term stability of Sn GDE was investigated, which revealed the degradation mechanism of Faradaic efficiency of target products. Based on the understanding of the degradation origin, the mitigation strategy was developed to achieve long-term stable operation. Finally, the dependence of the Sn GDE performance on the Sn nanoparticle surface structure was studied to provide insights into the structure-performance relationship. Although this research employed Sn electrodes, the results apply to the other catalysts as well. Specifically, the following issues were addressed:

1) **Chemistry of CO_2 reduction in electrical double layer (Chapter 2):** This chapter addressed the effects of the electrolyte including especially the electrostatic adsorption of alkali cations, specific adsorption of anion and electrolyte concentration on the potential (E_2) at outer Helmholtz plane and proton concentration ($[H^+]_s$) within the electrical double layer. The resulted variety of E_2 and $[H^+]_s$ contributes to the trend of Faradiac efficiency of formate and current density for CO_2 reduction with different kinds of electrolytes.
2) **Design, assembly, and performance of low temperature full electrochemical cells:** In order to avoid low solubility of CO_2 in aqueous electrolyte, Sn GDEs comprised of 100 nm Sn nanoparticle catalysts were employed for direct gas-phase CO_2 reduction. The microstructure of Sn catalyst layer in GDEs was optimized by tuning the proton conductor (Nafion) and Sn catalyst fraction to achieve simultaneous high current density and selectivity towards formate formation (**Chapter 3**). Afterwards, a bench-scale full electrochemical cell which embeds the Sn GDEs was designed and assembled (**Chapter 4**). This full electrochemical cell features a buffer layer of circulating liquid electrolyte which mediates the proton concentration at the Sn GDE

surface. Conversion of gas-phase CO_2 to formate with simultaneous high Faradaic and energy efficiencies was achieved at room temperature and ambient pressure in this full electrochemical cell incorporating Sn GDEs. The performance of cell was further improved through optimizing operation conditions in terms of buffer layer thickness and electrolyte pH.

3) **Stability of Sn GDEs in the full electrochemical cell (Chapter 5):** This chapter systematically investigated the origin of morphology evolution of 100 nm Sn nanoparticles during long-term cell operation. The severe pulverization of Sn nanoparticles from 100 nm to 2-3 nm in 60 hours mainly resultes from hydrogen diffusion induced stress. The degradation of Faradaic efficiency of formate results in the increase of ohmic resistance and hence a decline of cathode electrod potential due to pulverizastion of Sn nanoparticles. The selectivity towards formate production stabilizes after ceasing the pulverization by introducing SnO_2 nanoparticles of 3.5 nm close to a critical size which has a strong surface free energy to compensate the hydrogen diffusion induced strain.

4) **Dependence of Sn GDE performance on surface oxide thickness in the full electrochemical cell (Chapter 6):** The surface of Sn particles is covered by a thin oxide (SnO_x) layer. The dependence of Sn GDEs performance on the initial thickness of surface SnO_x layer was investigated in the full electrochemical cell. The current density shows a negligible dependence on the initial thickness of SnO_x layer, while the selectivity towards the formation of CO and formate exhibits a strong relationship with the initial SnO_x thickness.

References

1. Carbon Dioxide Information Analysis Center, http://cdiac.esd.ornl.gov/.
2. B. Metz et. al., *Climate Change 2007: Mitigation of Climate Change, Contribution of Working Group III to the Fourth Assessment Report of the Intergovernmental Panel on Climate Change,* Cambridge University Press (2007).
3. S. Bachu, *Prog. Energy Combust. Sci.*, **34,** 254-273 (2008).
4. C. Song, *Catal. Today*, **115,** 2-32 (2006).
5. B. Hu, C. Guild and S. L. Suib, *J. CO_2 Utilization,* **1,** 18-27 (2013).
6. G. Centi, E. A. Quadrelli and S. Perathoner, *Energy Environ. Sci.*, **6,** 171-1731 (2013).
7. H. Li, P. H. Opgenorth, D. G. Wernick, S. Rogers, T.-Y. Wu, W. Higashide, P. Malati, Y.-X. Huo, K. M. Cho and J. C. Liao, *Science,* **335,** 1596 (2012).
8. Z. H. Duan, R. Sun, C. Zhu and I. M. Chou, *Mar. Chem.*, **98,** 131-139 (2006).
9. M. K. Nikoo and N. A. S. Amin, *Fuel Process. Technol.*, **92,** 678-691 (2011).
10. D. T. Whipple and P. J. A. Kenis, *J. Phy. Chem. Lett.*, **1,** 3451-3458 (2010).
11. Y. B. Vassiliev, V. S. Bagotsky, N. V. Osetrova, O. A. Khazova and N. A. Mayorova, *J. Electroanal. Chem. Interfacial Electrochem.*, **189,** 271-294 (1985).
12. B. A. Rosen, A. Salehi-Khojin, M. R. Thorson, W. Zhu, D. T. Whipple, P. J. A. Kenis and R. I. Masel, *Science,* **334,** 643-644 (2011).
13. B. Metz, O. Davidson, H. d. Coninck, M. Loos and L. Meyer, *IPCC special report on carbon dioxide capture and storage,* (2005).
14. R. S. Haszeldine, *Science,* **325,** 1647-1652 (2009).
15. L. Shi, G. Yang, K. Tao, Y. Yoneyama, Y. Tan and N. Tsubaki, *Acc. Chem. Res.*, **46**, 1838-1847 (2013).
16. C. Crisafulli, S. Scirè, R. Maggiore, S. Minicò and S. Galvagno, *Catal. Lett.*, **59,** 21-26 (1999).
17. J. Yoshihara and C. T. Campbell, *J. Catal.*, **161,** 776-782 (1996).
18. J. Yoshihara, S. C. Parker, A. Schafer and C. Campbell, *Catal. Lett.*, **31,** 313-324 (1995).
19. C. Song, *Chem. Innovation,* **31,** 21-26 (2001).
20. B. Kumar, M. Llorente, J. Froehlich, T. Dang, A. Sathrum and C. P. Kubiak, *Annu. Rev. Phys. Chem.*, **63,** 541-569 (2012).
21. A. J. Morris, G. J. Meyer and E. Fujita, *Acc. Chem. Res.*, **42,** 1983-1994 (2009).
22. H. Takeda and O. Ishitani, *Coord. Chem. Rev.*, **254,** 346-354 (2010).
23. B. Durham, J. V. Caspar, J. K. Nagle and T. J. Meyer, *J. Am. Chem. Soc.*, **104,** 4803-4810 (1982).
24. C. A. Craig, L. O. Spreer, J. W. Otvos and M. Calvin, *J. Phys. Chem.*, **94,** 7957-7960 (1990).
25. J. Grodkowski, P. Neta, E. Fujita, A. Mahammed, L. Simkhovich and Z. Gross, *J. Phys. Chem. A,* **106,** 4772-4778 (2002).
26. J. Grodkowski and P. Neta, *J. Phys. Chem. A,* **104,** 1848-1853 (2000).
27. J. Grodkowski, T. Dhanasekaran, P. Neta, P. Hambright, B. S. Brunschwig, K. Shinozaki and E. Fujita, *J. Phys. Chem. A,* **104,** 11332-11339 (2000).
28. J. Hawecker, J.-M. Lehn and R. Ziessel, *J. Chem. Soc., Chem. Commun.,* 536-538 (1983).
29. L. Junfu and C. Baozhu, *J. Electroanal. Chem.*, **324,** 191-200 (1992).

30. B. Aurian-Blajeni, M. Halmann and J. Manassen, *Sol. Energy Mater.,* **8,** 425-440 (1983).
31. I. Taniguchi, B. Aurian-Blajeni and J. O. M. Bockris, *Electrochim. Acta,* **29,** 923-932 (1984).
32. K. Hirota, D. A. Tryk, T. Yamamoto, K. Hashimoto, M. Okawa and A. Fujishima, *J. Phys. Chem. B,* **102,** 9834-9843 (1998).
33. S. Kaneco, H. Katsumata, T. Suzuki and K. Ohta, *Chem. Eng. J.,* **116,** 227-231 (2006).
34. W. M. Sears and S. R. Morrison, *J. Phys. Chem.,* **89,** 3295-3298 (1985).
35. R. Hinogami, T. Mori, S. Yae and Y. Nakato, *Chem. Lett.,* **23,** 1725-1728 (1994).
36. R. Hinogami, Y. Nakamura, S. Yae and Y. Nakato, *Appl. Surf. Sci.,* **121-122,** 301-304 (1997).
37. P. Usubharatana, D. McMartin, A. Veawab and P. Tontiwachwuthikul, *Ind. Eng. Chem. Res.,* **45,** 2558-2568 (2006).
38. T. Shimidzu, T. Iyoda and Y. Koide, *J. Am. Chem. Soc.,* **107,** 35-41 (1985).
39. M. Anpo, S. Dohshi, M. Kitano, Y. Hu, M. Takeuchi and M. Matsuoka, *Ann. Rev. Mater. Res.,* **35,** 1-27 (2005).
40. M. Kitano, M. Matsuoka, M. Ueshima and M. Anpo, *Appl. Catal. A: General,* **325,** 1-14 (2007).
41. J.-P. Petit, P. Chartier, M. Beley and J.-P. Deville, *J. Electroanal. Chem. Interfacial Electrochem.,* **269,** 267-281 (1989).
42. M. Beley, J.-P. Collin, J.-P. Sauvage, J.-P. Petit and P. Chartier, *J. Electroanal. Chem. Interfacial Electrochem.,* **206,** 333-339 (1986).
43. E. E. Barton, D. M. Rampulla and A. B. Bocarsly, *J. Am. Chem. Soc.,* **130,** 6342-6344 (2008).
44. T. Arai, S. Sato, K. Uemura, T. Morikawa, T. Kajino and T. Motohiro, *Chem. Commun.,* **46,** 6944-6946 (2010).
45. B. Aurian-Blajeni, I. Taniguchi and J. M. Bockris, *J. Electroanal. Chem. Interfacial Electrochem.,* **149,** 291-293 (1983).
46. S. Ichikawa and R. Doi, *Catal. Today,* **27,** 271-277 (1996).
47. C. Cheung, U. Erb, G. Palumbo and M. S. E. A., *Mater. Sci. Eng. A,* **185,** 39-43 (1994).
48. Z. Zhan and L. Zhao, *J. Power Sources,* **195,** 7250-7254 (2010).
49. S. D. Ebbesen and M. Mogensen, *J. Power Sources,* **193,** 349-358 (2009).
50. S. H. Jensen, P. H. Larsen and M. Mogensen, *Int. J. Hydrogen Energy,* **32,** 3253-3257 (2007).
51. T. J. Huang and C. L. Chou, *Electrochem. Commun.,* **11,** 1464-1467 (2009).
52. T. Kim, S. Moon and S. I. Hong, *Appl. Catal. A: General,* **224,** 111-120 (2002).
53. F. Bidrawn, G. Kim, G. Corre, J. T. S. Irvine, J. M. Vohs and R. J. Gorte, *Electrochem. Solid-State Lett.,* **11,** B167-B170 (2008).
54. J. M. Saveant, *Chem. Rev.,* **108,** 2348-2378 (2008).
55. F. Abba, G. De Santis, L. Fabbrizzi, M. Licchelli, A. M. Manotti Lanfredi, P. Pallavicini, A. Poggi and F. Ugozzoli, *Inorg. Chem.,* **33,** 1366-1375 (1994).
56. J. M. Smieja and C. P. Kubiak, *Inorg. Chem.,* **49,** 9283-9289 (2010).
57. M. Rakowski Dubois and D. L. Dubois, *Acc. Chem. Res.,* **42,** 1974-1982 (2009).

58. R. Angamuthu, P. Byers, M. Lutz, A. L. Spek and E. Bouwman, *Science,* **327,** 313-315 (2010).
59. C. Finn, S. Schnittger, L. J. Yellowlees and J. B. Love, *Chem. Commun.,* **48,** 1392-1399 (2012).
60. E. Fujita, C. Creutz, N. Sutin and D. J. Szalda, *J. Am. Chem. Soc.,* **113,** 343-353 (1991).
61. J. W. Raebiger, J. W. Turner, B. C. Noll, C. J. Curtis, A. Miedaner, B. Cox and D. L. DuBois, *Organometallics,* **25,** 3345-3351 (2006).
62. A. Miedaner, B. C. Noll and D. L. DuBois, *Organometallics,* **16,** 5779-5791 (1997).
63. D. Ooyama, T. Tomon, K. Tsuge and K. Tanaka, *J. Organomet. Chem.,* **619,** 299-304 (2001).
64. R. J. Haines, R. E. Wittrig and C. P. Kubiak, *Inorg. Chem.,* **33,** 4723-4728 (1994).
65. M. Beley, J. P. Collin, R. Ruppert and J. P. Sauvage, *J. Am. Chem. Soc.,* **108,** 7461-7467 (1986).
66. M. Shionoya, E. Kimura and Y. Iitaka, *J. Am. Chem. Soc.,* **112,** 9237-9245 (1990).
67. I. S. Weitz, J. L. Sample, R. Ries, E. M. Spain and J. R. Heath, *J. Phys. Chem. B,* **104,** 4288-4291 (2000).
68. E. Barton Cole, P. S. Lakkaraju, D. M. Rampulla, A. J. Morris, E. Abelev and A. B. Bocarsly, *J. Am. Chem. Soc.,* **132,** 11539-11551 (2010).
69. G. Seshadri, C. Lin and A. B. Bocarsly, *J. Electroanal. Chem.,* **372,** 145-150 (1994).
70. R. P. S. Chaplin and A. A. Wragg, *J. Appl. Electrochem.,* **33,** 1107-1123 (2003).
71. M. Jitaru, D. A. Lowy, M. Toma, B. C. Toma and L. Oniciu, *J. Appl. Electrochem.,* **27,** 875-889 (1997).
72. Y. Hori, *Modern Aspects of Electrochemistry: Chapter 3 Electrochemical* CO_2 *reduction on metal electrodes,* Springer (2008).
73. A. Bandi, J. Schwarz and C. U. Maier, *J. Electrochem. Soc.,* **140,** 1006-1008 (1993).
74. S. Ikeda, T. Takagi, K. Ito and 60, *Bull. Chem. Soc. Jpn.,* **60,** 2517 (1987).
75. Y. Hori, H. Wakebe, T. Tsukamoto and O. Koga, *Electrochim. Acta,* **39,** 1833-1839 (1994).
76. F. Fischer and O. Prziza, *Berichte Der Deutschen Chemischen Gesellschaft,* **47,** 256-260 (1914).
77. R. Ehrenfeld, *Berichte Der Deutschen Chemischen Gesellschaft,* **38,** 4138-4143 (1905).
78. M. Gattrell, N. Gupta and A. Co, *J. Electroanal. Chem.,* **594,** 1-19 (2006).
79. H. Noda, S. Ikeda, Y. Oda and K. Ito, *Chem. Lett.,* 289-292 (1989).
80. Y. Hori, A. Murata and R. Takahashi, *J. Chem. Soc., Faraday Trans.,* **85,** 2309-2326 (1989).
81. W. Tang, A. A. Peterson, A. S. Varela, Z. P. Jovanov, L. Bech, W. J. Durand, S. Dahl, J. K. Norskov and I. Chorkendorff, *Phys. Chem. Chem. Phys.,* **14,** 76-81 (2012).
82. K. P. Kuhl, E. R. Cave, D. N. Abram and T. F. Jaramillo, *Energy Environ. Sci.,* **5,** 7050-7059 (2012).
83. Y. Hori, I. Takahashi, O. Koga and N. Hoshi, *J. Phys. Chem. B,* **106,** 15-17 (2001).
84. R. L. Cook, R. C. MacDuff and A. F. Sammells, *J. Electrochem. Soc.,* **135,** 1320-1326 (1988).
85. Y. Terunuma, A. Saitoh and Y. Momose, *J. Electroanal. Chem.,* **434,** 69-75 (1997).

86. S. Ishimaru, R. Shiratsuchi and G. Nogami, *J. Electrochem. Soc.,* **147,** 1864-1867 (2000).
87. G. Kyriacou and A. Anagnostopoulos, *J. Electroanal. Chem.,* **322,** 233-246 (1992).
88. C. W. Li and M. W. Kanan, *J. Am. Chem. Soc.,* **134,** 7231-7234 (2012).
89. Y. Chen, C. W. Li and M. W. Kanan, *J. Am. Chem. Soc.,* **134,** 19969-19972 (2012).
90. D. W. DeWulf, T. Jin and A. J. Bard, *J. Electrochem. Soc.,* **136,** 1686-1691 (1989).
91. J. K. W. Frese, *J. Electrochem. Soc.,* **138,** 3338-3344 (1991).
92. M. Le, M. Ren, Z. Zhang, P. T. Sprunger, R. L. Kurtz and J. C. Flake, *J. Electrochem. Soc.,* **158,** E45-E49 (2011).
93. M. Watanabe, M. Shibata, A. Kato, M. Azuma and T. Sakata, *J. Electrochem. Soc.,* **138,** 3382-3389 (1991).
94. M. Watanabe, M. Shibata, A. Kato, M. Azuma and T. Sakata, *J. Electrochem. Soc.,* **138,** 3395-3399 (1991).
95. M. Watanabe, M. Shibata, A. Katoh, M. Azuma and T. Sakata, *Denki Kagaku,* **59,** 508-516 (1991).
96. M. Watanabe, M. Shibata, A. Katoh, T. Sakata and M. Azuma, *J. Electroanal. Chem.,* **305,** 319-328 (1991).
97. A. Katoh, H. Uchida, M. Shibata and M. Watanabe, *J. Electrochem. Soc.,* **141,** 2054-2058 (1994).
98. Y. Hori, H. Wakebe, T. Tsukamoto and O. Koga, *Surf. Sci.,* **335,** 258-263 (1995).
99. I. Takahashi, O. Koga, N. Hoshi and Y. Hori, *J. Electroanal. Chem.,* **533,** 135-143 (2002).
100. Y. Hori, I. Takahashi, O. Koga and N. Hoshi, *J. Mol. Catal. A: Chem.,* **199,** 39-47 (2003).
101. R. Shiratsuchi, Y. Aikoh and G. Nogami, *J. Electrochem. Soc.,* **140,** 3479-3482 (1993).
102. B. D. Smith, D. E. Irish, P. Kedzierzawski and J. Augustynski, *J. Electrochem. Soc.,* **144,** 4288-4296 (1997).
103. Y. Hori, H. Konishi, T. Futamura, A. Murata, O. Koga, H. Sakurai and K. Oguma, *Electrochim. Acta,* **50,** 5354-5369 (2005).
104. P. Friebe, P. Bogdanoff, N. Alonso-Vante and H. Tributsch, *J. Catal.,* **168,** 374-385 (1997).
105. G. Nogami, H. Itagaki and R. Shiratsuchi, *J. Electrochem. Soc.,* **141,** 1138-1142 (1994).
106. J. Yano and S. Yamasaki, *J. Appl. Electrochem.,* **38,** 1721-1726 (2008).
107. J. Yano, T. Morita, K. Shimano, Y. Nagami and S. Yamasaki, *J. Solid State Electrochem.,* **11,** 554-557 (2007).
108. B. Jermann and J. Augustynski, *Electrochim. Acta,* **39,** 1891-1896 (1994).
109. A. A. Peterson, F. Abild-Pedersen, F. Studt, J. Rossmeisl and J. K. Norskov, *Energy Environ. Sci.,* **3,** 1311-1315 (2010).
110. A. A. Peterson and J. K. Nørskov, *J. Phy. Chem. Lett.,* **3,** 251-258 (2012).
111. W. J. Durand, A. A. Peterson, F. Studt, F. Abild-Pedersen and J. K. Nørskov, *Surf. Sci.,* **605,** 1354-1359 (2011).
112. Y. Hori, K. Kikuchi and S. Suzuki, *Chem. Lett.,* 1695-1698 (1985).
113. K. Hara, A. Kudo and T. Sakata, *J. Electroanal. Chem.,* **391,** 141-147 (1995).
114. S. Ikeda, T. Takagi and K. Ito, *Bull. Chem. Soc. Jpn.,* **60,** 2517-2522 (1987).

115. R. Shiratsuchi and G. Nagami, *J. Electrochem. Soc.*, **143,** 582-586 (1996).
116. C. E. Tornow, M. R. Thorson, S. Ma, A. A. Gewirth and P. J. A. Kenis, *J. Am. Chem. Soc.*, **134,** 19520-19523 (2012).
117. B. Innocent, D. Liaigre, D. Pasquier, F. Ropital, J. M. Leger and K. B. Kokoh, *J. Appl. Electrochem.*, **39,** 227-232 (2009).
118. M. Azuma, K. Hashimoto, M. Hiramoto, M. Watanabe and T. Sakata, *J. Electrochem. Soc.*, **137,** 1772-1778 (1990).
119. F. Koleli, T. Atilan, N. Palamut, A. M. Gizir, R. Aydin and C. H. Hamann, *J. Appl. Electrochem.*, **33,** 447-450 (2003).
120. T. Mizuno, K. Ohta, A. Sasaki, T. Akai, M. Hirano and A. Kawabe, *Energy Sources*, **17,** 503-508 (1995).
121. S. Kaneco, R. Iwao, K. Iiba, K. Ohta and T. Mizuno, *Energy*, **23,** 1107-1112 (1998).
122. M. N. Mahmood, D. Masheder and C. J. Harty, *J. Appl. Electrochem.*, **17,** 1159-1170 (1987).
123. C. Rice, R. I. Ha, R. I. Masel, P. Waszczuk, A. Wieckowski and T. Barnard, *J. Power Sources*, **111,** 83-89 (2002).
124. Y. M. Zhu, S. Y. Ha and R. I. Masel, *J. Power Sources*, **130,** 8-14 (2004).
125. C. V. Rao, C. R. Cabrera and Y. Ishikawa, *J. Phys. Chem. C*, **115,** 21963-21970 (2011).
126. N. V. Rees and R. G. Compton, *J. Solid State Electrochem.*, **15,** 2095-2100 (2011).
127. T. T. Cheng and E. L. Gyenge, *J. Electrochem. Soc.*, **155,** B819-B828 (2008).
128. K. L. Chu, M. A. Shannon and R. I. Masel, *J. Electrochem. Soc.*, **153,** A1562-A1567 (2006).
129. R. P. S. Chaplin and A. A. Wragg, *J. Appl. Electrochem.*, **33,** 1107-1123 (2003).
130. Y. H. Chen and M. W. Kanan, *J. Am. Chem. Soc.*, **134,** 1986-1989 (2012).
131. Y. Hori, H. Wakebe, T. Tsukamoto and O. Koga, *Electrochimica Acta*, **39,** 1833-1839 (1994).
132. J. P. Popić, M. L. Avramov-Ivić and N. B. Vuković, *J. Electroanal. Chem.*, **421,** 105-110 (1997).
133. K. W. Frese and S. Leach, *J. Electrochem. Soc.*, **132,** 259-260 (1985).
134. N. Furuya, T. Yamazaki and M. Shibata, *J. Electroanal. Chem.*, **431,** 39-41 (1997).
135. N. Hoshi, T. Suzuki and Y. Hori, *Electrochim. Acta*, **41,** 1647-1653 (1996).
136. N. Hoshi, T. Suzuki and Y. Hori, *J. Electroanal. Chem.*, **416,** 61-65 (1996).
137. H. Noda, S. Ikeda, Y. Oda, K. Imai, M. Maeda and K. Ito, *Bull. Chem. Soc. Jpn.*, **63,** 2459-2462 (1990).
138. K. Ohta, M. Kawamoto, T. Mizuno and D. A. Lowy, *J. Appl. Electrochem.*, **28,** 717-724 (1998).
139. D. T. Whipple, E. C. Finke and P. J. A. Kenis, *Electrochem. Solid-State Lett.*, **13,** D109-D111 (2010).
140. K. Hara, A. Tsuneto, A. Kudo and T. Sakata, *J. Electrochem. Soc.*, **141,** 2097-2103 (1994).
141. S. Kaneco, N.-h. Hiei, Y. Xing, H. Katsumata, H. Ohnishi, T. Suzuki and K. Ohta, *Electrochim. Acta*, **48,** 51-55 (2002).
142. S. Kaneco, H. Katsumata, T. Suzuki and K. Ohta, *Utilization of Greenhouse Gases: Electrochemical reduction of CO_2 on Cu electrode in methanol at low temperature*, (2003).

143. T. Mizuno, A. Naitoh and K. Ohta, *J. Electroanal. Chem.,* **391,** 199-201 (1995).
144. S. Kaneco, K. Iiba, H. Katsumata, T. Suzuki and K. Ohta, *J. Solid State Electrochem.,* **11,** 490-495 (2007).
145. A. Murata and Y. Hori, *Bull. Chem. Soc. Jpn.,* **64,** 123-127 (1991).
146. G. Z. Kyriacou and A. K. Anagnostopoulos, *J. Appl. Electrochem.,* **23,** 483-486 (1993).
147. M. R. Thorson, K. I. Siil and P. J. A. Kenis, *J. Electrochem. Soc.,* **160,** F69-F74 (2013).
148. E. Brunner, W. Hültenschmidt and G. Schlichthärle, *J. Chem. Thermodyn.,* **19,** 273-291 (1987).
149. S. Kaneco, K. Iiba, S.-k. Suzuki, K. Ohta and T. Mizuno, *J. Phys. Chem. B,* **103,** 7456-7460 (1999).
150. S. Kaneco, K. Iiba, N.-h. Hiei, K. Ohta, T. Mizuno and T. Suzuki, *Electrochim. Acta,* **44,** 4701-4706 (1999).
151. S. Kaneco, H. Katsumata, T. Suzuki and K. Ohta, *Electrochim. Acta,* **51,** 3316-3321 (2006).
152. A. Naitoh, K. Ohta, T. Mizuno, H. Yoshida, M. Sakai and H. Noda, *Electrochim. Acta,* **38,** 2177-2179 (1993).
153. T. Saeki, K. Hashimoto, A. Fujishima, N. Kimura and K. Omata, *J. Phys. Chem.,* **99,** 8440-8446 (1995).
154. S. Kaneco, K. Iiba, M. Yabuuchi, N. Nishio, H. Ohnishi, H. Katsumata, T. Suzuki and K. Ohta, *Ind. Eng. Chem. Res.,* **41,** 5165-5170 (2002).
155. S. Kaneco, K. Iiba, H. Katsumata, T. Suzuki and K. Ohta, *Electrochim. Acta,* **51,** 4880-4885 (2006).
156. R. L. Cook, R. C. Macduff and A. F. Sammells, *J. Electrochem. Soc.,* **137,** 187-189 (1990).
157. R. L. Cook, R. C. Macduff and A. F. Sammells, *J. Electrochem. Soc.,* **135,** 1470-1471 (1988).
158. S. Komatsu, M. Tanaka, A. Okumura and A. Kungi, *Electrochim. Acta,* **40,** 745-753 (1995).
159. M. Maeda, Y. Kitaguchi, S. Ikeda and K. Ito, *J. Electroanal. Chem.,* **238,** 247-258 (1987).
160. Y. Hori, H. Ito, K. Okano, K. Nagasu and S. Sato, *Electrochim. Acta,* **48,** 2651-2657 (2003).
161. D. W. Dewulf and A. J. Bard, *Catal. Lett.,* **1,** 73-79 (1988).
162. N. Furuya, K. Matsui and S. Motoo, *Denki Kagaku,* **56,** 980-984 (1988).
163. R. L. Cook, R. C. Macduff and A. F. Sammells, *J. Electrochem. Soc.,* **137,** 607-608 (1990).
164. M. Schwartz, M. E. Vercauteren and A. F. Sammells, *J. Electrochem. Soc.,* **141,** 3119-3127 (1994).
165. H. Yano, F. Shirai, M. Nakayama and K. Ogura, *J. Electroanal. Chem.,* **519,** 93-100 (2002).
166. H. Yano, T. Tanaka, M. Nakayama and K. Ogura, *J. Electroanal. Chem.,* **565,** 287-293 (2004).
167. H. Yano, F. Shirai, M. Nakayama and K. Ogura, *J. Electroanal. Chem.,* **533,** 113-118 (2002).

168. K. Hara and T. Sakata, *J. Electrochem. Soc.*, **144,** 539-545 (1997).
169. K. Hara, A. Kudo, T. Sakata and M. Watanabe, *J. Electrochem. Soc.*, **142,** L57-L59 (1995).
170. M. Schwartz, R. L. Cook, V. M. Kehoe, R. C. Macduff, J. Patel and A. F. Sammells, *J. Electrochem. Soc.*, **140,** 614-618 (1993).
171. T. Yamamoto, D. A. Tryk, A. Fujishima and H. Ohata, *Electrochim. Acta,* **47,** 3327-3334 (2002).
172. C. Delacourt, P. L. Ridgway, J. B. Kerr and J. Newman, *J. Electrochem. Soc.,* **155,** B42-B49 (2008).
173. H. Li and C. Oloman, *J. Appl. Electrochem.,* **35,** 955-965 (2005).
174. H. Li and C. Oloman, *J. Appl. Electrochem.*, **36,** 1105-1115 (2006).
175. H. Li and C. Oloman, *J. Appl. Electrochem.*, **37,** 1107-1117 (2007).
176. E. J. Dufek, T. E. Lister and M. E. McIlwain, *J. Appl. Electrochem.,* **41,** 623-631 (2011).
177. E. J. Dufek, T. E. Lister and M. E. McIlwain, *J. Electrochem. Soc.,* **158,** B1384-B1390 (2011).
178. E. J. Dufek, T. E. Lister and M. E. McIlwain, *Electrochem. Solid-State Lett.*, **15,** B48-B50 (2012).
179. C. Delacourt and J. Newman, *J. Electrochem. Soc.*, **157,** B1911-B1926 (2010).
180. A. S. Agarwal, Y. Zhai, D. Hill and N. Sridhar, *Chem. Sus. Chem.,* **4,** 1301-1310 (2011).
181. E. J. Dufek, T. E. Lister, S. G. Stone and M. E. McIlwain, *J. Electrochem. Soc.,* **159,** F514-F517 (2012).
182. B. A. Rosen, J. L. Haan, P. Mukherjee, B. Braunschweig, W. Zhu, A. Salehi-Khojin, D. D. Dlott and R. I. Masel, *J. Phys. Chem. C,* **116,** 15307-15312 (2012).

Chapter 2

Reduction Reaction Chemistry in Electrical Double Layer: Effects of Electrolyte on the Selectivity and Activity towards CO_2 Reduction

2.1 Introduction

One of the promising heterogeneous catalysts for electrochemical reduction of CO_2 is Sn, which maintains high selectivity for the production of formic acid/formate in aqueous electrolytes.[1-3] Liquid fuel such as formic acid with a free energy of combustion of -233 kJ mol^{-1} is a promising fuel for the generation of electricity in fuel cells.[4-9] The usual CO_2 reduction pathway, involves an initial adsorption step followed by a one-electron reduction to form the intermediate $CO_2^{\bullet -}$ species. The weakly adsorbed $CO_2^{\bullet -}$ goes through a protonation reaction and then the second electron-transfer to yield formate. The formation process of formate is companied by a parallel disproportionation of the stable $CO_2^{\bullet -}$ radical anions adsorbed to produce CO.[1, 10]

A wide range of Faradaic efficiencies for formate formation on the Sn electrodes have been reported, due largely to the nature of the electrolyte and the operating conditions (e.g. the potentials or current densities, temperatures, and pressures).[11-15] A greater Faradaic efficiency towards formate production was observed in 0.5 M $KHCO_3$ than in 0.1 M K_2CO_3 with a Sn granule electrode in a fixed-bed reactor.[11] The Faradaic efficiency of formate increased with the decreasing of electrolyte concentration, maximum ~88.4% in 0.1 M $KHCO_3$[13] versus ~70% in 0.5 M $KHCO_3$[16]. In addition to the carbonate electrolytes, Na_2SO_4 was investigated with a Sn based gas diffusion electrode, which resulted in a Faradaic efficiency of 57% at -1.8 V vs. SCE.[14] Electrolytes with lower pH could promote the formation of formic acid/formate on Sn electrodes.[17] Nonaqueous solvent has been utilized in order to obtain a higher concentration of CO_2. In the CO_2-methanol system, the Faradaic efficiencies of target products increased compared to the aqueous solution.[18, 19]

This chapter systematically studied the chemistry of CO_2 reduction within the electrical double layer with the aim to address the effects of electrolyte including the electrostatic adsorption of alkali cations, specific adsorption of anion and electrolyte concentration on the potential (E_2) and proton concentration ($[H^+]_{surface}$) at outer Helmholtz plane (OHP), at which the reaction occurs. Subsequently, the variation of E_2 and $[H^+]_{surface}$ with different electrolytes was correlated to the trend of Faradiac efficiency of formate and current density for CO_2 reduction.

2.2 Experimental: Electrochemical Test and Products Quantification

2.2.1 Electrochemical Test

The electrochemical reduction of CO_2 was conducted in a conventional three-electrode electrochemical cell. The working electrode was a Sn foil (Alfa Aesar, 99.998%) with an active surface area of 1 cm^2, which was etched in a nitric solution (ca. 1 mol l^{-1}) for 10 seconds to remove surface contaminants. A Pt foil (dimension: 3×3 cm^2) and an SCE were used as a counter and reference electrode, respectively. Before electrolysis, the electrolyte was pre-electrolyzed via a Pt foil at the potential of -2.0 V vs. SCE for at least 10 hours, during which CO_2 gas (purity 99.999%) bubbled through the aqueous electrolyte solution using a gas disperser to remove any dissolved oxygen. The electrolysis was then conducted under constant potentials for one hour by employing a potentiostat (Solartron 1470E). Electrolytes with an initial formate concentration of 6 × 10^{-3} mol l^{-1} were used to determine whether or not oxidation of the products occurred on the Pt-anode (counter electrode). It was observed that the amount of oxidized formate was less than 5% in 1 h electrolysis when bubbling Ar into 0.5 M Na_2SO_4. The electrolytes examined in this research include $KHCO_3$, K_2SO_4, KCl, Na_2SO_4, Cs_2SO_4, $NaHCO_3$, and $CsHCO_3$. All of these chemicals were certified ACS reagent grade and dissolved in distilled water (Siemens, Labstar^{TM}).

2.2.2 Nuclear Magnetic Resonance Products Quantification

^{1}H nuclear magnetic resonance (NMR) spectroscopy is a powerful and effective technique to determine the local chemical environment and concentration of protons in both solids and liquids.[20, 21] In this research, ^{1}H NMR was employed to quantify the concentration of formate products in aqueous solutions. The NMR data was acquired using a Varian Mercury 400 MHz instrument using the WET solvent suppression pulse sequence. The spectra were measured at room temperature with an acquisition time of 2.18 s, a relaxation delay of 20 s, and 32 free induction decay averages. Sodium 3-(trimethylsilyl) propionate 2, 2, 3, 3-d (4) (TSP) was used as the internal standard. TSP has three CH_3 groups accounting for a total of nine hydrogen atoms. The concentration of standard TSP solution is 0.6 mM. The NMR sample was prepared by withdrawing 500 μl of product solution from the electrolysis cell and depositing it into an NMR tube followed by adding 100 μl of TSP standard solution.

2.3 Results and Discussion

2.3.1 Quantification of the Formate Products

The typical ^{1}H NMR spectra for formate and TSP are shown in **Figure 2.1**. The chemical shift of the hydrogen atom in the CH group in formate ($HCOO^-$) is at ~8.443 ppm while 0 ppm is assigned to the hydrogen atoms in the CH_3 group of TSP. The area of an individual peak corresponds to the concentration of a specific chemical group. Indeed, the peak area for the CH group increases with the increasing duration of electrolysis as shown in **Figure 2.1**, which suggests an increased formate concentration in the electrolysis cell. Formate concentration was determined with the peak area of the hydrogen atom of CH in formate reference to that of hydrogen atoms of CH_3 in TSP.

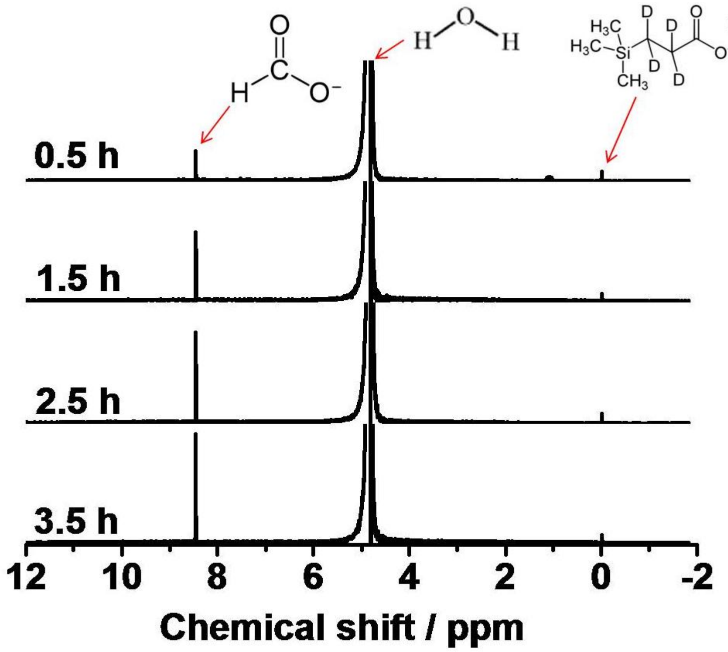

Figure 2.1. ^{1}H NMR spectra of formate produced from CO_2 reduction at E = -2 V vs. SCE in 0.5 M $KHCO_3$.

A calibration curve was made by plotting the concentrations of standard formic acid solutions versus the concentrations measured by NMR, as illustrated in **Figure 2.2**. A linear equation was obtained by fitting the calibration curve, by which the concentration of formate produced during electrolysis was calibrated. The Faradaic efficiency of formate was calculated using the following equation:

$$\eta_{\mathrm{formate}} = \frac{n_{\mathrm{formate}} \times 2F}{C} \tag{2.1}$$

where n_{formate} is the number of moles of formate produced, F is the Faraday's constant, and C is total coulomb of electrons passed across the Sn electrode during the duration of electrolysis.

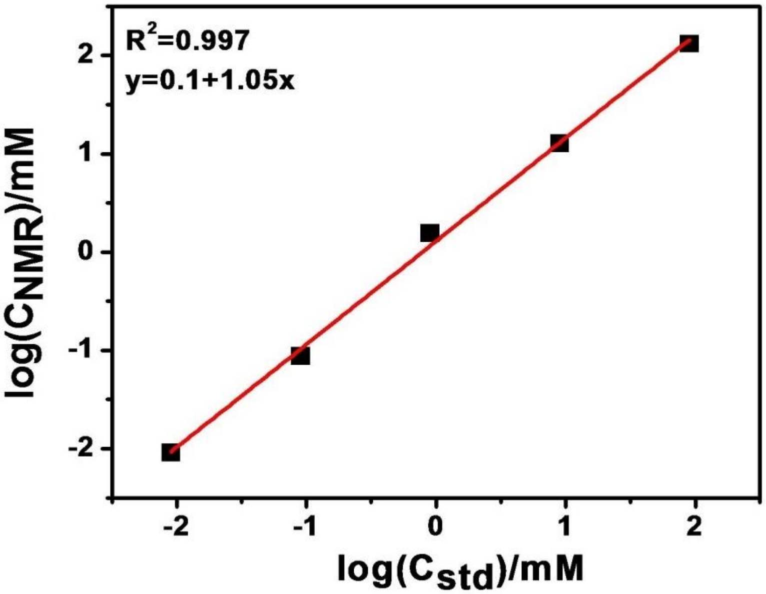

Figure 2.2. Calibration curve by plotting standard concentration of formic acid versus the NMR measured concentration.

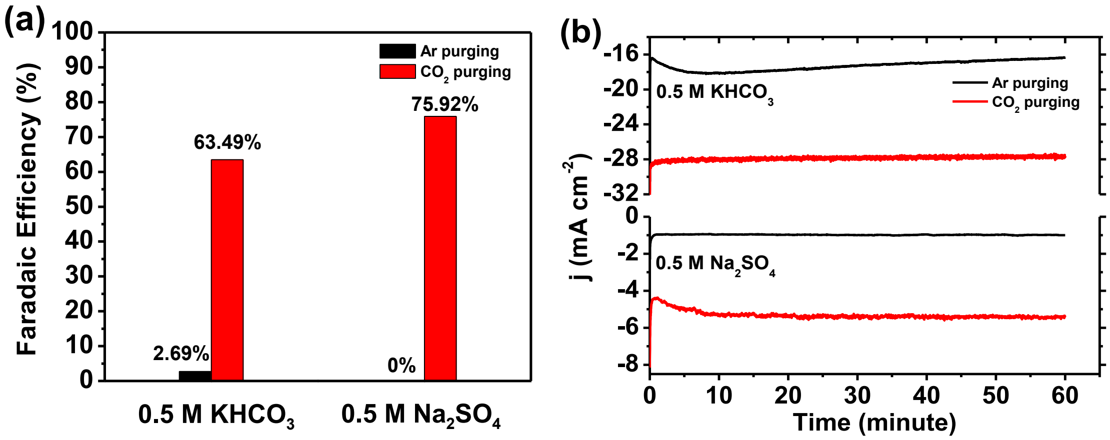

Figure 2.3. Comparison of (a) Faraday efficiency of formate and (b) total current density between Ar and CO_2 bubbling electrolyte at the electrolysis potential of -2 V vs. SCE.

Initial research focused on investigating the effects of purging gas, CO_2 or Ar, on the current density for the reduction reaction and the Faradaic efficiency towards formate production. The results obtained at the electrolysis potential of -2 V vs. SCE are shown in **Figure 2.3**. In 0.5 M Na_2SO_4 electrolyte with Ar bubbling, no formate was detected, yet upon replacing Ar with CO_2 purging the Faradaic efficiency towards formate production was ~75.9%. Moreover, the current density for the reduction reaction increases by five times when purging with CO_2 compared to Ar. A similar improvement in the Faradaic efficiency, from 2.7% to 63.5%, and in the current density, from -17.3 mA cm^{-2} to -27.9 mA cm^{-2}, was observed when replacing Ar with CO_2 purging in a 0.5 M $KHCO_3$ solution. It must be pointed out that a trace amount of formate was observed when purging with Ar in 0.5 M $KHCO_3$ electrolyte solution. This is attributed to the electrochemical reduction of CO_2 derived from HCO_3^- due to the homogenous acid-base reactions:

$$\mathrm{HCO_3^-} \leftrightarrow \mathrm{OH^-} + \mathrm{CO_2} \tag{2.2}$$

$$\mathrm{CO_3^{2-}} + 2\mathrm{H_2O} \leftrightarrow \mathrm{OH^-} + \mathrm{HCO_3^-} \tag{2.3}$$

2.3.2 *The Effect of Anion*

Figure 2.4 shows the effects of anions on the Faradaic efficiency of formate and reaction production rate as functions of the reaction time and electrolyte concentration. As shown in **Figure 2.4a**, **t**he potential profile for the Faradaic efficiency of formate shows a potential rise from -1.5 V to a peak (63.5%) at -2.0 V vs. SCE for 0.5 M $KHCO_3$, which is consistent with the literature result of ~67.5% measured in the tetraethylammonium perchlorate aqueous electrolyte,[22] but higher than 47%[11] obtained in 0.5 M $KHCO_3$. The trend appears similar for KCl, while the peak potential in KCl shifts to ~1.7 V vs. SCE. The potential profile of the Faradaic efficiency of formate observed in

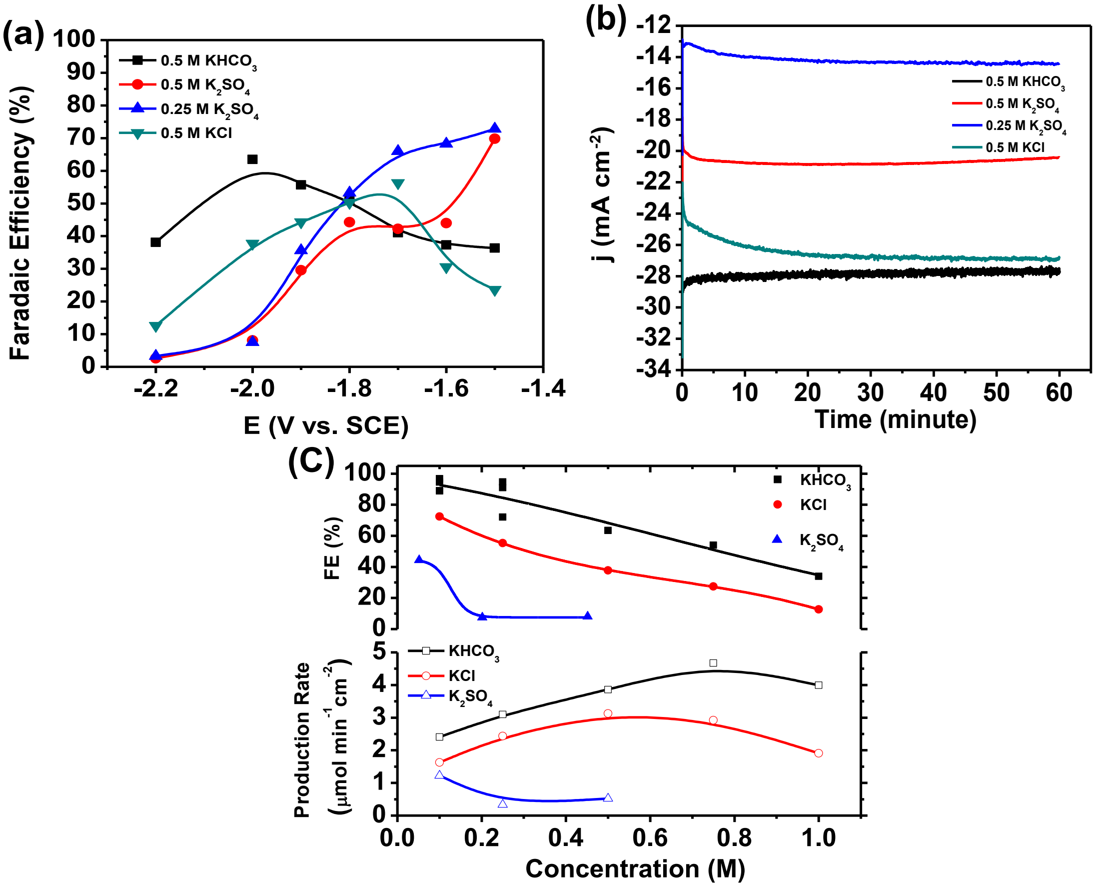

Figure 2.4. (a) Potential dependency of Faraday efficiency of formate, (b) typical current density at a potentiostatic electrolysis potential of -2.0 V vs. SCE of CO_2 reduction in electrolytes with different anions and (c) dependency of Faradaic efficiency and formate production rate on concentration of electrolyte with different anions. The electrolysis potential was held at -2.0 V vs. SCE.

K_2SO_4 differs dramatically in both KCl and $KHCO_3$. The Faradaic efficiency of formate decreased with the increasing of potential in electrolyte of K_2SO_4. Overall, the greatest Faradaic efficiency of formate appears in 0.25 M K_2SO_4 at potentials more positive than -1.8 V vs. SCE among the electrolytes. At potentials more negative than -1.8 V vs. SCE, the highest Faradaic efficiency of formate was observed in 0.5 M $KHCO_3$. At very negative potentials, which correspond to the higher current densities, the Faradaic efficiency of formate depends on the availability of reactants due to the homogenous acid-base reactions (Eqs. 2.2 and 2.3). $KHCO_3$ solution supplies the most availability of reactants for CO_2 reduction leading to a higher Faradaic efficiency of formate at potentials more negative than -1.8 V vs. SCE.[23, 24] **Figure 2.4b** shows the total reduction current density as a function of operation time, measured at -2.0 V vs. SCE. The highest total reduction current density was observed in 0.5 M $KHCO_3$ and is attributed to the equilibrium between HCO_3^- and CO_2, which can provide sufficient local dissolved CO_2 to the interface between the Sn electrode and the electrolyte for the reaction. For the other two electrolytes, KCl and K_2SO_4, the current density was limited by the diffusion of the dissolved CO_2.

Figure 2.4c shows the Faradaic efficiency and production rate of formate as a function of the concentration of electrolytes at a potential of -2.0 V vs. SCE. The Faradaic efficiency of formate increases as the concentration of electrolyte decreases for each electrolyte. The highest Faradaic efficiency of formate obtained in this research was ~95% in 0.1 M $KHCO_3$. The effect of the electrolyte concentration on the Faradiac efficiency of formate is due to the difference of the potential (E_2) at the outer Helmholtz plane (OHP), which will be discussed later. In contrast, the current density decreases as the electrolyte concentration decreases, due to two factors of decreased E_2 and electrolyte conductivity. The impact of E_2 on the current density is discussed later. The higher conductivity in a more concentrated electrolyte (e.g. 87.7 mS cm^{-1} for 0.5 M K_2SO_4 vs. 47.8 mS cm^{-1} for 0.25 M K_2SO_4 measured from the Zeta meter) contributes to the rise of the total current density.

2.3.3 *The Effect of Cation*

To investigate the effect of the cations, the emphasis was on alkali metal ions, Na^+, K^+ and Cs^+. The results are shown in **Figure 2.5**. The Faradaic efficiency of formate obtained from 0.5 M Na_2SO_4 is among the highest at potentials more positive than -1.8 V vs. SCE (**Figure 2.5a**). As the potential becomes more negative, the Faradaic efficiency of formate for 0.5 M K_2SO_4 exceeds that for 0.5 M Na_2SO_4. Under the consideration of Faradaic efficiency along with energy efficiency, the preferable choice of electrolytes is in the order: 0.5 M Na_2SO_4 > 0.5 M K_2SO_4 > 0.5 M Cs_2SO_4, which is corresponding to the decreasing order of cation size and will be explained in the next section. A similar sequence was observed for the Faraday efficiency of formate when an indium electrode was used in alkali carbonate solutions.[25]

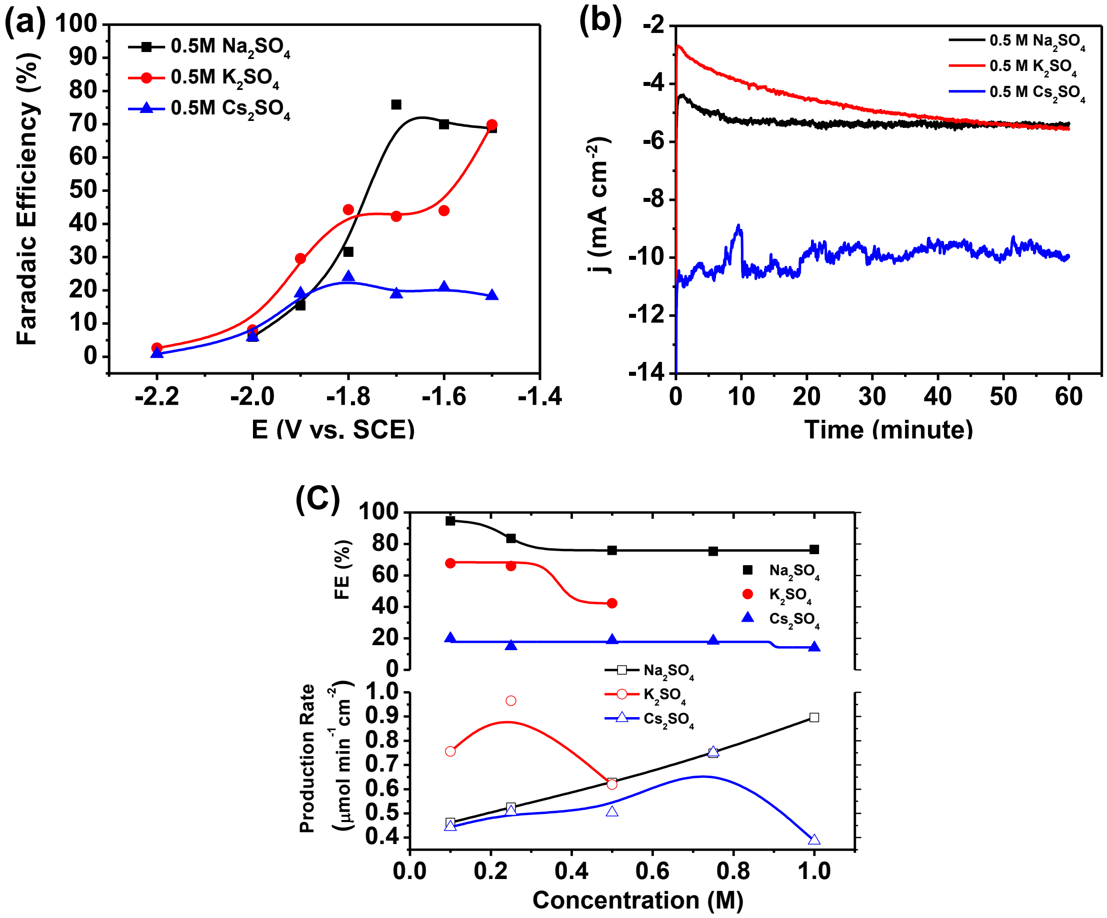

Figure 2.5. (a) Potential dependency of Faradaic efficiency of formate, (b) typical current density, and (c) dependency of Faradaic efficiency and production rate of formate on the concentration of electrolyte containing SO_4^{2-} and different cations. The electrolysis potential was -1.7 V vs. SCE.

Figure 2.5b compares the total reduction current density measured at a potential of -1.7 V vs. SCE, at which a relatively high Faradaic efficiency of formate was observed, as shown in **Figure 2.5a**. The Cs_2SO_4 electrolyte exhibits the highest reduction current while Na_2SO_4 electrolyte results in the most stable performance. The Faradaic efficiency and production rate of formate as a function of the electrolyte concentration are illustrated in **Figure 2.5c**. The Faradaic efficiency of formate increases as decreasing the electrolyte concentration. The largest Faradaic efficiency of formate was observed > 90% in 0.1 M Na_2SO_4, which shows higher selectivity than that of both K_2SO_4 and Cs_2SO_4. The production rate of formate exhibits a maximum in both K_2SO_4 and Cs_2SO_4, due to the combined effects from both the Faradaic efficiency and the current density. The production rate of formate increases with increasing concentration of Na_2SO_4. Even though the Faradaic efficiency in Na_2SO_4 electrolyte is the highest at -1.7 V vs. SCE, the current density in Na_2SO_4 is lower than that in K_2SO_4, which leads to a lower production rate in Na_2SO_4 than that in K_2SO_4. The lowest production rates were observed with Cs_2SO_4, because of its marginal Faradaic efficiencies of formate (< 20%).

The effects of the cations were further investigated by replacing SO_4^{2-} with bicarbonate ion HCO_3^-. **Figure 2.6a** and **2.6b** show the dependence of Faradaic efficiency of formate on the potential and the total reduction current density at -2.0 V vs. SCE, respectively. The trends are similar with these shown in **Figure 2.5**. The highest Faradaic efficiency of formate was obtained in $NaHCO_3$ while the lowest in $CsHCO_3$ at relatively less negative potential region. In contrast, the lowest current density was obtained in $NaHCO_3$ while the highest current density was observed in $CsHCO_3$ electrolyte. **Figure 2.6c** illustrates the concentration effects on the Faradaic efficiency and production rate of formate at -2 V vs. SCE. In general, the Faradaic efficiency towards formate production increases while the current density decreases as the electrolyte concentration decreases. At -2.0 V vs. SCE, $KHCO_3$ exhibits the highest Faradaic efficiency and production rate of formate compared to $NaHCO_3$ and $CsHCO_3$. The production rate of formate could reach over 3 μmol min^{-1} cm^{-2} in 1M $KHCO_3$ at a potential of -2.0 V vs. SCE. The results of Faradaic efficiency and production rate of formate as well as current density in various electrolytes are summarized in **Table 2.1**.

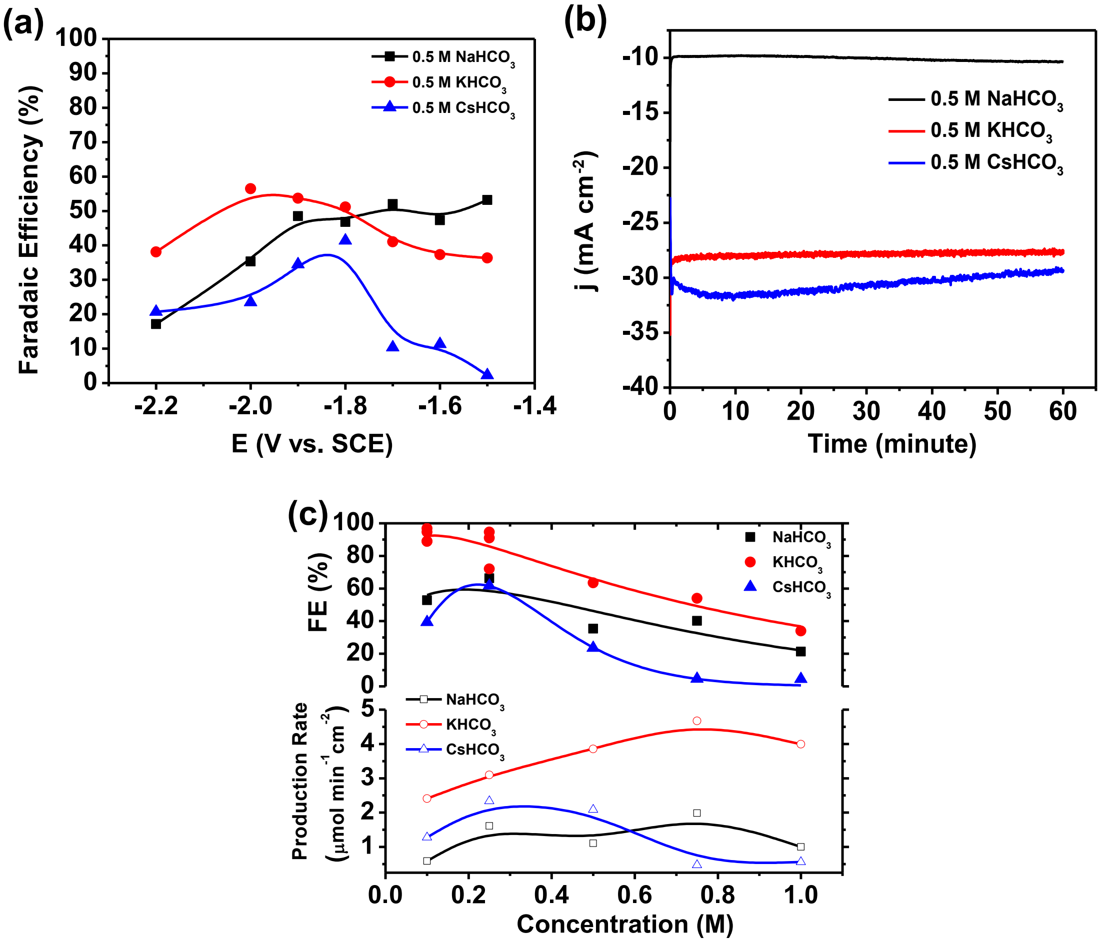

Figure 2.6. (a) Potential dependency of Faraday efficiency of formate and (b) typical current density, and (c) dependency of Faraday efficiency and production rate of formate on the concentration of electrolyte containing HCO_3^- and different cations. The electrolysis potential was -2.0 V vs. SCE.

2.3.4 *Theoretical Understanding of the Role of Electrolyte*

The electrochemical reactions, for instance CO_2 reduction in an aqueous electrolyte, take place in the electrical double layer, a structure depicting the distribution of the electrical potential near the surface of an electrode. In the electrical double layer, the plane at which the electrostatic adsorption ions are located is called the OHP, as shown in **Figure 2.7**. In some cases, an additional layer exists between the OHP and the electrode surface, named the inner Helmholtz plane (IHP), at which the specifically adsorbed ions are located. These specific adsorption ions are desolvated and maintain adsorption with the electrode surface through both chemical and electrostatic interactions, hence located at the inner side of OHP. The layer consisting of IHP and OHP is also named as the “Stern layer”. The layer beyond OHP is a diffuse layer, arising from the random motions of the ions. The “diffuse” alludes a concentration distribution of the counter ions, which reaches the highest level at OHP and decrease gradually to a homogeneous level in the bulk of the electrolyte. The diffuse-layer model was developed by Guoy and Chapan to advance the concept proposed by Helmholtz.[26] At present, the Gouy-Chapman-Stern (GCS) model is most commonly used to describe the structure of electrical double layer.[26]

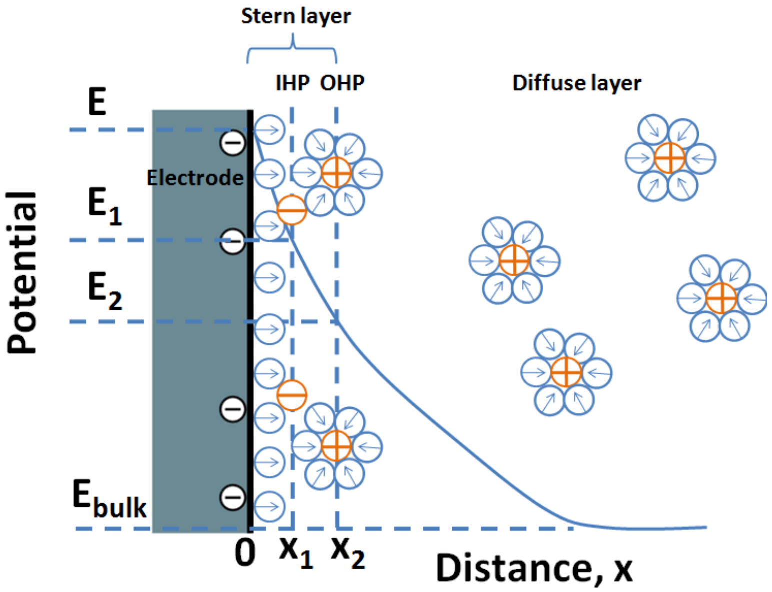

Figure 2.7. A schematic representation of the electrical double layer of a negatively charged interface. [37]

The potential at OHP, at distance x_2 from the electrode surface, is notated as E_2. This potential is defined with respect to the potential in the bulk solution. The most referred ζ potential is at the fluidic boundary, a so-called hydrodynamic slip plane, which is located outside of OHP. The ζ potential can be approximated to E_2, provided $\kappa\alpha >> 1$, where κ is the Debye length and α is the curvature radius of the electrode. This assumption is valid in our research, where a flat Sn foil is used as the electrode. There exists a relationship between E_2 and the charge q on the electrode without specific adsorption ions:[27]

$$q = \pm[\frac{RT\varepsilon}{2\pi}\sum C_i(e^{-\frac{z_iFE_2}{RT}} - 1)]^{1/2} \tag{2.4}$$

where, C_i is the bulk concentration of ion i in the electrolyte, z_i is the ionic valence, ε is the dielectric constant of aqueous solution, F and R is the Faraday's constant and gas constant, respectively, and T is the absolute temperature.

For a z-z electrolyte of a concentration C_{bulk}, Eq. (2.4) can be re-written as:

$$q = 2\left(\frac{RT\varepsilon C_{bulk}}{2\pi}\right)^{1/2} \sinh(\frac{|z|FE_2}{2RT}) \tag{2.5}$$

As a result, E_2 can be expressed as a function of C_{bulk}, provided that the charge q is independent upon the potential:

$$E_2 = B + \frac{RT}{|z|F}\ln C_{bulk} \tag{2.6}$$

$$B = \frac{RT}{|z|F}\ln[q\left(\frac{RT\varepsilon C_{bulk}}{2\pi}\right)^{\frac{1}{2}}] \tag{2.7}$$

where, E_2 is negative, B is related to ε of an aqueous solution and is a constant for a specific electrolyte solution. Eq. (2.6) implies that, in the electrolyte with the same cation and anion, E_2 becomes more negative with decreasing the concentration of the electrolyte.

The concentration of H^+ at the electrode surface, $[H^+]_{surface}$, plays a key role in the formate production as indicated in the reduction pathway (**Figure 1.10)**, which is a function of E_2, following:[28]

$$[H^+]_{surface} = [H^+]_{bulk}e^{-\frac{FE_2}{RT}} \qquad (2.8)$$

Hence, a more negative E_2 is expected to correspond to a higher $[H^+]$ at the electrode surface. The electrolyte with a more dilute concentration possesses higher (more negative) E_2, which in turn leads to more H^+ accumulating at the electrode's surface as described by Eq. (2.8). The Faradaic efficiency of formate in lower concentration electrolyte is higher because of the promotion of protonation of $CO_2^{-}\cdot$ by the existence of higher $[H^+]_{surface}$. On the other hand, the higher current density observed in a concentrated electrolyte can be attributed to the greater ionic conductivity, along with a more positive E_2 which has bigger absolute value between applied potential and E_2 thus a bigger driving force for the reaction. A higher ionic conductivity exists in a more concentrated electrolyte, as shown in **Figure 2.8a**. For instance, the conductivity increases from 10 mS cm^{-1} for 0.1 M $KHCO_3$ to 79.2 mS cm^{-1} for 1 M $KHCO_3$.

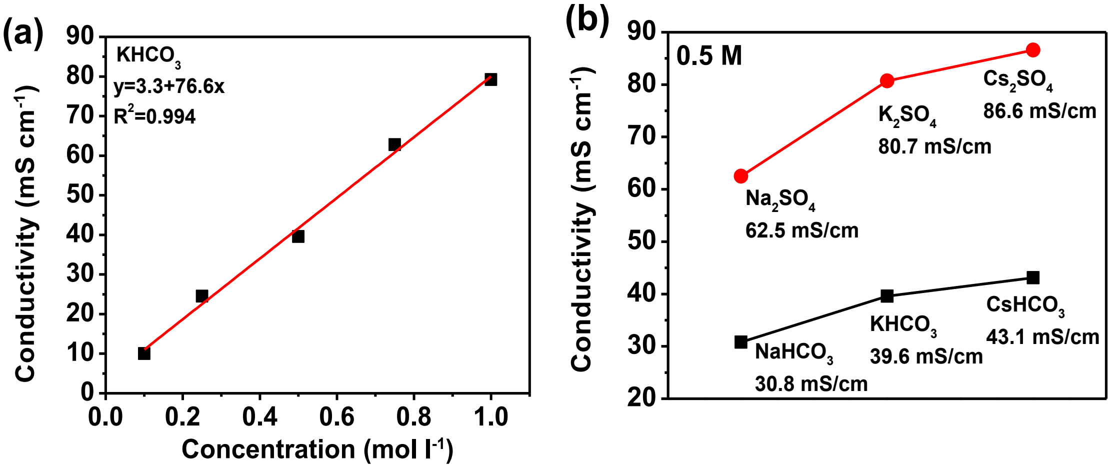

Figure 2.8. (a) Dependency of electrolyte conductivity on the concentration of $KHCO_3$ and (b) the conductivity of electrolyte (0.5 M) with different cations.

Table 2.1. Summary of results for electrochemical reduction of CO_2 on Sn electrode with various electrolytes.

Electrolyte	**Potential (V vs. SCE)**	**Current density (mA cm^{-2})**	**Faradaic efficiency (%)**	**Production rate (µmol min^{-1}cm^{-2})**
1 M $KHCO_3$	-2.0	41.47	34.0	3.99
0.5 M $KHCO_3$	-1.7	2.78	41.0	0.85
	-2.0	26.70	63.5	3.86
0.25 M $KHCO_3$	-2.0	13.48	94.6	3.10
0.5 M $NaHCO_3$	-1.7	5.09	52.0	0.83
	-2.0	10.00	24.3	0.76
0.5 M $CsHCO_3$	-1.7	2.92	10.4	0.10
	-2.0	27.53	23.5	2.09
0.5 M Cs_2SO_4	-1.7	9.99	18.7	0.50
	-2.0	30.79	5.9	0.56
0.5 M Na_2SO_4	-1.7	5.38	75.9	0.63
	-2.0	33.52	6.0	0.31
0.25 M Na_2SO_4	-1.7	4.41	83.5	0.53
	-2.0	9.32	46.4	0.67
0.5 M K_2SO_4	-1.7	4.53	44.8	0.66
	-2.0	24.29	8.1	0.52
0.25 M K_2SO_4	-2.0	14.36	7.5	0.33
0.5 M KCl	-2.0	19.16	37.8	1.57

The role of cation size on the Faradaic efficiency of formate can be explained by the difference of E_2 in various electrolytes because the degree of the electrostatic adsorption of cations on the OHP differs with respect to the size of the cations. The Sn electrode possesses a point of zero charge (PZC) around -0.65 V vs. SCE in neutral electrolytes.[29] In all the tests, a more negative potential than the PZC was applied to Sn electrode; therefore, the cations will be electrostatically adsorbed at the OHP. Even though the property of EDL is loosely dependent on the nature of the specific adsorbed cation as suggested by Grahame in his classical work,[30] E_2 is a function of the dielectric constant (ε) of an aqueous solution (as shown in Eqs. 2.6 and 2.7). The dielectric constant is closely related to the ionic size in terms of Hubbard-Onsager continuum dielectric friction theory. Indeed, for alkali cations, the ε of aqueous solution increases with the increasing of cation size.[31, 32] Consequently in the electrolyte with the same concentration and anion, the E_2 follows the order: $E_{2, Cs^+} > E_{2, K^+} > E_{2, Na^+}$, which is the sequence of ε increasing as the growth of cation size. Thus, the order of $[H^+]_{surface}$ follows the inverse way of E_2, $[H^+]_{surface,\ Cs^+} < [H^+]_{surface,\ K^+} < [H^+]_{surface,\ Na^+}$, which explains the highest Faradaic efficiency of formate with electrolyte containing Na^+ in the relatively less negative potential range. The highest current density existed in electrolyte with cation Cs^+ is also attributed to both the most positive E_2 (thus a biggest absolute value of difference between applied potential and E_2) and highest electrolyte conductivity as shown in **Figure 2.8b** among electrolytes containing Cs^+, K^+ and Na^+.

2.4 Conclusions

The effects of electrolyte on the selectivity and activity for the electrochemical reduction of CO_2 on the Sn electrode were investigated in detail. In the alkali metal ions, the selectivity towards formate production follows $Na^+ > K^+ > Cs^+$ in the relatively less negative potential range. However, Na^+ exhibits the lowest current density while Cs^+ shows the highest. The effects of the cation chemistry including size and concentration on the Faradaic efficiency of formate and reaction current density are understood by correlating them to the variation of E_2 and proton concentration at the OHP as well as the electrolyte conductivity. Among the anions of SO_4^{2-}, Cl^- and HCO_3^-, SO_4^{2-} favor higher Faradaic efficiency of formate while HCO_3^- exhibits the highest current density. The Faradaic efficiency of formate increases while the current density decreases as the electrolyte is diluted. If concern is only given to Faradaic and energy efficiencies, the best choice of electrolyte is Na_2SO_4. The highest Faradaic efficiency is 95% for 0.1 M Na_2SO_4 at potential of -1.7 V vs. SCE. From a consideration for the production rate of formate, $KHCO_3$ is the optimum electrolyte due to its balance between selectivity and current density. The highest yield rate of formate reached was 3.99 μmol min^{-1} cm^{-2} in 1 M $KHCO_3$ at -2.0 V vs. SCE.

References

1. R. P. S. Chaplin and A. A. Wragg, *J. Appl. Electrochem.*, **33,** 1107-1123 (2003).
2. Y. Chen and M. W. Kanan, *J. Am. Chem. Soc.*, **134,** 1986-1989 (2012).
3. Y. Hori, *Modern Aspects of Electrochemistry: Chapter 3 Electrochemical CO_2 reduction on metal electrodes,* Springer (2008).
4. C. Rice, R. I. Ha, R. I. Masel, P. Waszczuk, A. Wieckowski and T. Barnard, *J. Power Sources,* **111,** 83-89 (2002).
5. Y. M. Zhu, S. Y. Ha and R. I. Masel, *J. Power Sources,* **130,** 8-14 (2004).
6. C. V. Rao, C. R. Cabrera and Y. Ishikawa, *J. Phys. Chem. C,* **115,** 21963-21970 (2011).
7. N. V. Rees and R. G. Compton, *J. Solid State Electrochem.*, **15,** 2095-2100 (2011).
8. T. T. Cheng and E. L. Gyenge, *J. Electrochem. Soc.*, **155,** B819-B828 (2008).
9. K. L. Chu, M. A. Shannon and R. I. Masel, *J. Electrochem. Soc.,* **153,** A1562-A1567 (2006).
10. S. Kaneco, R. Iwao, K. Iiba, K. Ohta and T. Mizuno, *Energy,* **23,** 1107-1112 (1998).
11. F. Koleli, T. Atilan, N. Palamut, A. M. Gizir, R. Aydin and C. H. Hamann, *J. Appl. Electrochem.*, **33,** 447-450 (2003).
12. K. Hara, A. Kudo and T. Sakata, *J. Electroanal. Chem.*, **391,** 141-147 (1995).
13. Y. Hori, H. Wakebe, T. Tsukamoto and O. Koga, *Electrochim. Acta,* **39,** 1833-1839 (1994).
14. M. N. Mahmood, D. Masheder and C. J. Harty, *J. Appl. Electrochem.*, **17,** 1159-1170 (1987).
15. T. Mizuno, K. Ohta, A. Sasaki, T. Akai, M. Hirano and A. Kawabe, *Energy Sources,* **17,** 503-508 (1995).
16. Y. Hori, K. Kikuchi and S. Suzuki, *Chem. Lett.*, 1695-1698 (1985).
17. D. T. Whipple, E. C. Finke and P. J. A. Kenis, *Electrochem. Solid-State Lett.*, **13,** D109-D111 (2010).
18. T. Saeki, K. Hashimoto, A. Fujishima, N. Kimura and K. Omata, *J. Phys. Chem.,* **99,** 8440-8446 (1995).
19. S. Kaneco, K. Iiba, M. Yabuuchi, N. Nishio, H. Ohnishi, H. Katsumata, T. Suzuki and K. Ohta, *Ind. Eng. Chem. Res.,* **41,** 5165-5170 (2002).
20. L. Q. Wang, G. J. Exarhos, C. F. Windisch, C. H. Yao, L. R. Pederson and X. D. Zhou, *Appl. Phys. Lett.*, **90,** 3 (2007).
21. L. Q. Wang, X. D. Zhou, G. J. Exarhos, L. R. Pederson, C. Wang and C. F. Windisch, *Appl. Phys. Lett.*, **91,** 173107 (2007).
22. S. Ikeda, T. Takagi and K. Ito, *Bull. Chem. Soc. Jpn.*, **60,** 2517-2522 (1987).
23. M. Jitaru, D. A. Lowy, M. Toma, B. C. Toma and L. Oniciu, *J. Appl. Electrochem.,* **27,** 875-889 (1997).
24. S. R. Narayanan, B. Haines, J. Soler and T. I. Valdez, *J. Electrochem. Soc.*, **158,** A167-A173 (2011).
25. K. Ito, T. Murata and S. Ikeda, *Bull. Nagoya Inst. Techn.*, **27,** 209 (1975).
26. A. V. Delgado, E. Gonzalez-Caballero, R. J. Hunter, L. K. Koopal and J. Lyklema, *Pure Appl. Chem.*, **77,** 1753-1805 (2005).
27. P. Delahay, *Double layer and electrode kinetics,* Interscience publishers (1965).

28. E. A. Maznichenko, B. B. Damaskin and Z. A. Iofa, *Dokl. Akad. Nauk SSSR,* **138,** 1377-1379 (1961).
29. V. A. Safonov and M. A. Choba, *Electrochim. Acta,* **46,** 3103-3110 (2001).
30. D. C. Grahame, *Chem. Rev.,* **41,** 441-501 (1947).
31. Y. Z. Wei, P. Chiang and S. Sridhar, *J. Chem. Phys.,* **96,** 4569-4573 (1992).
32. R. M. Noyes, *J. Am. Chem. Soc.,* **84,** 513-522 (1962).

Chapter 3

On the Microstructure of Sn Gas Diffusion Electrode for the Electrochemical Conversion of CO_2 into Formate

3.1 Introduction

The microstructure of the cathode in proton exchange membrane fuel cells (PEMFCs) plays a critical role in gas diffusion, charge transfer and reduction reaction, thus determines the overall fuel cell performance. A generic catalyst layer in the gas diffusion electrode (GDE) consists of electrocatalyst and Nafion,[1-3] where Nafion allows the integration of porous catalyst layer with the electrolyte, thus increasing the three-dimensional reaction zone. Optimization of Nation fraction in the catalyst layer in PEMFCs has been extensively studied,[2-5] which was reported in the range of 30-36 wt.%, regardless of platinum loading in the electrodes.[2, 3] Adopting the configuration of PEMFCs for the electrochemical reduction of CO_2 offers a promising route of recycling CO_2 with simultaneous current density and efficiency.[6] Although numerous studies have been reported to understand CO_2 electro-reduction in the liquid phase,[7] the low solubility of CO_2 in aqueous solution (0.033 mol l^{-1} at 25 ^{o}C and 1 atm)[8], limits its potential for commercialization. One promising approach is to employ GDEs to directly convert gas-phase CO_2 to fuels,[9-11] because GDEs can be easily incorporated into full electrochemical cells for a large-scale conversion of CO_2.[12-14] Similar to oxygen reduction reaction (ORR), the addition of Nafion in the catalyst layer also improves the electrocatalytic activity towards CO_2 reduction by increasing the triple-phase boundary among reactant gases, electrolyte and catalyst particles. CO_2 electro-reduction, however, is far more sensitive to the local proton concentration than ORR because CO_2 reduction always competes with hydrogen evolution. As a consequence, it is necessary to investigate Nafion fraction in the GDEs for CO_2 reduction to achieve desirable current density and Faradaic efficiency.

In this chapter, we studied the effect of Nafion fraction in the Sn catalyst layer, the thickness of catalyst layer and Sn particle size on the activity and selectivity for CO_2 reduction. We observed a Nafion fraction lower than that for ORR to obtain the optimized performance.

3.2 Experimental

3.2.1 Preparation of Sn GDEs

The Sn GDE was prepared by spraying Sn catalyst ink onto the gas diffusion layer (Sigracet® GDL 10BC). The Sn catalyst ink was made by mixing Sn powders (Alfa Aesar, APS 100 nm), Nafion ionomer (DuPont), deionized water (Resistivity ≥ 18.2 MΩ cm^{-2}), and isopropanol (Sigma Aldrich), followed by ultrasonicating the mixture for one hour. In order to identify the best Nafion fraction, the weight ratio of Sn:Nafion was varied from 1:1 to 20:1. The Nafion fraction is also generally expressed as wt.% (dry weight of Nafion ionomer divided by the total weight of catalyst and Nafion ionomer, multiplied by 100). For these experiments, the Sn loading was kept constant at ~1.56 mg cm^{-2}. The geometric area of Sn GDE used was 4 cm^2. In order to study the effect of Sn loading on the activity and selectivity, different Sn GDEs with loadings varying from 0.67 mg cm^{-2} to 6.55 mg cm^{-2} were also prepared with the same Nafion fraction of 20 wt.% (weight ratio Sn:Nafion of 4:1). In addition, Sn powders (Sigma Aldrich) having size of 1-2 μm were chosen to study the effect of Sn particle size on the optimal Nafion fraction. The Sn loading was maintained at ~0.85 mg cm^{-2} for these GDEs.

3.2.2 Electrolysis

The performance of these Sn GDEs was evaluated in a half-cell setup (see **Figure 3.1a**) with a configuration of aqueous electrolyte/GDE/gas CO_2. This half-cell configuration enables a direct gas-phase CO_2 conversion at the triple-phase interfaces as shown in **Figure 3.1b**. The compartment for working electrode is separated from that for counter electrode by a proton exchange membrane (PEM, Nafion®, DuPont). The working electrode was Sn GDE and supplied with gas-phase CO_2 at 45 ml min^{-1} at 25 ^{o}C and 1 atm. CO_2 flew along a serpentine channel over Sn GDEs and diffused through the gas diffusion layer to Sn catalyst layer. A platinum foil (3×3 cm^2) and a saturated calomel electrode (SCE) were used as the counter and reference electrode, respectively. A stationary aqueous solution of 0.5 M $KHCO_3$ was used as the electrolyte. All the electrochemical measurements were conducted by employing Solartron 1470 Potentiostat/Galvanostat attached to a 1255B frequency response analyzer. CO_2 electrolysis was conducted under potentiostatic conditions for 0.5 h. The linear sweep voltammetry was conducted at a scan rate of 5 mV s^{-1}. The ohmic resistance between the salt bridge tip and Sn GDE was measured by electrochemical impedance spectroscopy (EIS) with an AC perturbation of 5 mV at the open circuit condition and a logarithmic decreasing frequency sweep from 100 kHz to 0.1 Hz. All the potentials mentioned below were corrected by the iR drop unless otherwise noted. Liquid products were quantified by using 1D ^{1}H nuclear magnetic resonance (NMR) spectroscopy, the details of which can be found in Chapter 2.[15] The quantity of charge needed to produce that concentration of formate as determined by NMR was calculated, and divided by the total charge passed during the chronoamperometry to determine the Faradaic efficiency of formate.

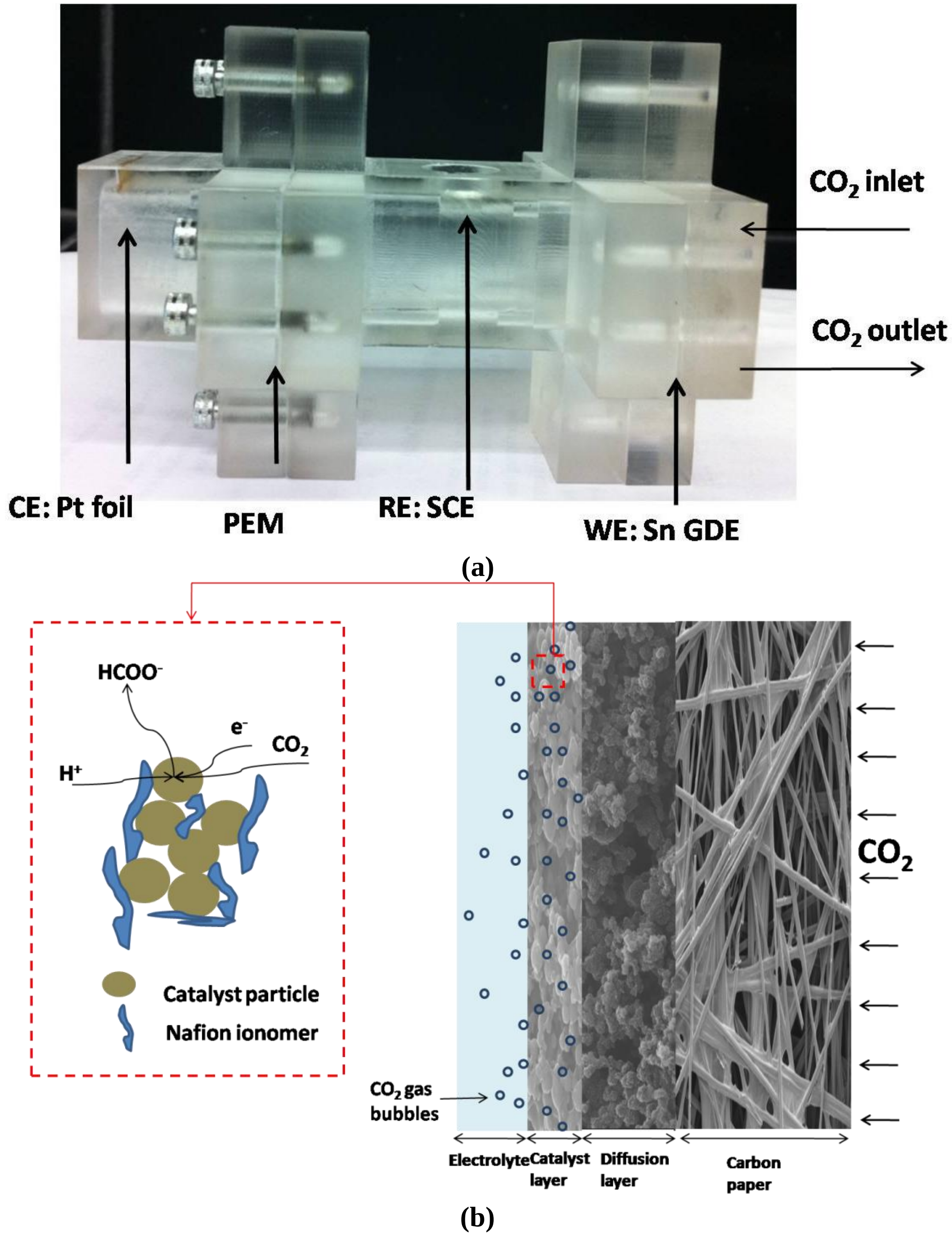

Figure 3.1. (a) A photo of half cell setup for measuring the electrocatalytic activity of Sn GDEs towards CO_2 reduction, and (b) a schematic of CO_2 reduction at the triple-phase interfaces.

3.3 Results and Discussion

Figure 3.2a illustrates a typical cross-sectional SEM image of Sn catalyst layer together with a diffusion layer. This catalyst layer is comprised of 100-nm Sn nanoparticles (Sn loading = 1.56 mg cm^{-2}) and Nafion (20 wt.%). The catalyst layer has a homogeneous thickness ~3.1 μm, which depends on Sn loading and Nafion fraction. The thickness of catalyst layer increases with increasing Sn loading and Nafion fraction. **Figure 3.2b** further shows the porous structure of the catalyst layer consisting of Sn agglomerates and the secondary pores located between these agglomerates, similar to Pt/C catalyst layer in a PEMFC.[2, 16] The catalyst layers with numerous pores are beneficial for the liquid electrolyte to penetrate and for reaction gas to diffuse.[17]

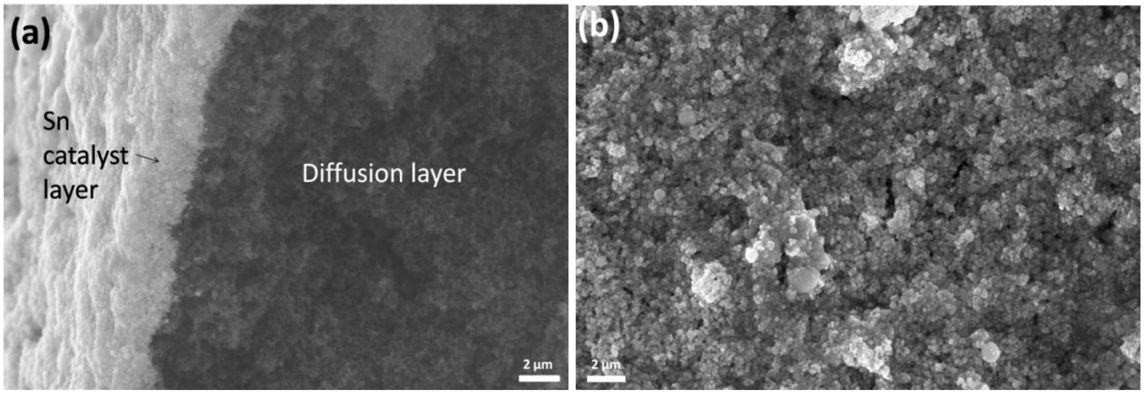

Figure 3.2. SEM images of (a) the cross-section and (b) surface of Sn catalyst layer. Sn catalyst layer consists of 100 nm Sn particles with Sn loading of 1.56 mg cm^{-2} and 20 wt.% Nafion.

Figure 3.3a shows the characteristic i-V curves of three Sn GDEs without iR compensation. The Sn loading of these electrodes was maintained at 6.55 mg cm^{-2} while the Nafion fraction was ~20 wt.%. The i-V curves were observed not to coincide with each other because of the difference in ohmic resistance between the salt bridge tip and Sn GDE (**Figure 3.3b**) resulting from the slight difference in salt bridge location during each measurement. After iR correction, as shown in **Figure 3.3c**, the three i-V curves overlap well with each other, indicating the reproducibility of Sn GDEs. Three Sn GDEs with a Sn loading of 1.56 mg cm^{-2} were also measured and exhibited similar reproducibility (**Figure 3.4**).

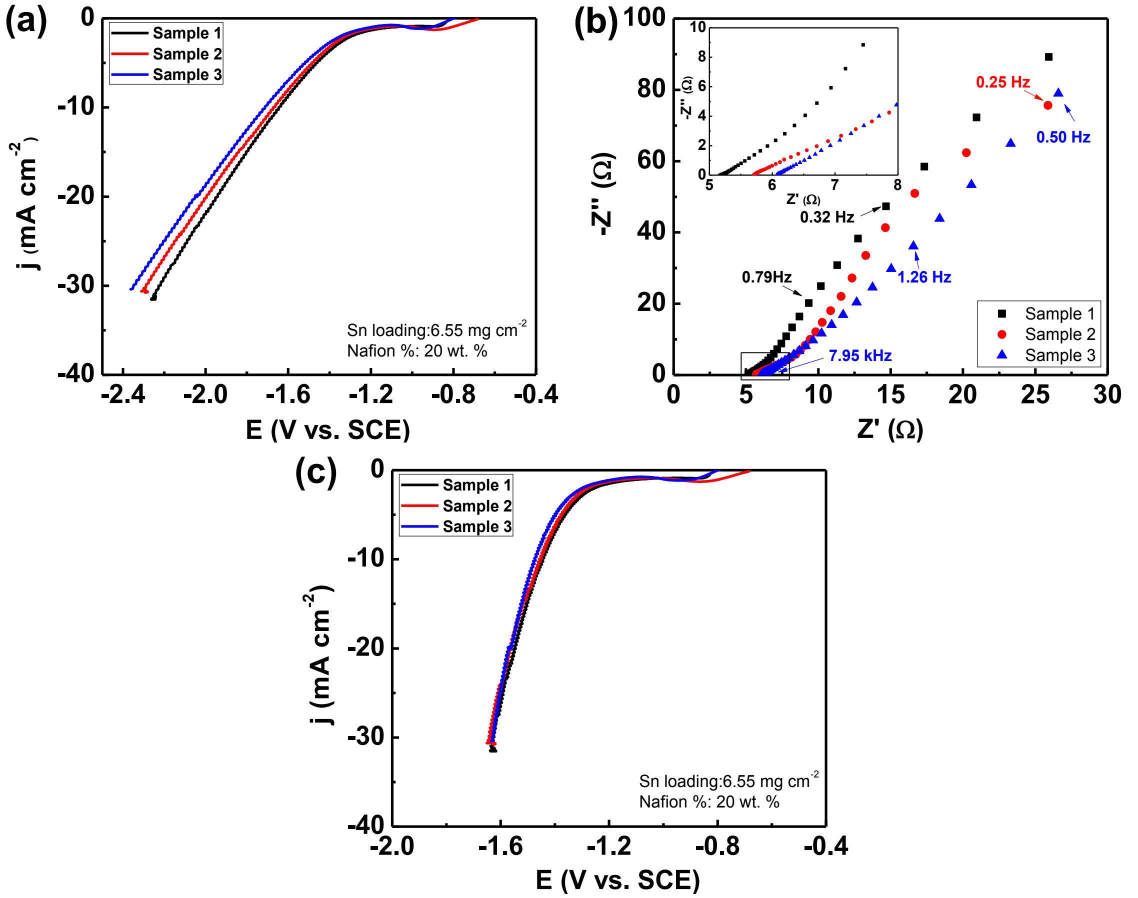

Figure 3.3. (a) i-V curves of three independent Sn GDEs for CO_2 reduction before iR compensation, (b) EIS measurement of ohmic resistance, (c) iV curves after iR compensation. The inset in (b) is a magnification of impedance in high frequency.

The composition of catalyst layer was varied by changing Nafion fraction, which played a decisive role in proton transfer, CO_2 diffusion, and eventually the activity and selectivity towards CO_2 reduction. **Figure 3.5a** shows i-V curves of the electrodes with different Nafion fractions ranging from 0 to 50 wt.% but with the same Sn loading of 1.56 mg cm^{-2}. The current density increased with increasing in Nafion fraction up to 20 wt.%, but then decreased with further increasing in Nafion fraction, suggesting the existence of an optimized Nafion fraction to facilitate CO_2 reduction reaction. A similar trend was observed for Faradaic efficiency towards formate production (**Figure 3.5b**) between the potential ranging from -1.4 to -1.7 V vs. SCE. The optimized Nafion fraction for formate production was ~20 wt.%. The electrode with this Nafion fraction exhibited a Faradaic efficiency towards formate formation as high as 80% at -1.6 V vs. SCE. The partial current density for formate exhibited the maximum with a Nafion fraction between 17 and 20 wt. % as shown in **Figure 3.5c**. A limiting partial current density of formate was observed when the Nafion fraction increased to 25 wt.% or higher, which suggests that CO_2 diffusion rate controls formate production at higher Nafion fractions.

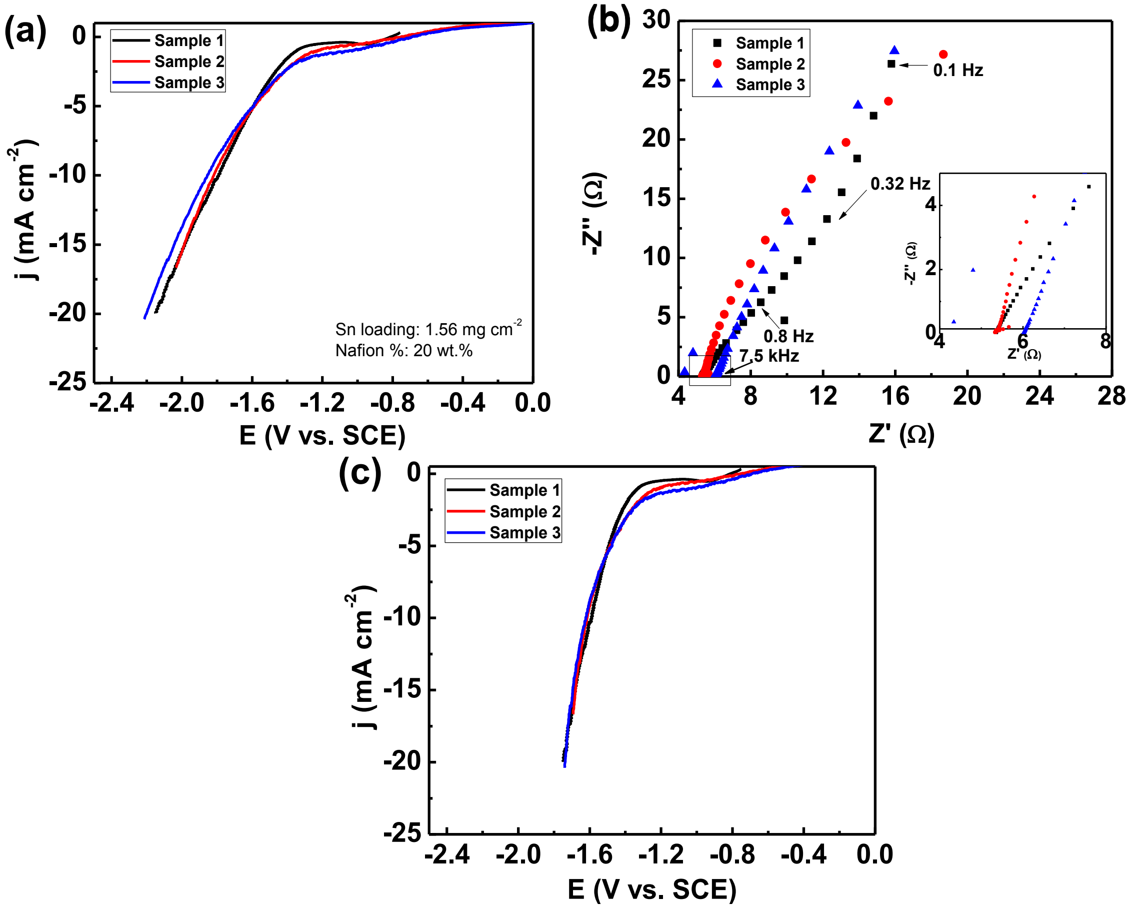

Figure 3.4. (a) i-V curves of three independent Sn GDEs for CO_2 reduction before iR compensation, (b) EIS measurement of ohmic resistance, (c) iV curves after iR compensation. The inset in (b) is a magnification of impedance in high frequency.

The mechanism by which Nafion fraction influences the electrode performance is attributed to the microstructural evolution as a function of Nation fraction. It is known that parameterizations of catalyst layer properties as a function of composition refer to the class of percolation problems.[18] To enable CO_2 reduction reaction, the pores for CO_2 diffusion and the Nation matrix for proton conduction need to form spanning network with a volume fraction above the percolation threshold.[5, 19] Moreover, it is preferable for the electrode to exhibit a percolating network consisting of catalyst particles for a good electronic conduction. The volume fraction for each component can be calculated based on Sn loading, catalyst layer thickness, and the densities of Sn particles and Nafion ionomer.[20] The Nafion fraction of 20 wt.% corresponds to a Nafion volume fraction ~0.50, indicating a balance is achieved among the electronic conduction, proton conduction and CO_2 diffusion, which allows for an efficient CO_2 reduction. As a result, Sn GDE with an optimized Nafion fraction of 20 wt.% exhibited both the highest current density and Faradaic efficiency of formate. This optimized Nafion fraction is found to be lower than 30-36 wt.% as reported for PEMFC cathodes. This is because, CO_2 reduction is perhaps more sensitive towards proton concentration than O_2 reduction, with hydrogen evolution reaction competing with CO_2 reduction reaction. A lower Nafion fraction corresponds to a lower proton concentration near the catalyst surface which suppresses hydrogen evolution while promoting CO_2 reduction. The poor performance of electrode with an insufficient Nafion fraction results from poor proton conduction and low catalyst utilization, while the poor electrocatalytic activity of electrode with an excessive Nafion fraction is due to the blockage of catalyst sites, reduced gas permeability, and increased mass transport polarization. [3, 4, 21]

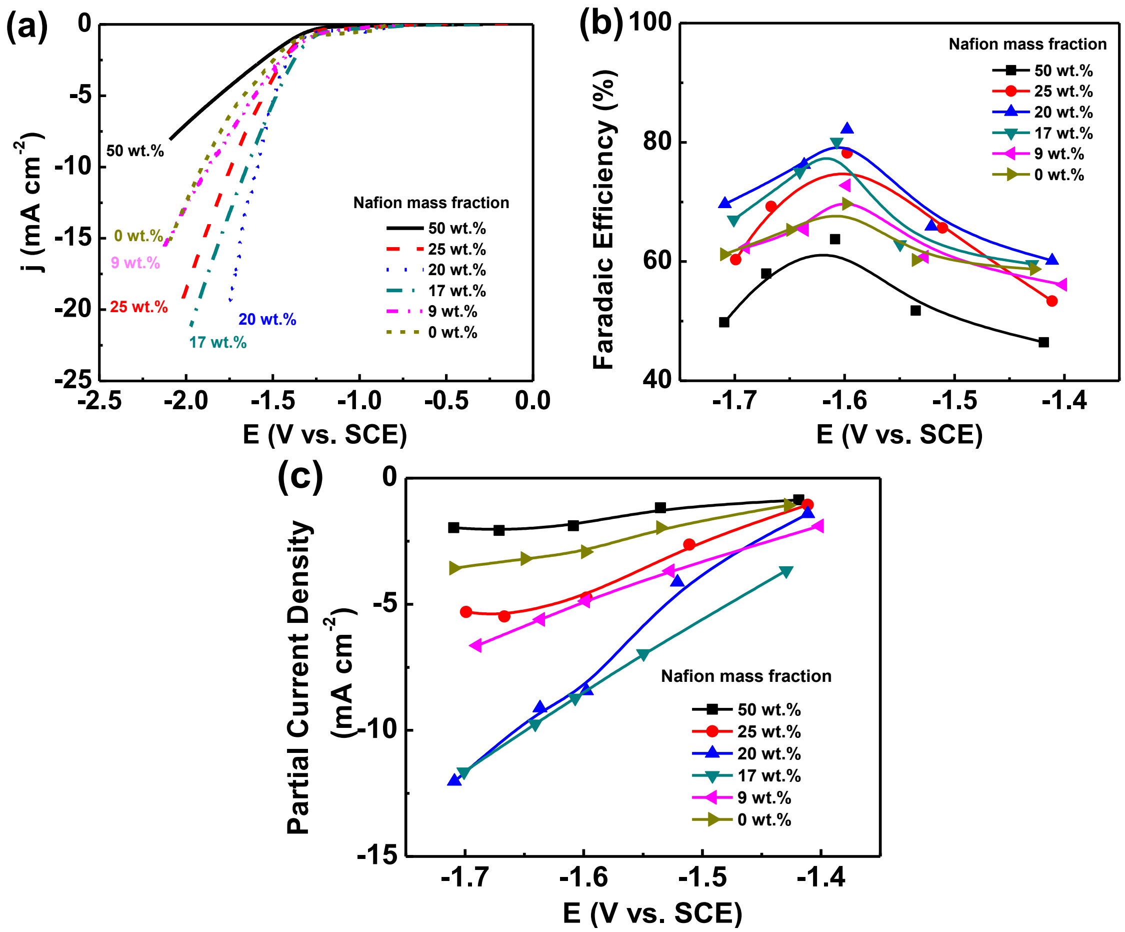

Figure 3.5. Performance of Sn GDEs with various Nafion fractions and fixed Sn loading of 1.56 mg cm^{-2}. Sn GDEs consist of 100 nm Sn particles. (a) IV characteristic curves, (b) Faradaic efficiency of formate, and (c) partial current density of formate at different potentials.

Further work was carried out to investigate the dependence of current density and Faradaic efficiency of formate on the thickness of Sn catalyst layer. The catalyst layer thickness was varied from 1.2 to 17.8 μm determined by SEM analysis, which was equivalent to Sn loading from 0.67 to 6.55 mg cm^{-2}. The Nafion fraction was maintained at 20 wt.% for all electrodes. **Figures 3.6a** and **3.6b** show a steady increase in current density with increasing Sn loading from 0.67 to 4.00 mg cm^{-2}. The increase of current density with increasing the thickness of the catalyst layer is largely due to the increase of the total area of triple phase boundaries, at which the CO_2 reduction reaction occurs. The current density started to decrease when Sn loading was > 4.00 mg cm^{-2}, which corresponded to a catalyst layer thickness of 9.2 μm. The decrease in current density when catalyst layer was thicker than 9.2 μm resulted from the increase of diffusion resistance of the reactants.[22] This layer, ~9 μm, is therefore corresponding to the effective reaction zone at the cathode, including both CO_2 reduction reaction and hydrogen evolution reactions. The Faradaic efficiency of formate was found to be independent of the catalyst layer thickness and remained constant around 72% at -1.6 V vs. SCE (**Figure 3.6c**). **Figure 3.6c** also shows a the partial current density of formate at -1.6 V vs. SCE, extracted from the results of total current density and Faradaic efficiency of formate.

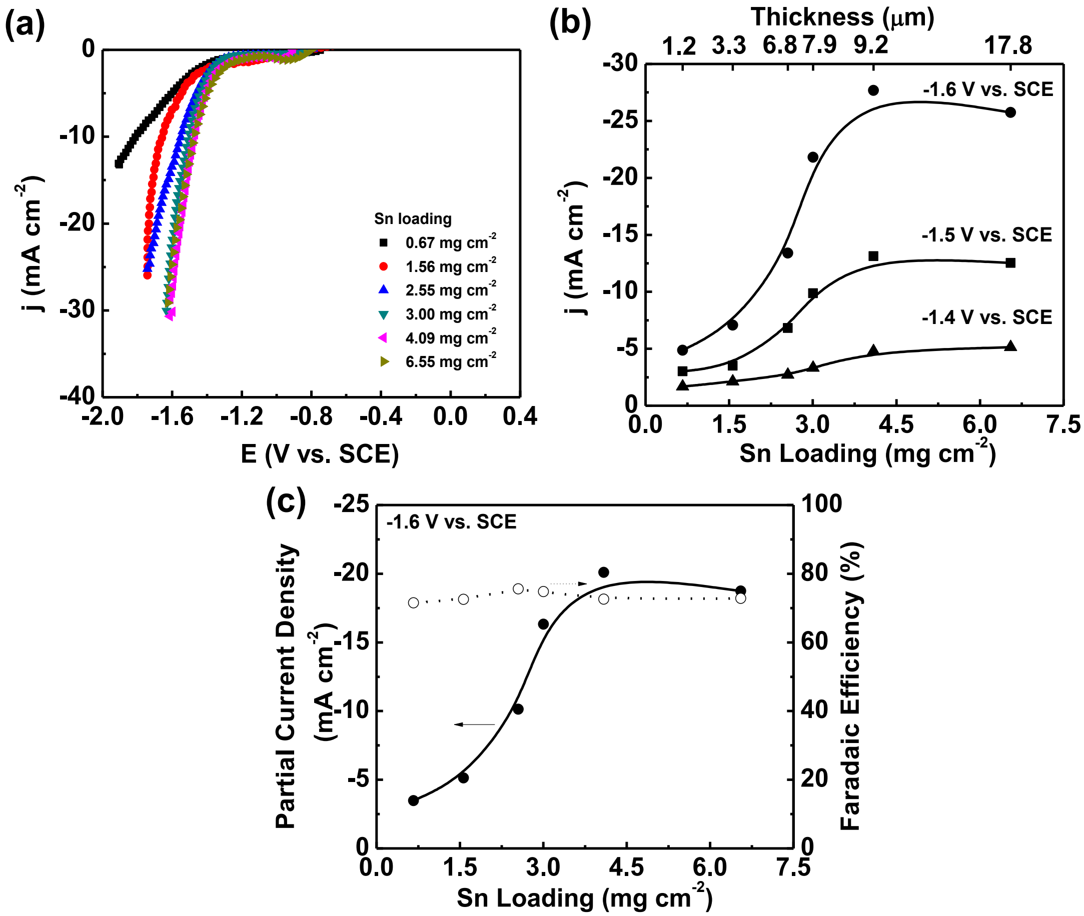

Figure 3.6. Comparison of electroactivity of Sn GDEs with various Sn loadings and fixed 20 wt.% Nafion. Sn GES consists of 100 nm Sn particles. (a) i-V curves, (b) current density versus Sn loading and Sn catalyst layer thickness, and (c) Faradaic efficiency and partial current density of formate at -1.6 V vs. SCE.

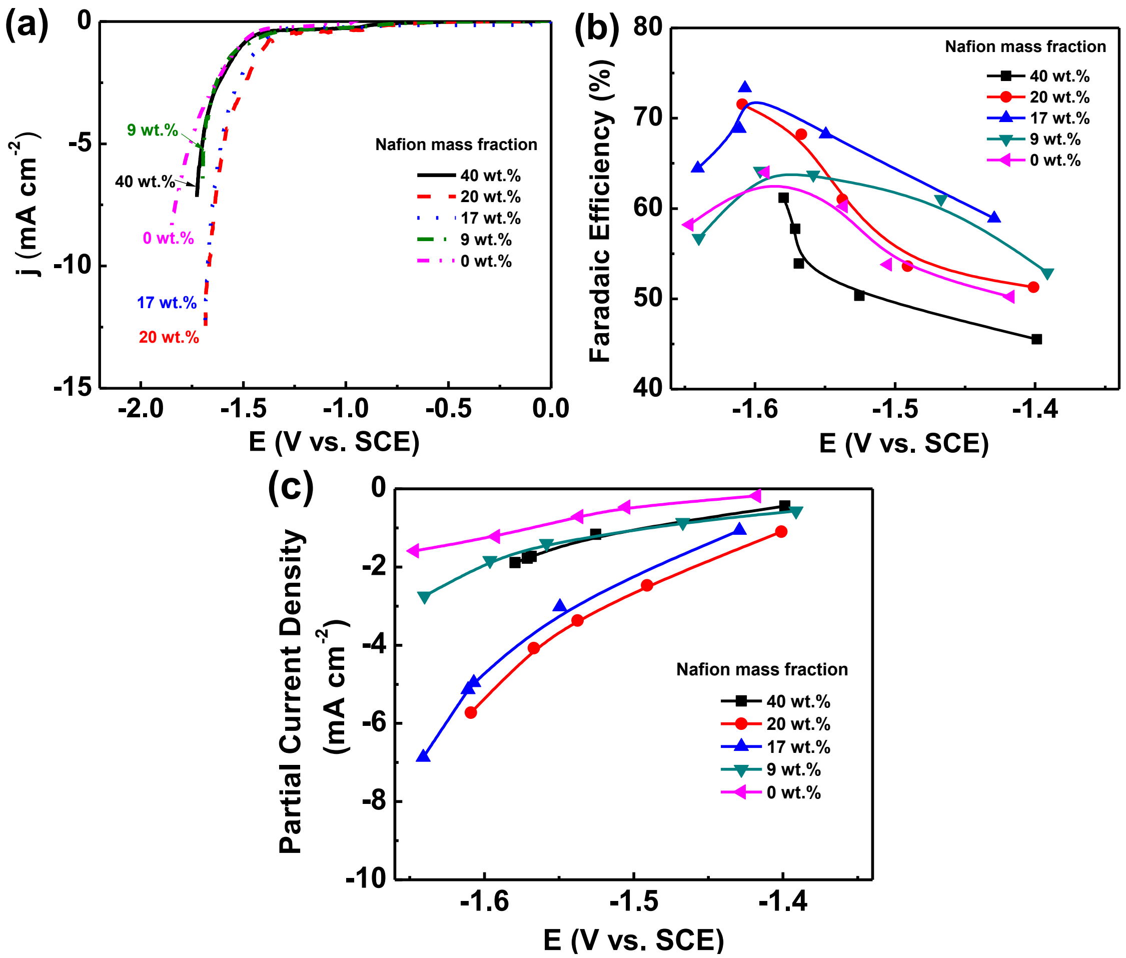

Figure 3.7. Performance of Sn GDEs with various Nafion fractions and fixed Sn loading of 0.86 mg cm^{-2}. Sn GDEs consist of Sn particles with size of 1-2 µm. (a) iV characteristic curves, (b) Faradaic efficiency of formate, and (c) partial current density of formate at different potentials.

The Faradaic efficiency towards the formation of formate was governed by two factors: (1) the local proton concentration in the reaction zone and (2) the local electrical field. In this work, the electrochemical cells were operated at a relatively low current density (< 30 mA/cm^2). Hence, an increase in the thickness of catalyst layer resulted in increasing current density, thus raised the local proton concentration, which was in favor of the formation of formate. At a constant applied cell potential, the increase of catalyst layer thickness and subsequently the current density, however, contributed to a decrease in the electrical field in the catalyst layer, which impeded the formation of formate. As a consequence, when the thickness of the catalyst layer was increased, the promoting contributions from the increase of local proton concentration towards formate formation were offset by the unfavorable effects of the decrease in the local electrical field. The overall effect was that the Faradaic efficiency of formate exhibited weak thickness dependence.

Figure 3.7 shows the dependency of total current density, Faradaic efficiency and partial current density of formate on the Nafion fraction in Sn GDEs consisting of Sn particles with size of 1-2μm. The highest total current density was obtained with the electrode having a Nafion fraction of 20 wt.% (Nafion volume fraction 0.47) while the electrode with a Nafion fraction of 17 wt.% (Nafion volume fraction 0.40) showed the greatest selectivity towards formate production. The electrode with a Nafion fraction of 17 wt.% and 20 wt.% exhibited a similar partial current density of formate, both of which were higher than the electrodes with the other Nafion fractions, especially at high potentials. The optimal Nafion fraction was between 17 and 20 wt.% for the Sn particles of 1-2 μm, similar to that for 100 nm specimens. The optimized Nafion fraction for 100 nm and 1-2 μm Sn particles showed a similar volume fraction Nafion, which is the key in determining the property of catalyst layer from the point view of percolation model.

3.4 Conclusions

The microstructure of Sn catalyst layer for CO_2 electro-reduction was systematically investigated in terms of Nafion fraction, catalyst loading and catalyst particle size. Impregnation of electrodes with Nafion, a proton conductor, extended the three-dimensional reaction zone. This optimized microstructure provided a desirable proton concentration, electronic conduction, and gas diffusion for high selectivity towards the formation of formate. Both the current density and Faradaic efficiency towards formate formation were at the maximum with the optimized Nafion fraction of 17-20 wt.% in Sn electrodes, which was found independent on the size of catalyst particles. The current density increased with increasing Sn loading up to 4.00 mg cm^{-2} corresponding to a catalyst layer thickness of ~ 9.2 µm. Further increase of Sn loading showed a negligible contribution to the total current density, suggesting the existence of maximum reaction penetration depth.

References

1. S. Litster and G. McLean, *J. Power Sources*, **130,** 61-76 (2004).
2. S. Mu and M. Tian, *Electrochim. Acta*, **60,** 437-442 (2012).
3. E. Antolini, L. Giorgi, A. Pozio and E. Passalacqua, *J. Power Sources*, **77,** 136-142 (1999).
4. G. Sasikumar, J. W. Ihm and H. Ryu, *Electrochim. Acta*, **50,** 601-605 (2004).
5. A. Suzuki, U. Sen, T. Hattori, R. Miura, R. Nagumo, H. Tsuboi, N. Hatakeyama, A. Endou, H. Takaba, M. C. Williams and A. Miyamoto, *Int. J. Hydrogen Energy*, **36,** 2221-2229 (2011).
6. D. T. Whipple and P. J. A. Kenis, *J. Phy. Chem. Lett.*, **1,** 3451-3458 (2010).
7. R. P. S. Chaplin and A. A. Wragg, *J. Appl. Electrochem.*, **33,** 1107-1123 (2003).
8. J. J. Carroll, J. D. Slupsky and A. E. Mather, *J. Phys. Chem. Ref. Data*, **20,** 1201-1209 (1991).
9. R. L. Cook, R. C. Macduff and A. F. Sammells, *J. Electrochem. Soc.*, **137,** 607-608 (1990).
10. T. Yamamoto, D. A. Tryk, A. Fujishima and H. Ohata, *Electrochim. Acta*, **47,** 3327-3334 (2002).
11. M. Shibata, K. Yoshida and N. Furuya, *J. Electrochem. Soc.*, **145,** 2348-2353 (1998).
12. B. A. Rosen, A. Salehi-Khojin, M. R. Thorson, W. Zhu, D. T. Whipple, P. J. A. Kenis and R. I. Masel, *Science*, **334,** 643-644 (2011).
13. D. T. Whipple, E. C. Finke and P. J. A. Kenis, *Electrochem. Solid-State Lett.*, **13,** D109-D111 (2010).
14. J. Wu, F. G. Risalvato, P. P. Sharma, P. J. Pellechia, F.-S. Ke and X.-D. Zhou, *J. Electrochem. Soc.*, **160,** F953-F957 (2013).
15. J. Wu, F. G. Risalvato, F.-S. Ke, P. J. Pellechia and X.-D. Zhou, *J. Electrochem. Soc.*, **159,** F353-F359 (2012).
16. M. Uchida, Y. Aoyama, N. Eda and A. Ohta, *J. Electrochem. Soc.*, **142,** 4143-4149 (1995).
17. Y. G. Yoon, G. G. Park, T. H. Yang, J. N. Han, W. Y. Lee and C. S. Kim, *Int. J. Hydrogen Energy*, **28,** 657-662 (2003).
18. M. Eikerling and A. A. Kornyshev, *J. Electroanal. Chem.*, **453,** 89-106 (1998).
19. E. Passalacqua, F. Lufrano, G. Squadrito, A. Patti and L. Giorgi, *Electrochim. Acta*, **46,** 799-805 (2001).
20. Q. P. Wang, M. Eikerling, D. T. Song, Z. S. Liu, T. Navessin, Z. Xie and S. Holdcroft, *J. Electrochem. Soc.*, **151,** A950-A957 (2004).
21. S. J. Lee, S. Mukerjee, J. McBreen, Y. W. Rho, Y. T. Kho and T. H. Lee, *Electrochim. Acta*, **43,** 3693-3701 (1998).
22. A. A. Kulikovsky, *Electrochem. Commun.*, **5,** 530-538 (2003).

Chapter 4

Design, Assembly, and Performance of Low Temperature Full Electrochemical Cells

4.1 Introduction

The design of the electrode and its reactor is a critical step for the feasible production of fuels from CO_2 on a large scale. The electrochemical reduction process, a.k.a. electrolysis, can take place over a wide range of temperatures, from room temperature to over 1000 ^{o}C. In the case of high temperature electrolysis, solid oxide electrolysis cells (SOECs) are exemplary for the electrochemical conversion of CO_2 into CO or co-electrolysis of H_2O and CO_2 to form syngas (CO and H_2). In general, SOECs exhibit a low overpotential and superior selectivity to CO formation as well as high current density.[1-3] The overarching challenges facing prolonged SOEC operation include the electrode degradation due largely to the formation of coke and volatile nickel-carbonyls. [4-6]

Low temperature electrolysis of CO_2 has been investigated extensively in electrochemical cells consisting solid polymer electrolyte.[7-15] Earlier work was carried out by using proton exchange membrane fuel cells (PEMFCs) to directly convert CO_2 to other species in gas phases.[7, 8] Various hydrocarbons, including CH_4, C_2H_4 and C_2H_6, were observed on a copper electrode deposited on Nafion® 117 membrane; the overall Faradaic efficiency, however was ~1% due to the acidity of the Nafion® membrane which promoted the competitive hydrogen evolution reaction over CO_2 reduction reaction.[12, 16] Modifications in the physical structure of PEMFCs were adopted to improve the activity and selectivity of the electrodes.[9-14] For instance, a 3D cathode consisting of a Sn-Cu mesh screen was investigated with Nafion® 117 membrane as a separator. This design allowed a co-current flow of CO_2 and catholyte through the cathode, thus providing an aqueous environment for CO_2 reduction.[9] As a consequence, the Faradaic efficiency toward formate formation was substantially improved to ~86% at a cell potential of 3 V. The high operation voltage resulted from great ohmic loss and cathodic overpotential.[9] In addition, the lower solubility of CO_2 in aqueous electrolytes[17] significantly affected cell performance at higher current densities because of mass transfer constraints. In another design, a glass fiber saturated with 0.5 M $KHCO_3$ was inserted between the Nafion® membrane and the Ag gas diffusion electrode (GDE) to prevent excessive buildup of protons near the cathode, which resulted in a significant increase of selectivity towards CO_2 reduction to CO.[12] The glass fibers, however could become dry during electrolysis due to the evaporation of water, resulting in degradation of cell performance. One approach to circumvent this drying issue was to operate the cell with a flowing electrolyte stream in place of saturated glass fiber.[13] With a continuous flowing electrolyte, formate production on Sn GDE was achieved at a Faradaic efficiency of ~70% by using 0.5 M KCl as the electrolyte at pH = 7, while the efficiency increased to ~90% at pH = 4. The cell, however, was operated at high voltages to obtain formate.[13] Recently, an ionic liquid was used as the catholyte with Ag GDE to convert CO_2 to CO, which showed substantial improvement over both Faradaic efficiency (~100%) and the overpotential (less negative than -0.2 V) towards CO formation due to the decrease of the free energy for formation of the intermediate $CO_2^{-}\cdot$.[18]

In this chapter, a full electrochemical cell was designed based on the PEMFC configuration by inserting a circulating liquid-phase electrolyte buffer layer between the Nafion® membrane and Sn GDE. This design demonstrates the feasibility to use current PEMFC hardware for electrochemical CO_2 conversion. The full electrochemical cell incorporates the gas diffusion electrode that fabricated and optimized in chapter 3, which enables the direct gas-phase CO_2 reduction. The intrinsic selectivity and activity of the Sn GDE in the full electrochemical cell were studied. This bench-scale full electrochemical cell precedes a future pilot-scale demonstration plant to generate fuels from CO_2 reduction. There are three key advantages of this cell design: (1) Insertion of a liquid-phase buffer layer significantly shifts the selectivity towards formate formation, (2) In comparison with stationary electrolytes, the continuous circulation of the electrolyte provides moderate convective mixing and maintains adequate pH near cathode surface necessary for CO_2 reduction, (3) A circulating electrolyte provides a cost-effective method for the accumulation of liquid products.

4.2 Experimental

4.2.1 Configuration of the Full Electrochemical Cell

The buffer layer adopted in this research resides between the Nafion® membrane and the cathode. The thickness of buffer layer was approximately 2.4 mm. The cathode was an optimized Sn GDE that has already described in chapter 3. The cathode had a geometric area of 4 cm^2 and a loading of Sn ~2 mg cm^{-2}. A gas diffusion layer (GDL) and a half catalyst-coated membrane (CCM) were hot pressed together to serve as the anode. The Sigracet® GDL 10BC was purchased from SGL group. The half CCM was made by spraying Pt/C catalysts (60%, Johnson Matthey) ink onto one side of a Nafion® 212 membrane (DuPont). The Pt loading was 0.3 mg cm^{-2}.

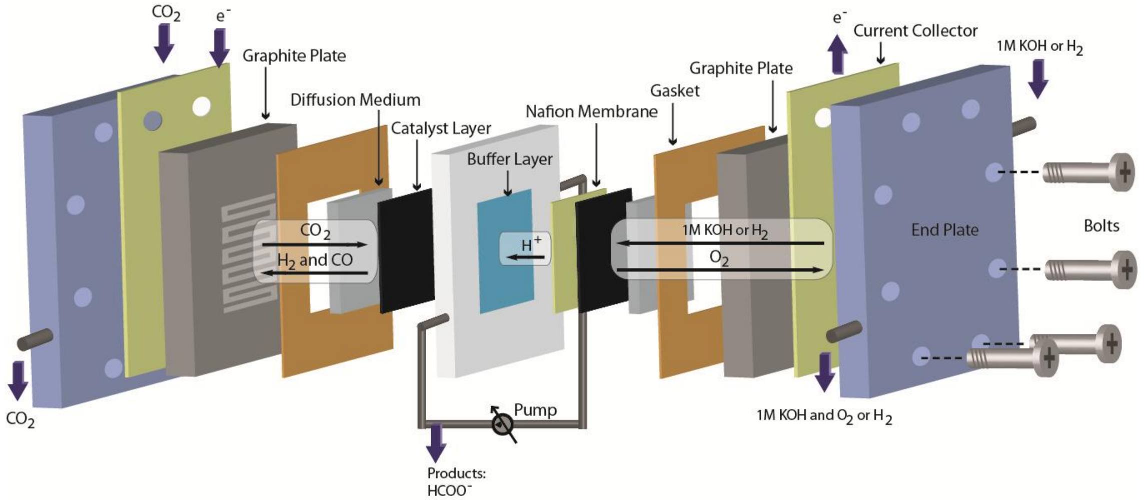

Figure 4.1. A schematic of the full electrochemical cell featuring a buffer layer of circulating liquid-phase electrolyte.

Figure 4.1 illustrates the schematic of the full electrochemical cell. All the reactant gases were supplied at ambient pressure (p^o = 1.013 bar) and room temperature (T = 298 K). The cathode side of the cell (where the electrochemical reduction of CO_2 occurs) was supplied with gas-phase CO_2 (99.998%) at a flow rate of 45 ml min^{-1}. The anode side of the cell was supplied with either H_2 (99.99%) at 150 ml min^{-1} or 1 M KOH (pH = 13.8, Sigma-Aldrich, reagent grade) solution at 10 ml min^{-1}. All the gases and solutions flowed along serpentine channels in graphite over which gold-plated metal hardware was chosen as the current collector. The aqueous electrolyte of 0.1 M $KHCO_3$ (pH = 7, Sigma-Aldrich, ACS reagent grade) was used as the buffer layer and circulated at a flow rate of 5 ml min^{-1}. The total volume of the electrolyte solution was 10 ml. The liquid products were accumulated in the electrolyte solution during electrolysis. The formate concentration was 2-100 μmol ml^{-1} at the end of 0.5 h electrolysis in the potential range, -0.8 to -2.8 V.

The anode reaction is either H_2 oxidation or oxygen evolution depending on the choice of the reactants. The reactions are shown in Eqs (4.1) and (4.2), respectively.

$$2H^+ + 2e^- = H_2 \qquad E^o = 0 \text{ V vs. SHE} \tag{4.1}$$

$$O_2 + 2H_2O + 4e^- = 4OH^- \qquad E^o = 0.41 \text{ V vs. SHE} \tag{4.2}$$

The electrochemical reduction of CO_2 into formic acid occurs at the cathode side and is shown below. The formic acid dissociates to formate ($HCOO^-$) in a neutral electrolyte.

$$CO_2 + 2H^+ + 2e^- = HCOOH \qquad E^o = -0.20 \text{ V vs. SHE} \tag{4.3}$$

4.2.2 Optimization of the Performance of the Full Electrochemical Cell

When investigating the effect of the buffer layer thickness and electrolyte pH, the full electrochemical cell was operated with H_2 and CO_2 fed to anode and cathode, respectively. The electrolyte was 0.5 M Na_2SO_4 (pH = 6.8, Sigma-Aldrich, ACS reagent grade). The pH was adjusted with concentrated H_2SO_4 or 1 M NaOH solution. Besides the 2.4 mm buffer layer, the other thicknesses including 0.8, 1.6, 2.9, 3.2, 4.0, 4.7, and 7.1 mm were included to compare the cell performance.

4.2.3 Electrochemical Measurements

Potentiostatic electrolysis was conducted at room temperature (25 ± 1 ^oC) and ambient pressure by means of a potentiostat (Princeton Applied Research PARSTAT 2273 Potentiostat/Galvanostats with a power booster up to 20 V/20 A and Bio-Logic VMP3 Potentiostats/Galvanostats) recording the current. Current density is expressed as the total current divided by the geometric surface area of the electrodes. The Faradaic efficiency is determined by means of the charges consumed to produce a specific product divided by the total charges passed during the electrolysis for 0.5 h. The individual electrode potential during potentiostatic electrolysis was measured as referred to the Ag/AgCl reference electrode which was placed in the middle of the buffer layer. The cell ohmic resistance was measured by electrochemical impedance spectroscopy at open circuit voltage, with amplitude of 5 mV and frequency range of 100 kHz to 0.1 Hz. For example, the total cell ohmic resistance was about 7.3 Ω corresponding to an area specific resistance (ASR) of 29.2 Ω cm^2 with the electrolyte of 0.1 M $KHCO_3$ and buffer layer thickness of 2.4 mm.

4.2.4 Product Analysis and Quantification

Liquid products were quantified by using 1D ^1H nuclear magnetic resonance (NMR) spectroscopy. The NMR data was acquired by using a Varian Mercury/VX 400 MHz spectrometer. More details can be found in chapter 2.[19] Gas products were quantified by using gas chromatography (GC, Inficon Micro 3000 GC). The residual reactant and product gases from the outlet of the cathodic compartment were vented directly into the gas-sampling loop of GC. The GC has two channels, one equipped with a packed 10 m MolSieve 5A column and the other with a packed 8 m Plot Q column. Each channel was connected with a thermal conductivity detector. Helium (Airgas, 99.999%) was used as the carrier gas to quantify CO concentration while argon (Airgas, 99.999%) was used to quantify hydrogen concentration. A standard gas mixture consisting of 1000 ppm CO and 1000 ppm H_2 in CO_2 was employed to calibrate the GC and to acquire the gas peak area conversion factor. The moles of CO produced during the electrolysis reaction were calculated from the GC peak area as follows:

$$n_{CO} = \frac{Peak\,area\ ratio}{\alpha} \times flow\,rate \times electrolysis\,time \times \frac{P^o}{RT} \qquad (4.4)$$

where α is the conversion factor based on calibration of the GC with a standard sample, p^o is 1.013 bar, T is 273 K, and R is the universal gas constant (8.314 J mol^{-1} K^{-1}). The flow rate of CO_2 was 41.2 sccm.

4.3 Results and Discussion

4.3.1 Role of the Liquid-phase Buffer Layer

Figure 4.2a shows the trend in Faradaic efficiency towards hydrogen evolution in a conventional PEMFC without a buffer layer, in which Pt/C is replaced by Sn at the cathode side. The Faradaic efficiency towards hydrogen production was ~100% when helium was supplied to the cathode. When CO_2 was used instead of helium, hydrogen was the only product observed until a cell potential of -1.8 V. As cell potentials were increased to more cathodic values, the Faradaic efficiency towards hydrogen evolution was found to decrease slightly by a few percentages. We used a chiller to condense volatile products in the cathode outlet tube. NMR analysis indicated the presence of formate in the liquid products; however, CO was not observed in GC trace analysis. In the absence of a buffer layer, hydrogen evolution reaction (HER) clearly dominated over the CO_2 reduction reaction. Similar results were also observed on Ag GDE in a PEMFC type electrolysis cell.[12] Moreover, the i-V curve indicated high activity towards HER as shown in **Figure 4.2b**. A high current density, ~1 to 2 A cm^{-2} was observed at moderate cell potentials, -1 to -2 V, which was consistent with the low total ASR of about 1.0 Ω cm^2 between this potential range (**Figure 4.2b**).

This dominance of HER over CO_2 electro-reduction can be understood by its favorable thermodynamics and facile kinetics.[20-25] HER in an aqueous medium occurs via two successive steps; the initial discharge of a hydronium ion (H_3O^+) to give adsorbed hydrogen atom H_{ads} (Volmer step) followed by combination of two adsorbed H_{ads} atoms (Tafel step) or adsorbed H_{ads} with H_3O^+ in the solution (Heyrovsky step) yielding H_2.[20, 22] This competition between HER and CO_2 reduction suggests the importance of controlling the H^+ concentration near the cathode surface to suppress HER, and thus facilitate CO_2 reduction. We used a buffer layer of circulating aqueous electrolyte to mediate this H^+ concentration.

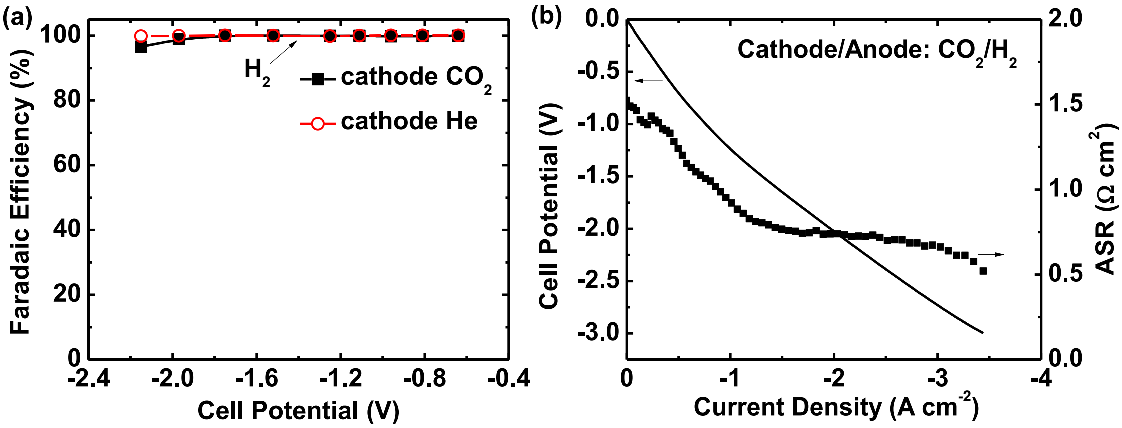

Figure 4.2. The performance of a full electrochemical cell without a buffer layer for CO_2 reduction. (a) Faradaic efficiency of H_2 and (b) polarization curve and ASR. The anode was supplied with H_2 (150 ml min^{-1}) while the cathode with He (45 ml min^{-1}) or CO_2 (45 ml min^{-1}) at $p^o = 1.013$ bar and T = 298.15 K. Catalyst loading was 2 mg cm^{-2} for Sn and 0.3 mg cm^{-2} for Pt on carbon powder support.

4.3.2 Full Cell with a Buffer Layer and Hydrogen Supplied to Anode

When a buffer layer circulating 0.1 M $KHCO_3$ was used, the selectivity towards formate at the cathode was significantly improved. **Figure 4.3** shows NMR spectra of ^1H in the formate group as a function of the applied cell potentials. Formate was the only liquid product, which was formed at a cell potential of -0.8 V. This corresponded to an overpotential of -0.19 V with respect to the apparent standard cell potential of -0.61 V when taking into consideration the anodic (H_2 oxidation, Eq. 4.1) and the cathodic reactions (CO_2 reduction, Eq. 4.3, apparent standard potential, $E^{o'} = -0.61$ V vs. SHE for pH = 7). This low overpotential is mainly attributed to the optimized microstructure of Sn

GDEs, which possess a large number of triple-phase boundaries where electrons, protons and CO_2 gases meet and react. Reduction of CO_2 at a lower overpotential is of substantial importance to achieve greater cell performance. Similar overpotential of ~-0.2 V was recently reported in a cell mediated by ionic liquids, which provided more favorable thermodynamics for $CO_2^{\bullet -}$ intermediate formation.[18, 26]

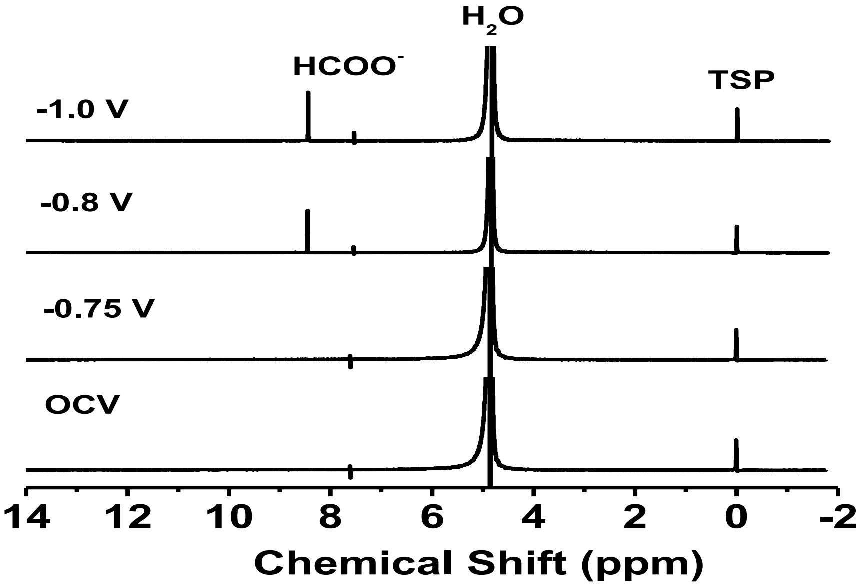

Figure 4.3. The NMR spectra of ^1H in the formate group as a function of the applied cell potentials. CO_2 reduction was carried out in the full electrochemical cell with a buffer layer at room temperature and ambient pressure. Electrolyte (0.1 M $KHCO_3$) was circulated at 5 ml min^{-1}. The anode and cathode were supplied with H_2 (150 ml min^{-1}) and CO_2 (45 ml min^{-1}), respectively, at $p^o = 1.013$ bar and T = 298.15 K.

Figure 4.4a illustrates the trend in Faradaic efficiency for different products as a function of applied cell potential. These results were found reproducible in four independent operations within acceptable range. The Faradaic efficiency towards formate formation started with 65% at -0.8 V and increased at more negative cell potentials. The maximum Faradaic efficiency was observed ~90% at -1.7 V. When 0.5 M Na_2SO_4 was used as buffer layer, formate was also formed at -0.8 V with a Faradaic efficiency of

~47%. The utilization of a circulating buffer layer and optimized microstructure of electrode were attributed to achieving a high Faradaic efficiency at a low overpotential towards formate formation on Sn GDE by mediating H^+ concentration near the cathode surface. The presence of H^+ is essential to form formate, through the protonation of the carbon in the intermediate $CO_2^{\bullet -}$, followed by a second electron transfer.[27] The excessive H^+ concentration, however results in preferable hydrogen evolution over CO_2 reduction as observed in the cell without a buffer layer. The Faradaic efficiency towards CO formation exhibited a similar trend as formate. The maximum Faradaic efficiency of CO was ~13% at -1.2 V. On the other hand, the Faradaic efficiency for hydrogen formation drastically dropped to ~20% and further decreased below 10% as potentials became more negative.

The energy efficiency is a key factor in determining the economic feasibility of converting CO_2 to fuels by utilizing electricity. The energy efficiency for formate was calculated using Eq. (4.5)[18, 24], as shown in **Figure 4.4a**.

$$Energy\ Efficiency = \frac{E^{o'} \times Faradaic\ Efficiency}{Applied\ Cell\ Potential} \tag{4.5}$$

where the apparent standard cell potential, $E^{o'}$ is -0.61 V, as predicted by Nernst equation. We observed a maximum energy efficiency of 50% for formate at -0.8 V with 0.1 M $KHCO_3$ as the buffer layer. The energy efficiency towards formate formation decreased at higher cell potentials due to increasing ohmic loss in the membrane and buffer layer.

The plots shown in **Figure 4.4b** are partial current densities of formate, CO and H_2 along with the total current density averaged over 30 min of electrolysis as a function of the cell potential. The total current density of the cell with a buffer layer was found to be much lower than that without a buffer layer due to the larger ASR (29.2 Ω cm^2) with a buffer layer compared to about 0.8 Ω cm^2 without a buffer layer. The large ASR with a buffer layer results from the electrolyte resistance of the aqueous buffer solution. The partial current density of formate was ~-1 mA cm^{-2} at -0.8 V which increased at higher cell potentials and reached ~-9.0 mA cm^{-2}, corresponding to a production rate of 3.0 μmol min^{-1} cm^{-2} at -1.7 V. The production rate of formate, corresponding to its partial current density, is limited by two factors: sluggish kinetics of CO_2 reduction and a high ohmic loss, which need to be improved in the future design of the cells and electrode materials.

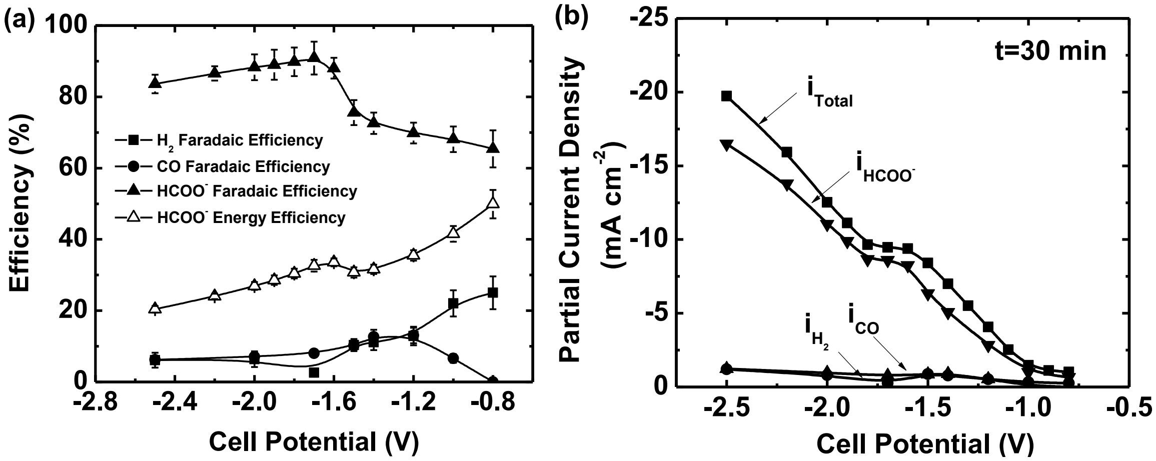

Figure 4.4. A detailed analysis of the products in a full electrochemical cell with a circulating aqueous-electrolyte buffer layer. (a) Faradaic efficiencies towards the production of liquid-phase formate, gas product CO and by-product H_2, and energy efficiency of formate, (b) total and partial current densities of products versus applied cell potential. The anode and cathode were supplied with H_2 (150 ml min^{-1}), and CO_2 (45 ml min^{-1}), respectively, at $p^o = 1.013$ bar and $T = 298.15$ K. Electrolyte (0.1 M $KHCO_3$) was circulated at 5 ml min^{-1}.

4.3.3 Full Cell with a Buffer Layer and Water Supplied to Anode

Artificial photosynthesis in a photo-electrochemical cell involves the utilization of solar light for water oxidation at the anode side and CO_2 reduction at the cathode side. In this work, we demonstrated the feasibility of simultaneous water oxidation and CO_2 reduction in our cell with a 0.1 M $KHCO_3$ buffer layer. Specifically, an aqueous 1 M

KOH solution and CO_2 were supplied to the anode and cathode, respectively, and the cell was operated in an electrolysis mode.

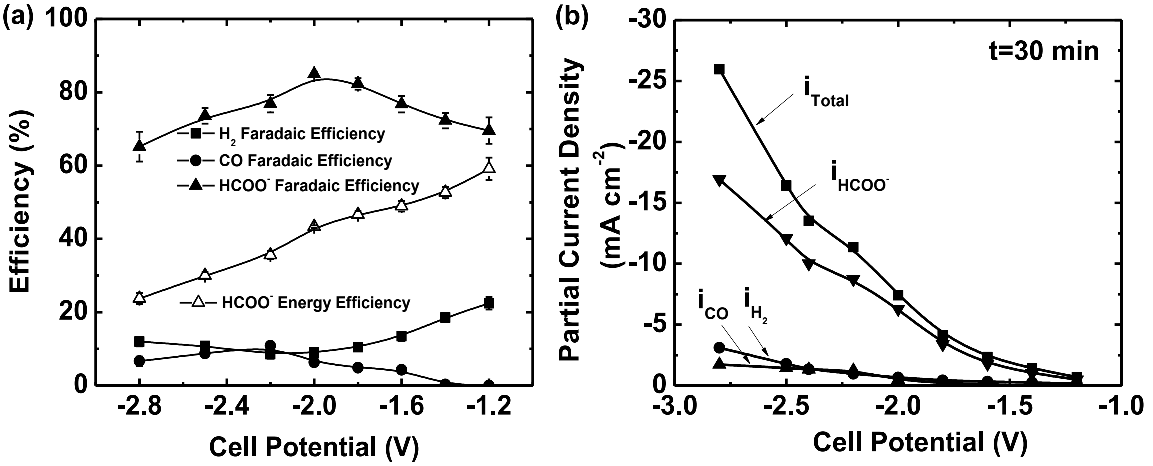

Figure 4.5. Simultaneous water oxidation and CO_2 reduction in the full electrochemical cell with a circulating aqueous-electrolyte buffer layer. (a) Faradaic efficiencies towards the production of formate, CO and H_2, and energy efficiency of formate, (b) total and partial current densities of products as a function of applied cell potential. The anode and cathode were supplied with 1 M KOH (10 ml min^{-1}) and CO_2 (45 ml min^{-1}) at $p^o = 1.013$ bar and T = 298.15 K, respectively. Electrolyte (0.1 M $KHCO_3$) was circulated at 5 ml min^{-1}.

Figures 4.5a and **4.5b** depict the Faradaic efficiency and partial current density as a function of cell potential. We observed the onset of formate production at -1.2 V with a Faradaic efficiency of 70% and partial current density of ~-1 mA cm^{-2}. A cell potential higher than when the cell was fed with hydrogen gas was needed to overcome the anodic overpotential required for water oxidation. Nevertheless, with respect to the apparent standard cell potential of -1.02 V for simultaneous water oxidation (Eq. 4.2) and CO_2 reduction (Eq. 4.3, $E^{o'}$ = -0.61 V vs. SHE for pH = 7), this overpotential of -0.18 V towards formate production was found to be nearly the same with H_2 supplied to anode, as discussed previously. We observed the highest Faradaic efficiency of 85% towards formate formation at -2.0 V. The measured partial current density and corresponding production rate for formate at this potential were -6 mA cm^{-2} and 2.0 μmol min^{-1} cm^{-2}, respectively. The maximum energy efficiency ~60% for formate production was obtained at -1.2 V as shown in **Figure 4.5a**. The Faradaic efficiency towards H_2 production reached a minimum of 8% at -2.2 V, at which the highest Faradaic efficiency of 10% towards CO formation was observed.

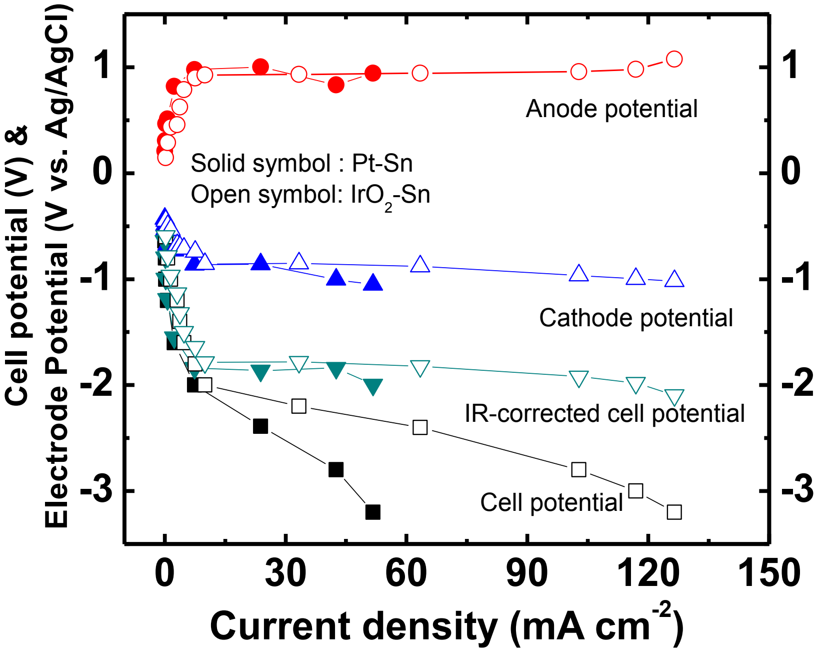

Figure 4.6. Individual anode and cathode potentials in the full electrochemical cell with a buffer layer of 0.1 M $KHCO_3$ when 1 M KOH (10 ml min^{-1}) was supplied to the anode and CO_2 (45 ml min^{-1}) to cathode at $p^o = 1.013$ bar and T = 298.15 K.

In order to obtain individual electrode polarization curves, the Ag/AgCl reference electrode was placed in the buffer layer. The individual electrode potential was further compensated by IR drop, as shown in **Figure 4.6**. The high overpotentials required for both oxygen evolution and CO_2 reduction, suggests the choice of electrocatalysts holds the key to achieve higher efficiency and current density. We used IrO_2 instead of Pt as catalyst at anode because of its higher activity towards oxygen evolution.[28, 29] The polarization curves showed less overpotential loss with IrO_2 as anode compared to Pt (**Figure 4.6**).

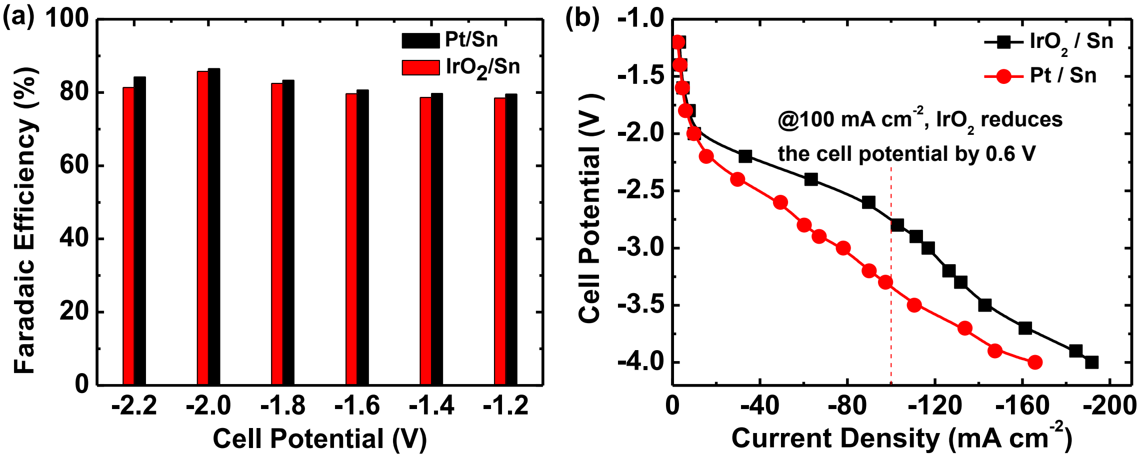

Figure 4.7. Comparison of (a) Faradaic efficiency of formate and (b) current density between IrO_2 and Pt as the anode catalysts. The cell was run with a buffer layer of 0.1 M $KHCO_3$ when 1 M KOH (10 ml min^{-1}) was supplied to the anode and CO_2 (45 ml min^{-1}) to cathode at $p^o = 1.013$ bar and T = 298.15 K.

Although the Faradaic efficiency for formate only increased slightly at cell potentials from -1 to -3 V, the total current density was found to increase by about 50% (**Figure 4.7**). This improvement is attributed to the higher activity towards oxygen evolution of IrO_2 than Pt. The comparison of activity towards oxygen evolution between IrO_2 than Pt was conducted in a full cell without the buffer layer in which the anode and cathode was supplied with 1 M KOH and Ar, respectively. IrO_2 exhibits lower overpotential for oxygen evolution that Pt as shown in **Figure 4.8**. The higher activity towards oxygen evolution of IrO_2 was further confirmed by the EIS results (**Figure 4.9**). Because of the negligible reaction resistance of hydrogen evolution on Pt, the diameter of the semi-circle of impedance was considered as the reaction resistance of oxygen evolution. The reaction resistance of oxygen evolution on IrO_2 is one magnitude order less than that on Pt, e.g. 1.2 vs. 10 Ω cm^2 at 200 mA. Further work, however, needs to be done to optimize electrodes for both oxygen evolution and CO_2 reduction, and consequently scale-up this approach to meet the requirements of commercial processes with a typical production rate on the order of 100 μmoles per minute per cm^2.

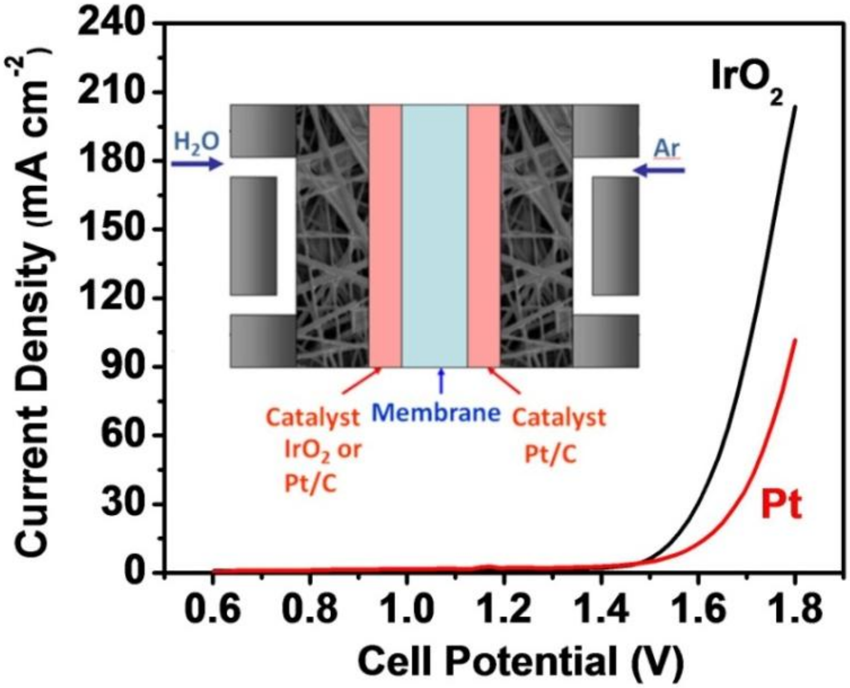

Figure 4.8. Polarization curves for oxygen evolution on IrO_2 and Pt. 1 M KOH (10 ml min^{-1}) was supplied to the anode and Ar (45 ml min^{-1}) to cathode at p^{o} = 1.013 bar and T = 298.15 K.

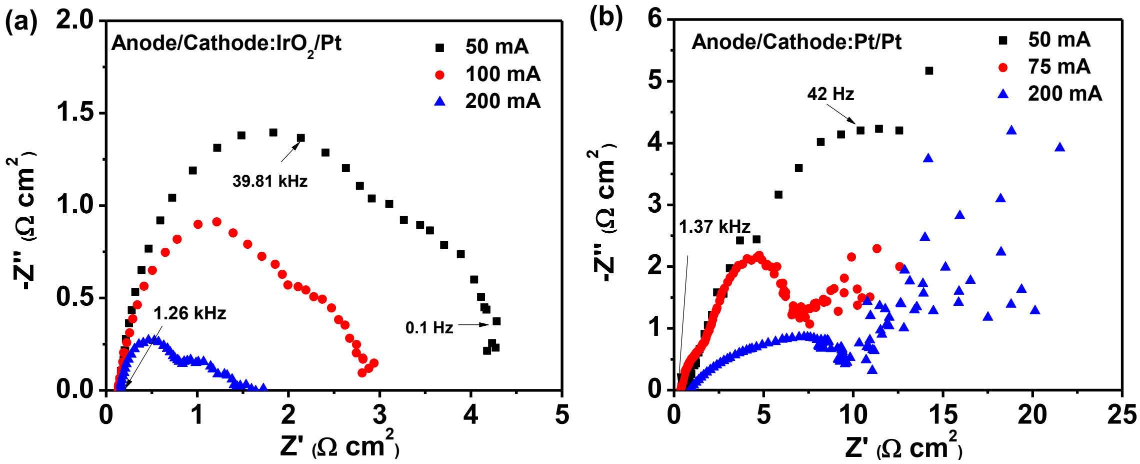

Figure 4.9. Impedance for oxygen evolution on (a) IrO_2 and (b) Pt. The measurement was conducted in the cell as shown in the inset of Figure 4.8.

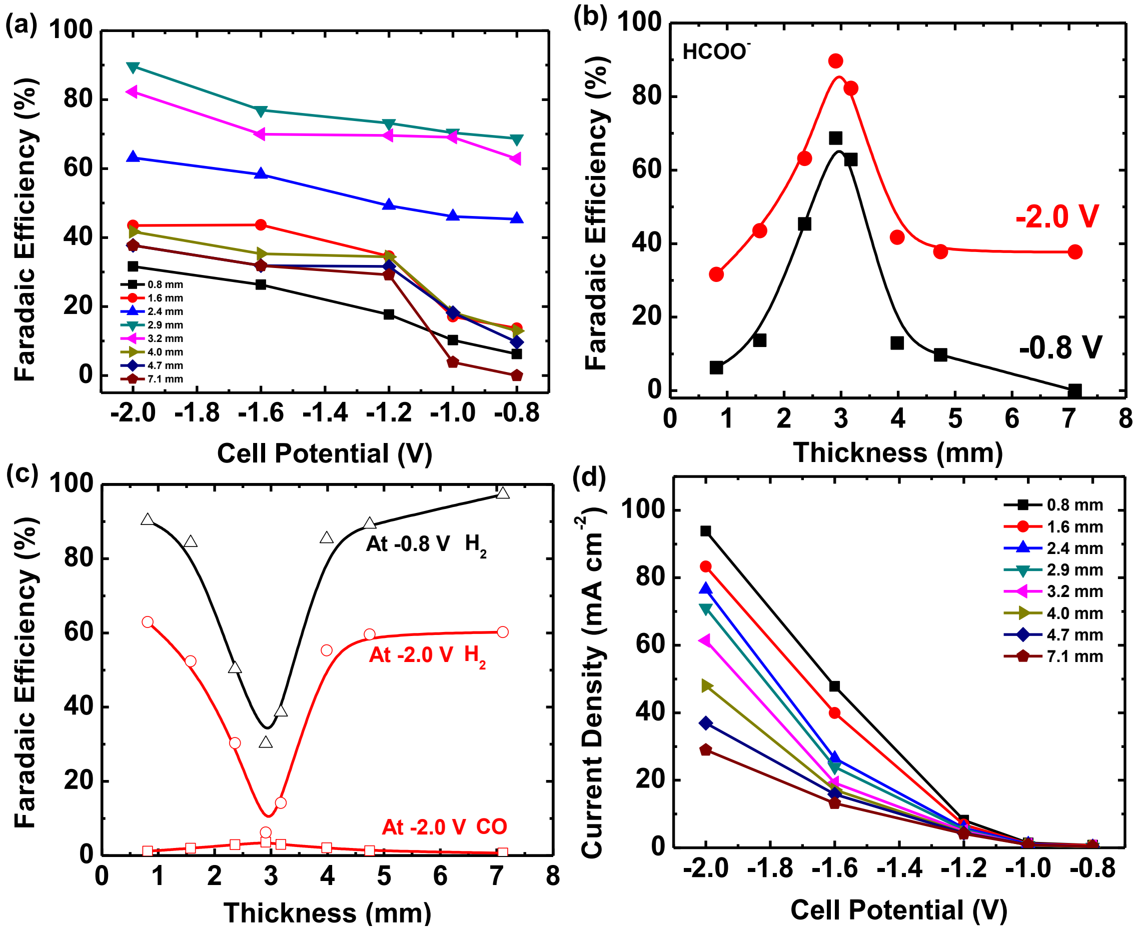

Figure 4.10. (a) Buffer layer thickness dependency of Faradaic efficiency towards formate production at various potentials, (b) Faradaic efficiency of formate versus buffer layer thickness at cell potentials of -0.8 and -2 V, (c) Faradaic efficiency of CO and H_2 versus buffer layer thickness at cell potentials of -0.8 and -2 V, and (d) polarization curves for different buffer layer thicknesses. The electrolyte is 0.5 Na_2SO_4 (pH = 6.8). The anode and cathode were supplied with H_2 (150 ml min^{-1}) and CO_2 (45 ml min^{-1}), respectively, at p^o = 1.013 bar and T = 298.15 K.

4.3.4 Optimum Buffer Layer Thickness

As mentioned above, the H^+ concentration at the electrode surface plays a key role in determining the selectivity towards CO_2 reduction. The authentic cathode potential is another parameter that significantly influences the selectivity. Both H^+ concentration at the electrode surface and authentic cathode potential could be adjusted by varying the thickness of buffer layer that is tuning the H^+ transport distance from cathode to anode and internal cell ohmic resistance. It indicates there exists an optimum thickness of buffer layer for the most efficient CO_2 reduction.

Figure 4.10a depicts the dependency of Faradaic efficiency of formate on the buffer layer thickness at cell potential range from -0.8 to -2 V. The full electrochemical cell was run with an un-adjusted 0.5 M Na_2SO_4 (pH = 6.8) as the electrolyte. The compartments of cathode and anode were supplied with CO_2 and H_2, respectively. The Faradaic efficiency of formate increased with the increasing of buffer layer thickness up to 2.9 mm at the same cell potentials. To clear present the trend of the dependence of Faradaic efficiency of formate on buffer layer thickness, the results at two cell potentials of -0.8 V and -2 V were extracted from **Figure 4.10a** and plotted in **Figure 4.10b**. The maximum Faradaic efficiency of formate reached 68% with 2.9 mm buffer layer at -0.8 V. No formate was produced in the cell with a buffer layer of thickness of 7.11 mm at -0.8 V. At -2.0 V, the peak Faradaic efficiency of formate was achieved at 90% in the cell with 2.9 mm buffer layer as well. The decreasing trend of Faradaic efficiency of formate at the buffer layer thickness > 2.90 mm was partly attributed to the decrease of authentic cathode potential. The thicker buffer layer caused more ohmic loss which resulted in the lower authentic cathodic potential.[30] **Figure 4.11** shows the ohmic resistance increased with the increase of buffer layer thickness. The difference in ohmic resistance between the thinnest (0.8 mm) and thickest (7.1 mm) buffer layers was as large as 10 Ω cm^2. The ohmic resistance as well as iR-corrected cathode potential versus buffer layer thickness was plotted in **Figure 4.12**. When the cell was operated at -2 V, the difference in the iR-compensated cathodic potentials became more substantial because of the high current density. The largest difference in cathodic potentials between the thinnest and thickest buffer layers was 0.40 V while the difference between the 2.9 mm buffer layer and 7.1 mm buffer layer was 0.33 V. However, when the cell was run at -0.8 V, the largest iR-compensated cathodic potential difference between the thinnest and thickest buffer layers was ~0.02 V because of low current density (< 2 mA cm^{-2}, see **Figure 4.10d**). It indicates there is the other major contribution to the decreasing of Faradaic efficiency of formate, which comes from the shortage of H^+ for protonation to form formate as thickness increases as discussed below.

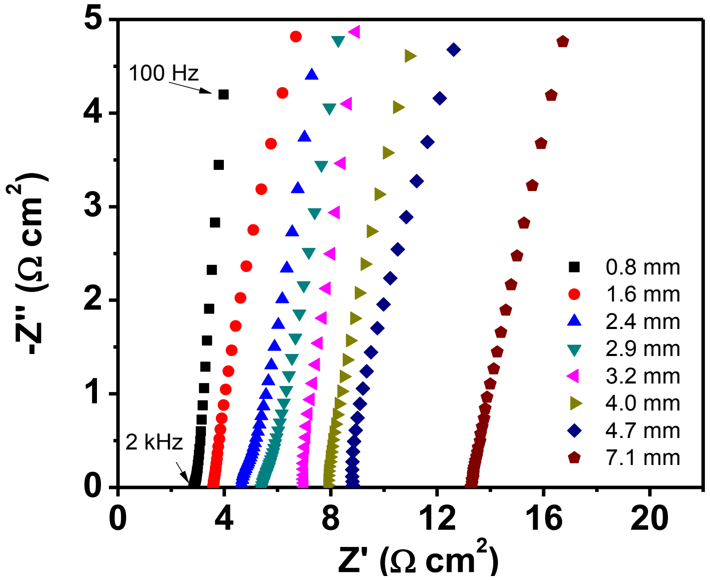

Figure 4.11. Internal ohmic resistance of the cells with different thicknesses of buffer layers. The impedance was measured at open circuit potential (OCV). The electrolyte was 0.5 M Na_2SO_4 (pH = 6.8). Ar and H_2 were purged to the cathode and anode compartment of the cell, respectively.

The Faradaic efficiency of formate increased by decreasing the iR-compensated cathodic potential (or increasing the buffer layer thickness) when the buffer layer is thinner than 2.9 mm. This is attributed to a stronger effect of H^+ concentration than cathode potential on CO_2 reduction. The H^+ concentration profile along the buffer layer thickness varies with the thickness. Operating with the thinnest buffer layer, H^+ needed the least time to transport from the anode to the cathode electrode/electrolyte interface. This resulted in the highest H^+ concentration at the interface which caused the dominance of H_2 evolution (**Figure 4.10c**). At a buffer layer thickness of 2.90 mm, a desirable H^+ concentration at the interface was achieved and consequently the protonation of C in $CO_2^{-}\cdot$ was promoted to form formate. With buffer layer thicker than 2.9 mm, the shortage of H^+ for protonation partly contributed to the lower Faradaic efficiency of formate. This contribution is more significant than that from decreasing cathode potential when operating at low cell potential, e.g. -0.8 V.

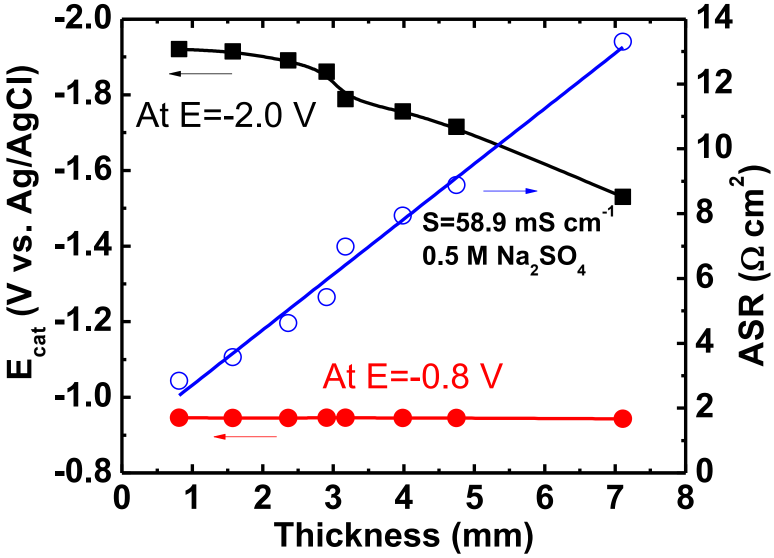

Figure 4.12. Ohmic resistance (extracted from Figure 4.11) as well as iR-corrected cathode potential versus buffer layer thickness.

The gas phase product of CO and by-product H_2 was also measured in-situ by GC during the cell running. No gas phase product of CO was detected at -0.8 V while CO was produced in a low yield at -2.0 V. **Figure 4.10c** plots the Faradaic efficiency of CO as a function of buffer layer thickness for cells running at -2.0 V, which has a similar behavior to formate. A maximum Faradaic efficiency of CO reached ~3.6% in the cell with a 2.9 mm buffer layer due to the contribution of protonation of O in $CO_2^{-}\cdot$.

4.3.5 Optimum Electrolyte pH

To further investigate the effect of H^+ concentration at the cathode surface on the selectivity towards CO_2 reduction, the full electrochemical cell was run with a pH adjusted 0.5 M Na_2SO_4 at the optimal buffer layer thickness of 2.9 mm. The pH of 0.5 M Na_2SO_4 was adjusted within the range of 1~10 by concentrated sulfuric acid or 1 M NaOH.

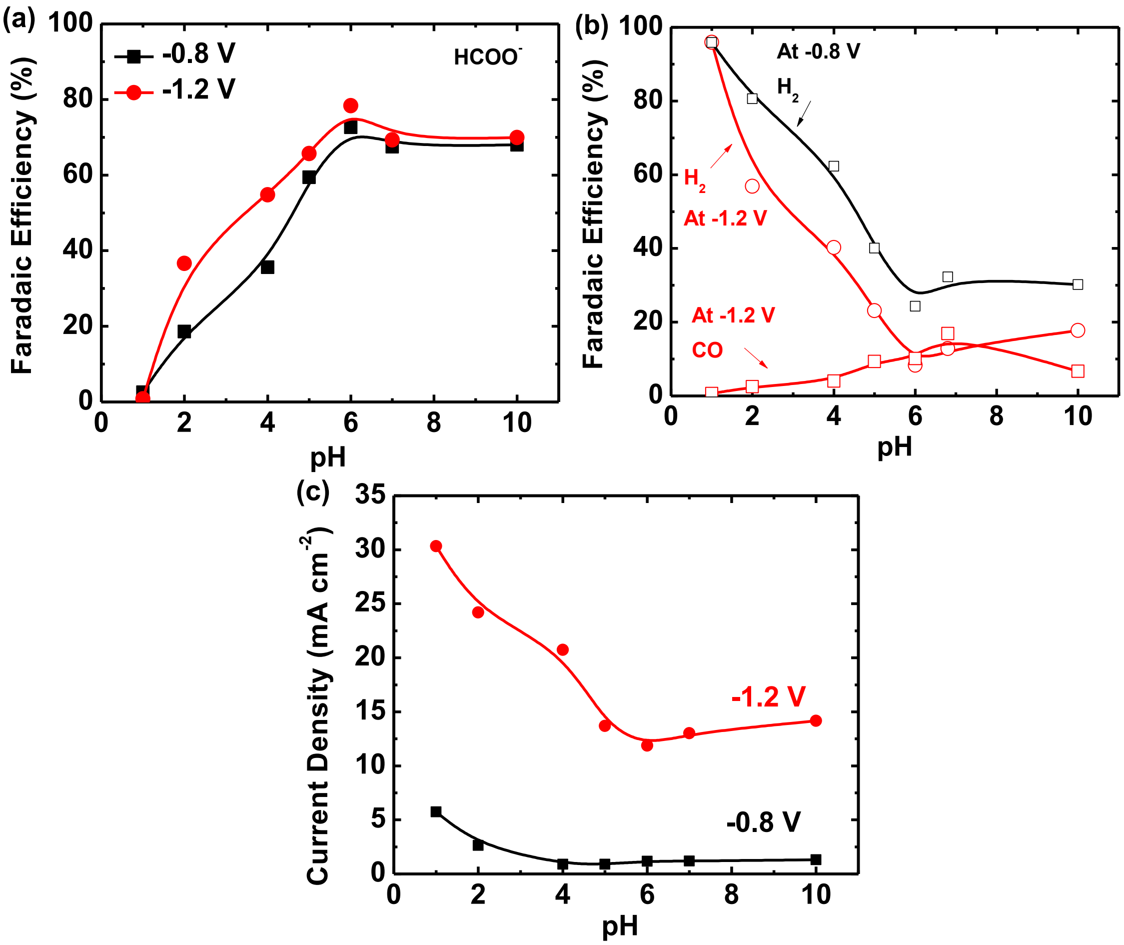

Figure 4.13. pH dependency of Faradaic efficiency towards formate production with the optimum buffer layer thickness of 2.9 mm. The anode and cathode were supplied with H_2 (150 ml min^{-1}), and CO_2 (45 ml min^{-1}), respectively, at p^o = 1.013 bar and T = 298.15 K.

According to Nernst equation, the apparent standard potential of CO_2 reduction shifts negatively and linearly with a slope of 0.0591 as the electrolyte pH increases. At the same cell potential, larger overpotential or driving force was applied to the Sn GDE with electrolyte of a lower pH compared to higher pH electrolyte. However, as shown in **Figure 4.13a**, the Faradaic efficiency of formate didn't increase in the order of increasing overpotential (or decreasing pH values of electrolyte). When using 0.5 M Na_2SO_4 with a pH =1, trace formate was detected at both potentials of -0.8 V and -1.2 V (**Figure 4.13a**). In contrast, the yield of H_2 evolution was as high as over 90% (**Figure 4.13b**), suggesting that electrolyte with pH = 1 provided excess H^+ under which H_2 evolution was the predominant reaction. Then upon increasing the pH of the electrolyte, the Faradaic efficiency of formate increased until reaching a peak at pH = 6. The peak Faradaic efficiency towards formate production was 73% and 78% at -0.8 V and -1.2 V, respectively. Afterwards, the Faradaic efficiency of formate dropped with further increasing of pH. No CO was produced over all pH values at -0.8 V. At -1.2 V, similar to the trend of Faradaic efficiency of formate with pH, the Faradaic efficiency for CO increased up to 17% at pH = 6.8 followed by a drop (**Figure 4.13b**). The results confirmed the stronger effect of H^+ at electrode/electrolyte interface on the selectivity towards CO_2 reduction than the potentials. **Figure 4.13c** shows the current density versus electrolyte pH. The trend of the current density with pH was consistent with that of H_2 yield. The current density exhibited the minimum at pH of around 6 because at which the H_2 evolution was suppressed.

4.3.6 Performance of Full cell with Optimum Operation Condition

The performance of the cell with the optimum buffer layer thickness of 2.9 mm and electrolyte pH of pH = 6 was investigated. The Faradaic efficiencies for the major products and total current densities are shown in **Figure 4.14**. The production of formate predominated over CO and H_2 at the whole potential range. The maximum Faradaic efficiency of formate reached over 90% at -2.0 V. A peak Faradaic efficiency of ~10% for CO production was obtained at potential of -1.2 V. A further evaluation of this optimal cell design was possible to calculate the energy efficiency of formate production. The energy efficiency results are displayed in **Figure 4.14a**. The highest energy efficiency of ~50% was obtained at -0.8 V. This maximum energy efficiency is slightly higher than the values achieved in the literatures (approximately 45%).[12, 13, 15] The energy efficiency decreased quickly as the cell potential (or current density) further increased due to increased ohmic loss in the cell. The current density increased as the cell potential shifted cathodically as shown in **Figure 4.14b**.

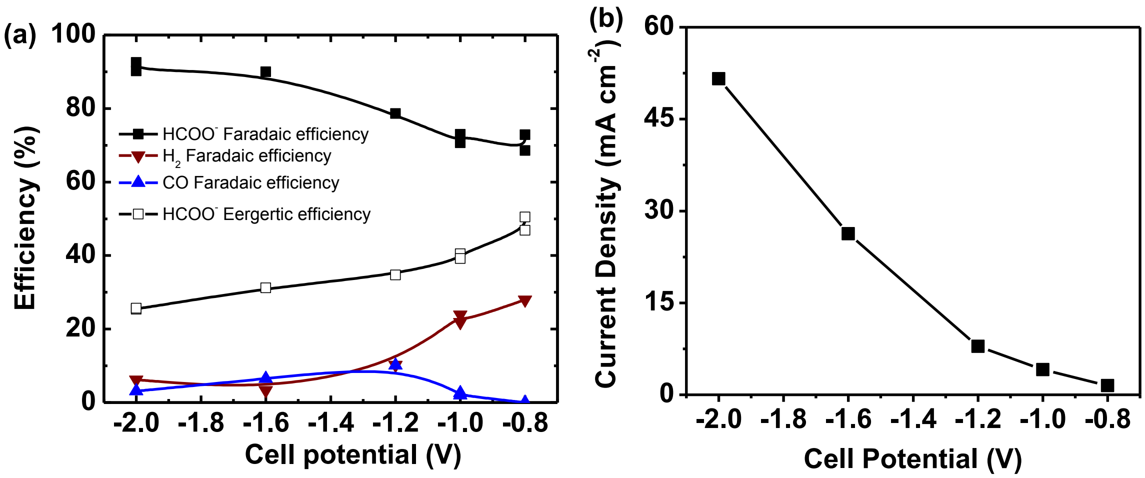

Figure 4.14. (a) Faradaic efficiency towards formate production and (b) polarization curve with the optimal buffer layer thickness of 2.9 mm and electrolyte pH of 6 (0.5 M Na_2SO_4). The anode and cathode were supplied with H_2 (150 ml min^{-1}), and CO_2 (45 ml min^{-1}), respectively, at $p^o = 1.013$ bar and T = 298.15 K.

By comparison, the performance of cells with a thinner (1.6 mm) and thicker (7.1 mm) buffer layer respectively was also measured with the electrolyte of pH = 6 in the same potential range of -0.8 ~ -2 V (**Figure 4.15**). The behavior of Faradaic efficiency of formate, CO and H_2 versus cell potential is similar to that in the optimal cell. However, in both cells with the 1.6 mm and 7.1 mm buffer layers, the evolution of H_2 predominates over CO_2 reduction, especially at low cell potentials. The peak energy efficiency of formate was obtained at -1.2 V and the magnitude was only ~22% and ~15% for 1.6 mm and 7.1 mm buffer layers, respectively.

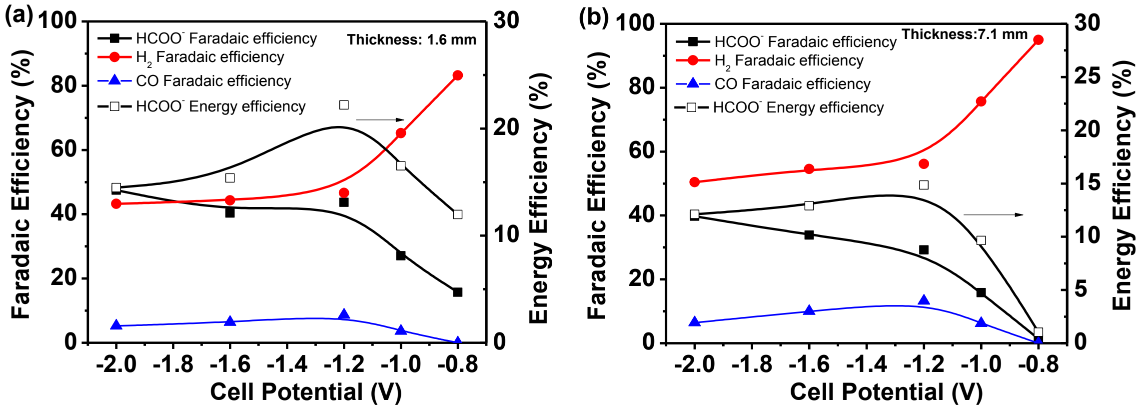

Figure 4.15. Faradaic efficiencies of $HCOO^-$, CO and by-product H_2 production in the cell equipped with a buffer layer at thickness of (a) 1.6 mm and (b) 7.1 mm. The electrolyte was pH adjusted 0.5 M Na_2SO_4 (pH = 6). The anode and cathode were supplied with H_2 (150 ml min^{-1}), and CO_2 (45 ml min^{-1}), respectively, at $p^o = 1.013$ bar and T = 298.15 K.

4.4 Conclusions

A full electrochemical cell with a PEMFC structure modified to include a buffer layer of circulating aqueous electrolyte is designed and assembled for the conversion of CO_2 to formate using a Sn GDE. In the presence of a buffer layer, the CO_2 reduction reaction dominates over hydrogen evolution reaction at the cathode, while hydrogen evolution reaction prevails in the absence of the buffer layer. Using this cell with a buffer layer of 0.1 M $KHCO_3$, at room temperature and ambient pressure, formate production is accomplished with high Faradaic (~90%) and energy efficiencies (~60%). Moreover, the formate starts to form at the overpotential of ~-0.2 V, irrespective of the fuel (H_2 or 1.0 M KOH) supplied to anode with the corresponding partial current density of ~-1 mA cm^{-2}. The highest partial current density for formate observed is ~-10 mA cm^{-2}, which can be increased by reducing ohmic resistance of the buffer layer and optimizing microstructures of the GDEs. The maximum formate concentration is ~100 μmol ml^{-1} at the end of 0.5 h electrolysis. An optimal buffer layer thickness of 2.90 mm and pH of 6 in electrolyte of 0.5 M Na_2SO_4 was observed for the highest yield of formate and CO in this full cell, which implies a stronger effect of H^+ concentration at the electrolyte/electrode interface on the selectivity towards target products from electrochemical reduction of CO_2. Under the optimum operation condition, the Faradaic efficiency of formate is 90% with 0.5 M Na_2SO_4 at -2 V which is similar to using 0.1 M $KHCO_3$, but the partial current density for formate increases to -45 mA cm^{-2}. This cell design employs current PEMFC configuration and thus can be easily scaled-up for the potential mass production of formate from CO_2, if the partial current density of formate can be increased to ~100 mA cm^{-2} at a moderate cell potential of -2.0 V.

References

1. Z. Zhan and L. Zhao, *J. Power Sources*, **195,** 7250-7254 (2010).
2. S. D. Ebbesen and M. Mogensen, *J. Power Sources,* **193,** 349-358 (2009).
3. S. H. Jensen, P. H. Larsen and M. Mogensen, *Int. J. Hydrogen Energy,* **32,** 3253-3257 (2007).
4. T.-J. Huang and C.-L. Chou, *Electrochem. Commun.*, **11,** 1464-1467 (2009).
5. T. Kim, S. Moon and S.-I. Hong, *Appl. Catal. A: General,* **224,** 111-120 (2002).
6. F. Bidrawn, G. Kim, G. Corre, J. T. S. Irvine, J. M. Vohs and R. J. Gorte, *Electrochem. and Solid-State Letters,* **11,** B167-B170 (2008).
7. R. L. Cook, R. C. MacDuff and A. F. Sammells, *J. Electrochem. Soc.,* **135,** 1470-1471 (1988).
8. R. L. Cook, R. C. Macduff and A. F. Sammells, *J. Electrochem. Soc.,* **137,** 187-189 (1990).
9. H. Li and C. Oloman, *J. Appl. Electrochem.,* **35,** 955-965 (2005).
10. H. Li and C. Oloman, *J. Appl. Electrochem.,* **36,** 1105-1115 (2006).
11. H. Li and C. Oloman, *J. Appl. Electrochem.,* **37,** 1107-1117 (2007).
12. C. Delacourt, P. L. Ridgway, J. B. Kerr and J. Newman, *J. Electrochem. Soc.,* **155,** B42-B49 (2008).
13. D. T. Whipple, E. C. Finke and P. J. A. Kenis, *Electrochem. Solid-State Lett.,* **13,** D109-D111 (2010).
14. E. Dufek, T. Lister and M. McIlwain, *J. Appl. Electrochem.,* **41,** 623-631 (2011).
15. S. R. Narayanan, B. Haines, J. Soler and T. I. Valdez, *J. Electrochem. Soc.,* **158,** A167-A173 (2011).
16. D. W. Dewulf and A. J. Bard, *Catal. Lett.,* **1,** 73-79 (1988).
17. Z. H. Duan, R. Sun, C. Zhu and I. M. Chou, *Mar. Chem.,* **98,** 131-139 (2006).
18. B. A. Rosen, A. Salehi-Khojin, M. R. Thorson, W. Zhu, D. T. Whipple, P. J. A. Kenis and R. I. Masel, *Science,* **334,** 643-644 (2011).
19. J. Wu, F. G. Risalvato, F.-S. Ke, P. J. Pellechia and X.-D. Zhou, *J. Electrochem. Soc.,* **159,** F353-F359 (2012).
20. N. Krstajić, M. Popović, B. Grgur, M. Vojnović and D. Šepa, *J. Electroanal. Chem.,* **512,** 16-26 (2001).
21. N. Krstajic, M. Popovic, B. Grgur, M. Vojnovic and D. Sepa, *J. Electroanal. Chem.,* **512,** 27-35 (2001).
22. O. Azizi, M. Jafarian, F. Gobal, H. Heli and M. G. Mahjani, *Int. J. Hydrogen Energy,* **32,** 1755-1761 (2007).
23. Aylmerke.Aw, A. Bewick, P. R. Cantrill and A. M. Tuxford, *Faraday Discuss.,* **56,** 96-107 (1973).
24. D. T. Whipple and P. J. A. Kenis, *J. Phy. Chem. Lett.,* **1,** 3451-3458 (2010).
25. S. Kapusta and N. Hackerman, *J. Electrochem. Soc.,* **130,** 607-613 (1983).
26. L. L. Snuffin, L. W. Whaley and L. Yu, *J. Electrochem. Soc.,* **158,** F155-F158 (2011).
27. R. P. S. Chaplin and A. A. Wragg, *J. Appl. Electrochem.,* **33,** 1107-1123 (2003).
28. M. Yagi, E. Tomita, S. Sakita, T. Kuwabara and K. Nagai, *J. Phys. Chem. B,* **109,** 21489-21491 (2005).

29. G. Beni, L. M. Schiavone, J. L. Shay, W. C. Dautremont-Smith and B. S. Schneider, *Nature,* **282,** 281-283 (1979).
30. D. van der Vliet, D. S. Strmcnik, C. Wang, V. R. Stamenkovic, N. M. Markovic and M. T. M. Koper, *J. Electroanal. Chem.,* **647,** 29-34 (2010).

Chapter 5

Stability of Sn Gas Diffusion Electrodes in the Full Electrochemical Cell: Degradation Mechanism and Mitigation Strategy

5.1 Introduction

There is an inherent trade-off between the electrocatalytic activity and the stability of electrocatalysts for CO_2 reduction similar to that encountered in the design of electrocatalysts for solid oxide fuel cell electrodes[1] and oxygen reduction reactions[2, 3]. This compromise was first revealed in Cu electrodes which were used to electrochemically reduce CO_2 to hydrocarbons like CH_4, C_2H_4 and alcohols in aqueous electrolytes.[4-6] The formation of CH_4 and C_2H_4 at the Cu electrode rapidly diminished after only 10 to 30 minutes from the start of CO_2 electrolysis. Several mechanisms were proposed as potential causes for this degradation. Black carbon intermediates formed during CO_2 reduction was considered as a potential poisoning product which would suppress the desired CO_2 reduction reaction.[5, 6] Some other authors agreed on the poisoning mechanism but presumed different intermediates like oxide or hydroxide were the cause of deactivation.[4, 7] The performance of these Cu electrodes was regenerated by applying anodic polarization. Other authors claimed that the accumulation of a soluble CO_2 reduction product, with unknown structure but with a very low vapor pressure, in the electrolyte caused a remarkable decrease in the selectivity of CO_2 reduction on copper electrodes.[8] Yet another, Hori et al[9] examined the deactivation of Cu electrode in detail on the basis of anodic stripping voltammetry and concluded that the deposition of Fe^{2+} and Zn^{2+} contaminants originally in the electrolyte prevented the further CO_2 reduction on the Cu electrode. So far the study of Cu electrode deactivation only focuses on the deposition of poisoning products while there was less effort making to investigate the change of electrode property.

Similar degradation of electrode performance was observed on Au, Ag and Sn for CO_2 reduction.[10-13] Sn has proved to be a promising electrocatalyst for CO_2 reduction, giving high yields of formate. However, the Faradiac efficiency towards formate production on Sn mesh electrode decayed rapidly to about 50% of the initial value after 100 min in a two-phase flowing cell.[12] The same rate of decline was observed for a Sn granule electrode in a fixed bed reactor.[13] So far no mechanism for the degradation of Sn electrodes has been proposed.

More research is required to better understand the deactivation mechanism of electrodes so that the approach can be developed to improve the lifetime of electrodes for CO_2 reduction. In this chapter, the stability of Sn gas diffusion electrode (GDE) consisting of nanometric scale Sn particles for CO_2 reduction was studied. The purpose of this research is to reveal the decay mechanism of selectivity towards CO_2 reduction on Sn GDEs when they are incorporated in the full electrochemical cell that has developed in chapter 4. Accompanying with monitoring the Faradaic efficiency towards target products formation the evolution of the micro-structure of the Sn catalyst layer was investigated in terms of Sn particle morphology, size, crystal structure and surface chemistry over long-term electrolysis of CO_2 reduction. This research is for the first time reporting pulverization of Sn particles along with its effect on the selectivity towards formate, CO, and H_2 production. Based on the exploration of the degradation mechanism, the mitigation strategy was developed to stabilize the Faradaic efficiency of target products by suppressing the pulverization.

5.2 Experimental

5.2.1 Long-term Electrolysis of CO_2 Reduction on Sn GDEs

The CO_2 reduction over long-term course was operated in the custom-designed full electrochemical cell as developed in chapter 4. The thickness of buffer layer was approximately 2.4 mm. The cathode was an optimized Sn GDE made up of 100 nm Sn particles with Sn loading of ~2 mg cm^{-2}. The full electrochemical cell was tested at a constant cell potential of -2.0 V controlled by a Solartron 1470E potentiostat/galvanostat. The individual electrode potential was monitored periodically with respect to the reference electrode Ag/AgCl in the buffer layer during cell operation. An a.c. impedance test was initiated before the stability test then again periodically throughout the stability test to monitor the ohmic resistance of the full electrochemical cell. The impedance measurement was performed at a constant cell potential of -0.8 V within the frequency range of 100 kHz~0.1 Hz by a Solartron 1255B frequency response analyzer connected to the Solartron 1470E potentiostat/galvanostat. The amplitude was set at 5% of the cell potential.

The conventional stability test was conducted with an electrolyte of 0.1 M $KHCO_3$ (Sigma Aldrich, ACS grade) circulating within the buffer layer at 7 ml min^{-1}. As a control, the full electrochemical cell was also tested with a pre-electrolyzed 0.1 M $KHCO_3$ which was purified overnight by a Pt foil (Alfa Aesar, 4×4 cm) working electrode at -2.5 V vs. Ag/AgCl in a traditional three-electrode cell. For both tests, the electrolyte was withdrawn for NMR analysis and periodically replaced with a fresh one.

5.2.2 Long-term Electrolysis of CO_2 Reduction on SnO_2 GDEs

The long-term electrolysis of CO_2 reduction was also conducted on SnO_2 GDEs which comprised of SnO_2 (Nano-Oxides, Inc.) with particle size 3-3.5 nm in order to suppress pulverization of catalyst particles. The SnO_2 GDEs had Nafion fraction of 20 wt.% and SnO_2 loading of ~2 mg cm^{-2}, which is the same as that of Sn GDEs. The CO_2 reduction on SnO_2 GDEs was operated under the condition analogy to that on Sn GDEs. To characterize the reduction of tin oxide, the cyclic voltammetry was conducted before and after long-term electrolysis between cell potential 0 and -2.7 V with a scan rate of 5 mV s^{-1}. The Ar was fed to the cathode when conducting cyclic voltammetry. The polarization curves were recorded periodically during the course of CO_2 reduction.

5.2.3 Dependence of the Intrinsic Activity and Selectivity on Sn Particle Size

The effect of Sn particle size on the intrinsic activity and selectivity was studied in a gas-tight traditional three-electrode cell. Sn particles with sizes of 40 μm (Alfa Aesar), 100 nm, 60 nm (US Research Nanomaterials, Inc.) and 5 nm were each employed for CO_2 reduction. The 5 nm Sn particles were pulverized from Sn particles initially at 100 nm after 40 hours of the cell operation. The catalyst ink, made of these Sn particles mixed into a solution of isopropanol and Nafion ionomer (5 wt%, Dupont) was sprayed onto a glassy carbon plate (1.6×0.5×0.3 cm) to be used as a working electrode. The Sn loading was maintained approximately at 2 mg cm^{-2}. Pt foil (3×3 cm) and Ag/AgCl (saturated KCl) served as counter and reference electrodes, respectively. The CO_2

reduction was conducted in the range between -1.6 and -2.0 V vs. Ag/AgCl and operated in a potentiostatic mode for 30 minutes at each potential.

5.2.4 Quantification of CO_2 Reduction Products

The gas-phase product was quantified by a gas chromatograph (GC) (Inficon Micro 3000 GC) as described previously. A GC run was initiated every 3 minutes in the first 10 min and then every 15 minutes during the rest of the stability test. The quantification of liquid-phase product in the electrolyte was accomplished periodically using a Varian Mercury/VX 400 MHz nuclear magnetic resonance (NMR) spectrometer.[14]

5.2.5 Physical Characterization

Transmission electron microscopy (TEM) images were taken in an H-9500 300 kV transmission electron microscope (Hitachi, Japan). Scanning electron microscopy (SEM) images and energy-dispersive X-ray spectra (EDS) were acquired with a Zeiss ultra plus thermal field emission SEM instrument (Carl Zeiss SMT AG, Germany). Powder X-ray diffraction (XRD) patterns were obtained with a Rigaku D/MAX2500 X-ray diffractometer. X-ray photoelectron spectra (XPS) were obtained with a Kratos AXIS Ultra DLD XPS microprobe equipped with a hemispherical energy analyzer and a monochromatic Al Kα source.

5.3 Results and Discussion

5.3.1 Pulverization of Sn Particles

During the long-term performance test, pulverization of 100 nm Sn particles was observed at cathode. **Figure 5.1** shows electron microscopy images of Sn GDE after different time intervals during the long-term operation. TEM images in **Figures 5.1a-f** clearly demonstrate the morphology and size evolution of Sn particles. The pulverization of Sn particles was observed first after 3 hours as indicated by the fracture of some of the originally spherical 100 nm particles into irregularly shaped 30-40 nm particles (**Figure 5.1a-b)**. Sn particles were pulverized to 20-30 nm after 7 hours (**Figure 5.1c)** and further to 4-5 nm after 15 hours (**Figure 5.1d**). Afterwards, only mild pulverization was observed. The particles were fractured to 3-4 nm after 30 hours (**Figure 5.1e**) and to ~3 nm after 42.5 hours (**Figure 5.1f**). After this point the pulverization became difficult and the size remained at 2.5-3 nm after 60 hours (**Figure 5.1g**). These pulverized Sn nanoparticles were eventually subjected to rapid oxidation to tin oxide as suggested by high magnification TEM image which shows the SnO_2 (110) crystal lattice (**Figure 5.1g)**.

Pulverization of Sn particles was verified by SEM of the Sn GDEs. **Figure 5.2a** shows a fresh Sn GDE. The SEM image clearly shows Sn particles with an approximate particle size of 100 nm which are connected by the dispersed Nafion ionomer network. The inset in **Figure 5.2a** is the EDS analysis, which shows only tin and no unwanted trace metals on the fresh Sn GDE. After 1 h of running, the Sn particles and Nafion network were mostly intact as shown in **Figure 5.2b**, but the EDS detected some deposition of Zn. The deposited Zn accounts for ~4.2wt.% referred to Sn. After 3 hours of running, the Sn particle pulverization could be observed, which is consistent with the TEM analysis. Smaller pulverized Sn particles were scattered on the surface of the larger Sn particles as seen in **Figure 5.2c**. The image also shows that the destruction of the Nafion ionomer network begins within the same time frame. After 24.5 hours the Sn particles were completely pulverized into smaller ones (**Figure 5.2d**). The smaller Sn particles appeared to aggregate together (**Figure 5.2e**) as the cell continues running for 60 hours. After 60 hours of operation the total deposition of Zn accounts for 5wt.% (**Figure 5.2f**).

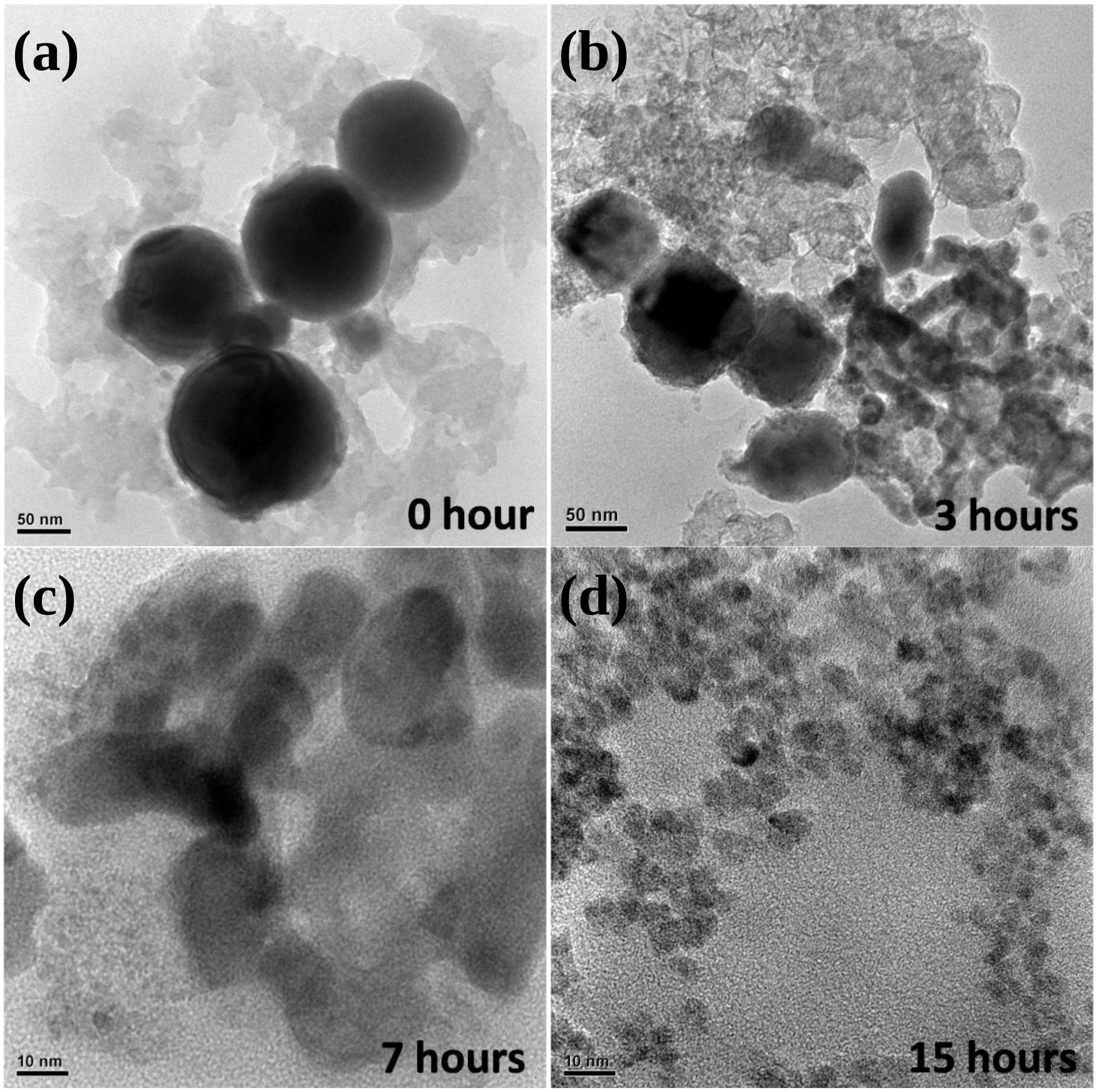

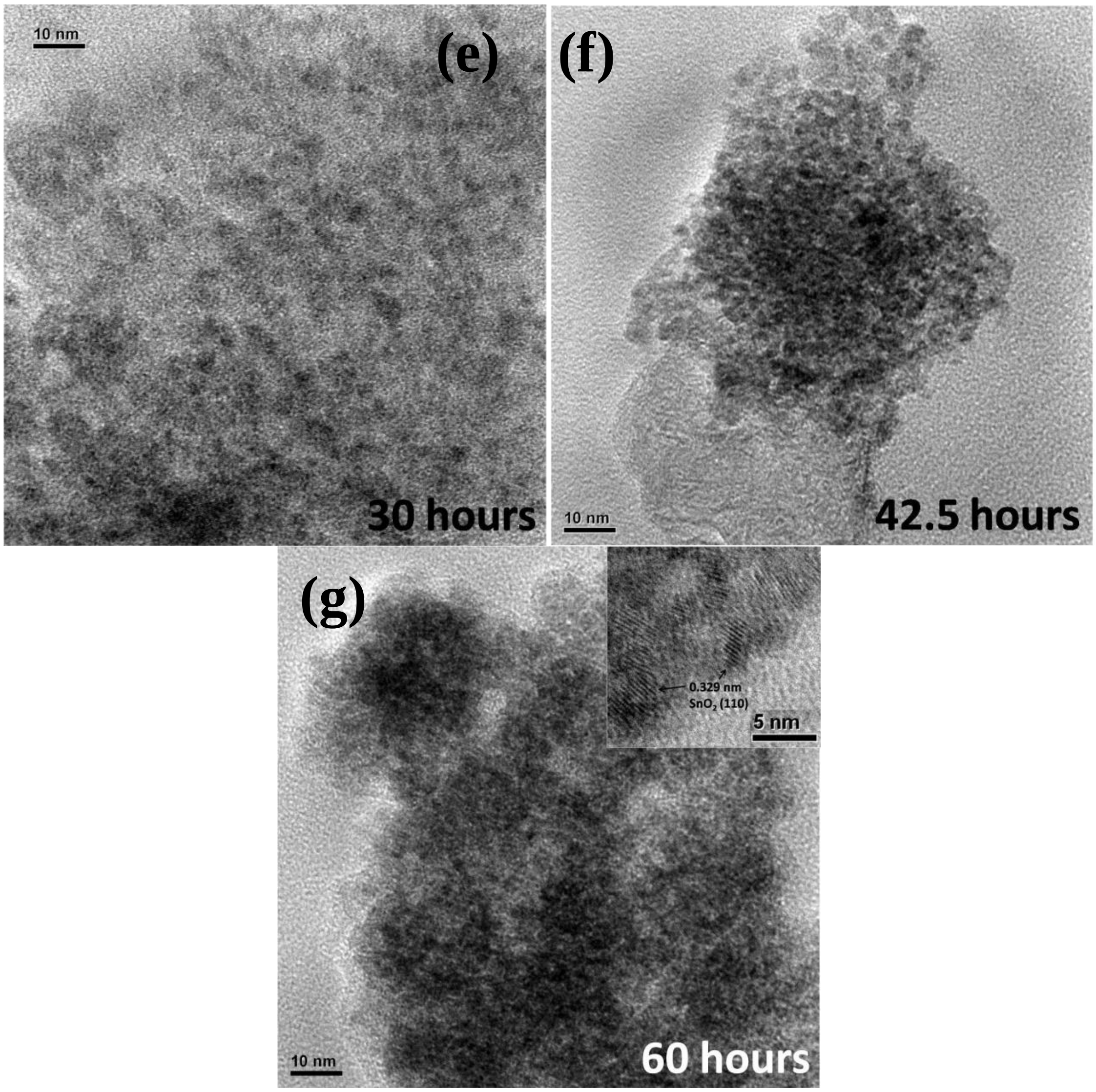

Figure 5.1. (a)-(g) TEM image of morphology and size evolution of 100 nm Sn particles during long-term operation. The inset of (g) shows the 3 nm Sn particle is readily oxidized into SnO_2.

The bulk structure of Sn GDEs after pulverization was further studied by XRD. Compared to the fresh Sn GDE, the intensity of diffraction peaks for metallic beta-Sn became weak while oxide peaks for SnO (101) and (200), and SnO_2 (101) and (200) appeared in the XRD pattern of Sn GDE after 60 hours operation **(Figure 5.3a)**, because most of the pulverized Sn particles were readily oxidized when exposed to the air, which is consistent with high magnification TEM results. The surface chemistry of Sn GDE before and after durability test was examined by XPS **(Figure 5.3b)**. The high-resolution Sn 3$d_{5/2}$ spectrum was fit to two peaks at 486.5 and 484.7 eV that correspond to $Sn^{4+/2+}$ (SnO_x) and Sn^0, respectively.[15] For a fresh Sn GDE, the atomic ratio of the corrected peak areas for SnO_x and Sn^0 was 94:6, indicating the presence of a ~5 nm native SnO_x layer around the Sn particles.[16, 17] After testing for 60 hours, the XPS spectrum exhibited a SnO_x : Sn^0 ratio of 98:2, indicating an increased thickness of SnO_x layer, covering the surface of Sn GDE.

The pulverization of Sn particles occurs because of the tension stresses introduced by hydrogen diffusion.[18] The hydrogen transfer process in the Sn electrode can be expressed as follows:[19]

1. electrosorption-desorption of hydrogen at the solid phase:

   $Sn + H^+ + e^- \leftrightarrow SnH_{ads}$ (Volmer reaction) (5.1)

2. hydriding-dehydriding of the solid-phase (solid state transfer of hydrogen):

   $SnH_{ads} \leftrightarrow SnH_\alpha$ (solid solution) (5.2)

   $SnH_\alpha \leftrightarrow SnH_\beta$ (Sn hydride) (5.3)

3. evolution of molecular hydrogen:

   $2SnH_{ads} \leftrightarrow 2Sn + H_2$ (Tafel reaction) (5.4)

   $2SnH_{ads} + H_2O + e^- \leftrightarrow 2Sn + H_2 + OH^-$ (Heyrovsky reaction) (5.5)

The hydrogen ion adsorbs onto the electrode surface to generate hydrogen ad-atom by an initial charge transfer step (Eq. 5.1). Due to slower kinetics of chemical and/or electrochemical recombination steps resulting in hydrogen evolution (Eq. 5.4 and 5.5), most of the hydrogen ad-atoms diffuse into the bulk of solid phase, forming a solid solution in the host lattice (SnH_α phase, Eq. 5.2). This hydrogen diffusion induces stress driving the fracture of Sn particles. In addition on attainment of a certain limiting concentration of hydrogen, a metal hydride (SnH_β phase, Eq. 5.3) starts to develop. The Sn hydride further escapes as gas or decomposes as Sn metallic dendrites which also results in the pulverization of Sn particles.

Similar pulverization of Sn anode has also been observed during charge-discharge cycle of a Li-ion battery due to Li^+ insertion and extraction.[20-23] Pulverization occurs until the particle reaches a critical size where the strain induced by ion insertion and extraction is compensated by the increased surface free energy of the pulverized particles.[18, 24, 25] In our case, pulverization almost ceased when the particle size reached 3-4 nm after ~42.5 hours of operation.

The control experiments were done to rule out the effect of reactant CO_2 and cell potential on the Sn particle pulverization. For the former effect, the reactant CO_2 was replaced with an inert gas He. A 0.1 M Na_2SO_4 was employed as the electrolyte instead of 0.1 M $KHCO_3$ with the purpose of eliminating the involvement of dissolved CO_2 which has equilibrium with HCO_3^-. This setup was run for 42.5 hours at -2 V. High magnification SEM images were taken after the run as shown in **Figure 5.4a**. The image shows that there is clearly Sn particle pulverization and the smaller particles have aggregated together. In order to verify the effect of cell potential on particle pulverization, two different long term samples were run under standard operating conditions. One of the tests was run at -0.8 V, a relatively low potential compared to -2 V. The purpose was to see if lowering the potential had any effect on pulverization. The image in **Figure 5.4b** shows that Sn particles were pulverized as extensively as in the test of -2.0 V after 42.5 hours.

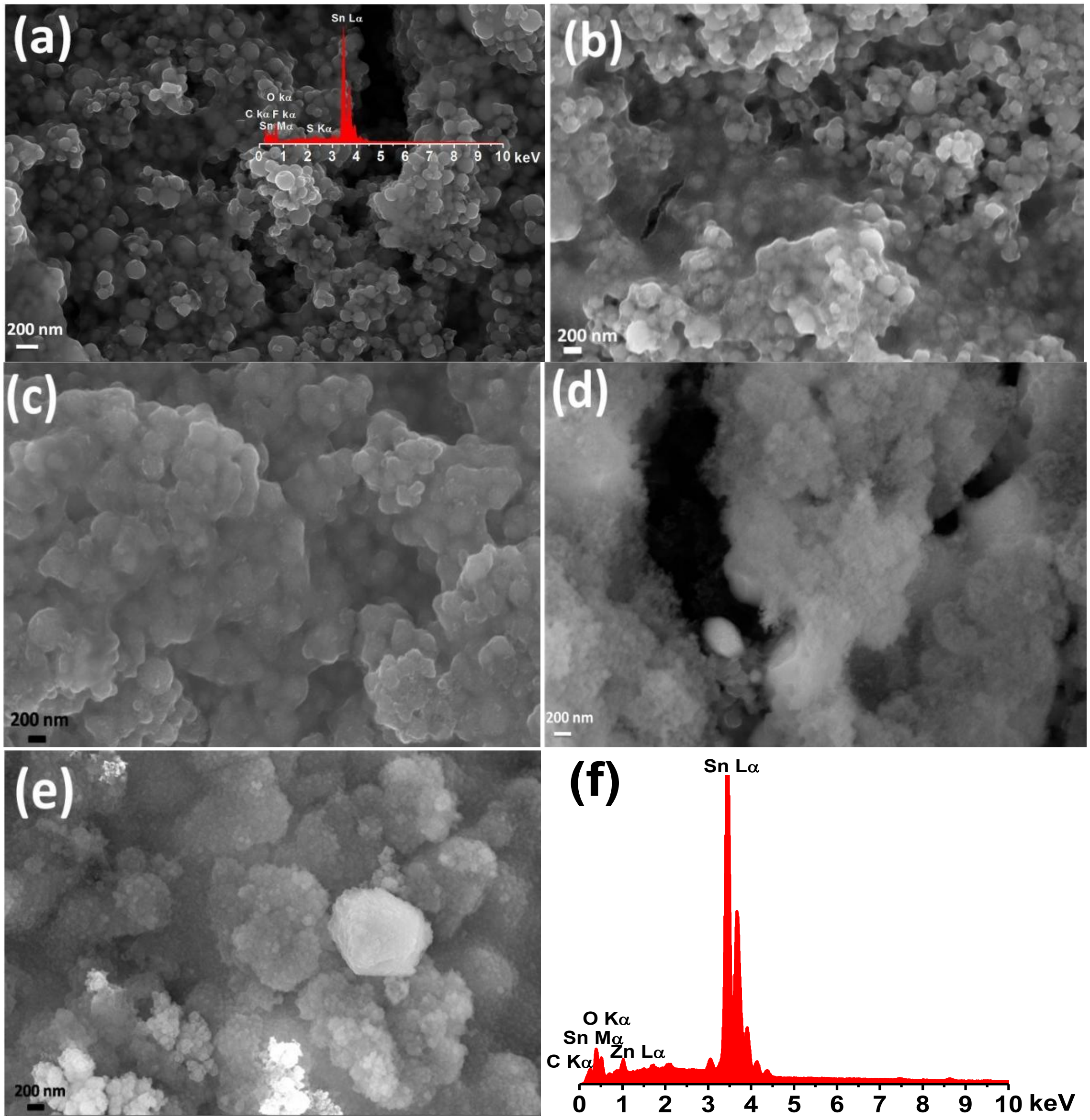

Figure 5.2. SEM images of Sn GDE after standard running for (a) 0 h, (b) 1h, (c) 3h, (d) 24.5 h, (e) 60 h, and (f) EDS of Sn GDE sample after 60 h running.

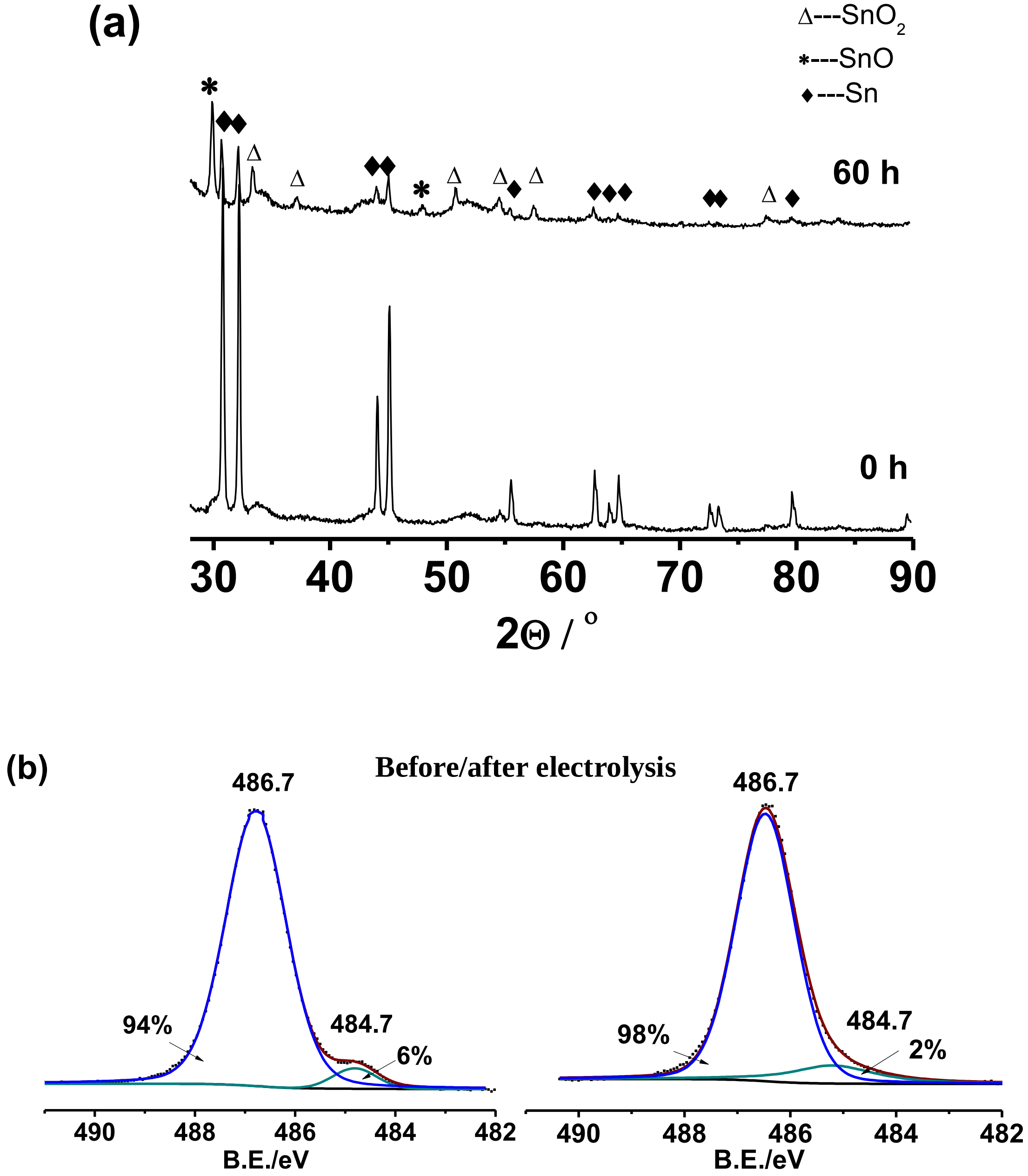

Figure 5.3. (a) XRD patterns and (b) XPS analysis of Sn GDEs before and after electrolysis for 60 hours.

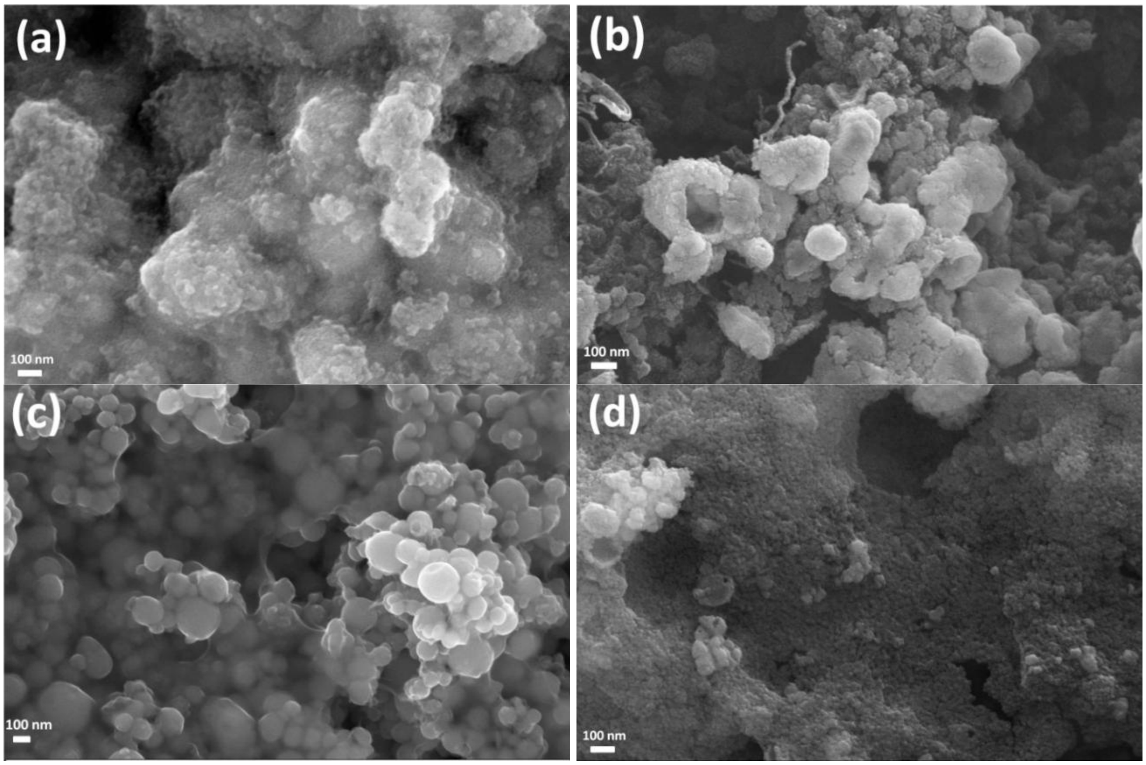

Figure 5.4. SEM images of the Sn GDE after the controlled running for 42.5 hours. (a) sample after running with H_2/He at potential of -2 V, (b) sample after running with H_2/CO_2 at potential of -0.8 V, (c) edge Sn GDE sample after running with H_2/CO_2 at potential of -2 V, (d) center Sn GDE sample after running with H_2/CO_2 at -2 V.

A Sn GDE with an area larger than the active buffer layer was used in another test. The test was run at -2 V for 42.5 hours. SEM images were taken of both samples from the edge and center of the Sn electrode. The sample from the edge was not in contact with the electrolyte and thus no electrochemical reactions occurred, while the sample at the center catalyzed CO_2 reduction. The purpose of the test was to isolate the effect that potential itself has on the pulverization of particles. The SEM image in **Figure 5.4c** shows that no pulverization occurred to the Sn particles on the electrode edge over the course of the test. However, the sample from the center of the Sn GDE as shown in **Figure 5.4d** suffers from severe pulverization as mentioned earlier.

These two runs indicate that the pulverization of Sn particles happens only when electrochemical reactions occur on the Sn GDE. The adsorbed hydrogen atom insertion/extraction accompanying CO_2 reduction or H_2 evolution is the primary cause of Sn particle pulverization.

One more control experiment was conducted without the buffer layer of aqueous electrolyte to confirm the hydrogen atom insertion/extraction induced stress resulted pulverization. This setup excludes the possibility of Sn dissolution and re-deposition by reacting with OH^- in the aqueous electrolyte. After running for 50 hours at -14 mA cm^{-2} similar to that under standard operation, the Sn particles were pulverized clearly as shown in the SEM of image of **Figure 5.5**.

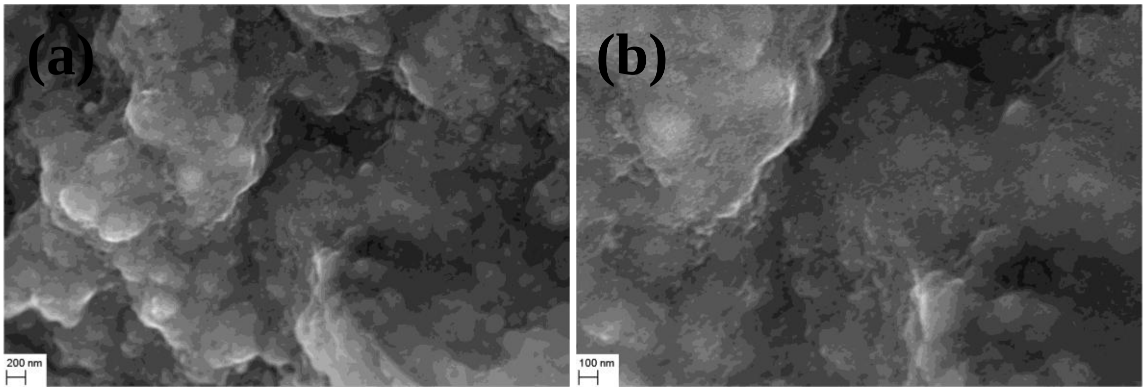

Figure 5.5. SEM images of the Sn GDE after the controlled running for 50 hours at -14 mA cm^{-2} in a full cell without the buffer layer. (a) Low magnification and (b) high magnification.

5.3.2 Selectivity towards CO_2 Reduction

Throughout the performance test, the selectivity and activity towards the production of formate and CO were quantified periodically. The total catalytic activity indicated by the total current density was generally stable over the period of 60 hours as shown in **Figure 5.6a**. The average total current density was ~17 mA cm^{-2} at applied cell potential of -2 V. In contrast, the selectivity varied towards the production of formate, CO, and the by-product H_2 during the long-term operation as shown in **Figure 5.6b**. Specifically, the Faradaic efficiency towards formate production decreased from 90% to

81% at an average rate of ~0.9% hr^{-1} during the first 10 hours. Thereafter, the Faradaic efficiency towards formate production degraded slowly at an average rate of ~0.5% hr^{-1}, reaching 56% after 60 hours. The Faradaic efficiency of CO increased from 3% at the start of electrolysis to a maximum of 14% over the course of first 20 hours followed by a slow decline to 7% after 60 hours. In contrast, the Faradaic efficiency towards H_2 evolution increased monotonically from initial 3% to 31% over the entire period of 60 hours.

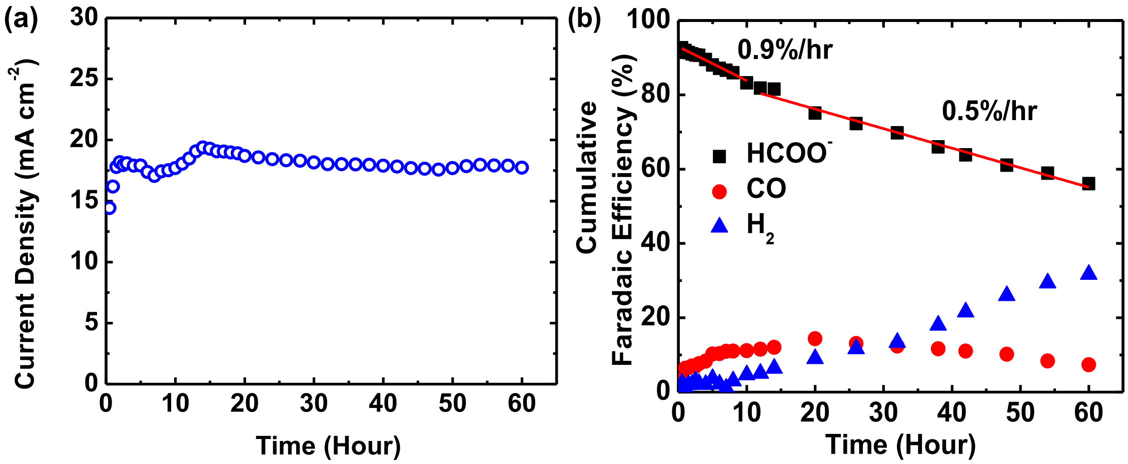

Figure 5.6. (a) Recorded total current density and (b) Faradaic efficiency towards production of formate, CO and H_2 over the test course of 60 hours in as-received 0.1 M $KHCO_3$. The cathode and anode compartment was supplied with CO_2 at 45 ml min^{-1}and H_2 at 150 ml min^{-1}, respectively, at room temperature and ambient pressure. The 0.1 M $KHCO_3$ solution was pumped to the buffer layer at 7 ml min^{-1}.

A similar stability test was also conducted using a pre-electrolyzed electrolyte in order to rule out the trace metal contamination as a cause of degradation in the selectivity. With the purified electrolyte, no trace metal depositions such as Zn^{2+}, Fe^{2+} on the surface of Sn GDE were detected by EDS at the end of 60 hours electrolysis. In this condition, the total current density was maintained at ~18 mA cm^{-2} at -2 V over 110 hours (**Figure 5.7a**). Moreover, as shown in **Figure 5.7b**, similar trends in selectivity towards formate, CO and H_2 were obtained as compared to the as-received electrolyte. The degradation of formate slowed down and trended to a steady state of ~45% after 60 hours. **Figure 5.8a and 5.8b** show the low and high magnification SEM images of the Sn GDE after running for 60 hours in pre-electrolyzed electrolyte of 0.1 M $KHCO_3$, respectively. The Sn particles are pulverized after 60 hours as in as-received electrolyte. The results suggest that pulverization accounts for the loss of selectivity towards CO_2 reduction.

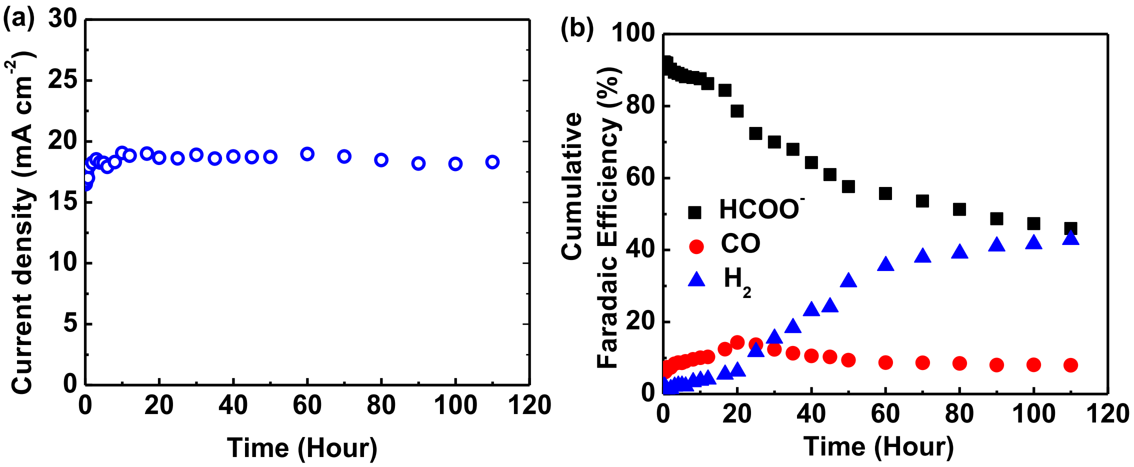

Figure 5.7. (a) Recorded total current density and (b) Faradaic efficiency towards production of formate, CO and H_2 over the test course of 110 hours in pre-electrolyzed 0.1 M $KHCO_3$. The cathode and anode compartment was supplied with CO_2 at 45 ml min^{-1}and H_2 at 150 ml min^{-1}, respectively, at room temperature and ambient pressure. The 0.1 M $KHCO_3$ solution was pumped to the buffer layer at 7 ml min^{-1}.

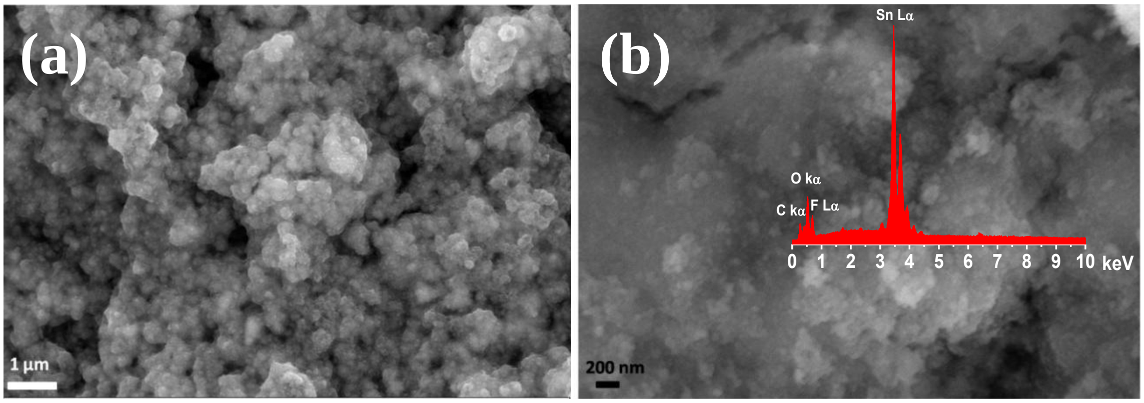

Figure 5.8. (a) Low magnification and (b) high magnification SEM images of a conventional Sn GDE after long-term running for 60 h in a pre-electrolyzed electrolyte. The inset in (b) is the EDS of GDE.

5.3.3 Correlation between Sn Particles Pulverization and Selectivity Degradation

Sn particles pulverization was hypothesized as the primary cause of degradation of selectivity towards CO_2 reduction. To support this hypothesis, the dependence of the intrinsic activity and selectivity towards CO_2 reduction on Sn particle size was firstly studied. **Figure 5.9a** shows the trend in Faradaic efficiency of formate and CO versus potential for different electrodes consisting of 5 nm, 60 nm, 100 nm and 40 µm Sn particles. The selectivity for CO and formate formation increased with decrease in the particle size. The Sn electrode with 5 nm pulverized Sn particles exhibited the highest Faradaic efficiency towards CO and formate production. In addition, the electrode with 5 nm pulverized Sn particles showed a comparable total current density to the 60 and 100 nm particles while Sn particles of 40 µm demonstrated the lowest total current density which was averaged over 30 minutes electrolysis (**Figure 5.9b**). These results show no intrinsic loss in the activity or selectivity of the pulverized particles compared to 100 nm fresh particles. The observed degradation in the Sn GDE must therefore be attributed to other factors.

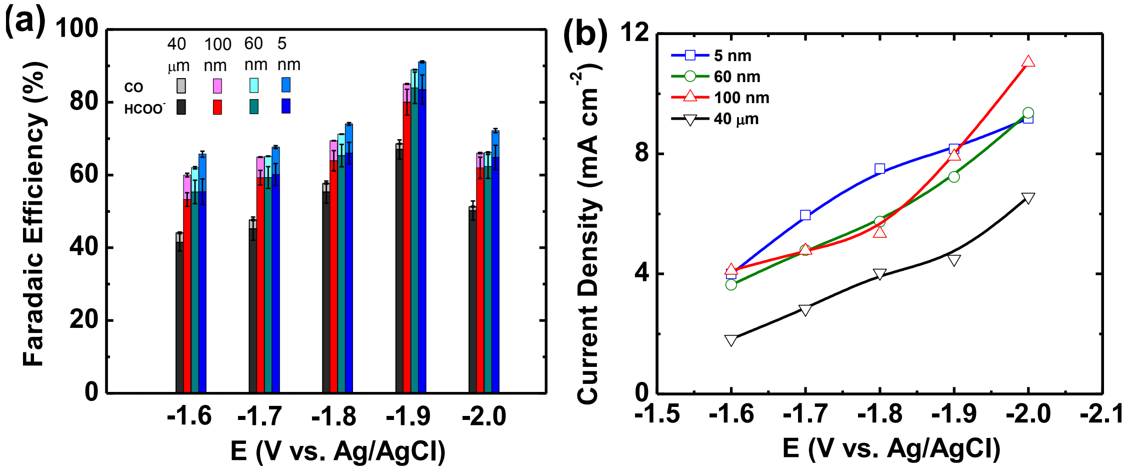

Figure 5.9. The effect of Sn particle size on the activity and selectivity towards formate and CO formation. (a) Faradaic efficiency towards formate and CO formation, and (b) total current density as a function of potential.

Particles pulverization has a significant impact on ohmic loss, and this was investigated as another potential factor for degradation. Sn particles pulverization causes the loss of electrical contact between the Sn particles and carbon substrate (decreasing the contact area) leading to difficulty of electron transportation.[26] As a result, an increase in area specific resistance (ASR) of the full electrochemical cell was observed (**Figure 5.10a**) during long term cell operation in the pre-electrolysis electrolyte. The ASR increased by 49% from an initial value of 22.7 Ω cm^2 to 33.7 Ω cm^2 after 60 hours due to Sn particle pulverization**.**[20, 27] After that, the ASR increasing rate became smaller which may be due to the fact that Sn particles pulverized close to critical size. The ASR increased to 35.6 Ω cm^2 after 110 hours. The increase in ASR resulted in the decrease of authentic iR-corrected cell potential (**Figure 5.10b**). As a consequence, both the iR-compensated cathode and anode potentials decreased as the test time elapsed (**Figure 5.10c**). The cathode potential decreased rapidly in the first 5 h corresponding to a sharp increase of ASR. Afterwards, the cathode potential declined more slowly, reaching -1.54 V vs. Ag/AgCl after 60 hours and -1.48 V vs. Ag/AgCl after 110 hours compared to -1.80 V vs. Ag/AgCl initially. For the case of a fresh Sn GDE, cathode potential of -1.54 V vs. Ag/AgCl corresponds to a cell potential of -1.3 ~ -1.4 V at which the observed Faradaic efficiency for formate and CO is ~60% and 10%, respectively, which is close to that after 60 hours running. Thus, the decrease of authentic cell potential (or cathode potential) mainly accounted for the decrease in selectivity towards CO_2 reduction, especially formate production.

Additonally, pulverization leads to a non-uniform distribution of Nafion as seen from the comparison between **Figures 5.2a** and **5.2e**. This reduced the contact surface area between Nafion and Sn particles. Thus, the triple-phase (proton/electron/gas) boundary length was reduced which in sequence partly contributed to the decline of selectivity towards CO_2 reduction. The current density remains stable due largely to the compensation of increased surface area of catalyst particles after pulverization to the decreased electrode potential.

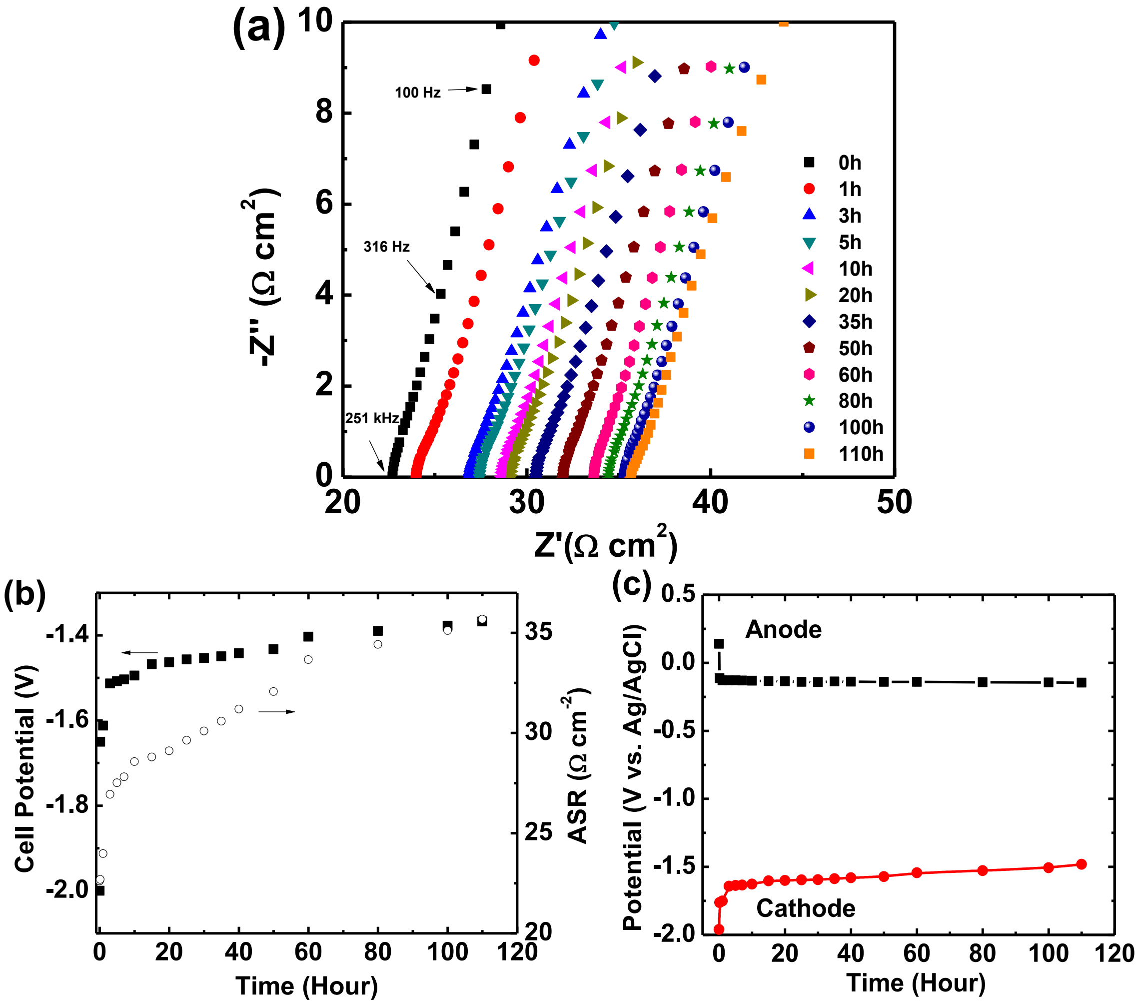

Figure 5.10. (a) in-situ EIS of the full electrochemical cell, (b) deceasing iR-compensated total cell potential and increasing ohmic resistance, and (c) decreasing iR-compensated cathode and anode potential during the long-term operation.

5.3.4 Mitigation of Degradation of Selectivity towards CO_2 Reduction

With the observation that the pulverization was mitigated when the particle was cracked down to have the critical size, SnO_2 nanoparticles with the mean particle size of

3.5 nm were employ as catalyst for CO_2 reduction. SnO_2 nanoparticles were chosen because Sn nanoparticles of 3.5 nm hardly exist in the atmosphere due to its ready oxidization when exposed to the air. Sn particles of 100 nm have been characterized to have a ~3.5 nm oxide scale by TEM and XPS (data can be seen in Chapter 6).

The XRD pattern of SnO_2 nanoparticles in **Figure 5.11** shows broad diffraction peaks of (110), (101), (211) and (112). The crystallite size is calculated about 2 nm based on the full width at the half maximum of peak (110) according to Scherrer equation. [28]

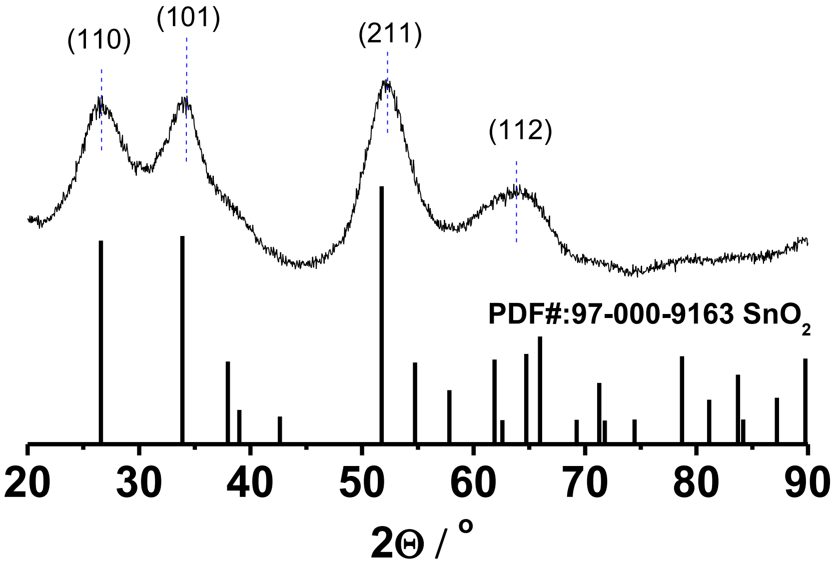

Figure 5.11. XRD pattern of SnO_2 nanoparticles.

Figure 5.12a and 5.12b show the TEM images of fresh polycrystalline SnO_2 nanoparticles with size of about 3.5 nm. After continuous running for 174 hours, the particle size maintained at about 3.5 nm and no pulverization was observed as shown in **Figure 5.12c and 5.12d**. The disappearance of SnO_2 reduction peaks in the cyclic voltammetry (**Figure 5.13**) after electrolysis indicates the reduction of SnO_2 during the electrolysis in the reaction depth. At the end of electrolysis, the SnO_2 electrode was taken out to run the XRD immediately. The diffraction peaks corresponding to Sn (200) and (101) appeared in the XRD pattern, confirming the reduction of SnO_2 to Sn (**Figure**

5.14). It’s interesting that the diffraction peaks of Sn reduced from SnO_2 shows sharp rather than broad. There still existed broad peaks of SnO_2 (101) and (211) from the bottom of the electrodes suggesting the reduction of SnO_2 nanoparticles was limited by the reaction depth. The reduced Sn will be re-oxidized to form SnO_2 when exposed to air as shown in the selected area electron diffraction (inset in Figure 5.12c) and high resolution TEM images (inset in Figure 5.12d) .

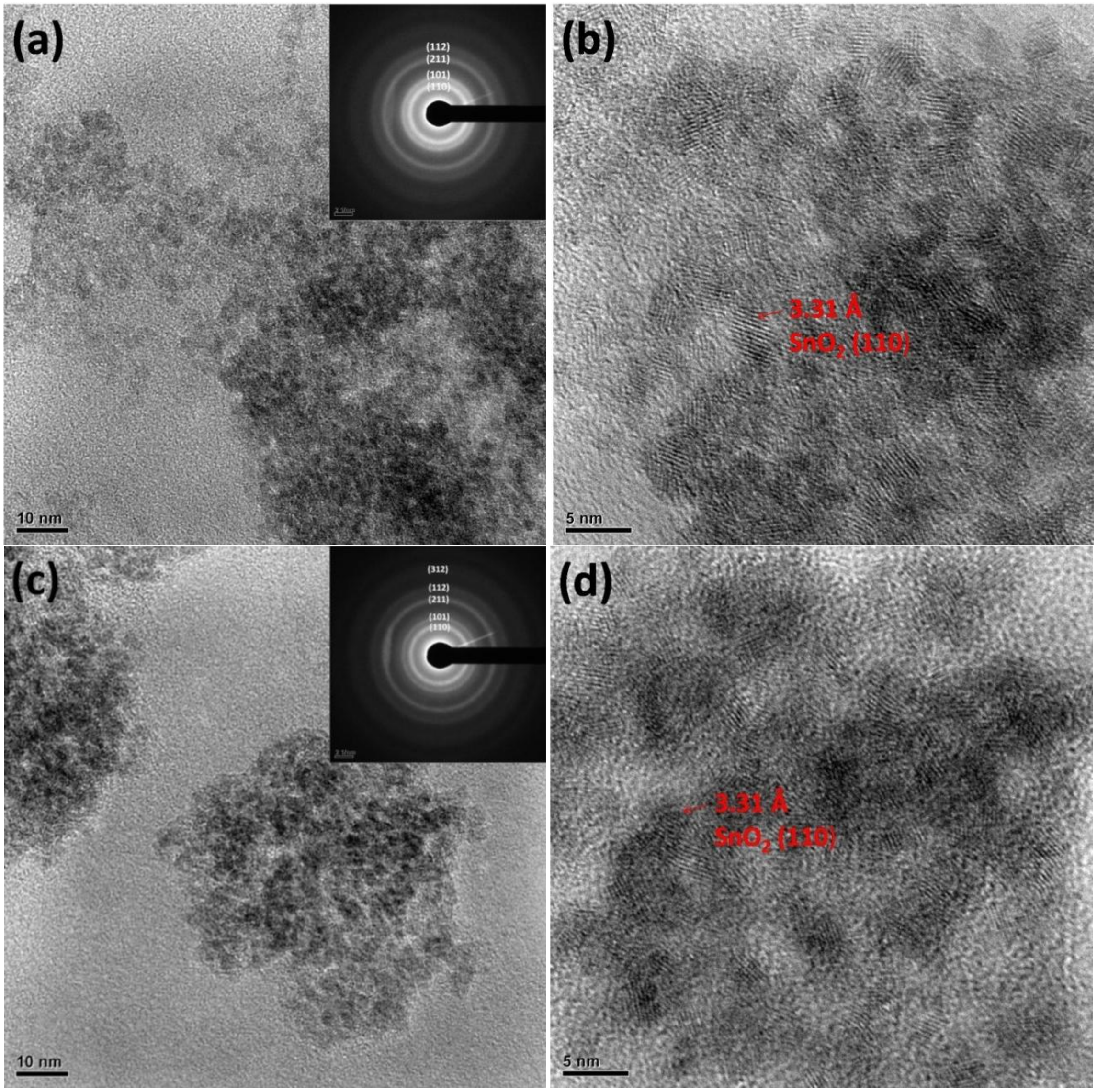

Figure 5.12. TEM images of SnO_2 nanoparticles. (a) and (b) fresh SnO_2 nanoparticles , and (c) and (d) after operation for 174 hours. The insets in (a) and (c) are SAED of SnO_2 nanoparticles.

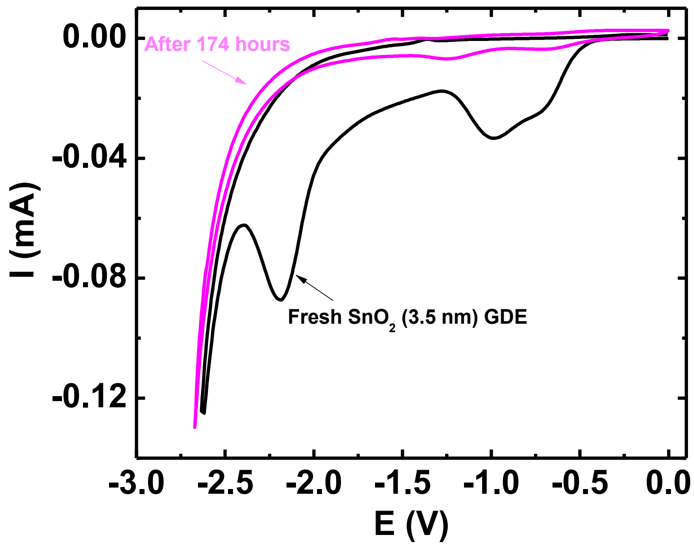

Figure 5.13. Cyclic voltammetry of the SnO_2 GDEs before and after electrolysis.

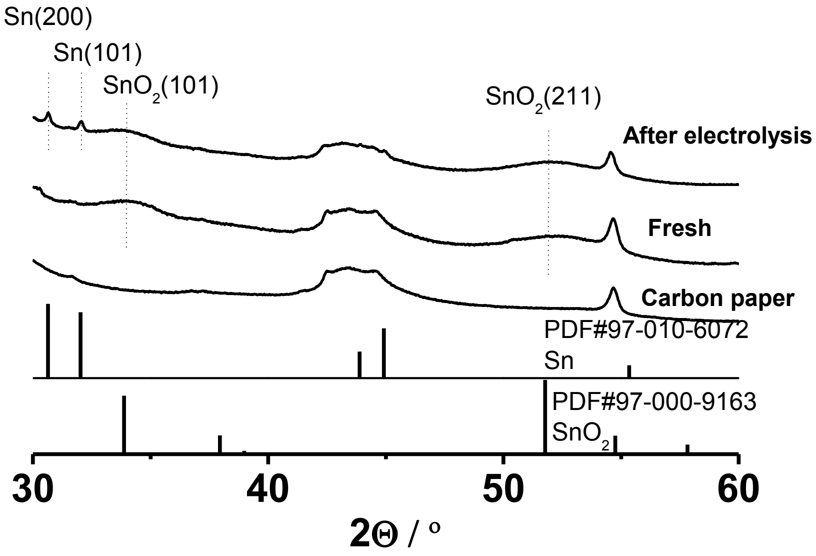

Figure 5.14. XRD pattern of SnO_2 GDE before and after operation for 174 h.

The Faradaic efficiencies of CO and $HCOO^-$ for SnO_2 GDEs were monitored periodically during the long-term test (**Figure 5.15a**). The Faradaic efficiencies of CO and $HCOO^-$ experienced a pulse in the first 3~6 hours, which might result from the reduction of SnO_2 to Sn accompanying with CO_2 reduction. The Faradaic efficiencies of CO and $HCOO^-$ firstly increased with the reducing of SnO_2 to Sn, and then dropped because of the further increasing of Sn clusters resulted from oxide reduction, which promotes the hydrogen evolution as will be discussed in detail in next chapter. After total reduction of SnO_2 to Sn within the reaction depth, the Faradaic efficiencies of CO and $HCOO^-$ stabilized at 6% and 70%, respectively. The current density maintained at about 12-13 mA cm^{-2} over 174 hours (**Figure 5.15b**). The i-V polarization curves recorded during the electrolysis course at different time confirmed the stability of the current density (**Figure 5.16**).

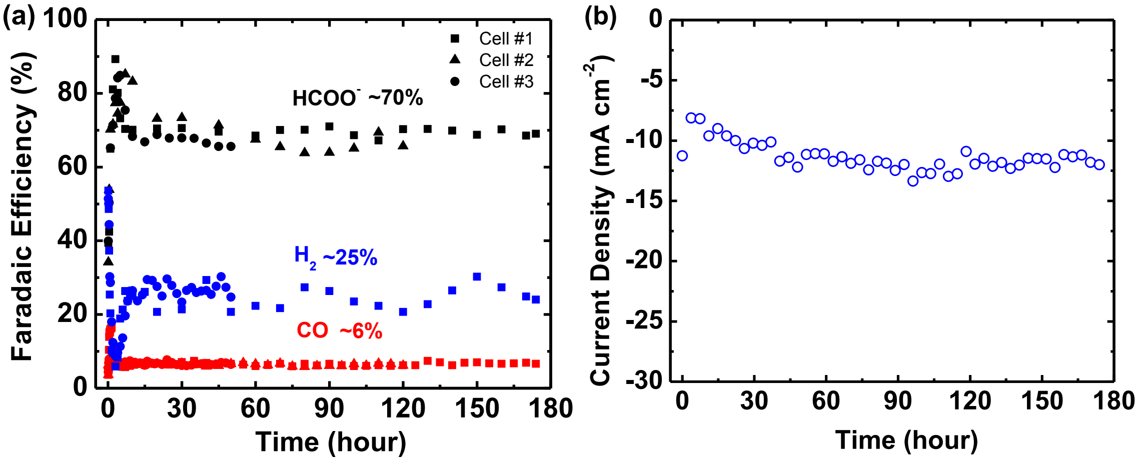

Figure 5.15. (a) Faradaic efficiency of CO, $HCOO^-$ and H_2, and (b) current density versus time. The cell was operated at -2 V with as-received 0.1 M $KHCO_3$.

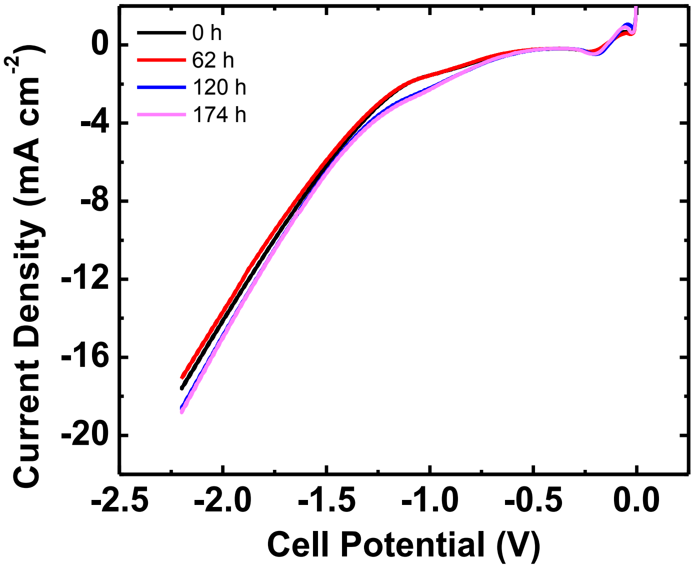

Figure 5.16. i-V polarization curves of SnO_2 GDE during the long-term durability test.

The improved stability of performance for SnO_2 GDE was primarily attributed to the prevention of pulverization. Without the pulverization, the cell ohmic resistance increased slightly from 22.5 Ω cm^2 initially to 25.2 Ω cm^2 after 174 hours (**Figure 5.17a and 5.17b**). In contrast, the cell ohmic resistance increased sharply from 22.5 Ω cm^2 initially to 35.6 Ω cm^2 after 110 hours when using easily-pulverized Sn particles of 100 nm. Moreover, the cathode potential stabilized at -1.88 V vs. Ag/AgCl (**Figure 5.17c**).

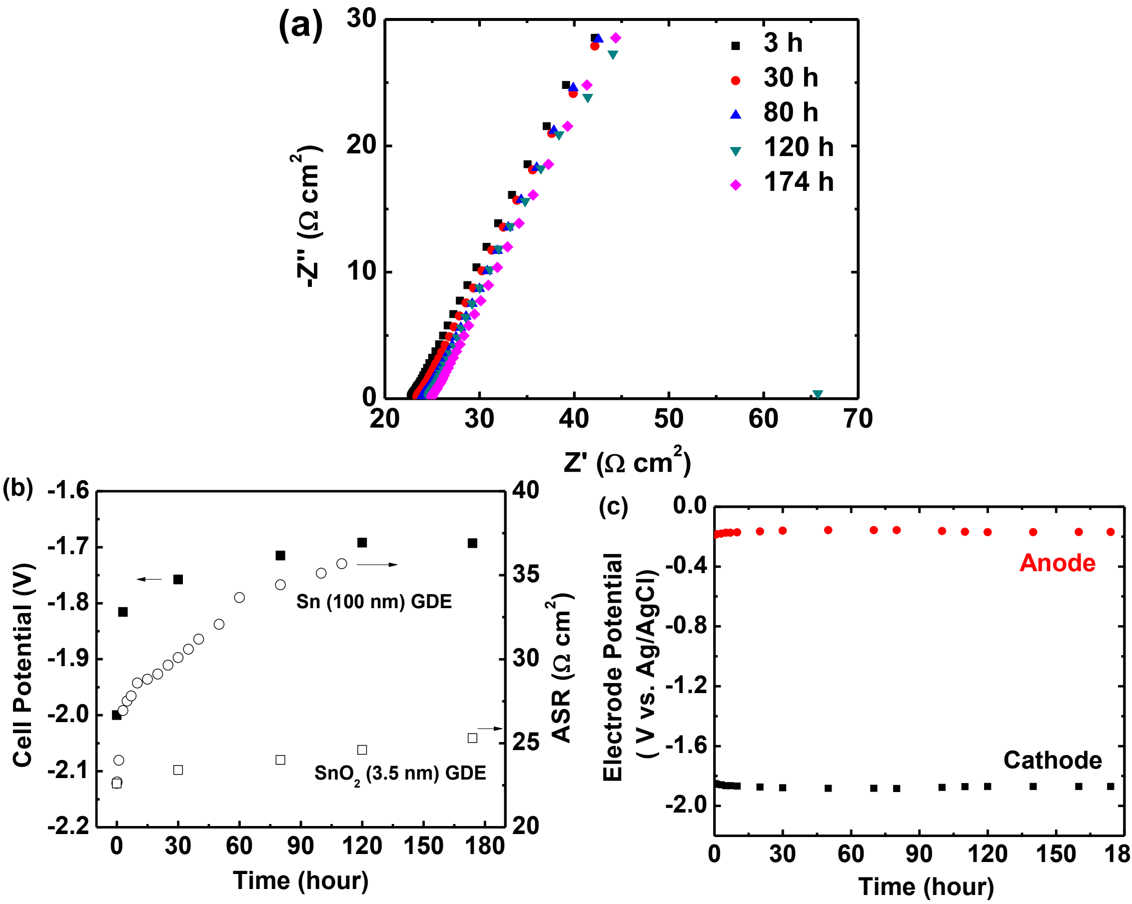

Figure 5.17. ASR and iR-compensated cell and electrode potentials during operation for 174 h.

The short-term performance of SnO_2 GDEs in the potential range between -0.8V and -2.2 V with an interval of 0.2 V was studied (**Figure 5.18**). The CO_2 electrolysis was conducted for 1 hour at each potential after SnO_2 GDE was undergone a pre-electrolysis for 1 hour at -2 V with Ar fed to cathode. The Faradaic efficiency of $HCOO^-$ achieved the maximum of ~90% at -2.0 V while the peak Faradaic efficiency of CO of ~10% was observed at -1.2 V. The total current density as well as the partial current densities of CO and $HCOO^-$ increased with the negative shift of cell potentials. No diffusion limitation to the partial current densities of CO and $HCOO^-$ was observed. The partial current densities of CO and $HCOO^-$ were comparable to that of Sn GDEs made of 100 nm Sn particles. Therefore, SnO_2 GDEs with 3.5 nm SnO_2 nanoparticles were considered as a promising alternate to Sn GDEs with improved stability and comparable short-term performance.

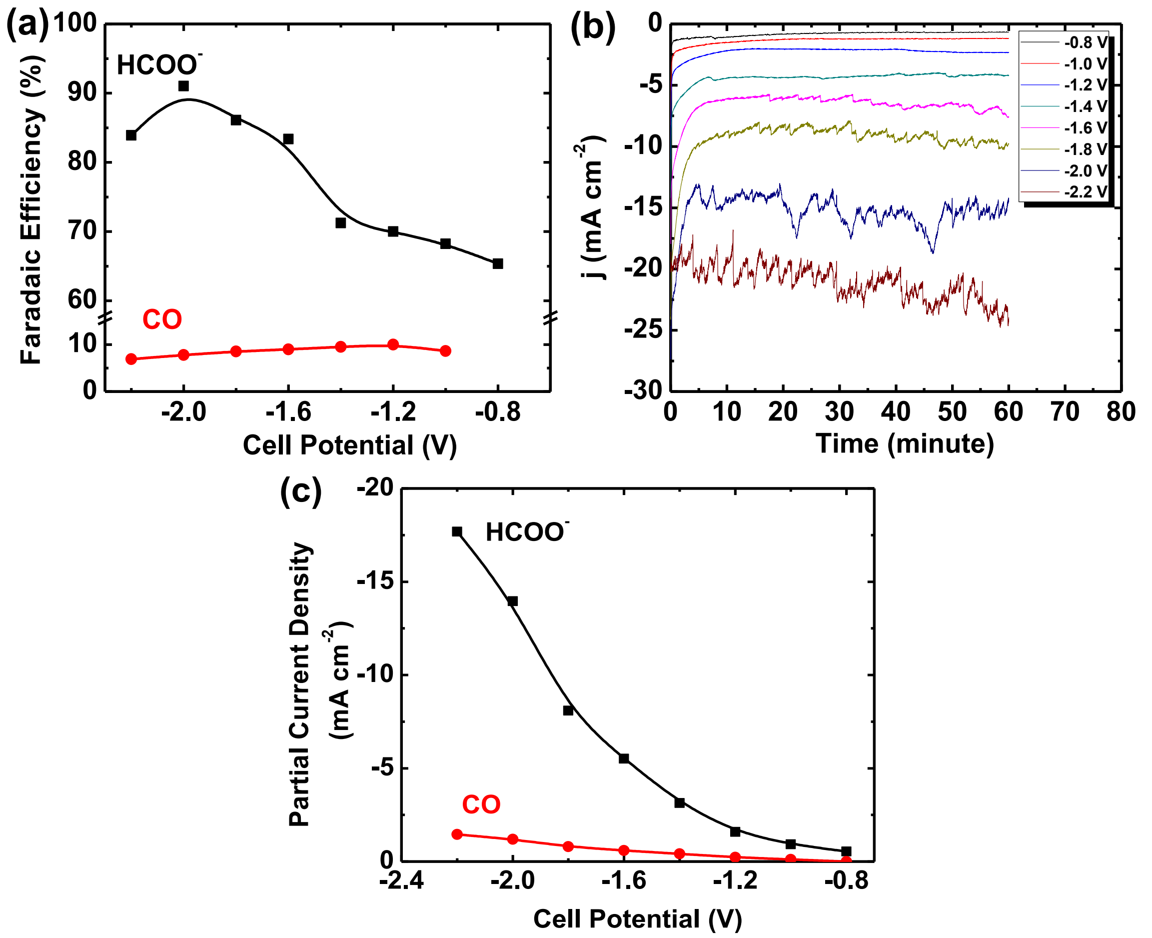

Figure 5.18. Electrocatalytic activity of SnO_2 GDE towards CO_2 reduction at potential range of -0.8 to -2.2 V. (a) Faradaic efficiency of CO and $HCOO^-$ versus cell potential, (b) current density with time , and (c) partial current density of CO and $HCOO^-$ versus cell potential. Before employed in CO_2 reduction, the SnO_2 GDE was pre-electrolyzed at -2 V for 1 hour under Ar.

5.4 Conclusions

Sn particles with 100 nm are observed to pulverize during long-term operation of CO_2 reduction in the electrochemical full cell. Pulverization is drastically severe for the first 15 hours, however, becomes mild afterwards due to strong effect of surface mechanics as the particles approach the critical size. The degradation of selectivity of Sn particles towards CO_2 reduction is accompanied with pulverization. In a long-term electrolysis with purified electrolyte at -2 V, the Faradaic efficiency towards formate production degrades from an initial value of 90% to 45% and the Faradaic efficiency towards CO production drops to 7% after 110 hours while the Faradaic efficiency of H_2 increases monotonically over the entire test period. The current density keeps stable at 17-18 mA cm^{-2} at -2 V over the electrolysis course. The pulverized Sn particles, however, exhibit no loss in intrinsic activity and selectivity towards CO_2 reduction as compared to intact fresh Sn particles. The decline of selectivity towards CO_2 reduction, especially formate production, is mainly attributed to the decrease of the cathode potential since the increasing of ohmic resistance resulting from pulverization. The pulverization is mitigated when using 3.5 nm SnO_2 nanoparticles instead of 100 nm Sn particles, and subsequently the electrode potential is stabilized. As a result, the Faradaic efficiency of formate and CO remains steady at about 70% and 6%, respectively, at -2 V after a pulse in the first 3~6 hours.

References

1. H. Yokokawa, N. Sakai, T. Horita, K. Yamaji, M. E. Brito and H. Kishimoto, *J. Alloys Comp.,* **452,** 41-47 (2008).
2. X. W. Yu and S. Y. Ye, *J. Power Sources,* **172,** 145-154 (2007).
3. Y. Y. Shao, G. P. Yin and Y. Z. Gao, *J. Power Sources,* **171,** 558-566 (2007).
4. B. Jermann and J. Augustynski, *Electrochim. Acta,* **39,** 1891-1896 (1994).
5. D. W. DeWulf, T. Jin and A. J. Bard, *J. Electrochem. Soc.,* **136,** 1686-1691 (1989).
6. S. Wasmus, E. Cattaneo and W. Vielstich, *Electrochim. Acta,* **35,** 771-775 (1990).
7. G. Kyriacou and A. Anagnostopoulos, *J. Electroanal. Chem.,* **322,** 233-246 (1992).
8. P. Friebe, P. Bogdanoff, N. Alonso-Vante and H. Tributsch, *J. Catal.,* **168,** 374-385 (1997).
9. Y. Hori, H. Konishi, T. Futamura, A. Murata, O. Koga, H. Sakurai and K. Oguma, *Electrochim. Acta,* **50,** 5354-5369 (2005).
10. P. Kedzierzawski and J. Augustynski, *J. Electrochem. Soc.,* **141,** L58-L60 (1994).
11. C. Delacourt, P. L. Ridgway, J. B. Kerr and J. Newman, *J. Electrochem. Soc.,* **155,** B42-B49 (2008).
12. H. Li and C. Oloman, *J. Appl. Electrochem.,* **35,** 955-965 (2005).
13. F. Koleli, T. Atilan, N. Palamut, A. M. Gizir, R. Aydin and C. H. Hamann, *J. Appl. Electrochem.,* **33,** 447-450 (2003).
14. J. Wu, F. G. Risalvato, F.-S. Ke, P. J. Pellechia and X.-D. Zhou, *J. Electrochem. Soc.,* **159,** F353-F359 (2012).
15. G. T. Baronetti, S. R. de Miguel, O. A. Scelza and A. A. Castro, *Appl. Catal.,* **24,** 109-116 (1986).
16. B. R. Strohmeier, *Surf. Interface Anal.,* **15,** 51-56 (1990).
17. Y. H. Chen and M. W. Kanan, *J. Am. Chem. Soc.,* **134,** 1986-1989 (2012).
18. Y.-T. Cheng and M. W. Verbrugge, *J. Appl. Phys.,* **104,** 083521-6 (2008).
19. J. Kleperis, G. Wójcik, A. Czerwinski, J. Skowronski, M. Kopczyk and M. Beltowska-Brzezinska, *J. Solid State Electrochem.,* **5,** 229-249 (2001).
20. C. Wang, A. John Appleby and F. E. Little, *J. Power Sources,* **93,** 174-185 (2001).
21. W. M. Zhang, J.-S. Hu, Y.-G. Guo, S. F. Zheng, L. S. Zhong, W. G. Song and L.-J. Wan, *Adv. Mater.,* **20,** 1160-1165 (2008).
22. J. Y. Huang, L. Zhong, C. M. Wang, J. P. Sullivan, W. Xu, L. Q. Zhang, S. X. Mao, N. S. Hudak, X. H. Liu, A. Subramanian, H. Fan, L. Qi, A. Kushima and J. Li, *Science,* **330,** 1515-1520 (2010).
23. J. W. Wang, X. H. Liu, S. X. Mao and J. Y. Huang, *Nano Lett.,* **12,** 5897-5902 (2012).
24. X. H. Liu, L. Zhong, S. Huang, S. X. Mao, T. Zhu and J. Y. Huang, *ACS Nano,* **6,** 1522-1531 (2012).
25. I. Ryu, J. W. Choi, Y. Cui and W. D. Nix, *J. Mech. Phys. Solids,* **59,** 1717-1730 (2011).
26. J. M. Tarascon and M. Armand, *Nature,* **414,** 359-367 (2001).
27. L. Y. Beaulieu, K. C. Hewitt, R. L. Turner, A. Bonakdarpour, A. A. Abdo, L. Christensen, K. W. Eberman, J. L. Krause and J. R. Dahn, *J. Electrochem. Soc.,* **150,** A149-A156 (2003).
28. P. Scherer, *Göttinger Nachrichten Math. Phys.,* **2,** 98-100 (1918).

Chapter 6

Dependence of Sn Electrode Performance on Surface Oxide Thickness in the Full Electrochemical Cell

6.1 Introduction

Tin (Sn) and copper (Cu) are considered as promising electrocatalysts to convert CO_2 to fuels (e.g. formate, methanol or hydrocarbons) because of their low cost, easy availability and high overall Faradaic efficiency towards fuel production. In general, an underlying requirement for a desirable electrocatalyst for electrochemical conversion of CO_2 is its capability of mediating multiple electron and proton transfers at relatively low overpotentials to promote CO_2 reduction reaction while suppressing the competing hydrogen evolution reaction.[1-4] Hence, understanding and tailoring the surface chemistry and morphology of the electrocatalysts become requisite to optimize the electrode performance.[5-7] Indeed, oxidized Cu electrodes containing a Cu_2O surface layer displayed superior activity towards methanol production[5, 6] than native Cu electrodes which primarily yielded CO_2 to CH_4 and C_2H_4[3, 7, 8]. Electrodes derived from metal oxides, e.g. Cu and Au prepared by reducing a micron thick Cu_2O and Au oxide films, respectively, have shown a great improvement over both activity and stability compared to polycrystalline metals.[9, 10]

Sn electrodes are known to possess a native oxidized exterior layer[11] which was found to be essential for the efficient reduction of CO_2 on a Sn foil electrode.[12] So far, the investigation has mostly focused on the foil electrodes carried out in a three-electrode electrolysis cell. In this chapter, we report studies of the dependence of electrochemical properties of Sn nanoparticles-based gas diffusion electrodes (GDEs) on the thickness of oxide layer by employing a full electrochemical cell based on PEMFC configuration. This design demonstrates the feasibility to utilize the electrocatalysts with an optimal oxide layer for electrochemical conversion of CO_2 at a future pilot-scale. Sn nanoparticles with an average particle size ~100 nm were chosen for applications in GDEs which are easily incorporated into low temperature full electrochemical cells.[13]

6.2 Experimental

6.2.1 Materials

$KHCO_3$ (99.7%), Nafion perfluorinated resin solution (5 wt.%) and isopropanol (99.5%) were purchased from Sigma-Aldrich; hydrogen (99.999%), argon (99.999%), helium (99.999%), and carbon dioxide (99.999%) were purchased from Airgas; Nafion® 212 membrane was purchased from Dupont; Pt/C (60%) was obtained from Johnson Matthey; Sn nanoparticles (ASP 100 nm) were purchased from Alfa Aesar; the graphite gas diffusion layer (GDL 10 BC) was ordered from SGL group. All chemicals were used without further purification. Electrolyte solutions were prepared with DI water (Siemens, Labstar™).

6.2.2 Annealing Procedure

Sn nanoparticles of 0.2 g were placed in a tube furnace (Thermo Scientific) under an air atmosphere at the specified temperature (100~180 ^{o}C) and time period (6~24 h). Sn nanoparticles were then allowed to cool slowly to room temperature over several hours.

6.2.3 Electrode Preparation

The Sn GDEs were prepared from the native and annealed Sn nanoparticles. The detail of electrode preparation has been described in Chapter 3. In short, a suspension of Sn nanoparticles and Nafion perfluorinated resin solution along with a 50/50 mixture of water and isopropanol were formed by ultrasonicating for at least 30 min before being sprayed onto GDLs to form GDEs with a Sn loading of ~2 mg cm^{-2}. The Sn GDEs were then heat-treated at 130 ^oC for 30 min in the vacuum oven and allowed to cool slowly back to room temperature before testing. The Pt ink was sprayed onto one side of Nafion® 212 membrane. The Nafion® 212 membrane side consisting of Pt catalysts was hot-pressed with a GDL at 130 ^oC and 50 PSI for 5 min to serve as an anode. The Pt loading was 0.3 mg cm^{-2}.

6.2.4 Physical Characterization

High-resolution transmission electron microscopy (HRTEM) images were acquired with a JEM-2100F TEM with a field-emission gun. Powder X-ray diffraction (XRD) patterns were collected by a Rigaku/Miniflex diffractometer with Cu K radiation detector. X-ray photoelectron spectra (XPS) were obtained with a PHI Versa Probe II Scanning XPS Microprobe. The oxide layer thickness can be calculated using the calculations of the type developed by Strohmeier and Carlson defined as follows:

$$d = \lambda_{ox} sin\theta \ln(\frac{N_m \lambda_m I_{ox}}{N_{ox} \lambda_{ox} I_m} + 1) \qquad (6.1)$$

where θ is the photoelectron take-off angle (90^o), λ_{ox} and λ_m are the inelastic mean free path (IMFP) of the oxide and metal, I_{ox} and I_m are the area percentages of the oxide and metal peaks from the high-resolution spectrum, and N_m and N_{ox} are the volume densities of the metal atoms in the metal and oxide, respectively. The IMFP can be acquired from NIST Electron Inelastic-Mean-Free-Path Database.

6.2.5 Electrochemical Testing in the Full Electrochemical Cell

The electrochemical test was carried out in a custom-designed full electrochemical cell involving a buffer layer with circulating aqueous electrolyte as developed in Chapter 4. The cell ran at T = 298.15 K and $P^o = 1.013$ bar. An electrolyte of 0.1 M $KHCO_3$ was pumped through the buffer layer at a rate of 7 mL min^{-1}. The anode side of the full electrochemical cell was supplied with H_2 at a rate of 150 ml min^{-1}. The cathode side of the full electrochemical cell was supplied with CO_2 at a rate of 45 ml min^{-1}. The electrolysis was conducted under a constant cell potential of -1.2 V for 2 hours by employing a potentiostat/galvanostat (Solartron 1470E) after first reducing each Sn GDE under Ar for 30 minutes at -2.0 V. Tests were also conducted at constant potentials for 30 minutes to analyze the GDEs selectivity towards the formation of CO and $HCOO^-$ over the potential range from -0.8 V to -2.0 V. In order to verify the removal of SnO_x after pre-electrolysis, linear scan voltammetry was conducted from -0.3 V to -2.0 V at 50 mV s^{-1} with Ar supplying to the cathode. The individual electrode potential during potentiostatic electrolysis was measured as referred to the Ag/AgCl reference electrode which was placed in the middle of the buffer layer. In order to correct IR drop, the ohmic resistance between the cathode and reference electrode was measured by electrochemical impedance spectroscopy at open circuit voltage, with amplitude of 5 mV and frequency range of 100 kHz to 0.1 Hz. During the electrolysis of CO_2, the cathodic compartment of the cell was continuously purged with CO_2 gas (99.999%) and vented directly into the sampling loop of a gas chromatograph (GC) to enable the quantification of gas-phase products. The liquid-phase products were quantified by ^1H nuclear magnetic resonance.[14]

6.3 Results and Discussion

6.3.1 Propagation of Oxide Layer by Annealing

Initial research focused on the analysis of the local chemistry and structure of oxide layers by utilizing transmission electron microscopy (TEM), X-ray diffraction (XRD), X-ray photoelectron spectroscopy (XPS) and Auger electron spectroscopy (AES). **Figure 6.1a** shows the space of lattice fringes in the high resolution TEM (HRTEM) is 0.296 nm for the surface layer of as-received Sn nanoparticles, which corresponds to the (101) reflection of SnO. The thickness of this native oxide layer is ~3.5 nm. TEM images of annealed Sn nanoparticles are shown in **Figures 6.1b to 6.1f**. The oxide layer thickness was ~5.4 nm in nanoparticles annealed at 100 °C for 6 h and 16.0 nm in the specimen annealed at 180 °C for 24 h. **Table 6.1** summaries the thicknesses of all specimens studied in this work. For Sn nanoparticles annealed at 180 °C for 24 h, the presence of SnO_2 (110) reflection is observed in the SnO_x layer (**Figure 6.1f**). **Figure 6.2** shows the XRD spectra of the as-received and annealed Sn nanoparticles**.** In the as-received Sn nanoparticles, all the reflections correspond to β-Sn allotrope. A shoulder peak at 29.94^o appears in the XRD pattern of Sn nanoparticles annealed at 100 ºC for 6 h, which corresponds to (101) reflection of SnO. The intensities of SnO reflections increase with annealing temperatures up to 180 ºC for 12 h. When Sn nanoparticles were annealed at 180 ºC for 24 h, the peaks corresponding to SnO_2 appears at 26.59^o for (110) and 33.87^o for (101) reflections, indicating the oxidation of SnO to form SnO_2.

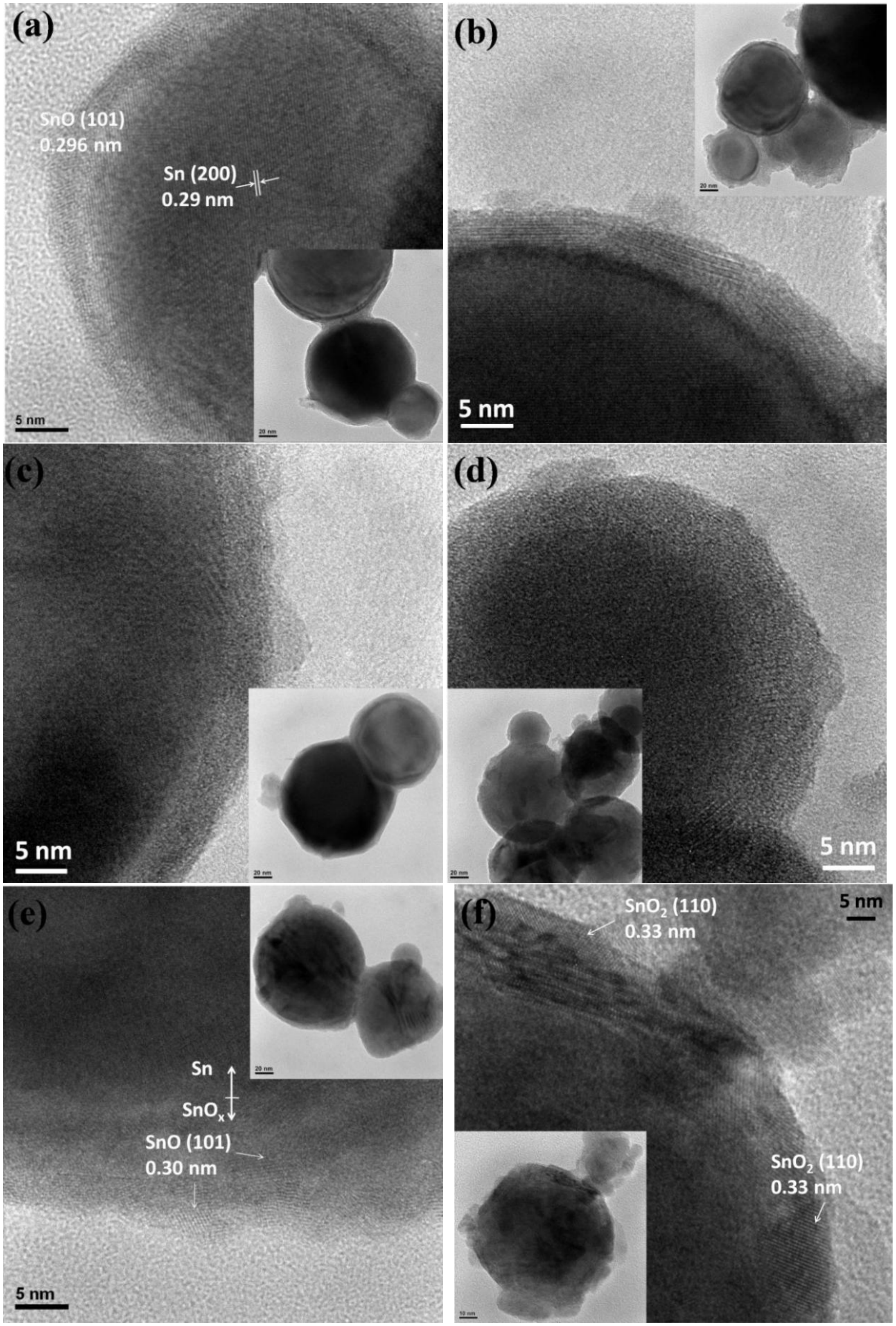

Figure 6.1. TEM of as-received and annealed Sn nanoparticles. (a) as-received Sn nanoparticles, and Sn nanoparticles annealed at (b) 100 ºC for 6 h, (c) 140 ºC for 6 h, (d) 180 ºC for 6 h, (e) 180 ºC for 12 h, and (f) 180 ºC for 24 h.

Table 6.1. Percentage of SnO_x and Sn at the Sn nanoparticle surface from XPS analysis and initial SnO_x layer thickness from TEM analysis.

Particles	**Sn %**	**SnO_x %**	**SnO_x thickness (nm)**
As-received	9	91	3.5 ± 0.4
Annealed 100 ºC 6 h	6	94	5.4 ± 0.6
Annealed 140 ºC 6 h	5	95	5.9 ± 0.4
Annealed 180 ºC 6 h	2	98	7.0 ± 0.9
Annealed 180 ºC 12 h	1	99	11.8 ± 1.1
Annealed 180 ºC 24 h	0	100	16.0±1.8

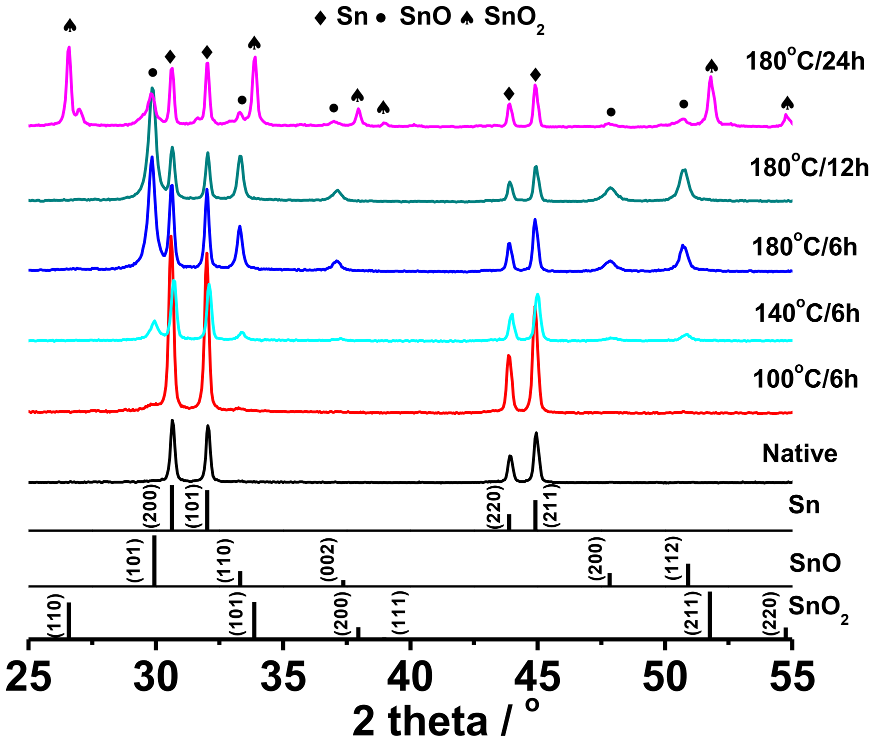

Figure 6.2. XRD patterns of as-received and annealed Sn nanoparticles.

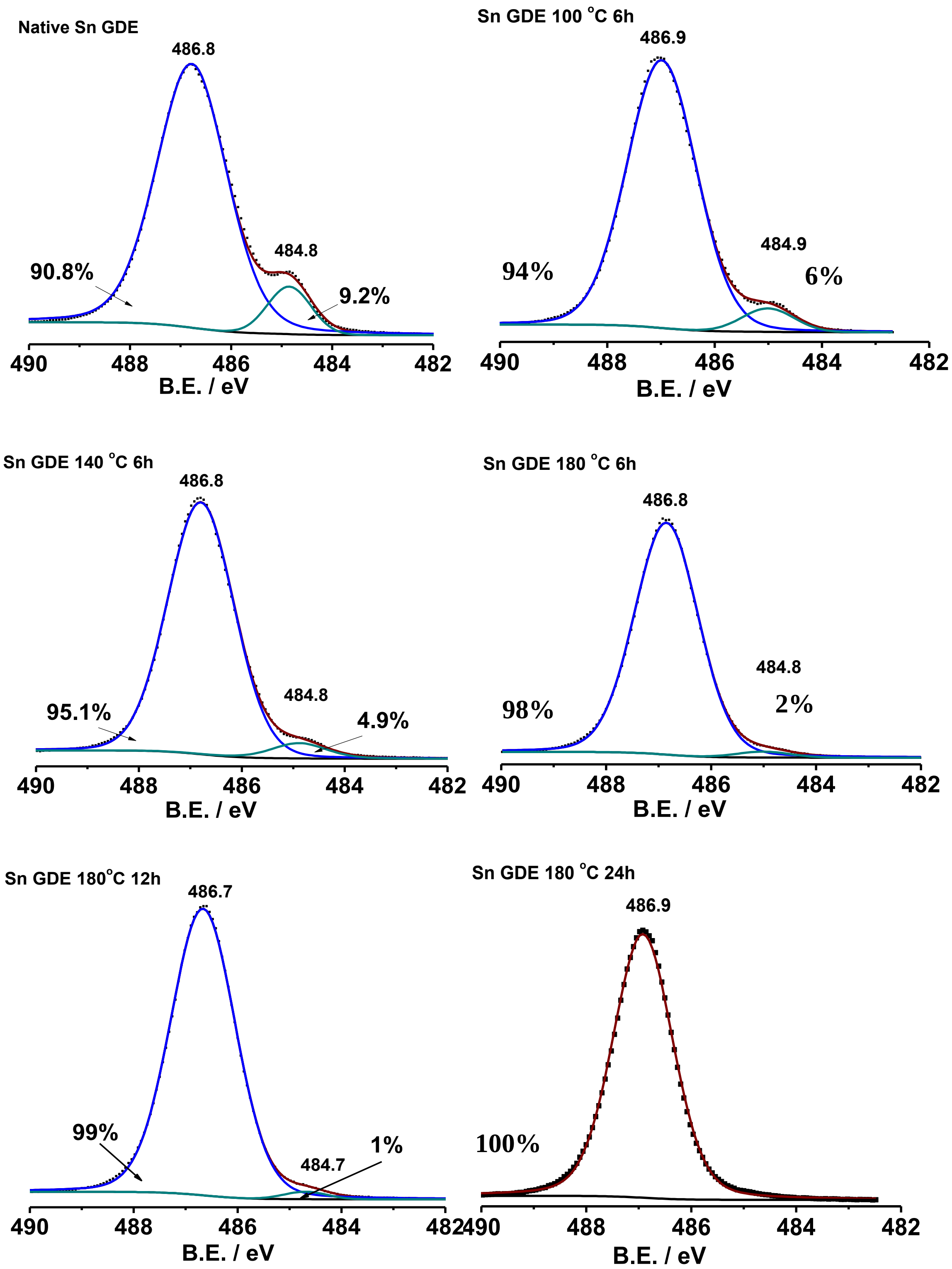

Figure 6.3. XPS of as-received and annealed Sn nanoparticles.

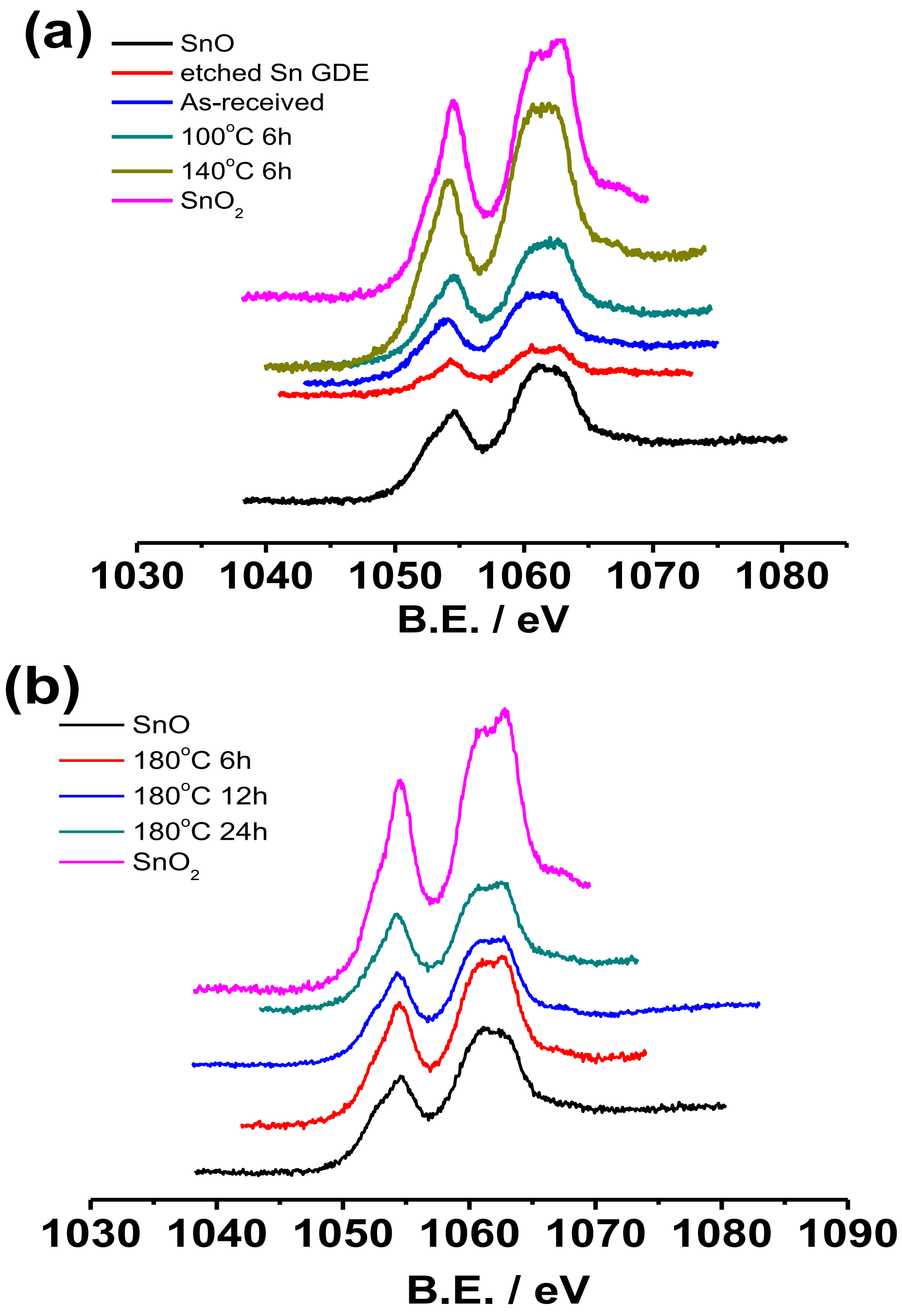

Figure 6.4. Auger spectra of etched Sn GDE, and as-received and annealed Sn particles together with commercial SnO and SnO_2 particles.

More surface analysis requires the use of XPS, which is capable of providing analysis of oxidation states of tin in the outer layer of ~10 nm of the specimen. **Figure 6.3** shows XPS spectrum of Sn $3d_{5/2}$, which consists of two peaks at the binding energies of 486.5 and 484.7 eV corresponding to $Sn^{4+/2+}$ (SnO_x) and Sn^o, respectively.[12, 15] The peaks were fit to yield an atomic ratio of 91: 9 for SnO_x : Sn^o, indicating a native SnO_x layer with a thickness of ~5 nm,[16, 17] which is slightly larger than that observed from TEM results. The increase of SnO_x/Sn^o atomic ratio with the increase of annealing temperature and duration is consistent with observations from XRD and HRTEM. AES of Sn MNN shows that SnO, not SnO_2, is the only phase observed in oxide layer in the as-received and annealed Sn nanoparticles, even at 180 °C for 12 h. The only exception is the specimen annealed at 180 °C for 24 h, in which SnO_2 appears (**Figure 6.4**). Longer annealing time (24 hours) resulted in the formation of SnO_2, suggesting the transformation from SnO to SnO_2 is a kinetically sluggish process.

6.3.2 Performance of Sn Nanoparticles with Various Oxide Layer Thicknesses

Linear sweep voltammetry was used to monitor the reduction of SnO_x layer in GDEs prepared from Sn nanoparticles annealed at 180 ºC for 24 h, which have the thickest oxide layer. After 20 min pre-electrolysis, SnO_x layer was removed as indicated by the absence of reduction peak for SnO_x layer (**Figure 6.5**).

The electrochemical reduction of CO_2 was then carried out at a cell potential of -1.2 V over 2 hours. **Figure 6.6a** shows the total geometric current density and the Faradaic efficiency towards CO production as a function of time with Sn GDEs consisting of as-received Sn nanoparticles (denoted as native Sn GDEs). The current density experiences a pulse in the first 10 seconds before stabilizing around -3 mA cm^{-2}. During this 2-hour electrolysis, the accumulative Faradaic efficiency towards CO and $HCOO^-$ production is 26% and 64%, respectively, with hydrogen evolution accounting for the remainder of the current.

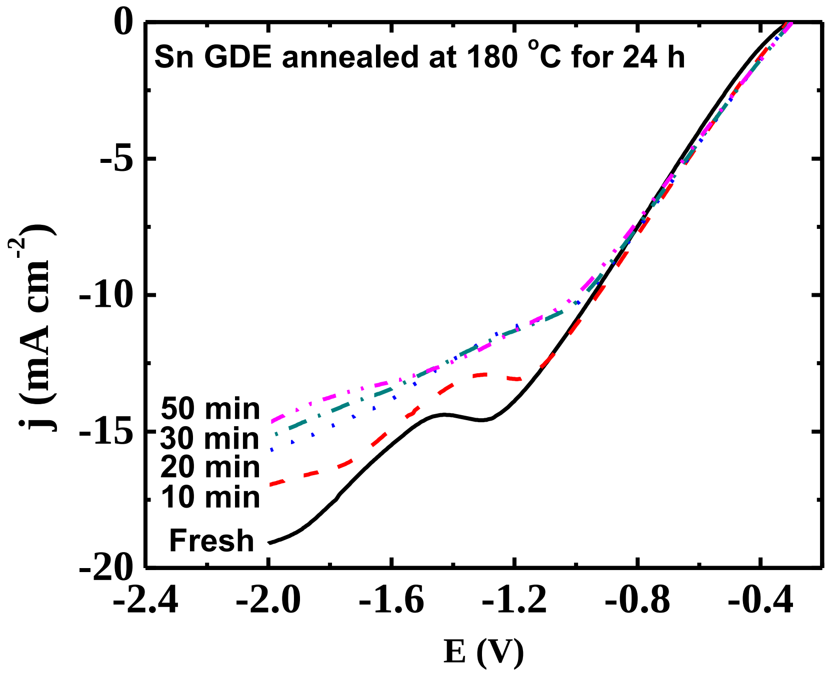

Figure 6.5. Linear scan voltammetry of Sn GDE annealed at 180 °C for 24 h before and after pre-electrolysis for a variety of duration. The SnO_x scale was removed after pre-electrolysis for 20 min at -2 V under Ar.

Figures 6.6b-6.6f show the performance of Sn GDEs consisting of annealed Sn nanoparticles with various thicknesses of oxide layer. These Sn GDEs exhibit similar current densities of -3 mA cm^{-2} to that of native Sn GDEs; however, the selectivity towards CO and $HCOO^-$ displays a dependence on initial oxide layer thickness. The Faradaic efficiency towards CO formation increases slightly with increasing oxide layer thickness, achieving the maximum of 35% for Sn GDEs with a SnO_x layer thickness of 7.0 nm (annealed at 180 °C for 6 h). With increasing the thickness, the Faradaic efficiency towards CO formation decreases to ~25% in the specimen with ~12 nm thick oxide. In contrast to the trend of Faradaic efficiency of CO, the Faradaic efficiency of $HCOO^-$ decreases with increasing SnO_x layer thickness. The Faradaic efficiency of $HCOO^-$ stabilizes around 40% in the sample with an oxide layer of 7 nm or thicker. The SnO GDE and SnO_2 GDE comprised of commercial SnO and SnO_2 powder (see XRD in

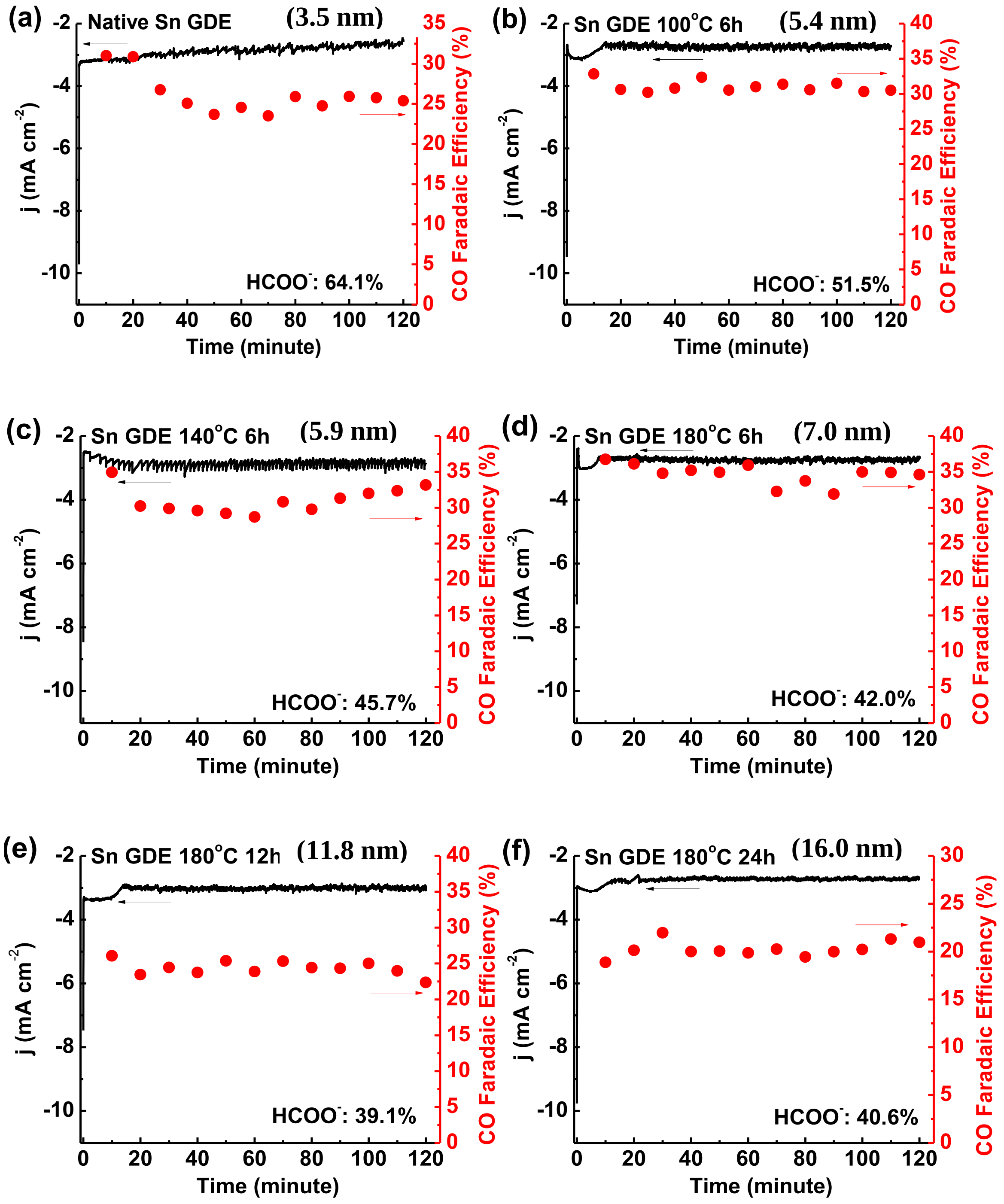
(a)
Native Sn GDE
(3.5 nm)
HCOO⁻: 64.1%
(b)
Sn GDE 100°C 6h
(5.4 nm)
HCOO⁻: 51.5%
(c)
Sn GDE 140°C 6h
(5.9 nm)
HCOO⁻: 45.7%
(d)
Sn GDE 180°C 6h
(7.0 nm)
HCOO⁻: 42.0%
(e)
Sn GDE 180°C 12h
(11.8 nm)
HCOO⁻: 39.1%
(f)
Sn GDE 180°C 24h
(16.0 nm)
HCOO⁻: 40.6%
j (mA cm⁻²)
-2
-4
-6
-8
-10
CO Faradaic Efficiency (%)
0
5
10
15
20
25
30
35
40
Time (minute)
0
20
40
60
80
100
120

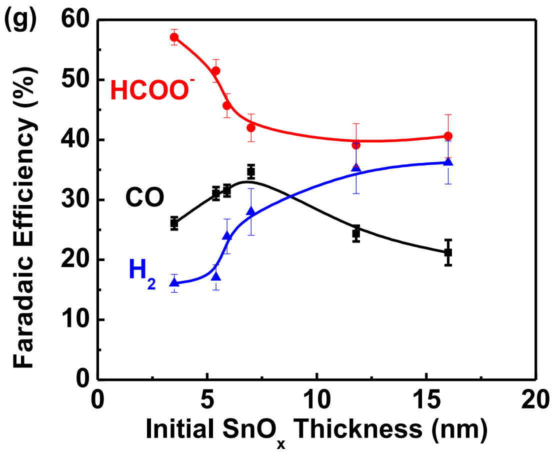

Figure 6.6. CO_2 reduction electrolysis data at a cell potential of -1.2 V for Sn GDEs made of as-received and annealed Sn nanoparticles. (a-f) Total current density versus time, Faradaic efficiency of CO versus time and cumulative Faradaic efficiency of $HCOO^-$ for electrodes with progressively thicker SnO_x layers. The electrode was firstly reduced at a cell potential of -2.0 V for 30 min under Ar before being employed for CO_2 reduction. (g) Faradaic efficiencies of CO, H_2 and $HCOO^-$ versus initial thickness of SnO_x layer.

Figure 6.7 and XPS in **Figure 6.8**, respectively, exhibited Faradaic efficiencies of $HCOO^-$ (~35%) and CO (20-25%) close to that for the Sn GDE with the thickest oxide layer (16 nm) as shown in **Figure 6.9**. This result differs from trends seen in oxide-derived Cu and Au bulk electrodes, in which Faradaic efficiencies towards CO and $HCOO^-$ production increases monotonically with increasing oxide layer thickness.[9, 10] In addition, we carried out CO_2 reduction on the SnO_2 GDE without pre-electrolysis, in which the reduction reactions of tin oxide to Sn and CO_2 to CO and formate occurred simultaneously. The Faradaic efficiency of formate was about 35% at the end of electrolysis and the Faradaic efficiency of CO reached to ~25% in one hour (**Figure 6.10**), which are similar to those of SnO_2 GDE with pre-electrolysis. Hence, the contribution of the existence of SnO_x towards improvement of the electocatalytic activity of Sn particles is negligible.

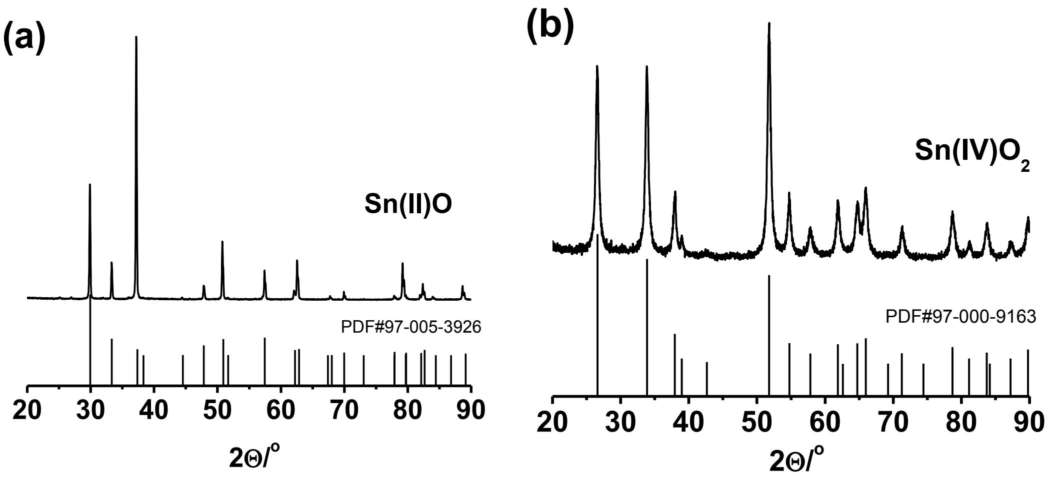

Figure 6.7. XRD patterns of commercial (a) Sn(II)O and (b) Sn(IV)O_2 powders.

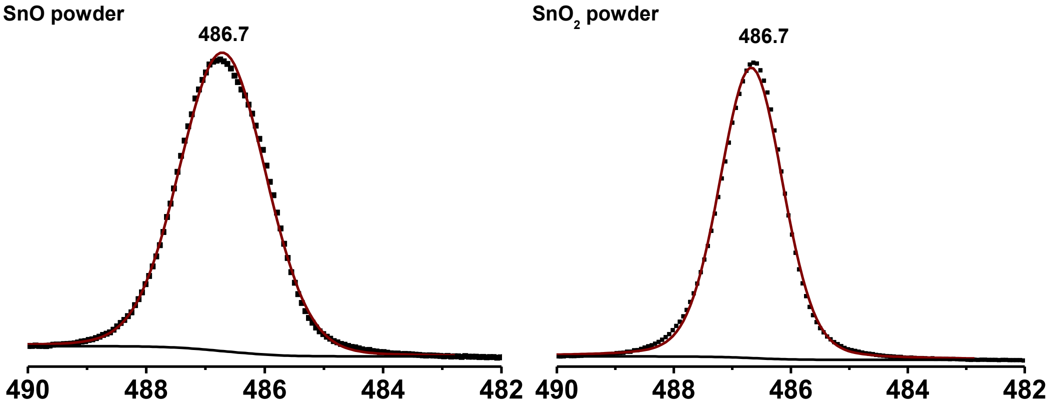

Figure 6.8. XPS of commercial (left) Sn(II)O and (right) Sn(IV)O_2 powders.

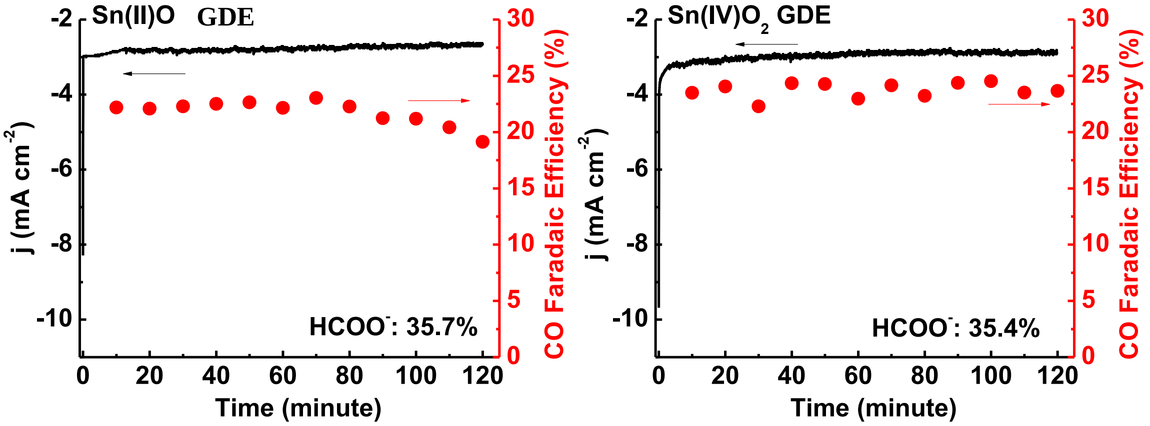

Figure 6.9. Electrochemical performance of commercial SnO (left) and SnO_2 (right) powders for CO_2 reduction at -1.2 V. Before initiating CO_2 reduction, both electrodes were reduced at -2 V for 30 min with Ar supplied to the cathode.

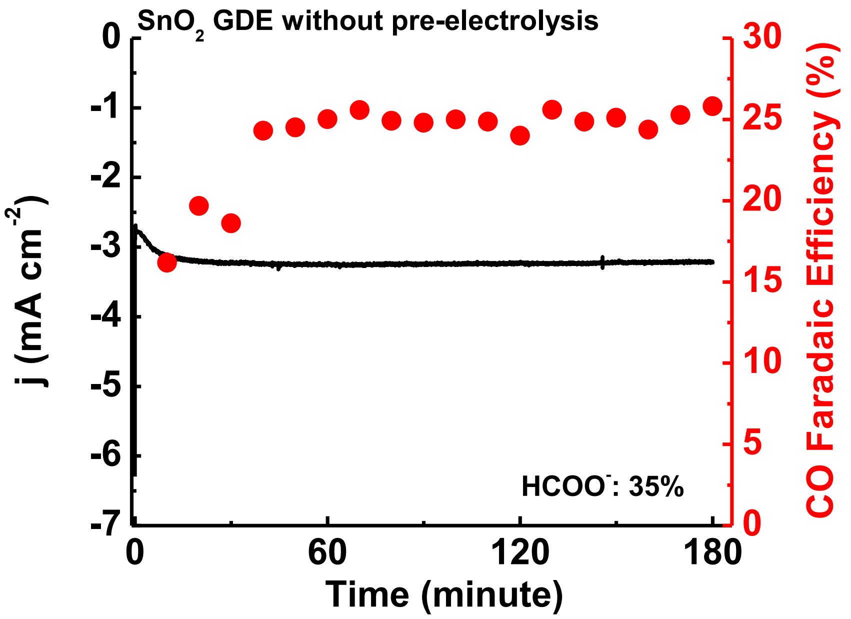

Figure 6.10. Performance of SnO$_2$ GDE without pre-electrolysis for CO$_2$ reduction at -1.2 V for 3 hours.

Figure 6.6g summaries the Faradaic efficiencies as a function of the initial oxide layer thickness. Each thickness was investigated in three different electrodes to obtain a statistical distribution of the Faradaic efficiency. The Faradaic efficiencies of HCOO$^-$ and CO display a strong, yet non-linear, dependence on the initial oxide layer thickness. The native Sn GDEs with a 3.5 nm oxide layer shows the highest Faradaic efficiency for HCOO$^-$ while the Sn GDEs with a 7.0 nm SnO$_x$ layer exhibits the highest Faradaic efficiency for CO. Sn GDEs with the thickest SnO$_x$ layer (16 nm) have the lowest Faradaic efficiencies for both CO and HCOO$^-$. The decreasing of total electrocatalytic activity towards CO$_2$ reduction with increasing SnO$_x$ layer is attributed to enhancement of hydrogen evolution on Sn clusters which possesses a low-coordination number after being reduced from the SnO$_x$.

To further characterize the effects of initial SnO$_x$ layer thickness on the electrocatalytic activity, the performance of native Sn GDE with as-received nanoparticles Sn (3.5 nm) and Sn GDE with Sn nanoparticles (16 nm) annealed at 180 °C for 24 h (for brevity annealed Sn GDE) was compared at a cell potential range between -0.8 and -2.0 V. **Figure 6.11a** shows the comparison of Faradaic efficiencies of CO and $HCOO^-$. At a relatively low cell potential of -0.8 V, the Faradaic efficiency of $HCOO^-$ is two-fold higher for the native Sn GDE than for the annealed Sn GDE; while at more cathodic cell potentials the Faradaic efficiency of $HCOO^-$ is only 20-40% higher. The Faradaic efficiency for CO is 20-30% higher in native Sn GDE, which possesses a thin SnO_x layer of 3.5 nm.

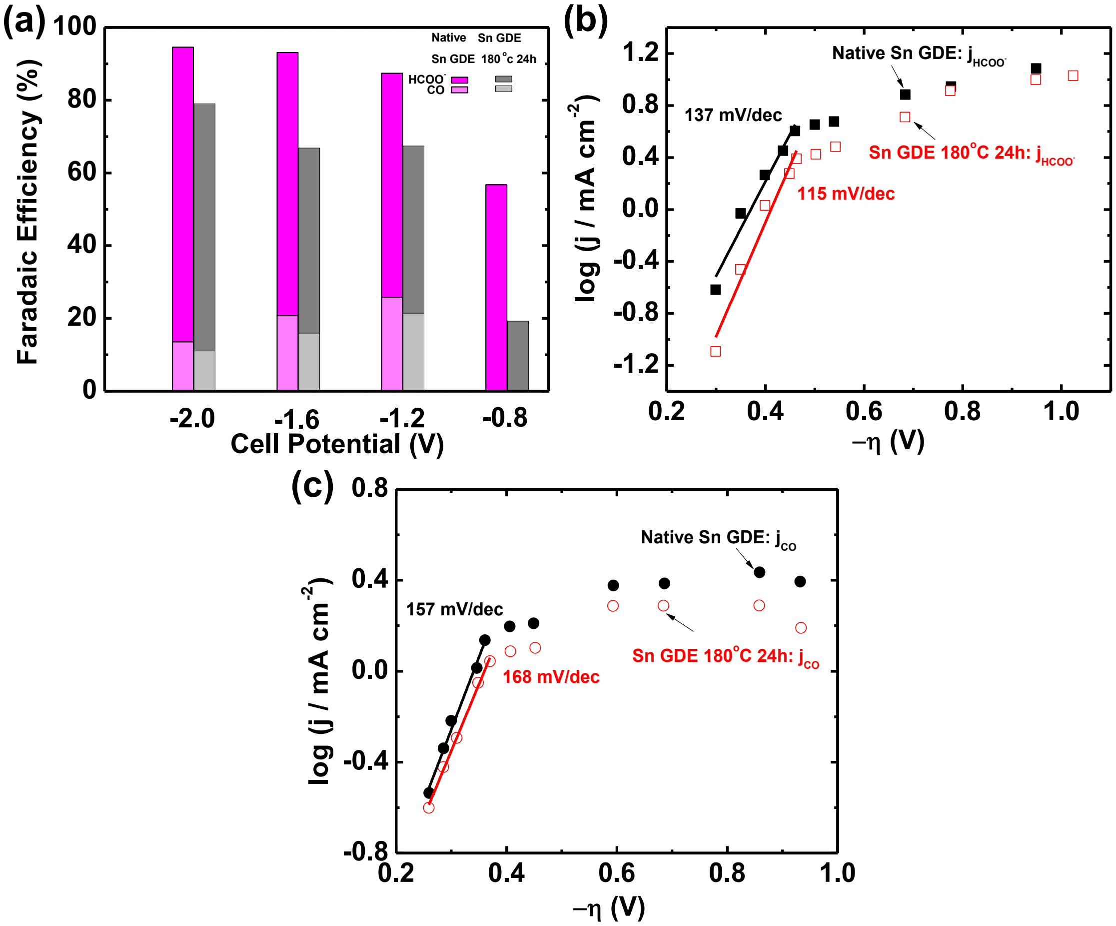

Figure 6.11. Comparison of the electrocatalytic activity and selectivity of the native Sn GDE and Sn GDE annealed at 180 °C for 24 h. (a) Faradaic efficiencies for $HCOO^-$ and CO at various potentials, and partial current densities of (b) $HCOO^-$ and (c) CO versus potential. Hydrogen formation accounts for the remainder of the current.

To investigate the mechanism by which CO_2 is reduced in the full electrochemical cells, Tafel plots for $HCOO^-$ and CO were extracted for Sn GDEs **(Figure 6.11b)**. The reduction of CO_2 to $HCOO^-$ on native Sn GDE shows a slope of 137 mV/decade at the overpotential range from -0.3 to -0.5 V while it shows a slope of 115 mV/decade for annealed Sn GDE. The data point at low overpotential regime deviates a little from linear due to the difficulty of quantifying extremely low concentration of $HCOO^-$ by using NMR. The reduction of CO_2 to CO shows a Tafel slope of 157 mV/decade and 168 mV/decade for native and annealed Sn GDEs, respectively, at overpotentials ranging from -0.2 to -0.4 V. In literature, a wide range of Tafel slopes for CO_2 reduction from 120 mV/decade to 350 mV/decade has been reported.[9, 18-20] These slopes indicate a rate-determining initial electron transfer to CO_2 forming a surface adsorbed $CO_2^{-\bullet}$ intermediate. The difference in Faradaic efficiency between native and annealed Sn GDEs suggests that Sn nanoparticle surface possessing less new nucleated Sn clusters following thinner SnO_x layer reduction has a stronger ability to thermodynamically stabilize the intermediate $CO_2^{\bullet -}$ while suppressing H_2 evolution.

6.4 Conclusions

In summary, our results show that there exists SnO_x thickness dependence for the selectivity towards the production of $HCOO^-$ and CO during the electrochemical reduction of CO_2. The electrode with Sn nanoparticles of a native 3.5 nm SnO_x layer shows the highest Faradaic efficiency towards the formation of $HCOO^-$. The maximum Faradaic efficiency toward CO formation was observed in the electrode with Sn nanoparticles possessing a 7.0 nm thick oxide layer; while the Faradaic efficiency for hydrogen increases with increasing the initial oxide thickness. This study demonstrates the importance of the surface chemistry and morphology of Sn nanoparticles in CO_2 reduction catalysis. It may be beneficial to study the structure–activity relationship in electrocatalysts analogous to Sn with a native oxide layer on the catalyst surface.

References

1. R. L. Cook, R. C. Macduff and A. F. Sammells, *J. Electrochem. Soc.*, **137,** 187-189 (1990).
2. D. T. Whipple, E. C. Finke and P. J. A. Kenis, *Electrochem. Solid-State Lett.*, **13,** D109-D111 (2010).
3. K. P. Kuhl, E. R. Cave, D. N. Abram and T. F. Jaramillo, *Energy Environ. Sci.*, **5,** 7050-7059 (2012).
4. N. S. Spinner, J. A. Vega and W. E. Mustain, *Catal. Sci. Tech.*, **2,** 19-28 (2012).
5. J. K. W. Frese, *J. Electrochem. Soc.*, **138,** 3338-3344 (1991).
6. M. Le, M. Ren, Z. Zhang, P. T. Sprunger, R. L. Kurtz and J. C. Flake, *J. Electrochem. Soc.*, **158,** E45-E49 (2011).
7. W. Tang, A. A. Peterson, A. S. Varela, Z. P. Jovanov, L. Bech, W. J. Durand, S. Dahl, J. K. Norskov and I. Chorkendorff, *Phys. Chem. Chem. Phys.*, **14,** 76-81 (2012).
8. Y. Hori, I. Takahashi, O. Koga and N. Hoshi, *J. Phys. Chem. B*, **106,** 15-17 (2002).
9. C. W. Li and M. W. Kanan, *J. Am. Chem. Soc.*, **134,** 7231-7234 (2012).
10. Y. Chen, C. W. Li and M. W. Kanan, *J. Am. Chem. Soc.*, **134,** 19969-19972 (2012).
11. C. Nayral, E. Viala, P. Fau, F. Senocq, J.-C. Jumas, A. Maisonnat and B. Chaudret, *Chem. Eur. J.*, **6,** 4082-4090 (2000).
12. Y. H. Chen and M. W. Kanan, *J. Am. Chem. Soc.*, **134,** 1986-1989 (2012).
13. J. Wu, F. G. Risalvato, P. P. Sharma, P. J. Pellechia, F. S. Ke and X. D. Zhou, *J. Electrochem. Soc.*, **160,** F953-F957 (2013).
14. J. Wu, F. G. Risalvato, F. S. Ke, P. J. Pellechia and X. D. Zhou, *J. Electrochem. Soc.*, **159,** F353-F359 (2012).
15. K. Balakrishnan and J. Schwank, *J. Catal.*, **127,** 287-306 (1991).
16. B. R. Strohmeier, *Surf. Interface Anal.*, **15,** 51-56 (1990).
17. T. A. Carlson and G. E. McGuire, *J. Electron. Spectrosc. Relat. Phenom.*, **1,** 161-168 (1972).
18. R. Schrebler, P. Cury, F. Herrera, H. Gómez and R. Córdova, *J. Electroanal. Chem.*, **516,** 23-30 (2001).
19. J. Ryu, T. N. Andersen and H. Eyring, *J. Phys. Chem.*, **76,** 3278-3286 (1972).
20. Y. B. Vassiliev, V. S. Bagotsky, N. V. Osetrova, O. A. Khazova and N. A. Mayorova, *J. Electroanal. Chem. Interfacial Electrochem.*, **189,** 271-294 (1985).

Chapter 7

Conclusions and Future Direction

The electrochemical reduction of CO_2 to fuels by leveraging the electricity from renewable energy sources has the potential to address the issues of fossil fuel shortage and environmental deterioration resulting from excessive CO_2 emissions. An economically viable electrolysis system for CO_2 reduction requires simultaneously high current density and energy efficiency, and long-term stability. So far, the development of electrochemical reduction of CO_2 system is slow due to the lack of scientific understanding of CO_2 reduction mechanism. This dissertation firstly studied the fundamental topic of the effects of electrolyte on the activity and selectivity towards CO_2 reduction, which provides insights into the CO_2 reduction chemistry at the electrode/electrolyte interface. And then, a full electrochemical cell featuring a circulating electrolyte buffer layer based on the current proton exchange membrane fuel cell (PEMFC) was designed to meet the requirements of both high current density and energy efficiency for the CO_2 reduction process. The microstructure of the Sn gas diffusion electrode (GDE) consisting of 100 nm Sn nanoparticles was optimized and incorporated into the full electrochemical cell. Following the study of activity and selectivity towards CO_2 reduction on the Sn GDEs in the full electrochemical cell, the long-term stability of Sn GDE was investigated, which revealed the degradation mechanism of Faradaic efficiency of target products. Based on the understanding of the degradation origin, the mitigation strategy was developed to achieve long-term stable operation. Finally, the dependence of the Sn GDE performance on the Sn nanoparticle surface structure was studied to provide insights into the structure-performance relationship. In details, the following issues were addressed in this work:

1) **Study of the electrochemistry of CO_2 reduction at electrode/electrolyte interface to reveal the effects of electrolyte.** The electrostatic adsorption of different cations with different dielectric constant and electrolyte concentration influence the potential at outer Helmholtz plane (OHP) which subsequently affects the proton concentration at the electrode surface. As a result, the activity and selectivity towards formate formation are strongly dependent on the electrolyte property. In the case of alkali metal ions, the selectivity towards formate production follows $Na^+ > K^+ > Cs^+$ in the relatively less negative potential range. Because the electrolyte with Na^+ holds the most negative potential at OHP and hence the highest proton concentration at the electrode surface to promote the protonation of $CO_2^{\bullet -}$ to form formate. However, Na^+ exhibits the lowest current density while Cs^+ shows the highest one due to two factors, the biggest absolute value of difference in the potential at OHP and applied potential and the highest electrolyte conductivity. The Faradaic efficiency of formate increases as the electrolyte dilutes, because the potential at OHP decreases leading to the increase of proton concentration at the electrode surface as the concentration of electrolyte drops. In contrast, the current density decreases when the concentration of electrolyte drops due to the decrease of potential at OHP as well as the electrolyte conductivity. Among the anions of SO_4^{2-}, Cl^- and

HCO_3^-, SO_4^{2-}favor higher Faradaic efficiency of formate while HCO_3^- exhibits the highest current density.

2) **Design of a low temperature full electrochemical cell for scalable conversion of CO_2 into fuels.** A full electrochemical cell with a PEMFC structure modified to include a buffer layer of circulating aqueous electrolyte was designed and assembled for the conversion of CO_2 to formate using a Sn GDE. The Sn GDE consisting of 100 nm Sn nanoparticles was employed for direct gas-phase CO_2 reduction in order to eliminate the limit of low solubility of CO_2 in aqueous solution. The microstructure of Sn catalyst layer was optimized with Nafion content of 17-20 wt.% to achieve the highest current density and Faradaic efficiency of formate. Using this cell with a buffer layer of 0.1 M $KHCO_3$, at room temperature and ambient pressure, the formate started to form at the overpotential of ~-0.2 V, irrespective of the fuel (H_2 or 1.0 M KOH) supplied to anode with the corresponding partial current density of ~-1 mA cm^{-2}. The maximum Faradiac efficiency (~90%) of formate occurred at -1.7 V~-2.0 V, at which the energy efficiencies was 30-40% and current density was over -10 mA cm^{-2}. An optimal buffer layer thickness of 2.90 mm and pH of 6 was observed for the highest yield of formate and CO in this full electrochemical cell due to the stronger effect of H^+ concentration at the electrode/electrode interface on the selectivity towards target products. This cell design employs current PEMFC configuration and thus can be easily scaled-up for the potential mass production of formate from CO_2, if the partial current density of formate can be further

increased to ~100 mA cm^{-2} at a moderate cell potential of -2.0 V by lowering the ohmic resistance.

3) **Exploration of the degradation mechanism of Sn GDEs during long-term operation and development of the mitigation strategy**. Sn nanoparticles with size of 100 nm were observed to pulverize into 2-3 nm due to hydrogen atom diffusion induced stress after 60 hours operation in the electrochemical full cell. The pulverization of Sn nanoparticles resulted in the increase of ohmic resistance due to the loss of electrical contact area between Sn particles and gas diffusion layer substrate. Consequently the IR-corrected cell and electrode potentials decreased, which mainly accounts for the degradation of selectivity towards formate production on Sn nanoparticles based Sn GDE. The pulverization was mitigated when using 3.5 nm SnO_2 nanoparticles due to surface mechanics and hence the electrode potential was stabilized. As a result, the Faradaic efficiencies of formate (70%) and CO (6%) remained steady during long-term operation of 174 hours. The current density maintained stable during long-term run.

4) **Investigation of the dependence of Sn GDEs performance on the initial thickness of surface tin oxide layer.** The surface of Sn particles is covered by a thin oxide (SnO_x) layer. The dependence of Sn GDEs performance on the initial thickness of surface SnO_x layer was investigated in the full electrochemical cell. The current density shows a negligible dependence on the initial thickness of SnO_x layer, while the selectivity towards the formation of CO and formate exhibits a strong relationship with the initial SnO_x thickness. Electrodes with a native SnO_x layer of ~3.5 nm exhibited the highest Faradaic efficiency (64%) of

formate at -1.2 V. The Faradaic efficiency towards CO production reached a maximum (33%) for the electrode with a SnO_x thickness of 7.0 nm. The Faradaic efficiency towards hydrogen production was observed to increase with increasing the initial thickness of SnO_x layer. These results suggest the underlying importance of surface structure on the selectivity and activity of Sn electrode for CO_2 reduction and provide insight into the development of efficient catalysts.

The conversion of CO_2 into fuels is a research area which attracts more and more interests. However, the development of this technology is limited by the lack of fundamental knowledge of reaction process. There is a lot of work to be done to address the issues in terms of reaction mechanism, catalyst activity and stability, electrolyte and reactor design and so on. The following section highlights just a few future research directions with a focus on questions and topics stemming from the results of this work:

1) The efficient catalysts are the key for an economically viable electrochemical reduction of CO_2 process. The *in-situ* characterization is needed to study the surface structure and composition change of Sn electrodes during the reduction of CO_2, which is helpful to provide insights into the active sites for CO_2 reduction. Similarly, this *in-situ* study should extend to the surface of other metals, especially Cu, to explore the hydrocarbon formation mechanism. The exploration of the role of metal oxides playing in the CO_2 reduction process is beneficial to develop novel nanostructured catalysts. In addition, current research in catalyst emphasizes on the metal, which should be open to others, like oxides and composite materials.

2) The local proton concentration plays a vital role in determining the selectivity towards CO_2 reduction, which has extensively shown in this work. More work is needed to further understand the competition between H_2 evolution reaction and hydrogen protonation process. In addition, the protonation of C versus O in CO_2 molecular is worth investigating to reveal the formation mechanism of hydrocarbons and alcohols. This research would rely on the development of spectroscopic characterization of relevant transient catalytic intermediates.

3) This work designs a full electrochemical cell for electrochemical water oxidation at the anode and CO_2 reduction at the cathode. Multiphysical modeling is required to understand the ion (especially H^+) distribution across the buffer layer, the effect of electrolyte circulating rate, cell temperature and reaction gas pressure on the performance. The ultimate goal is driving the CO_2 reduction process with renewable energy sources such as solar energy. Therefore, modifications to the full electrochemical cell are necessary to achieve photo-splitting of water at the anode, which subsequently provides protons and electrons for CO_2 reduction at the cathode. Moreover, this full electrochemical cell could be further modified to become a tandem cell for photo-electrochemical reduction of CO_2. In this case, the tandem cell consists of a photoanode and a photocathode to expand the energetic range of light collected by the system. The photoanode (e.g. TiO_2 or WO_3) is designed to absorb high energy UV light while the photocathode (e.g. Cu_2O) absorbs predominately visible light.

4) Long-term stability is essentially important for an industry application. This stability partly includes the durability of cell components, e.g. catalyst layer in the

GDEs. Although this work provides a mitigation strategy to Sn GDEs, new origins of degradation may appear for newly developed active materials, which need special attention. On the other hand, the effects of contaminants on the operation of the cell will be important, particularly using CO_2 feedstock captured from flue gases.

Appendix A. Regions of Electrochemical Stability of Water

A key task for CO_2 research is to suppress hydrogen evolution because the thermodynamic reduction potential of hydrogen evolution is close to that of CO_2 reduction. The **Figure A.1** describes the electrochemical stability of water at 25 °C and standard pressure as a function of the potential and the pH of the electrolyte.

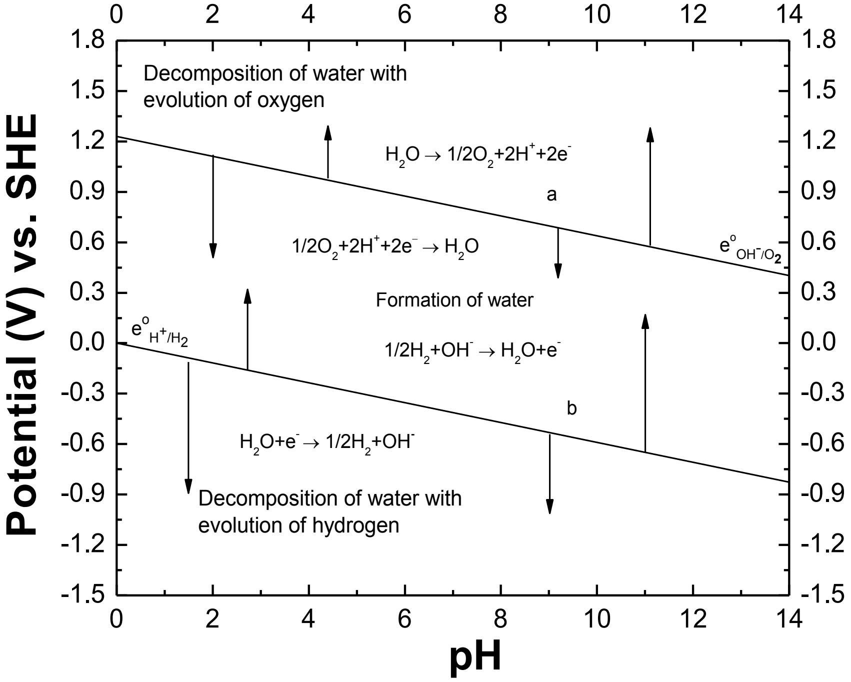

Figure A.1. Regions of electrochemical stability of water.

In **Figure A.1**, the reversible potential of the hydrogen line, line "b", results from the hydrogen evolution reaction in an acidic solution:

$$2H^+ + 2e^- \rightarrow H_2$$

In an alkaline solution, the equivalent reaction is:

$$2H_2O + 2e^- \rightarrow H_2 + 2OH^-$$

The half cell electrode potential as a function of the pH of the solution is defined as:

$$e^o_{H^+|H_2} = e^o_{H^+|H_2} - 0.059pH$$

The area below line “b” corresponds to the area where the water decomposition with hydrogen evolution reaction occurs.

The area in **Figure A.1** between the oxygen equilibrium potentials, (line “a”), and the hydrogen lines, is where the water is stable. At this region water may be synthesized from oxygen and hydrogen. The area above the line “a” corresponds to region where the water decomposes with formation of oxygen.

$$2H_2O \rightarrow O_2 + 4H^+ + 4e^-$$

and

$$4OH^- \rightarrow O_2 + H_2O + 4e^-$$

The Nernst equation for the oxygen equilibrium potentials is defined as:

$$e_{O_2|H_2O} = e^o_{O_2|H_2O} - 0.059pH$$

At pH = 0, the equilibrium electrode potential for the reaction is 1.22 V vs. SHE, while that of OH^-, at pH = 14, is 0.401 V vs. SHE at unit activity. The area above line “a” corresponds to region where the water decomposition proceeds with formation of oxygen.

Appendix B. Single Full Electrochemical Cell Assembly and Measurement

1. The components of the single full electrochemical cell consist of end-plate, current collector plate, graphite flow field, gasket, anode electrode of half-MEA, buffer layer and cathode electrode, as displayed in **Figure B.1(a)**.

2. Clean the cell hardware, especially the flow fields, with a residue-free solvent such as acetone and ethanol, rinse with distilled or deionized water, and dry.

3. Build-up the cell by laying components.

1) Anode gasket on anode flow field
2) Anode electrode of half-MEA within the cut-out in the gasket with the membrane facing outward
3) Buffer layer over the half-MEA aligned using alignment pins
4) Cathode electrode covering the cut-out in the buffer layer
5) Cathode flow field
6) Cathode current collector plate and end plate combination

4. Lightly lubricate the threads of the bolt with a non-reactive/non-flammable lubricant.

5. Feed bolts through the cathode end plate holes and into the anode end plate and finger-tighten.

6. Torque to desired level (e.g. 150 in.-lb.) using a star/cross pattern at approximately 10 to 15 in.-lb. increments.
7. A ready assembled cell as shown in **Figure B.1(b)**.
8. Check for gross gas leaks.
9. Pump electrolyte solution and check the electrolyte leaks.
10. Conduct the electrolysis under either potentiostatic or galvanostatic mode using four-electrode connection.
11. Collect the electrolyte and measure the volume for later NMR quantification of the liquid product concentration.
12. Rinse the cell by pumping the fresh electrolyte between two measurements and then start a new measurement.

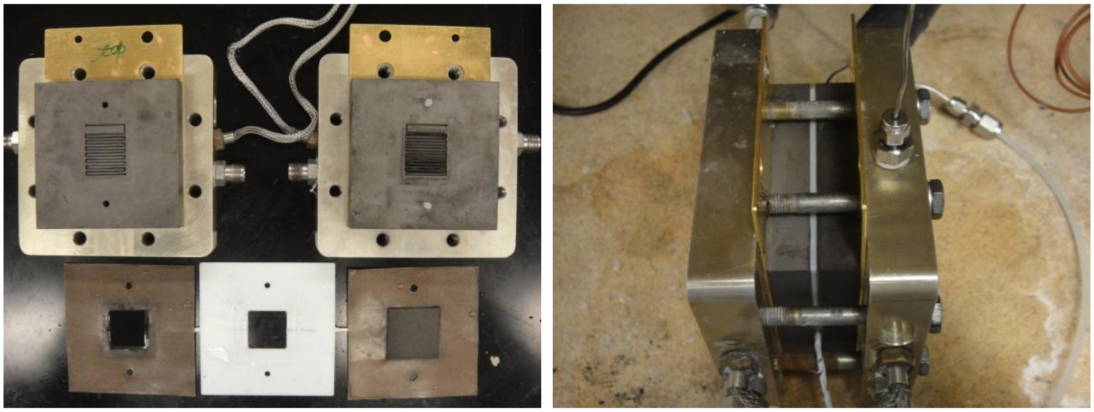

(a) (b)

Figure B.1. (a) A single full electrochemical cell ready for assembly, and (b) an assembled full electrochemical cell with a buffer layer.

Appendix C. Nuclear Magnetic Resonance Product Quantification[1,2]

Nuclear Magnetic Resonance (NMR) is a powerful non-selective, nondestructive analytical tool that enables you to ascertain molecular structure including relative configuration, and even intermolecular interactions of an analyte. Although NMR is also capable of obtaining relative and absolute concentration of an analyte, it requires carful operation since differences in the T_1 (T_1 is 1/R, where R is the rate of relaxation. After one T_1, approximately 63% of the magnetization has returned to the Z-axis) of analytes can lead to differing peak areas when measurements are made under differing conditions, such as different number of scans or solution compositions. In addition, there are other factors, such as shimming and phasing that can cause differences in peak areas. Despite these difficulties, we found NMR to be extremely useful for detection of electrochemical products because it could be performed directly on the electrolyte solution without the need to remove the $KHCO_3$. To avoid problems arising from the analyte and internal standard having different T_1s, the same spectral acquisition parameters were used for all quantification spectra. In addition, solvent suppression was used to decrease the intensity of the water peak so that the smaller CO_2 reduction product peaks were visible. Moreover, a linear regression line of calibration which was obtained from the NMR measurement of the authentic samples was employed in order to remove the instrumental error. The compound of sodium 3-(trimethylsilyl) propionate 2, 2, 3, 3-d (4) (TSP) dissolved in D_2O was used as the internal standard species. The structure of TSP is displayed in Figure C.1. TSP is non-volatile which allows for use and storage of the same internal standard solution for all of the product measurements in our study without appreciable change in concentration. The ^{1}H signal of CH_3 group in TSP is 0 ppm, so it won't interfere with peaks arising from CO_2 reduction products.

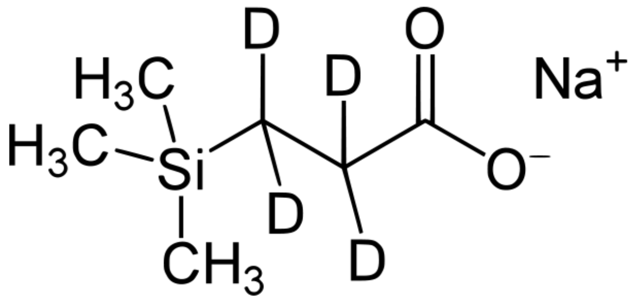

Figure C.1. Chemical structure of sodium 3-(trimethylsilyl) propionate 2, 2, 3, 3-d (4) (TSP).

Our 1D ^{1}H NMR spectra were acquired using a Varian Mercury 400 MHz instrument in a wet sequence model. Data was collected at room temperature. In the measurement of NMR, in addition to the spectrometer frequency (400 MHz in our case), the other parameters such as pulse width, acquisition time, spectral width and relaxation delay play key roles in obtaining accurate peak areas. The typical one cycle of pulse sequence is shown in **Figure C.2**. In a typical NMR acquisition, this pulse sequence will be repeated many times in order to improve signal-to-noise (S/N), which increases as the square root of the number of scans. Prior to applying a radio frequency pulse, a slight majority of nuclear spins are aligned parallel to the static magnetic field (B_0). Application of a short radio frequency pulse at the appropriate frequency will rotate the magnetization by a specific angle [$\theta = 360(\lambda/2\pi)B_1t_p$ degrees, where $(\lambda/2\pi)B_1$ is the radio frequency field strength and t_p is the time of the pulse]. Pulses are generally described by this angle of rotation (also called flip angle). The amount of rotation is dependent on the power and width of the pulse in microseconds. For example, a 30° pulse width is the amount of time the pulse of energy is applied to the particular sample in order to flip all the spins into a plane with angle of 30º relative to the Z-plane. The acquisition time is the duration of the decaying sine wave which represents the process of Free-induced decay (FID). The spectral width is the range of frequencies over which NMR signals are to be detected. After the radio frequency pulse, the nuclear spins do not instantly return to equilibrium; rather, they relax according to a time constant called T_1, so relaxation delay needs to be set long enough to eliminate the varied attenuation of the signals and inaccurate integration.

The typical parameters used in our NMR acquisition were: pulse width=30º, acquisition time = 2.18 s, relaxation delay = 20 s, spectral width = 6410.3 Hz, and 32 FID scans.

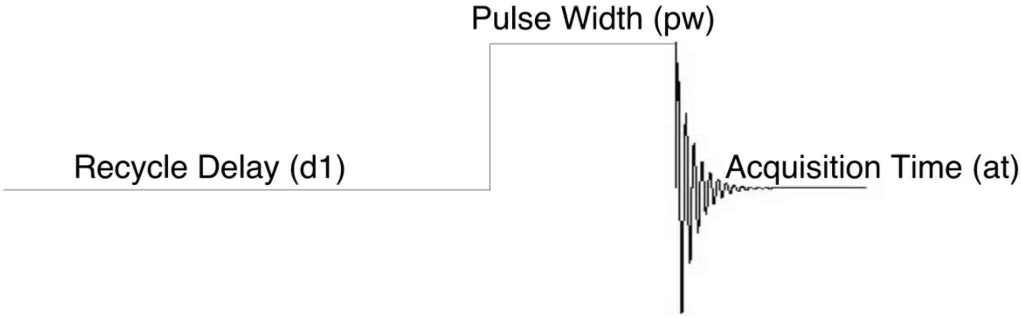

Figure C.2. Schematic representation of one cycle of a simple ‘1PULSE’ pulse sequence.

References

[1]. T.C. Farrar, *An Introduction To Pulse NMR Spectroscopy,* Farragut Press, Chicago, 1987.
[2]. Joseph P. Hornak, *The Basics of NMR*, http://www.cis.rit.edu/htbooks/nmr/inside.htm.

Appendix D. Coupling Oxygen Evolution and CO_2 Reduction in the Full Electrochemical Cell

When the anode of the full electrochemical cell was supplied with 1 M KOH and cathode fed with CO_2, oxygen evolution and CO_2 reduction occurred at the anode and cathode, respectively, to mimic the process of biosynthesis. In this case, the K^+ instead of H^+ transports through the Nafion membrane to balance the charge in the cell. The K^+ moles in the electrolyte of 0.1 M Na_2SO_4 match the electron moles that passed during the electrolysis of CO_2 (**Figure D.1**).

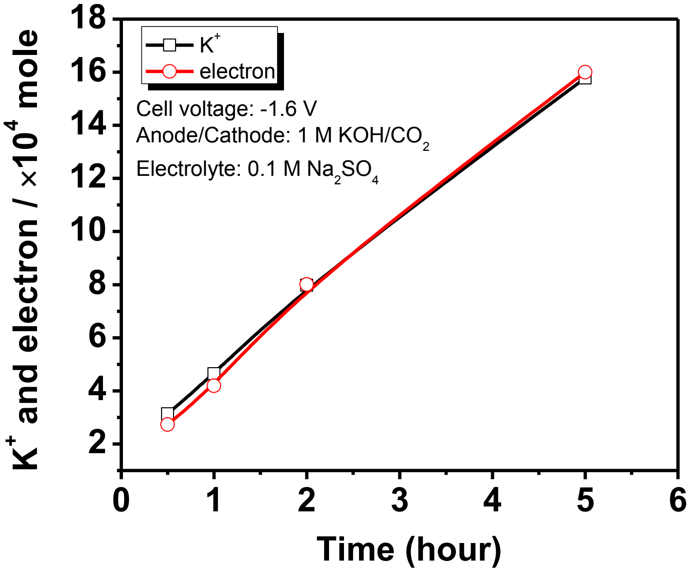

Figure D.1. K^+ moles in the electrolyte matching the electron moles that passed during the electrolysis of CO_2.

Appendix E. Author's Publications

1. **J. Wu**, F. Xia, M. Pan and X. D. Zhou, Oxygen Reduction Reaction on Active and Stable Nanoscale $TiSi_2$ Supported Electrocatalysts, *J. Electrochem. Soc.,* **159**, B654, 2012.
2. **J. Wu,** F. G. Risalvato, F. Ke, P. J. Pellechia and X. D. Zhou, Electrochemical Reduction of Carbon Dioxide I. Effects of the Electrolyte on the Selectivity and Activity with Sn Electrode, *J. Electrochem. Soc.*, **159**, F353, 2012.
3. **J. Wu**, F. G. Risalvato, P. P. Sharma, F. Ke, P. Pellechia, and X. D. Zhou, Electrochemical reduction of carbon dioxide: II. Design, Assembly and Performance of Low Temperature Full Electrochemical Cells, *J. Electrochem. Soc.*, **160**, F953, 2013.
4. **J. Wu**, F. G. Risalvato, S. Ma, and X. D. Zhou, Electrochemical Reduction of Carbon Dioxide III. The Role of Oxide Layer Thickness on the Performance of Sn Electrode in a Full Electrochemical Cell, *J. Mate. Chem. A*, in press.
5. A. Shahani**, J. Wu**, L. Wu, Q. Wang and X. D. Zhou, Morphological Transformations and Electrochemical Properties of Hydrothermally Synthesized MnO_2 Nanostructures, *ECS Trans.*, **40**, 185, 2011.
6. **J. Wu**, F. G. Risalvato and X. D. Zhou, Effects of the Electrolyte on Electrochemical Reduction of CO_2 on Sn Electrode, *ECS Trans.*, **41**, 49, 2012.
7. **J. Wu**, B. Harris, P. P. Sharma, and X. D. Zhou, Morphological Stability of Sn Electrode for Electrochemical Conversion of CO_2, *ECS Trans.*, **58**, 71, 2013.

8. **J. Wu,** P. P. Sharma, B. Harris, and X. D. Zhou, On the Microstructure of Sn Gas Diffusion Electrodes for Electrochemical Conversion of CO_2 into Formate, *ECS Electrochem. Lett.,* under review.
9. **J. Wu**, A. Shahani, L. Wu, Q. Wang and X. D. Zhou, Morphological Transformations and Electrochemical Properties of One Dimensional MnO_2 Nanostructures, *J. Mate. Chem. A*, under review.
10. **J. Wu**, B. Harris, P. Sharma, B. N. Popov and X. D. Zhou, Unraveling the Origin of Electrode Degradation and Designing Novel Stable and Active Electrodes for Electro-reduction of Carbon Dioxide. Submitted to *Nature-Communication.*